ISSN 1068-3755, Surface Engineering and Applied Electrochemistry, 2011, Vol. 47, No. 1, pp. 1–3. © Allerton Press, Inc., 2011.
Original Russian Text © Kh.M. Iliev, Z.M. Saparniyazova, K.A. Ismailov, M.Kh. Madzhitov, 2011, published in Elektronnaya Obrabotka Materialov, 2011, No. 1, pp. 5–7.

ELECTRICAL PRECISION TREATMENT OF MATERIALS

Formation of Nanoclusters of Gadolinium Atoms in Silicon

Kh. M. Iliev, Z. M. Saparniyazova, K. A. Ismailov, and M. Kh. Madzhitov
Tashkent State Technical University, ul. Universitetskaya 2, Tashkent, 100095 Republic of Uzbekistan
e-mail: mavlonov_g@mail.ru

Received June 7, 2010

Abstract—A technology of stagewise low-temperature diffusion of gadolinium into silicon that makes it possible to form nanoclusters of impurity atoms with a significant magnetic moment distributed throughout the volume of the material has been developed. It is shown that, unlike the samples obtained by high-temperature diffusion doping, the samples prepared by the new technology do not have surface erosion, and alloys and silicides are not formed in the near-surface region. Nanoclusters of impurity atoms of gadolinium in the volume of the crystal lattice of the silicon are studied using an MIK-5 infrared microscope. It is found that, in the stagewise low-temperature diffusion, the temperature and time of the diffusion have an effect not only on the depth of penetration of the impurities but also on the sizes of the resulting clusters; these factors can also prevent the formation of clusters. The study of the effect of low-temperature treatments on the size and distribution of clusters shows that, upon annealing in the temperature range of 500–700°C, the ordering of the clusters of gadolinium impurity atoms is observed. A further increase in the annealing temperature leads to the destruction of gadolinium clusters in the silicon bulk.

DOI: 10.3103/S1068375511010066

Semiconductor materials with nanoscale structures, particularly those with nanoclusters of impurity atoms, are of great scientific and practical interest [1, 2]. A number of new interesting physical phenomena are revealed in these materials; they make a substantial contribution to the development of present-day micro- and nanoelectronics [3], in particular, to the formation of nanoclusters of atoms of rare-earth elements.

The development of a technology for the formation of clusters of impurity atoms of rare-earth elements with controlled structures and properties in a silicon lattice is one of the most urgent and challenging objectives of modern nanoelectronics. As a matter of fact, the formation of clusters of impurity atoms of rare-earth elements in silicon makes it possible not only to control the basic parameters of the silicon and its magnetic properties but also to reveal a number of new as yet unknown physical phenomena [4].

The low values of the diffusion coefficients of rare-earth elements [5] cause some difficulties when employing high-temperature diffusion for the formation of nanoclusters of these impurity atoms in the silicon crystal lattice.

Therefore, the technology of stagewise low-temperature diffusion of gadolinium into silicon is developed; it offers the possibility to form nanoclusters of impurity atoms with a significant magnetic moment distributed throughout the volume of the material. These magnetic clusters make it possible not only to control the magnetic properties of the material but also to use these materials for the development of new spintronic devices. The results of studying the samples' surface after diffusion showed that, unlike the samples obtained by high-temperature diffusion doping, the samples prepared by the new technology exhibit no surface erosion, and alloys and silicides are not formed in the near-surface region.

Nanoclusters of impurity atoms of gadolinium in the volume of the silicon crystal lattice are studied using an MIK-5 infrared microscope. The MIK-5 offers the possibility to examine not only the surface of a silicon sample but also all its layers; that is, we can study a sample throughout the entire volume.

Figure 1 depicts a micrograph of a silicon sample subjected to the diffusion of gadolinium by the conventional high-temperature diffusion technology. The figure shows that clusters are not formed in the sample doped with gadolinium by the conventional technology. The micrograph of the surface of a silicon sample doped with gadolinium by the stagewise low-temperature diffusion is presented in Fig. 2. To determine the depth of penetration of the diffusing impurity of gadolinium and the presence of its clusters in the bulk, the silicon samples prepared by the new diffusion technology were subjected to successive grinding of 50 μm starting from the surface with the subsequent measurement of the specific resistivity by the four-probe technique and examination under a microscope. After each grinding, the presence of gadolinium clusters was checked microscopically. It is found that, for a silicon sample with a thickness of 1000 μm, the gadolinium penetrated to a depth of 700 μm from the surface, and clusters are formed in a layer with a thickness of

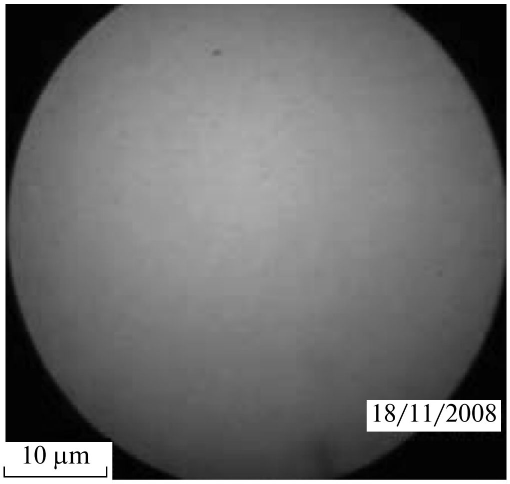

Fig. 1. Micrograph of the bulk of a silicon sample subjected to the diffusion of gadolinium by the conventional high-temperature diffusion technology.

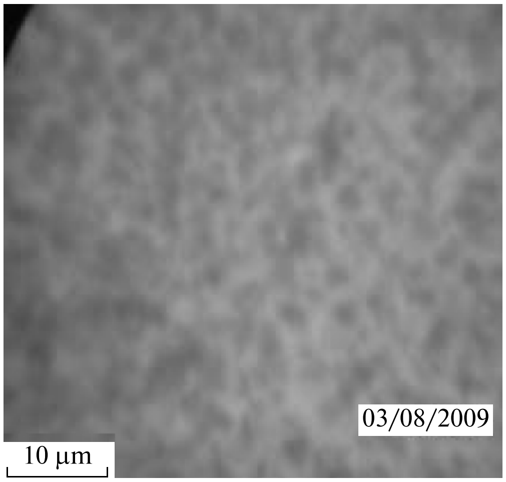

Fig. 2. Micrograph of the surface of a silicon sample doped with gadolinium by the stagewise low-temperature diffusion.

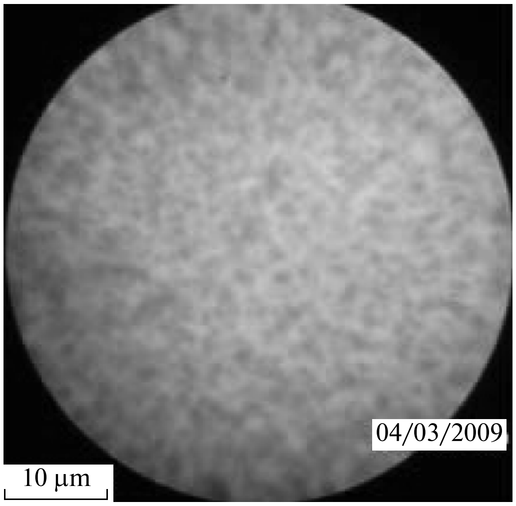

Fig. 3. Micrograph of a sample of silicon doped with gadolinium by the stagewise low-temperature diffusion after the removal of a 350-μm-thick layer (gadolinium clusters became apparent on the sample's surface).

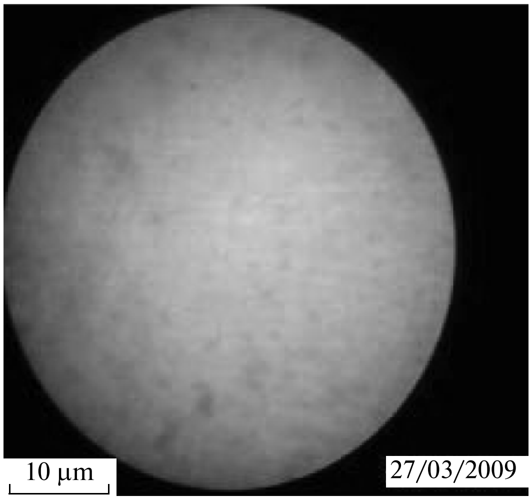

Fig. 4. Micrograph of a silicon sample prepared by the two-stage diffusion of gadolinium at relatively low final temperatures and holding times.

400 μm and are distributed uniformly throughout the thickness. After removing a layer with a thickness of 350 μm, the gadolinium clusters became apparent on the sample's surface (Fig. 3).

We found that, in the stagewise low-temperature diffusion, the temperature and time of the diffusion have an effect not only on the depth of penetration of the impurities but also on the sizes of the resulting clusters; these factors can also prevent the formation of clusters. Figure 4 presents a micrograph of a silicon sample prepared by the two-stage diffusion of gadolinium at relatively low final temperatures and holding time. It is evident that the number of resulting clusters is extremely scarce and their sizes are small, i.e., on the order of hundreds of nanometers.

With a further increase in the number of diffusion stages, their duration, and temperature, we obtained large clusters of gadolinium impurity atoms with a size of a few microns, which were uniformly distributed throughout the sample volume.

Interesting results were obtained for the three-stage diffusion. In this case, clusters were formed with the participation of defects of the silicon crystal lattice (Fig. 5).

The study of the effect of low-temperature treatments on the sizes and distribution of the clusters showed that, upon annealing in the temperature range

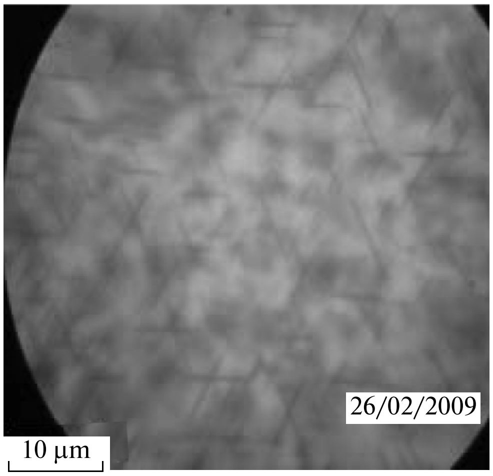

Fig. 5. Micrograph of a silicon sample prepared by the three-stage diffusion of gadolinium at relatively high final temperatures and a long holding time.

of 500–700°C, the ordering of the clusters of gadolinium impurity atoms is observed. A further increase in the annealing temperature leads to the destruction of the gadolinium clusters in the silicon bulk.

The analysis of these studies and the results on the formation of clusters of impurity atoms of gadolinium showed that more exacting studies of this phenomenon will make it possible to determine the technological conditions and modes for moving clusters to the desired places and preparing various devices such as diodes, transistors, resistors, and capacitors in the bulk of a semiconductor on their basis.

Preliminary studies showed that these materials exhibit fairly high resistance to radiation and high values of negative magnetoresistance at room temperature.

REFERENCES

1. Mil'vidskii, M.G. and Chaldyshev, V.V., Nanoclusters in Semiconductors: a New Approach to the Formation of Properties of Materials, *Fiz. Tekh. Poluprovodn.*, 1998, vol. 32, no. 5, pp. 513–520.
2. Suzdalev, I.P., *Nanotekhnologiya: fizikokhimiya nanoklasterov, nanostruktur i nanomaterialov* (Nanotechnology: Physicochemistry of Nanoclusters, Nanostructures, and Nanomaterials), Moscow: KomKniga, 2006.
3. Bakhadirkhanov, M.K., Ayupov, K.S., Mavlyanov, G.Kh., Zikrillaev, N.F., Isamov, S.B., and Koveshnikov, S.V., Studies of the Dependence of Negative Magnetoresistance in Silicon on the Concentration of Nanoclusters of Manganese Atoms, *Trudy mezhdunarodnoi konferentsii "Kremnii-2009"* (Proc. Int. Conf. on Silicon), Novosibirsk, 2009.
4. Bagraev, N.G. and Romanov, V.V., Magnetism of III–V Crystals Doped with Rare-Earth Elements, *Fiz. Tekh. Poluprovodn.*, 2005, vol. 39, no. 10, pp. 1173–1182 [*Semiconductors* (Engl. Transl.), vol. 39, no. 10, p. 1131].
5. Nazyrov, D.E., Diffusion of Europium in Silicon, *Fiz. Tekh. Poluprovodn.*, 2003, vol. 37, no. 5, pp. 570–571 [*Semiconductors* (Engl. Transl.), vol. 37, no. 5, p. 551].

ISSN 1068-3755, Surface Engineering and Applied Electrochemistry, 2011, Vol. 47, No. 1, pp. 4–8. © Allerton Press, Inc., 2011.
Original Russian Text © S.S. Belevskii, A.P. Kosova, S.P. Yushchenko, E. A. Yakhova, A.I. Shul'man, A.I. Dikusar, 2011, published in Elektronnaya Obrabotka Materialov, 2011, No. 1, pp. 8–13.

ELECTRICAL SURFACE TREATMENT METHODS

Changes in the Properties of a Citrate Electrolyte Used to Manufacture Cobalt-Tungsten Coatings

S. S. Belevskii[a], A. P. Kosova[b], S. P. Yushchenko[a, b], E. A. Yakhova[b], A. I. Shul'man[b], and A. I. Dikusar[a, b]

[a] *Institute of Applied Physics, Academy of Sciences of Moldova, ul. Academiei 5, Chisinau, MD-2028 Republic of Moldova*
[b] *Shevchenko Pridnestrov'e State University, ul. 25 Oktyabrya 128, Tiraspol, Republic of Moldova*
e-mail: dikusar@phys.asm.md

Received August 20, 2010

Abstract—The study of the electroconductivity of a citrate solution that contains cobalt sulfate (0.2 M) and sodium wolframate (0.2 M) used to obtain cobalt-tungsten coatings is carried out. A significant decrease in the conductivity in time of this solution as compared to aqueous and citrate complexes of cobalt was registered. It was shown that the observed changes occurred due to the generation of a mixed heteronuclear complex (probably polymeric) in the solution. The fractioning of the solution by gel filtration showed that all the changes resulted from the conversion of the substance with a high molecular weight.

DOI: 10.3103/S1068375511010042

INTRODUCTION

Electrolytic coatings with alloys based on metals from the iron group with refractory metals obtained from citrate and gluconate solutions are found to be the best alternatives for replacing the electrolytic chromium coatings that are widely used at present [1–9]. Study [10], which deals with the changes of the properties of a citrate electrolyte in order to develop cobalt-tungsten coatings in the process of their long-term development, shows that the properties of the latter were observed to change not only in the process of electrolysis but also upon the long storage of the electrolyte after its preparation. This study is aimed at a detailed examination of the changes in time in the properties of a citrate electrolyte used for manufacturing cobalt-tungsten coatings.

EXPERIMENTAL

Electroconductivity Study

In this work, an electroconductivity change was the main criterion for the estimate of the changes in time in the properties of a citrate electrolyte. A KEL-1M2 conductometer and platinum electrodes were used to measure it. The composition of the basic solution (whose electroconductivity was measured) used as an electrolyte to obtain nanocrystalline cobalt-tungsten coatings was as follows, mol/l: Na_2WO_4—0.2; $COSO_4$—0.2; $C_6H_8O_7$ (citric acid)—0.04; $Na_3C_6H_5O_7$ (sodium citrate)—0.25; H_3BO_3—0.65 (pH = 6.7) [5, 6, 9–15]. For comparison, the electroconductivities of the ingredients of this electrolyte, namely, an aqueous solution of cobalt sulfate (0.2 M, pH = 3.4 ± 0.2) and solutions of cobalt sulfate (0.2 M) in a citrate buffer mixture at various pH values (4, 6.4, 7.3) were measured. The latter contained all of the components of the primary electrolyte without sodium wolframate. The value of the specific electroconductivity (S/m) served as the one to be measured. Since the pH of the primary solution was 6.7, it was acidized during the electroconductivity (for the viscosity, see below) measuring by citric acid and alkalized by alkaline solutions.

The measurements of the electroconductivity were carried out for a few months after preparing the solutions. Since no special thermal condition measures were taken, certain measurements yielded the temperature dependencies (at different pHs of both the total solution and its components). Therefore, all the temporal changes are presented below as the values of the specific electroconductivity related to a certain (fixed) temperature of the solution.

Viscosity Measurement

In order to determine the nature of the observed changes, the measurements of the viscosity of the solutions were carried out using an Ubellode viscosimeter (the capillary diameter was 0.54 mm). The value of the kinematic viscosity (cm^2/s, cSt) was used as the value to be measured. An allowance for the temperature change was made in the same way as in the case of measuring the electroconductivity.

The Gel Filtration Chromatography of the Solutions

In order to determine the reasons for the changes in the properties of the electrolyte solution, gel chromatographic separation into components was used.

Dependence in time of the specific electroconductivity (S/m) of the electrolytes*

No.	Electrolyte	Electroconductivity κ (S/m)		$\frac{\kappa_n - \kappa_k}{\kappa_n} 100\%$
		Initial κ_n (first week)	Terminal κ_k (40–60 days)	
1	$CoSO_4$ (0.2 M) pH = 3.4 ± 0.2	1.37 ± 0.06	1.30 ± 0.02	5.1
2	Citrate Co (0.2 M) pH = 4	3.19 ± 0.03	2.95 ± 0.04	7.5
3	Citrate Co (0.2 M) pH = 6.4	3.72 ± 0.20	3.43 ± 0.06	7.8
4	Citrate Co (0.2 M) pH = 7.3	4.33 ± 0.08	4.16 ± 0.03	3.9
5	Citrate cobalt–tungsten electrolyte pH = 6.7	4.73	3.24 ± 0.04	31.5

* The values for electrolytes 1–4 are relevant to a temperature of 20°C, and it is 16°C for electrolyte 5.

In this study, a 108-cm-high and 1.0 cm-in-diameter chromatographic column was used with a Sephadex-G-10 matrix. This material makes it possible to separate the components of a solution with respect to their molecular masses; the compounds of larger molecular mass leave the column faster (at a smaller volume of the buffer passed through the column). The electrolyte of the above composition (pH = 6.8) was used as a specimen for the chromatographic separation. The buffer for the chromatographic column was a solution of the following composition (mol/l): $C_6H_8O_7$ (a citric acid)—0.04; $Na_3C_6H_5O_7$ (sodium citrate)—0.25; H_3BO_3—0.65 with pH = 6.8, which was relevant to the pH used for the separation of the specimen. A peristaltic pump (Peristaltic Pump P-3) was used for pumping the buffer. The rate of the liquid flow was 38.76 ml/h.

The volume of the specimen that was introduced into the column was 1.18% of its total volume. The solution that was leaving the chromatographic column was divided into fractions, which were further used in the measurements of optical density. The fractions were collected every 2 minutes. The spectra of the specimens in the ultraviolet and visible spectrum were measured using a Specord M 40 two-beam spectrophotometer. In order to construct the dependences of the optical density on the volume of the transmitted buffer, the values of the optical density at a constant wave length corresponding to the maximum absorption of the solutions of the fractions in the considered part of the optical spectrum were used.

RESULTS AND DISCUSSION

Changes in Time of the Electroconductivity

The table lists the results of measuring the electroconductivity immediately after preparing the solutions and after their long-term storage in contact with the air oxygen. The electrolyte was stored in a graduated bottle; i.e., contact with the oxygen of the air was restricted. It should be noted that changes were observed in all of the solutions under study; however, they significantly differed in their quantity. For all the solutions, except for the cobalt-tungsten citrate electrolyte, the changes (1) were within the limits of a few percent for two months, and (2) variations of the measured values were detected (table) during the first week after the electrolyte had been prepared. This allowed us to calculate the mean values for electrolytes 1–4 during the first week after their preparation, along with the standard deviations for both the first week of the measurements and after two months (the mean values and the standard deviations are presented in the appropriate columns of the table).

The results from the table show that, e.g., for the solution that contains an aquacomplex of cobalt (solution 1), the changes during the two months' storage are within the limits of the measurement error (about 5%, and, at the standard deviation of the measurements, for the first week, they are about 4%). The partial Co(II) oxidation is a probable reason for these changes.

The electroconductivity of a citrate complex of cobalt is substantially higher due to the formation of a complex; moreover, it may change depending on the pH (electrolytes 2–4). It should be noted that the measured values of the electroconductivity are strongly depended (again, due to the formation of a complex) on the kind of added acid (citric or sulfuric) by means of which concrete value of pH is attained (Fig. 1). The results that are shown in the table for solutions 2–4 were obtained using solutions of citric acid to attain the required pH value.

However, even in these cases, the electroconductivity's changes are within the limits of a few percent in the solutions with two months' storage (see table). More significant and abrupt *k* changes are observed in the citrate cobalt-tungsten electrolyte (solution 2, table, Fig. 2).

In the first ten days after the preparation, the electroconductivity changes by more than 20% (Fig. 2), and, after two months of storage, it decreases by more than 30% (see the table). The reasons for such marked changes had to be revealed.

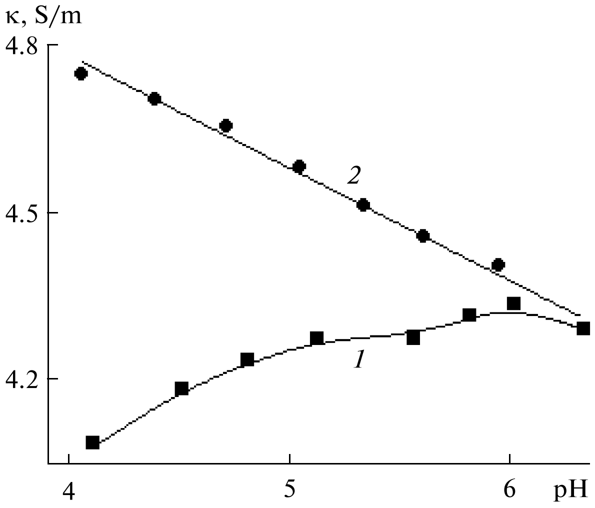

Fig. 1. Effect of the pH on the specific electroconductivity of a citrate cobalt-tungsten electrolyte at 23°C. The acidification is performed using (*1*) citric and (*2*) sulphuric acids.

The Effect of the Solution's pH on the Electroconductivity and Viscosity of the Studied Systems

The comparison of the results presented in Figs. 1, 2, and 4 shows that the complex-formation involves both change in the electroconductivity and the viscosity of the solutions. Moreover, a greater change in the viscosity is observed in a mixed solution of the electrolyte (Fig. 4). It is seen that, in this case, a substantial increase of the viscosity occurs both in the acid region of pH and in the alkaline one (Fig. 4). A certain correlation between the results of the measurements of the electroconductivity and the viscosity of the considered solutions is also registered.

The most probable reason for this behavior is the generation of the products of the complex formation with a sufficiently high molecular mass. This decreases the electroconductivity in the region of acid values of the pH (both for the citrate complex of cobalt and the cobalt-tungsten electrolyte, Fig. 3). An increase of the electroconductivity in the alkaline region (which was accompanied by an increase of the viscosity in the cobalt-tungsten solution) results from the change in pH that was attained by the addition of the alkaline.

The obtained results show that the complex-formation in a mixed electrolyte that contains citrate complexes of cobalt and tungsten may be accompanied by the formation of complex compounds with enhanced molecular mass, probably, polynuclear heterometallic complexes of these elements.

Chromatographic Study of the Peculiarities of the Systems Using Gel Filtration

The above peculiarities of the considered systems are obtained by examining the pH's effect on the properties of the solutions. However, the appropriate measurements of the electroconductivity of the solutions performed during their long-term storage showed no changes in the pH under these conditions. On the other hand, it seems evident that it is the formation of polynuclear heterometallic citrate complexes of cobalt and tungsten with high molecular mass that can be the reason for the observed changes in the electroconductivity. The results of a gel chromatographic analysis (Figs. 5, 6) may confirm this statement.

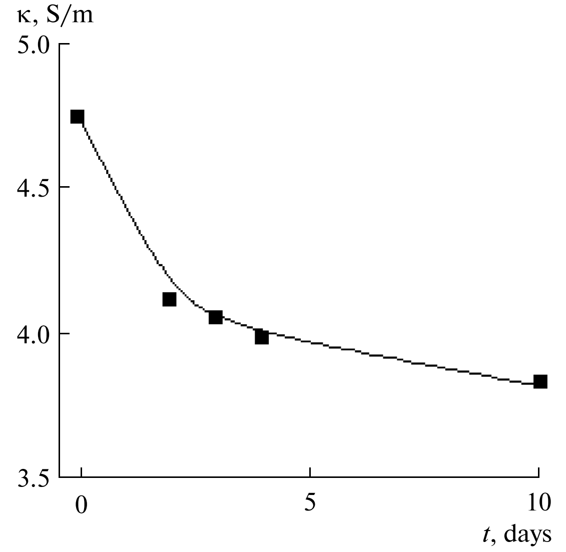

Fig. 2. Change of the specific electroconductivity of a citrate cobalt-tungsten electrolyte at 16°C in the first 10 days after its preparation.

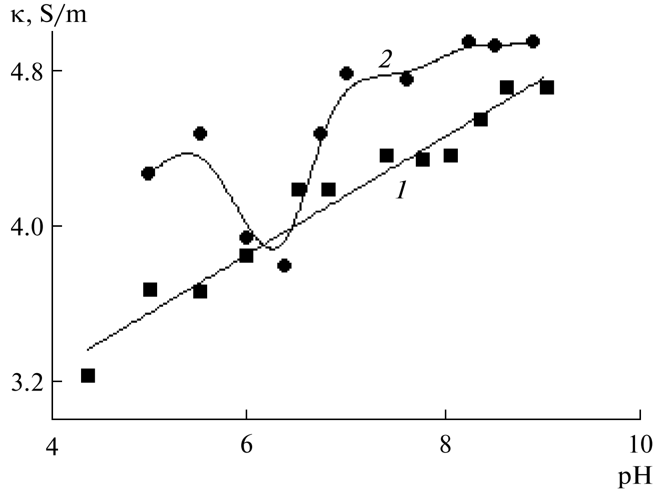

Fig. 3. Dependence of the specific electroconductivity of a 0.2 M citrate solution of cobalt (*1*) and a citrate cobalt-tungsten electrolyte (*2*) on the pH at 20°C.

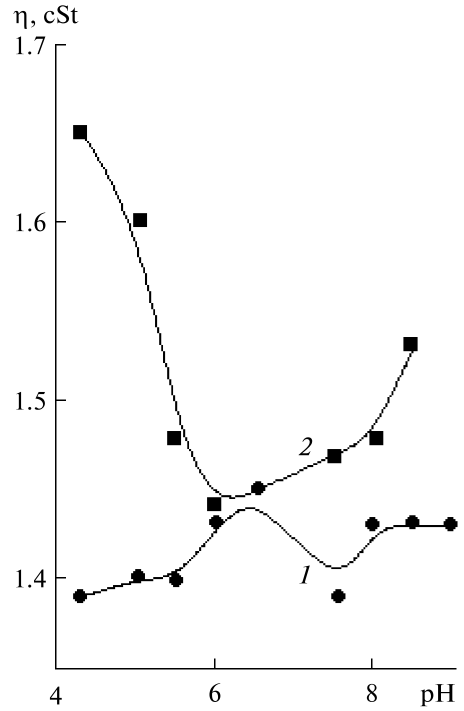

Fig. 4. Dependence of the kinematic viscosity of a 0.2 M citrate solution of Co (*1*) and a citrate cobalt-tungsten electrolyte (*2*) on the pH at 20°C.

The presented data show that different fractions of the electrolyte under study have different behaviours in time. The fractions that absorb in the ultraviolet region of the spectrum undergo no temporal changes (Fig. 5). (The small distinctions in the chromatograms may rather be indicative of the accuracy of the chromatographic variant of the separation that we used).

Taking into account that the absorption in the ultraviolet region may result from either a wolframate ion or its citrate complex (the presence of mixed heterocomplexes in them is less feasible, although not improbable), as well as from the fact that the yield of these fractions from the chromatographic column occurs after the transmission of a substantial volume of a buffer, these fractions represent the fractions of the solution with a relatively low molecular mass. It is these fractions of the solution that undergo no temporal changes.

On the other hand, substantial changes are observed for the fractions that absorb in the visible region of the spectrum (Fig. 6). Firstly, it is obvious that they represent the products with a higher molecular mass (the absorption maxima are shifted to the region of smaller volumes of elution). Secondly, it is seen that at least a few forms of the complexes will transform into a smaller quantity in due course with one of the forms being dominant.

Since it is the absorption in the visible region of the spectrum that it is related to, we may consider that the fractions with an enhanced molecular mass are either the citrate complexes of tungsten or (which is more probable) the mixed heterocomplexes. Obviously, it is a temporal transformation of these complexes that is one of the reasons for the changes in the solution's properties.

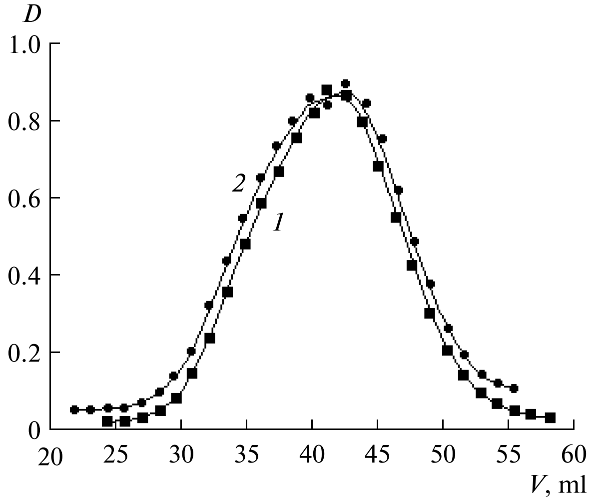

Fig. 5. Chromatograms of a citrate cobalt-tungsten solution freshly prepared (*1*) and after 3.5 months' storage (*2*). The optical density *D* of the solutions was fixed in the ultraviolet region of the spectrum (253 nm).

Indeed, for the citrate complexes that contain no ions of wolframate, (a) substantial temporal changes in the electroconductivity are absent, and (b) substantial changes in the viscosity typical for mixed heterocomplexes of the metals are not observed.

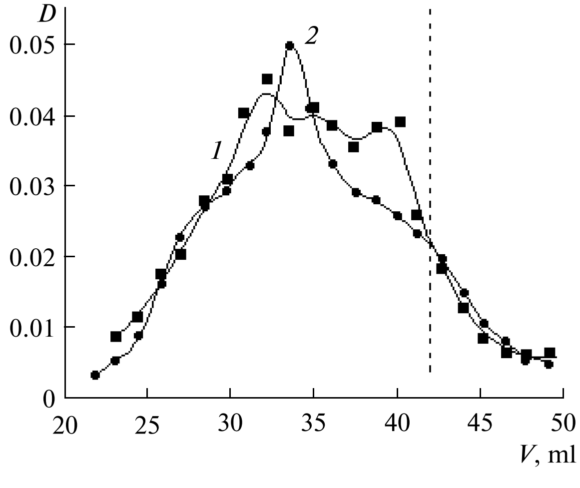

Fig. 6. Chromatograms of a citrate cobalt-tungsten solution freshly prepared (*1*) and after 3.5 months' storage of the electrolyte (*2*). The optical density *D* of the solutions was fixed in the visible region of the spectrum (515 nm). The dashed line is relevant to the absorption maximum of the fractions in the ultraviolet region of the spectrum (Fig. 5).

The obtained results in total show that the observed changes of the properties of the cobalt-tungsten citrate electrolyte used to develop the CoW electrolytic alloys are due to the (a) formation of a mixed heteronuclear complex immediately in the solution (possibly a polymer) and (b) the kinetic complex formation of the components of the solution with enhanced molecular mass.

CONCLUSIONS

The study of the electroconductivity of the citrate solutions used to obtain the cobalt-tungsten coatings and that contained cobalt sulfate (0.2 M) and sodium wolframate (0.2 M) showed that the electroconductivity, unlike that of an aqueous solution of cobalt sulfate and citrate complexes of cobalt at the same concentration, changes substantially (drops). It was shown that the observed changes occur due to the formation of a mixed heteronuclear complex immediately in the solution (possibly a polymer). Fractionating the solution using gel filtration showed that the registered changes occur due to the changes of the solution components with a higher molecular mass.

ACKNOWLEGMENTS

The financing of the research was performed in the framework of the state programs of the Republic of Moldova (Electrophysic and Electrochemical Surface Processes on Micro- and Nanometric Scales; Multilayer Nanostructural Materials Obtained using Electrochemical Methods: The Study of the Tribological, Corrosion, and Magnetic Properties).

The authors thank prof. A.D. Shutov for assistance in preparing for the chromatographic experiments and the discussion of their results.

REFERENCES

1. Brenner, A., *Electrodeposition of Alloys*, New York: Academic Press Inc., 1963.
2. Eliaz, N., and Gileadi, E., Induced Codeposition of Alloys of Tungsten, Molybdenum and Rhenium with Transition Metals, In *Modern Aspects of Electrochem.*, Springer, New-York: 2008, no. 42, pp. 191–301.
3. Vas'ko, A.T., *Elektrokhimiya molibdena i vol'frama* (Electrochemistry of Molybdenum and Tungsten), Kiev: Naukova Dumka, 1977.
4. Weston, D.P., Shipway, P.H., Harris, S.J., and Cheng, M.R., Friction and Cobalt-Tungsten Alloy Coatings for Replacement of Electrodeposited Chromium, *Wear*, 2009, no. 267, pp. 934–943.
5. Tsyntsaru, N., Belevsky, S., Dikusar, A., and Celis, J.-P., Tribological Behavior of Electrodeposited Cobalt-Tungsten Coatings: Dependence on Current Parameters, *Trans. Inst. Metal Finish.*, 2008, no. 86, pp. 301–307.
6. Tsyntsaru, N., Belevskii, S.S., Volodina, G.F., Bersirova, O.N., Yapontseva, Yu.S., Kublanovskii, V.S., and Dikusar, A.I., Composition, Structure and Corrosion Properties of Coatings of CoW Alloys Electrodeposited under Direct Current, *Surf. Eng. Appl. Electrochem.*, 2007, vol. 43, no. 5, p. 312–317.
7. Santana, R.A.C., Campos, A.R.N., Medeirosv, E.A., Oliveira, A.L.M., Silva, L.M.F., and Prasad, Sh., Studies on Electrodeposition and Corrosion Behavior of a Ni–W–Co Amorphous Alloy, *J. Mater. Sci.*, 2007, vol. 42, no. 22, pp. 9137–9144.
8. Bobanova, Zh.I., Dikusar, A.I., Cesiulis, H., Celis, J.-P., Tsyntsaru, N.I., and Prosycevas, I., Micromechanical and Tribological Properties of Nanocrystalline Coatings Electrodeposited from Citrate–Ammonia Solutions, *Russ. J. Electrochem.,* 2009, vol. 45, no. 8, pp. 895–901.
9. Tsyntsaru, N., Cesiulis, H., Bobanova, J., Croitoru, D., Dikusar, A., and Celis, J.-P., Electrodeposition and Tribological Characterization of Nanostructural Co–W and Fe–W Alloys, *Proc. Int. Conf. Balttrib., Kaunas, Lithuania* 2009, pp. 259–264.
10. Silkin, S.A., Belevskii, S.S., Tsyntsaru, N.I., Shulman, A.I., Shchuplakov, A.N., and Dikusar, A.I., Influence of Long-Term Operation of Electrolytes on the Composition, Morphology and Stress-Strain Properties of Surface Produced at Deposition of Co–W Coatings from Citrate Solutions, *Surf. Eng. Appl. Electrochem.*, 2009, vol. 45, no. 1, pp. 1–12.
11. Silkin, S.A., Tin'kov, O.V., Petrenko, V.I., Tsyntsaru, N.I., and Dikusar, A.I., Electrodeposition of Co–W Alloys: the Role of Temperature, *Electron. Obrab. Mater.*, 2006, no. 4, pp. 11–18.
12. Tsyntsaru, N., Dikusar, A., Cesiulis, H., Selis, J.-P., Bobanova, J., Sidel'nikova, S., Belevsky, S., Yapontseva, Yu., Bersirova, O., and Kublanovsky, V., Tribological and Corrosion Properties of Electrochemical Coatings on the Base of Cobalt and Iron Superalloys, *Powder Metallurgy and Metal Ceramics*, 2009, nos. 7, 8, pp. 66–78.
13. Kublanovsky, V., Bersirova, O., Yapontseva, Yu., Tsyntsaru, N., Belevsky, S., and Dikusar, A., Pulse Electrodeposition of Cobalt–Tungsten Alloys from Citrate Electrolyte on Steel, Its Corrosion Characteristics, *Phys. Chem. Mech. Mater.*, 2007, no. 6, pp. 80–90.
14. Belevsky, S.S., Tsyntsaru, N.I., and Dikusar, A.I., Electrodeposition of Nanocrystalline Co–W Coatings from Citrate Electrolytes Under Controlled Hydrodynamic Conditions. Part II: The Electrodeposition Rate and Composition of the Coatings, *Surf. Eng. Appl. Electrochem.*, 2010, vol. 46, no. 2, pp. 91–99.
15. Silkin, S.A., Belevskii, S.S., Gradinar, A.S., Petrenko, V.I., Yakovets, I.V., and Dikusar, A.I., Electrodeposition of Nanocrystalline Co–W Coatings from Citrate Electrolytes under Controlled Hydrdynamic conditions. Part III: The Micro- and Macrodistribution Rates, the Structure and the Mechanical Properties, *Surf. Eng. Appl. Electrochem.*, 2010, vol. 46, no. 3, pp. 206–214.

ISSN 1068-3755, Surface Engineering and Applied Electrochemistry, 2011, Vol. 47, No. 1, pp. 9–17. © Allerton Press, Inc., 2011.
Original Russian Text © L.P. Kornienko, G.P. Chernova, V.V. Mihailov, A.E. Gitlevich, 2011, published in Elektronnaya Obrabotka Materialov, 2011, No. 1, pp. 14–23.

ELECTRICAL SURFACE TREATMENT METHODS

Use of the Electrospark Alloying Method to Increase the Corrosion Resistance of a Titanium Surface

L. P. Kornienko[a], **G. P. Chernova**[a], **V. V. Mihailov**[b], **and A. E. Gitlevich**[b]
[a]*Frumkin Institute of Electrochemistry, Russian Academy of Sciences, pr. Leninskii 31, Moscow, 119991 Russia*
[b]*Institute of Applied Physics, Academy of Sciences of Moldova, ul. Akademiei 5, Chisinau, MD 2028 Republic of Moldova*
e-mail: scherbakov@ipc.rssi.ru, vmihailov@phys.asm.md

Received July 15, 2010; in final form October 27, 2010

Abstract—It is shown that the electrospark alloying of a titanium surface by palladium helps to enhance its corrosion stability in 10–40% solutions of H_2SO_4 at 100°C by 1–2 orders of magnitude. Mechanized alloying, as well as the additional heat treatment of electrospark palladium coated titanium (annealing in vacuum and electrothermal treatment in an electrolytic plasma), significantly raises its corrosion stability.

DOI: 10.3103/S106837551101011X

INTRODUCTION

As the surface composition and structure determine the resistance of a solid body to the external chemical and mechanical actions, it is expedient from the standpoints of economy and technology to alloy only the working surfaces of machine elements. The latter fact has stimulated interest in the scientific elaboration of various methods of surface alloying of metals and melts, in particular, interest in the electrospark alloying (ESA) developed by B.R. Lazarenko and N.I. Lazarenko [1].

The ESA method offers several advantages over surface volume alloying and other techniques. It permits one to produce coatings of any current-conducting metals and alloys, requires no previous careful preparation of the surface, allows one to carry out the treatment of separate components of fabricated structures, and the part is not heated in the course of the alloying. The additional diffusion of the coating material deep into the specimen proceeds under the action of the flowing current. The metals mechanically and chemically react with each other to produce a solid solution and possible intermetallides, thus providing a good adherence of the surface layer with the base and deep penetration of the coating material without high temperature annealing [1, 2].

However, it is rather difficult to produce smooth and uniform coatings by the method of electrospark metallization. This fact greatly limited the use of the ESA method to obtain corrosion resisting coatings.

It is known that, with cathode alloying, the protective effect can be ensured by a nonuniform coating as well, as is determined by the electrochemical mechanism [3].

The aim of this work is to examine the possibility to use the method of ESA of titanium by palladium in order to increase its corrosion resistance in hot solutions of sulfuric acid.

Titanium possesses good technological properties, enhanced durability, and it is easily passivated in many media and usually has high corrosion resistance due to the low values of the current in the passive state. Besides, titanium is characterized by low values of the passivation current and high positive values of the pitting formation potential. However, titanium's instability in solutions of nonoxidizing acids substantially decreases the area of its application as a construction material [4].

It is known that the metals of the platinum group are the most efficient cathodes. In this work, palladium has been selected as the cathode additive because it possesses a high cathode efficiency, its cost is less than that of other metals of the platinum group, and it is abundant enough.

EXPERIMENTAL PROCEDURE

The electrospark alloying of titanium VT1-0 by palladium has been carried out with the help of industrial setups of the "Elitron" and "EFI" type as worked out by the Institute of Applied Physics of the Academy of Sciences of Moldova.

In order to determine the best conditions of the ESA of titanium by palladium, we studied the effect of the spark discharge parameters (modes), the specific time of the alloying, the interelectrode medium's composition, and the electrode–tool scanning method on the content of palladium in the alloyed layer and the rate of the palladium-coated titanium's corrosion.

In order to study the dynamics of the surface layer's formation, there was obtained the dependence of the

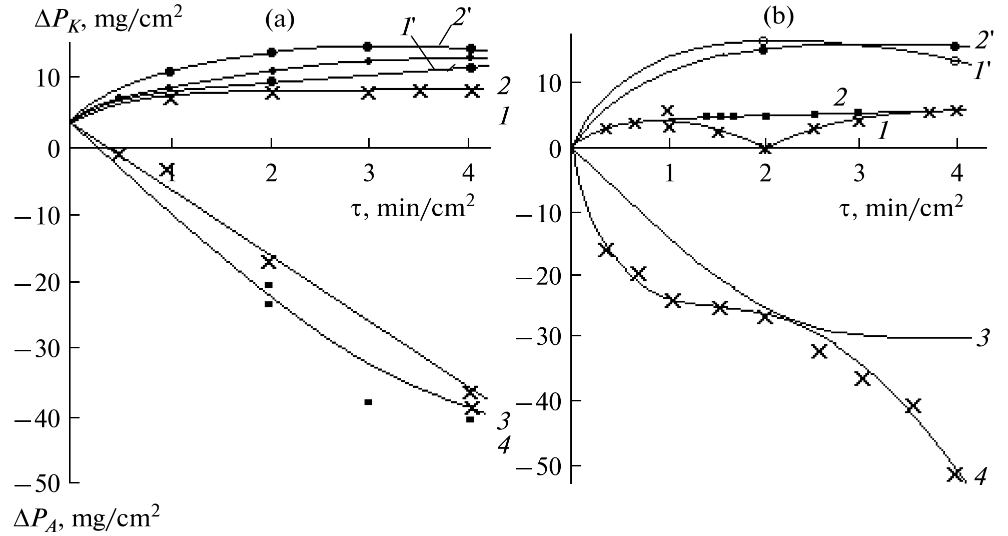

Fig. 1. The change of the titanium's specimen mass ΔP_K (curves *1*, *2*), the change of the palladium content in the alloyed layer ΔP_K (curves *1*', *2*'), and the diminution of the palladium electrode's mass ΔP_A (curves *3*, *4*) versus the electrospark alloying time: (a) under "mild" conditions; (b) under "severe" conditions.

cathode's (the titanium specimen) mass growth and the anode's (palladium) mass diminution on the ESA time under different conditions of machining (Fig. 1).

The data on the growth of the cathode's mass were compared with the true content of palladium in the alloyed layer determined by the photocolorimetric analysis [5]. The palladium and titanium–palladium phases were transferred into the solution through the method of anode galvanostatic polarization by a direct current in 10 % hydrochloric acid [6].

Corrosion tests were carried out on cylindrical specimens or parallel-piped-wise specimens with an area 1–3 cm^2 with a thread hole in the end face to fasten a metallic contact isolated from the solution by a teflon tube and washers. The experiments were performed in a thermostatted three-electrode cell at 100°C in the air atmosphere in 10, 20, 30, and 40% solutions of H_2SO_4 being chemically pure or analytically pure. The volume of the solution in the cell was 100 ml. The potentials were measured with respect to a silver–chloride electrode and recalculated with respect to a standard hydrogen electrode. The electrochemical investigations were conducted with the help of a potentiostat P-5827.

The phase composition of the palladium-coated titanium was determined through the use of a diffractometer (Dron-2). The distribution of palladium on the surface and in the depth was studied with the aid of an X-ray microanalyzer (XRMA) using a Camebax device.

RESULTS AND DISCUSSION

It is seen from the diagram that, in the case of alloying under "mild" conditions (the discharge energy is 0.03–0.1 J), the Pd content (Fig. 1a, curves *1*', *2*') in the surface layer is some higher (by 1.7–2.7 mg/cm^2) than the cathode weight increment and grows in time from 3.4 to 11 mg/cm^2. When the treatment time grows, the losses of the palladium anode progressively and almost linearly increase (Fig.1a, curves *3*, *4*).

In the case of alloying under "severe" conditions (the discharge energy is 0.1–6.4 J), the Pd content in the surface layer changes from 13.3 to 16.4 mg/cm^2 (Fig. 1b, curves *1*', *2*'); it is higher than in the case of spark machining under "mild" conditions and greatly exceeds the cathode weight increment (Fig. 1b, curves *1*, *2*). The curves of the palladium anode erosion have a nonlinear nature (Fig. 1b, curves *3*, *4*).

With the alloying time increasing to over 2 min/cm^2, under "mild" conditions, the Pd content in the alloyed layer grows slightly (from 5.6 to 8.6 mg/cm^2), and, under "severe" conditions, it decreases from 16.4 to 14.3 mg/cm^2, while the total flow rate of the palladium electrode progressively grows in time.

The diminution of the cathode weight increment in time can be connected with the following:

—the considerable evaporation and spraying of the liquid phase of a material;

—the erosion of the titanium substrate growing with the increase of the discharge energy;

—the drastic changing of the properties of the cathode surface layers due to the formation of intermetallides, oxides, solid solutions, and structural alterations in the course of the ESA, thus causing the changing of the erosion's nature [2].

The X-ray phase analysis has shown that Pd, intermetallic compounds of Ti and Pd with different compositions (Ti_2Pd, Ti_2Pd_3, Ti_3Pd_5, TiPd, $TiPd_2$), and Ti

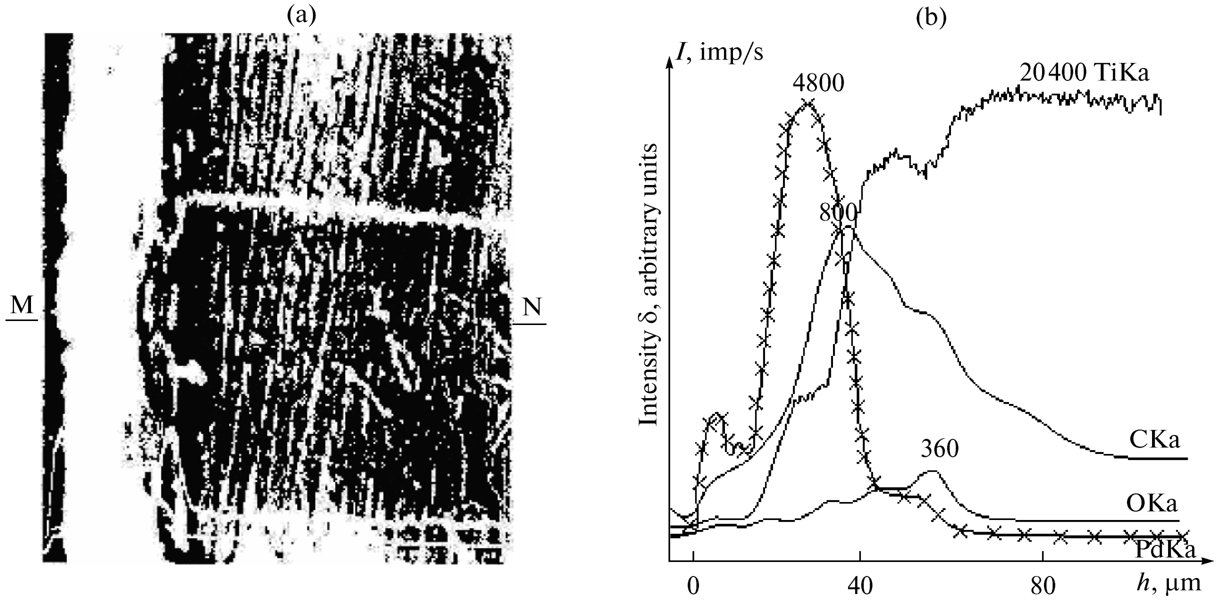

Fig. 2. Electron-microscopic picture of a crosscut microsection of a titanium specimen with an electrospark palladium coating: 800× magnification (a); the change of the content of the palladium, titanium, carbon, and oxygen across the depth of the specimen as determined by XRMA (b). MN is the line of the scanning.

and its oxides (Ti_2O_3, Ti_3O_5, TiO_2) enter into the composition of the surface phases of the palladium-coated titanium.

According to the data of the X-ray microanalysis (XRMA), Pd-containing phases and Pd are distributed on the surface as a discontinuous nonuniform layer.

Microstructural investigations and the XRMA data of crosscut microsections have shown (Fig. 2) that, in the case of the electrospark palladium-coating of titanium, on its surface there is formed a white layer, the thickness of which changes on average from 5 to 30 μm and depends on the conditions and the specific time of the alloying. Pd and Ti, as well as slight amounts of carbon; oxygen; and, evidently, nitrogen enter into the composition of the white layer. Then, there is observed a transition zone—a sublayer (≈40 μm thick)—the region of the thermal action of the impulse discharges. There is no diffusive penetration of Pd into this region.

The results of the corrosive and electrochemical tests in 10% sulfuric acid at 100°C have shown that, independently of the discharge parameters and the alloying time, under these conditions, all the specimens are in the passive state. Their corrosion potentials change from 0.2 to 0.77 V (Table 1). The corrosion rate is 1—2 orders of magnitude less and changes from 0.08 to 1.33 $g/m^2 \cdot h$. Under these conditions, titanium quickly dissolves at the rate of 18.7 g/m^2 h with the potential being –0.56 V.

With the acid concentration increasing to 40%, the corrosion rate grows to 2.6 g/m^2 h, yet, even under such aggressive conditions, it is almost two orders of magnitude less than that of Ti, the corrosion rate of which is about 200 g/m^2 h (Fig. 3).

The corrosion rate of the specimens alloyed under "severe" conditions is higher despite the high content of Pd in the alloyed layer. Under "severe" conditions, the rate of the mass transfer grows, but the quality of the generated layers is lower due to the appearance of various pores, cracks, and burns.

With the alloying time increasing from 2 to 4 min/cm^2, the corrosion resistance reduces, especially in the case of alloying under "severe" conditions. Probably, this fact is connected with the damage of the Ti layer formed in the course of the alloying and enriched by Pd due to the growth of the residual and thermal stresses over the ultimate resistance of this layer as a result of the repetitive action of the electric impulses [2].

Long corrosion tests in 10% sulfuric acid at 100°C have shown that the specimens alloyed under "mild" conditions at the specific time of machining of 1—2 min/cm^2 have the largest resource of the protective effect—350 hours. Palladium-coating under "severe" conditions with the increase of the machining time up to 4 min/cm^2 result in the reduction of the protection resource to 260 hours.

Thus, owing to the high cathode efficiency of the electrospark palladium coatings, namely, Pd and intermetallides, Ti is in a passive state (its potentials are in the range from 0.2 to 0.77 V). At the same time, this region is the cathode one for Pd; under these conditions palladium ions do not pass into the solution [8].

Table 1. The influence of the conditions (10% H_2SO_4, 100°C) and the specific time (10 h) of the electrospark alloying of titanium by palladium on the palladium content in the alloyed layer, its potential, and the corrosion rate

Number of the specimen	Installation type, alloying conditions	Greatest discharge power, J	Specific time of alloying, min/cm^2	Pd content, mg/cm^2	Corrosion rate, g/m^2 h	Corrosion potential, V
1	Elitron-10, "soft"	0.10	0.5	3.4	0.08	0.51
2			1	6.4	0.24	0.44
3			2	11.3	0.18	0.41
4			3	11.0	0.18	0.41
5			4	10.1	0.47	0.40
6	Elitron-14, "soft"	0.03–0.05	2	5.6	0.19	0.44
7			4	8.6	0.54	0.38
8	Elitron-14, "severe"	0.08–0.15	2	16.4	0.92	0.22
9			4	13.3	1.33	0.20
10	Elitron-22, "severe"	0.42	2	15.1	0.52	0.38
11			4	15.6	0.63	0.38
12	EFI-46F, 1 "soft"	0.03	1–2	3.3	0.10	0.77
13	EFI-46F, 2"soft"	0.09	1	4.7	0.11	0.67
14			2	6.4	0.17	0.44
15	EFI-46F 4, "severe"	0.84	0.3	2.7	0.85	0.30
16			1	6.7	0.40	0.42
17			2	8.9	0.52	0.42
18	EFI-46F 6, "severe"	6.4	1–2	–	0.59	0.38
Ti	–	–	–	–	18.70	–0.56
Pd	–		–	–	0.00	0.79

There has been investigated the influence of the interelectrode medium's (vacuum, argon, air) composition and the way of the electrode's displacement with respect to the alloyed surface (mechanized and manual) on the formation of the coating and its corrosion resistance [9]. The longitudinal velocity of the specimen's displacement with respect to the electrode–tool is selected keeping in mind the necessary condition—

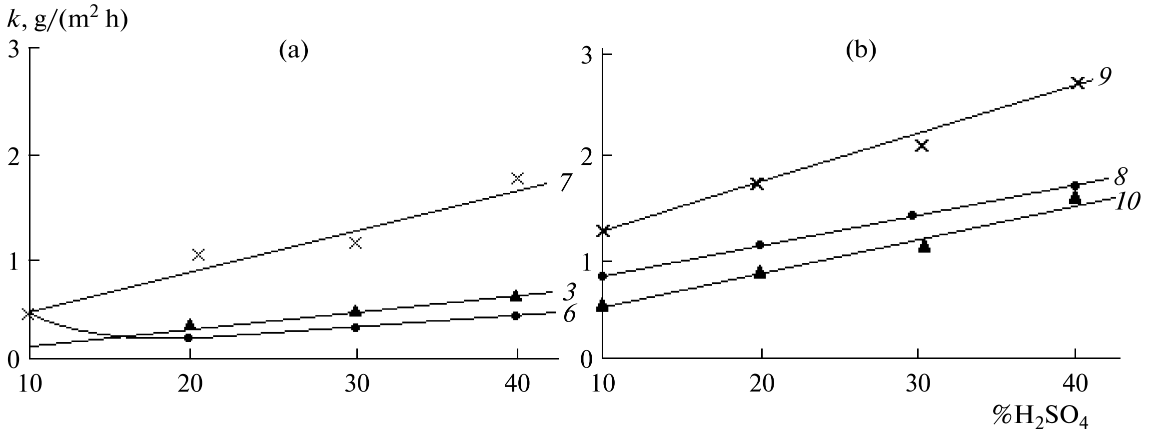

Fig. 3. Corrosion rate of titanium with the electrospark palladium coatings versus the concentration of H_2SO_4 at 100°C: (a) palladium coating under "mild" conditions; (b) palladium coating under "severe" conditions. The numbers of the curves correspond to the numbers of the specimens in Table 1. Curves *3*, *6*, *8*, and *10* correspond to the specific time of alloying of 2 min/cm^2, and curves *7* and *9*, to 4 min/cm^2. The test time was from 5 to 10 h.

Table 2. The influence of the interelectrode medium's (atmosphere) content and the electrode scanning method on the palladium content in the alloyed layer, its phase composition, and the rate of the palladium-coated titanium's corrosion. The test time was 15 h

Scanning method	The medium's composition	Ti cathode weight increment, mg/cm^2	Pd content, mg/cm^2	Pd anode erosion, mg/cm^2	Corrosion rate, g/(m^2 h)	X-ray analysis
Mechanized	Vacuum 0.0133 MPa	3.63	6.06	7.89	0.06	Ti_2Pd_3, Ti
	Argon 0.5054 MPa	8.06	8.13	12.49	0.008	Pd, Ti_3Pd_5, TiPd, Ti
	Air	6.58	6.71	12.09	0.012	Pd, Ti_3Pd_5, TiPd, Ti, Ti_2O_3
Manual	Air	3.88	3.40	8.00	0.1	Ti_3Pd_5, TiPd, Ti

the production of a uniform layer over the whole surface of the processed surface, and each next discharge should occur after the specimen's axis is displaced by one fourth of the cathode pit diameter. The number of the electrode–tool passages is 10.

In the case of alloying through the mechanized method in Ar and in the air, it is established that the applied layer has the same phase composition (Pd, TiPd, and Ti_3Pd_3), the values of the Pd content in the alloyed layer and the weight increment of the specimens are close, and the anode erosion is almost the same (Table 2).

The phase composition of the specimens alloyed in the air is more uniform (Ti_2Pd_3 and Ti), and the Pd content is half as large as the weight increment. This is probably connected with the growth of the Ti erosion at the expense of the increase in the vacuum and of the rate of the metal evaporation from the surface in the discharge zone. Besides, with the air pressure reducing, the conditions of the heat dissipation into the environment are impaired, which causes the longer maintaining of high temperatures in the discharge zone [2].

The most enriched Pd coatings containing 8.13 mg/cm^2 of Pd are formed at ESA in an atmosphere of Ar. Probably, this is connected with the absence of interaction between the electrode materials and the medium's components, in particular, with the absence of oxidizing processes, as well as the changes proceeding in the discharge channel itself. Owing to the low electric conductance of Ar, the interelectrode gap breakdown can happen at the distances at which the transfer of Pd onto Ti grows [2].

The specimens alloyed in the air and a vacuum have Pd contents of 6.71 and 6.06 mg/cm^2, respectively, with the anode erosion being half as much in the air.

The specimens alloyed in the air with hand scanning as a rule have a Pd content half as much (3.4 mg/cm^2) as when the mechanized process is carried out. It is evidently connected with the less steady way of the electrode–tool displacement over the alloyed surface as compared with the mechanized one, thus resulting in the nonuniform distribution of the alloying component.

Prolonged testing has shown that the specimens alloyed by the mechanized method begin to be activated only in 960 hours, and those activated by the manual scanning—in 260–350 hours.

The X-ray phase analysis shows that, in the course of the corrosion, the phase composition of the surface layer changes. Thus, after 600 hours of testing, the specimen alloyed in Ar is more saturated with palladium phases (Pd, $TiPd_2$) in comparison with what was recorded at the beginning of the corrosion testing (Pd and Ti_3Pd_5 were found on its surface). This fact points to the dissolution of the less saturated Pd phases at the beginning of the testing and the accumulation of the dispersed Pd and more enriched Pd phases on the Ti surface.

Thus, the mechanized scanning allows one o increase by almost 3 times the period of the passive state of Ti in comparison with the manual one, which is evidently connected with the larger content of Pd in the alloyed layer and its more uniform distribution. Alloying in an Ar atmosphere allows one to produce coatings the most enriched by palladium and possessing the greatest corrosion resistance.

As the alloyed layer's thickness (at an average from 5 to 30 μm) under corrosive conditions is limited, there could happen the undercut etching of the Pd and loss of its contact with the titanium, thus causing depassivation and the growth of the specimen's corrosion rate.

To introduce the Pd into the Ti to a great depth, the palladium-coated Ti specimens were subjected to annealing in a 10^{-4} mm of mercury vacuum at 1150°C for 30, 60, and 180 min.

It was established by the X-ray phase analysis that intermetallide Ti_2Pd, which is less enriched by palladium, and Ti are present on the surface of the palladium-coated Ti after the annealing [10].

The X-ray microspectrographic analysis shows that the distribution of Pd over the surface becomes more uniform after the annealing (Fig. 4). The content of Pd

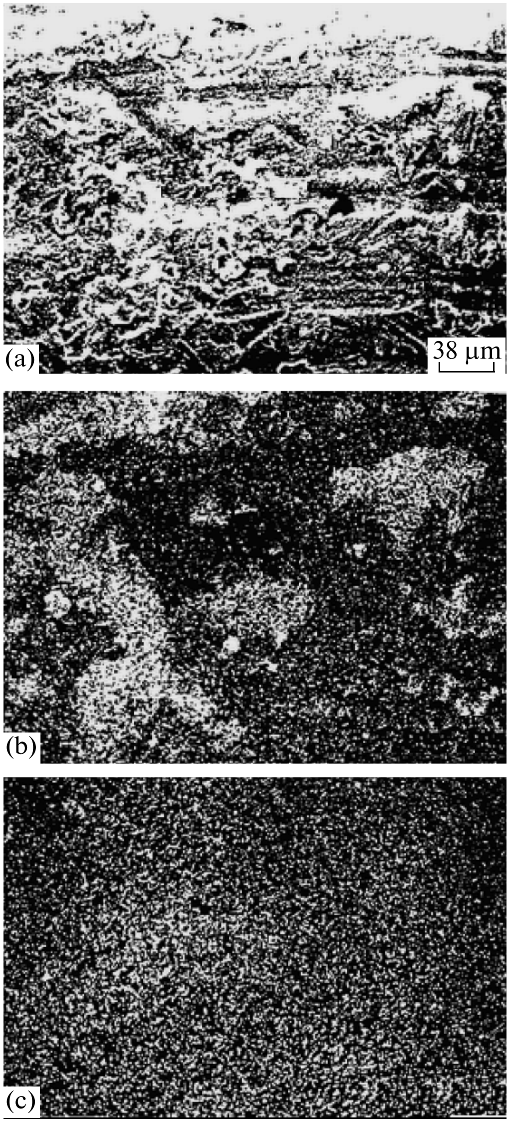

Fig. 4. Electron-microscopic pictures of the titanium surface with the electrospark palladium coating: (a) general view; (b, c) the same place in the palladium (X-rays); (a, b) before, (c) after annealing.

in the surface layer decreases (Fig. 5). Thus, after annealing for 30 minutes, the intensity of the analytic line L_α of the Pd was reduced by 5 times. The depth of the Pd penetration into the Ti after the annealing grew. On average, it was 5 –30 μm on the unannealed specimens. After 30 min of annealing, it amounted up to 130–150 μm, and, after 60 minu, up to 180–200 μm. After 3 h of annealing, Pd was found at a depth of ≈750 μm in the specimens. It should be noted that the annealing is attended with the considerable growth of the titanium substrate grain, thus it is inexpedient to increase the time of the thermal treatment to over an hour. In the course of the annealing, the Pd penetrates into Ti nonuniformly; in the X-ray spectrograms, there are observed some peaks corresponding to local pile ups of Pd and intermetallides along the boundaries of grains or blocks in the crystal, as the boundaries of the grains are evidently the sources of vacancies simplifying the diffusion.

The corrosion rate of the specimens after the annealing in 10% H_2SO_4 at 100°C during the first 5–10 h of the testing decreased by 2.5–3 times in comparison with the unannealed ones and was 0.03–0.08 g/m^2 h for the specimens alloyed under “mild” conditions and 0.12–0.14 g/m^2 h for the ones alloyed under “severe” conditions. For the unannealed specimens, it was 0.1–0.2 g/m^2 h and 0.3–0.5 g/m^2 h. With the testing time increasing, the corrosion rate grows, and, by 7000 h, it amounts up to 1.3 g/m^2 h, yet, in this very case, the corrosion rate is more than an order of magnitude lower than for Ti without the coating. The specimen’s activation occurs after 980 hours of corrosion, whereas the unannealed palladium-coated titanium is activated even after 250–350 h of testing. It is possible that the increase of the corrosion rate in the course of the prolonged corrosion testing is connected with the formation, during the annealing, of a diffusion profile in the depth with the ever-dropping concentration of Pd. At the beginning of the corrosion testing, the Ti ions pass into the solution from the phases more enriched by palladium and more corrosion resistant. As these phases dissolve with the increase of the time during which the specimens are in the corrosion solution, Ti ions pass from the phases less enriched by palladium and correspondingly less corrosion resistant until the concentration of Pd is sufficient to maintain the passive state.

There was investigated the influence of case hardening by anode heating in an electrolyte plasma (AHEP) on the corrosion properties of palladium-coated Ti. A solution consisting of 15% NH_4Cl and 10% $(CH_3)_2CO$ is used as an electrolyte at AHEP. AHEP makes it possible to substantially reduce (up to some minutes) the time of the thermal treatment in comparison with the diffusion annealing [11].

The X-ray phase analysis and the data of the XRMA of the surface and crosscut microsections have shown that, at the AHEP of the palladium-coated Ti, coatings of a complex composition containing Pd, intermetallides of different compositions (Ti_2Pd, Ti_2Pd_3, $TiPd_2$), titanium carbides, and oxicarbides (TiC_xO_3) are formed on its surface. The distribution of Pd over the surface after the electrolyte–plasma treatment does not become uniform. The examination of the distribution of the elements over the specimen’s depth has shown that, in the course of the anode heating, a Pd profile similar to the diffusion one does not form (Fig. 6). The coatings are clearly separated from the base.

An oxicarbide layer ≈3 μm thick, being solid (rather uniform throughout the thickness), light, and not etched is formed on pure titanium as a result of the treatment (Fig. 6a). The composition of the coating on

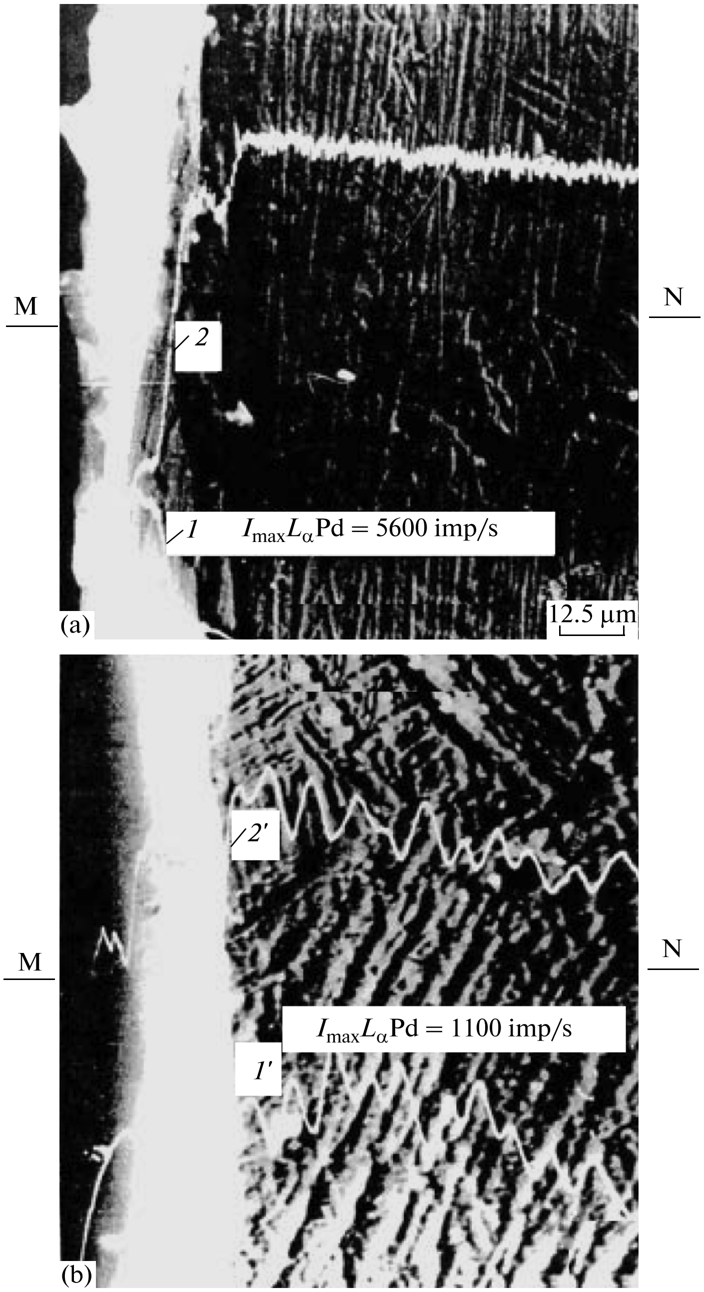

Fig. 5. The change of the content of palladium (*1*, *1'*) and titanium (*2*, *2'*) over the specimen's depth; (a) before, (b) after annealing. MN is the line of scanning.

the specimen of the palladium-coated Ti that was worked in plasma is nonuniform and its thickness is not everywhere the same (Fig. 6b). Pd-containing phases and oxicarbides enter into its composition [12]. There is no growth of substantially titanium substrate's grain in the course of case hardening.

It is shown that, after case hardening of palladium-coated titanium, the Pd content decreased in the alloyed layer by ≈2.5 mg/cm^2 and was 4.05–6.37 mg/cm^2 depending on the conditions of the spark machining. There was also observed the reduction of the specimen's roughness at the expense of the anode dissolution of the surface layer. Evidently, both factors are connected with the specific erosion of the specimens.

The potentials of the corrosion of the palladium-coated titanium case hardened in 10% H_2SO_4 at 100°C are determined in the region of the titanium's passivity and are in the range from 0.45 to 0.65 V. They are of the same order of magnitude as the palladium-coated titanium before the anode heating, and, in this case, the corrosion rate decreases by more than an

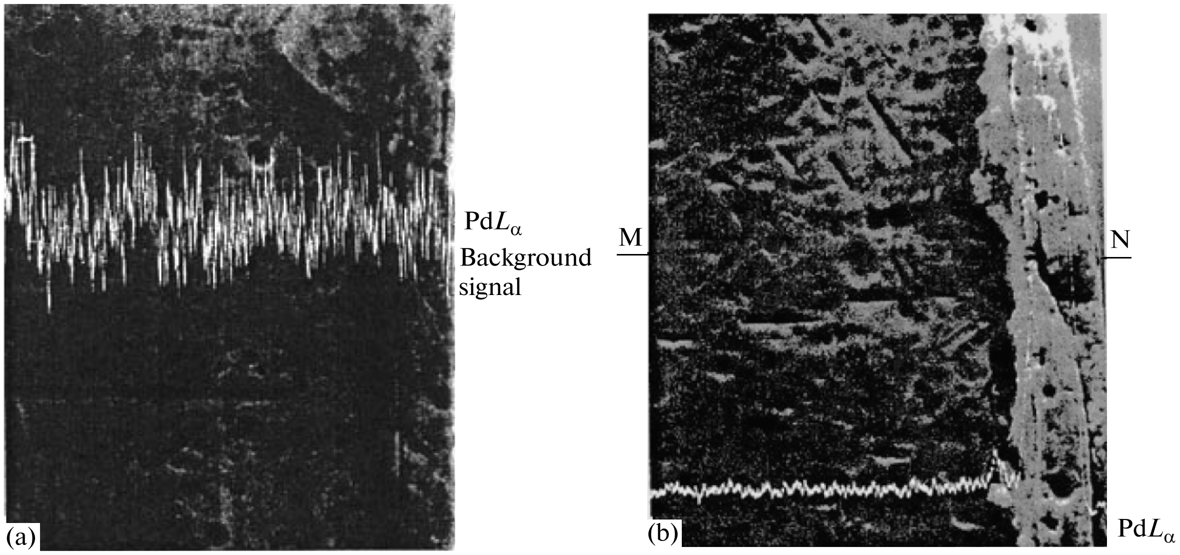

Fig. 6. Electron-microscopic pictures of crosscut microsections of the specimens of titanium (a) and palladium-coated titanium (b) subjected to anode heating in the electrolyte plasma (160 V, 3 min, cooling in the air). 1000x magnification. MN is the line of scanning.

order of magnitude and is equal to some thousandths and hundredths of fractions of g/m^2 h.

According to the analysis of the solution, in the course of the 5-hour testing, it remained constant and was determined by the transition of Ti ions into the solution. Pd ions were not found in the solution. The prolonged corrosion testing shows that the corrosion rate grows with the increase of the corrosion time; however, it remains rather low (0.086 g/m^2 h) even after 400 hours of corrosion; the corrosion potentials do not leave the deeply passive region (0.4–0.7 V).

Pure Ti after anode heating passes into the passive state and mass losses were not found during 6 hours of testing, thus indicating the high corrosion resistance of the oxide–carbide layers forming on the Ti in the course of the plasma treatment. However, after a deep scratch is made on the surface of the case hardened specimens of pure and palladium-coated titanium, the first one is activated, whereas the palladium-coated one remains in the passive state.

Thus, the passive state and high corrosion resistance of the palladium-coated case hardened titanium is connected with the presence both of palladium-containing phases and of oxide–carbide ones in the coating. The former ones provide the establishment and maintenance of a stable passive state and perform the electrochemical protection of the Ti owing to their high cathode efficiency. The oxide–carbide layers perform a sheathing protective action, i.e., play a screening role, due to their high corrosion resistance. Their presence in the pores and discontinuity flaws of the electrospark palladium coating greatly reduce the area of the uncoated sections.

CONCLUSIONS

It is shown that the alloying of the titanium surface by palladium through the electrospark method increases its corrosion resistance by 1–2 orders of magnitude in solutions of sulfuric acid at high temperatures, as caused by the presence in the coating composition of Pd and Ti–Pd intermetallides transiting the titanium into a passive state. It is ascertained that the content of Pd in the alloyed layer depends on the discharge energy and the specific time of the electrospark machining.

It is shown that the mechanized ESA by palladium in comparison with the manual one allows one to considerably increase the titanium resistance, which is connected with the great content of Pd in the surface layer and its more uniform distribution. The mechanized alloying in vacuum, argon, and air has shown that the coatings the most enriched by palladium are formed in an atmosphere of argon.

Many-component coatings with a complex structure are formed on the surface of titanium in the course of ESA by palladium. Their composition includes Ti, Pd, intermetallides of different compositions of the Ti–Pd system, oxides, carbides, nitrides, and oxicarbides and oxynitrides of titanium. The thickness and composition of the layers depend on the conditions of the ESA and the electrolyte–plasma treatment.

It is shown that the corrosion potentials established on the palladium-coated Ti are in the potential region being the cathode one for the intermetallides and Pd. Under these conditions, Pd does not pass into the solution. The rate of the corrosion of the palladium-coated titanium in the passive state is determined by the rate of the dissolution of Ti from the intermetallides and the Ti from the palladium-uncoated sections at the established corrosion potentials.

It is shown that annealing in vacuum at 1150° increases the corrosion resistance of Ti by 2–2.5 times due to the more uniform distribution of the Pd-containing phases and the formation of an extended diffusion profile of Pd in the titanium.

Case hardening by AHEP leads to the growth of the corrosion resistance by more than an order of magnitude, which is connected with the formation of the mixed palladium-containing and oxide–carbide layers.

REFERENCES

1. Lazarenko, B.R. and Lazarenko, N.I., *Elektroiskrovaya obrabotka tokoprovodyashchikh materialov*, (Electrospark Machining of Current Conducting Materials), Moscow: Izd. Akad. Nauk SSSR, 1968.
2. Gitlevich, A.E., Mihailov, V.V., Parkanskii, N.Ya, and Revutskii, V.M., *Elektroiskrovoe legirovanie metallicheskikh poverkhnostei*, (Ellectrospark Alloying of Metal Surfaces), Kishinev: Shtiintsa, 1985.
3. Tomashov, N.D. and Chernova, G.P., *Otkrytiya v SSSR*, (Inventions in the USSR), Moscow: Gos. Komitet SSSR po delam izobretenii i otkrytii, 1973, no. 165, p. 25.
4. Tomashov, N.D., *Titan and korrozionnostoikie splavy na ego osnove*, (Titanium and Corrosion Resistive Alloys on its Basis), Moscow: Metallurgiya, 1985.
5. Ponomaryov, A.I., Bykovskaya, Yu.I., and Veselago, L.I., *Analiz splavov na osnove niobiya, titana, khroma,* (Analysis of Alloys Based on Niobium, Titanium, Chrome), Moscow: Nauka, 1979.
6. Tomashov, N.D, Chernova, G.P, and Chukalovskaya, T.V., On Accumulation of Palladium in Titanium–Palladium Alloys at their Corrosion and Self-Passivation in Sulfuric Acid. Study of the Processes of Self-Passivation of Ti-Pd Alloys and Accumulation of Palladium on their Surface at Corrosion in Sulfuric Acid Solutions, *Zashch. Met.*, 1971, vol. 7, no. 3, pp. 279–283.
7. Chernova, G.P., Kornienko, L.P., Gitlevich, A.E., Mihailov, V.V., Plavnik, G.M., Khrustalyova, G.N., and Tomashov, N.D., The Effect of Conditions of Electrospark Alloying of Titanium Surface by Palladium on Composition of Forming Phases and Corrosion Resistance of Titanium, *Zashch. Met.*, 1988, vol. 24, no. 1, pp. 53–59.
8. Kornienko, L.P., Tomashov, N.D., and Chernova, G.P., Electrochemical and Corrosion Behavior of Intermetallides with Composition Ti_2Pd and TiPd and Titanium with Electrospark Palladium Coatings, *Zashch. Met.*, 1993, vol. 29, no. 3, pp. 359–367.
9. Kornienko, L.P., Tomashov, N.D., Chernova, G.P., Bukov, K.G., and Fedotov, L.N., Effect of Electrospark Alloying Conditions (Gaseous Medium Composition and Electric Scanning Conditions) on Corrosion Resistance of Palladium-Coated Titanium, *Elektr. Obrab. Mater.*, 1992, no. 2, pp. 9–12.
10. Chernova, G.P., Kornienko, L.P., Gitlevich, A.E., Topala, P.A., Zalavutdinov, R.Kh, Plavnik, G.M., Khrustalyova, G.N., and Tomashov, N.D., Effect of Annealing on Corrosion Behavior of Titanium with Electrospark Palladium Coating, *Zashch. Met.*, 1990, vol. 26, no. 3, pp. 433–437.
11. Duradji, V.N. and Parsadanyan, A.S., *Nagrev metallov v elektrolitnoi plazme,* (Heating of Metals in Electrolyte Plasma), Kishinev: Shtiintsa, 1988.
12. Kornienko, L.P., Duradji, V.N., Chernova, G.P., Gitlevich, A.E., Zalavutdinov, R.Kh, Khrustalyova, G.N., and Plavnik, G.M., Increase of Corrosion Resistance of Titanium with Electrospark Palladium Coating by Anode-Plasma Heating in Aqueous Electrolyte, *Zashch. Met.*, 2003, vol. 39, no. 1, pp. 45–52.

ISSN 1068-3755, Surface Engineering and Applied Electrochemistry, 2011, Vol. 47, No. 1, pp. 18–22. © Allerton Press, Inc., 2011.
Original Russian Text © A.I. Komarov, V.I. Komarova, A.D. Rud', N.I. Kuskova, 2011, published in Elektronnaya Obrabotka Materialov, 2011, No. 1, pp. 24–29.

Intensification of Microplasma Discharges in the Formation of Ceramic Coatings on Aluminum Alloys Exposed to Carbon Nanoparticles

A. I. Komarov[a], V. I. Komarova[a], A. D. Rud'[b], and N. I. Kuskova[c]

[a]*Joint Institute of Mechanical Engineering, National Academy of Sciences of Belarus,*
ul. Akademicheskaya 12, Minsk, 220072 Belarus

[b]*Kurdyumov Institute of Metal Physics, National Academy of Sciences of Ukraine,*
bul'v. Akademika Vernadskogo 36, Kiev, 03142 Ukraine

[c]*Institute of Pulse Processes and Technologies, National Academy of Sciences of Ukraine,*
pr. Oktyabr'skii 43-a, Nikolaev, 54018 Ukraine

e-mail: komarova@inmash.bas-net.by

Received July 15, 2010

Abstract—The effect of carbon nanomaterials (ultradispersed diamond–graphite blends, and ultradispersed diamonds) on the microplasma oxidation of aluminum alloys is studied. It is shown that the introduction of carbon nanomaterials into the electrolyte leads to the intensification of the coating formation process. This is evident from the increase in the coating's thickness by a factor of 1.8–2.5 depending on the chemical composition of the alloys. A more significant effect is found for diamond–graphite blends. The surface modification with particles of nanodiamond and nanographite leads to an increase in the microhardness, wear resistance, and bearing capacity and to a decrease in the friction coefficient.

DOI: 10.3103/S1068375511010108

INTRODUCTION

The range of use of aluminum alloys in products of mechanical engineering is significantly limited due to their strong tendency for seizure, low strength characteristics, and poor wear resistance. In this regard, technical solutions are often implemented using special structural elements, i.e., plates, inserts, and sleeves of antifriction materials, in particular, iron and steels. It is obvious that, in this case, a significant part of the advantages of aluminum alloys with respect to their specific weight and corrosion resistance is lost. In addition, these designs are not easily producible and economically sound.

One of the promising technologies for eliminating these disadvantages is the microplasma oxidation (MPO) of aluminum alloys, which results in the formation of ceramic coatings on their surfaces; the coatings consist mostly of γ-Al_2O_3 and α-Al_2O_3 (corundum). This composition provides high physicomechanical and tribotechnical properties of the coatings [1].

MPO offers the possibility to form coatings with a thickness of up to 300 μm both on the external and internal surfaces of workpieces without changing their initial sizes; it provides high adhesion to the base and chemical and thermal stability of the hardened layer. It also increases the wear resistance; strength; and hardness, which achieves 20–25 GPa, which is much higher than the hardness of many structural materials (Fig. 1). However, the process of the formation of ceramics with a thickness sufficient for the efficiency of tribojoints during their entire lifetime is relatively long; in some cases, it is more than 3 h [2]. This is particularly relevant for silumins, which, according to the opinion held in the literature [2], is a difficult subject for MPO. At the same time, these alloys are widely used for producing different-purpose friction units. In

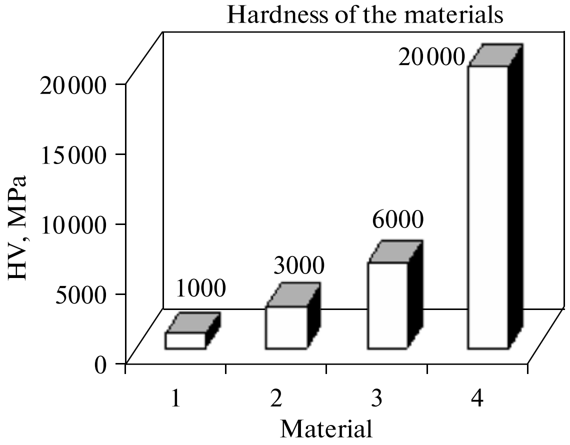

Fig. 1. Hardness of the ceramic coating, anodized layer, steel, and aluminum: (*1*) aluminum, (*2*) anodic oxidation, (*3*) steel, and (*4*) microarc oxidation.

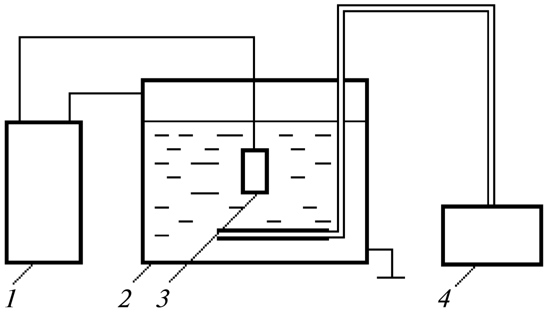

Fig. 2. Diagram of a microarc oxidation setup: (*1*) the power supply, (*2*) the process tank with the electrolyte, (*3*) the workpiece, and (*4*) the bubbler.

this regard, it is of current concern to enhance the efficiency of the MPO process.

The aim of this work is to study the possibility of intensifying the MPO process using carbon nanoparticles.

RESEARCH TECHNIQUE

For the studies, we used samples of aluminum alloys with different chemical compositions. The ceramics were formed using MPO equipment (Fig. 2) in the anode–cathode mode in a silicate–alkaline electrolyte comprising 2 g/l KOH and 3.5 g/l Na_2SiO_3. The carbon additives were an ultradispersed diamond-containing blend (UDDG) and ultradispersed diamonds (UDDs). The concentration of these components in the electrolyte was varied from 0.5 to 5.0 g/l [3]. The main studies were carried out for the UDDG, because, according to our data, it yields a higher effect (Fig. 3). It is also economically advantageous.

The X-ray diffraction analysis was performed using a DRON-3M diffractometer in monochromated CuK_α radiation; the metallographic studies were carried out using a MIM-8 microscope with digital image recording. The tribotechnical tests were performed using a scheme with the reciprocating movement of a counter body relative to a stationary sample under conditions of boundary friction in a medium of I-40A industrial oil and without lubricants. The tests were carried out at a pressure of $p = 2–36$ MPa and a sliding velocity of 0.1 m/s. The wear of the samples was determined according to the weight loss by weighing on a VLR-200 analytical balance.

RESULTS AND DISCUSSION

The results showed that the addition of the UDDG into the electrolyte has a significant effect on the formation of the coatings. First of all, this is evident from the growth of their thickness, which increases by a factor of 1.5–2.8 in comparison with the base electrolyte depending on the alloy's composition.

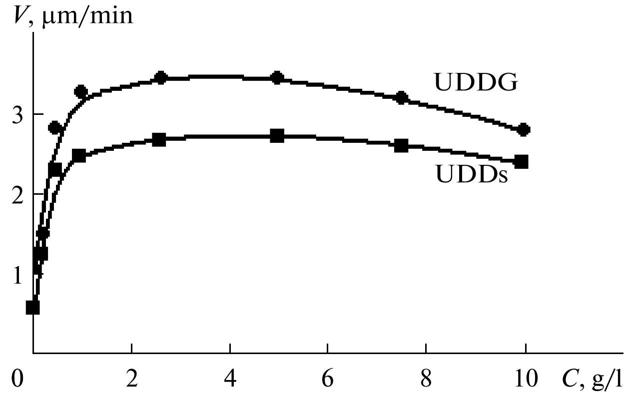

Fig. 3. Coating growth rate versus the concentration of carbon nanoparticles in the electrolyte.

Figure 4 shows, by way of an example, the microstructure of the ceramic coatings formed on AK5M2 and AK10 silumins in a base electrolyte containing the UDDG. A comparison of the microstructures shows that the addition of carbon nanoparticles into the elec-

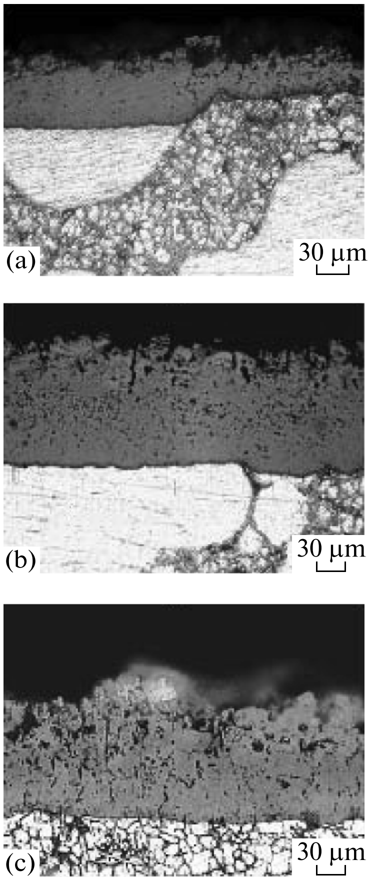

Fig. 4. Microstructure of the coating formed on the (a, b) AK5M2 and (c) AK10 alloys in (a) the base electrolyte and (b, c) with an UDDG additive: (*1*) the coating and (*2*) the metal base.

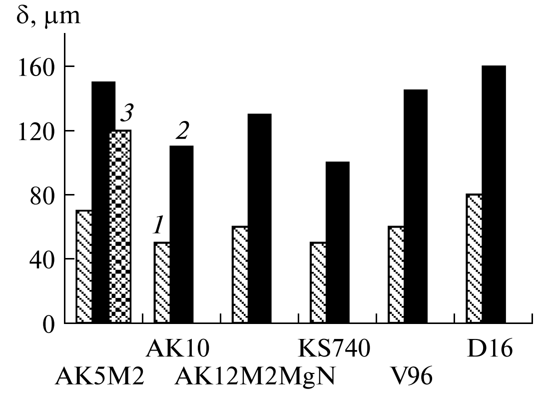

Fig. 5. Effect of the modification with UDDs and UDDGs on the coating's thickness on the alloys under study: (*1*) unmodified, (*2*) modified with the UDDG, and (*3*) modified with UDDs.

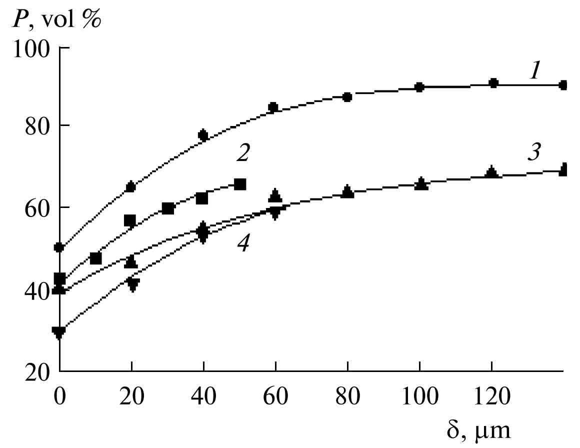

Fig. 6. Distribution of α-Al_2O_3 from the surface to the base in the (*1*, *3*) modified and (*2*, *4*) unmodified coatings formed on the (*1*, *2*) D16 and (*3*, *4*) AK5M2 alloys.

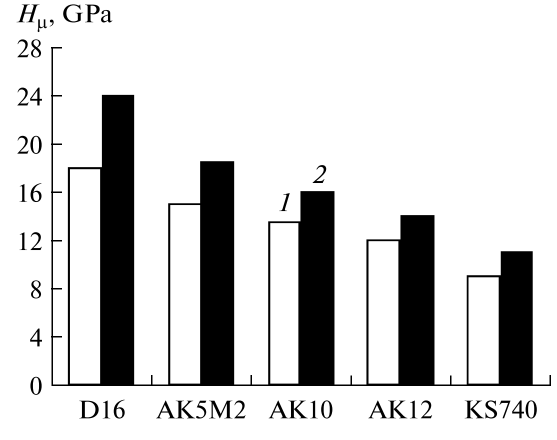

Fig. 7. Microhardness of the UDDG-modified ceramic coating on various aluminum alloys: (*1*) without carbon nanomaterials and (*2*) modified with carbon nanomaterials.

trolyte has a significant effect on the growth of the coating's thickness. The nanoparticles also contribute to the equalization of the coating's thickness in different structural components of the alloy (Fig. 4b).

The use of the UDDG in the MPO process made it possible to form fairly uniform coatings (with a thickness of 100–140 μm) on alloys with a higher content of silicon as compared with the AK5M2 and AK10 alloys, in particular, on AK12M2MgN eutectic and KS740 hypereutectic silumins (Fig. 5).

The observed effect of the growth of the oxide layer's thickness can significantly shorten the duration of the microplasma process. In addition, the exposure to carbon nanoparticles leads to the improvement of the physicomechanical characteristics of the resulting ceramic coatings due to the changes in their phase composition.

According to the X-ray diffraction data, the coatings formed in the electrolyte with UDDG additives have a high concentration of the high-temperature modification of alumina α-Al_2O_3. It is noteworthy that the highest concentrations of corundum (85–90%) are registered for the D16 alloy, which hardly contains silicon at all (Fig. 6, curve *1*). However, for the ceramics formed in the electrolyte with the UDDG on silumins, the volume fraction of α-Al_2O_3 is also fairly high (Fig. 6).

The increase in the concentration of α-Al_2O_3 in the ceramics formed under the action of the UDDG can be attributed to the following. The incorporation of carbon nanoparticles into the coating decreases the dielectric strength of the oxide layer, which leads to a decrease in the breakdown voltage and, as a consequence, to an increase in the duration of the microplasma discharges. This contributes to the more intense heating of the coating material and provides favorable conditions for phase transformations, in particular, γ-$Al_2O_3 \longrightarrow \alpha$-$Al_2O_3$, which is known to require the highest temperature (1470 K), which significantly exceeds the temperature of the formation of γ-Al_2O_3 (600–770 K). This leads to an increase in the corundum concentration in the coating and, therefore, to an improvement of its physicomechanical properties, in particular, its microhardness (Fig. 7).

In addition to increasing the strength properties, the modification with carbon nanoparticles also provides an improvement in the tribotechnical characteristics of the coatings. The test results show that the friction coefficient f of the unmodified coating on steel in the dry friction mode at a contact pressure $p = 3$ MPa at the stage of steady-state wear is 0.70–0.75 (Fig. 8).

The modification of the coatings in the process of microplasma treatment in electrolytes with UDDG additives results in a decrease in the friction coefficient, which settles at a level of 0.58–0.65 under the same test conditions. Lower values of the friction coefficient of 0.28–0.30 are obtained in the case of ceramic–ceramic coupling (Fig. 8). The decrease in

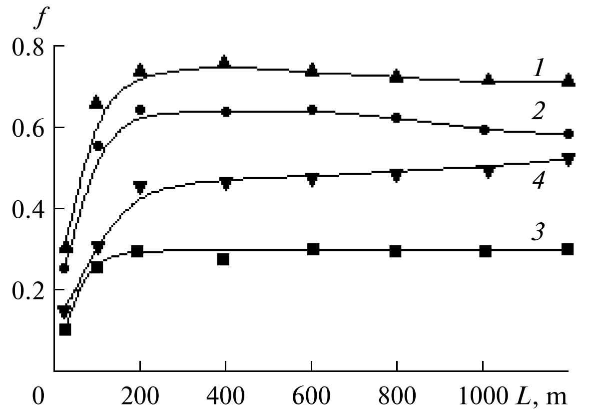

Fig. 8. Dependence of the friction coefficient of the (*1*, *4*) unmodified and (*2*, *3*) modified ceramics on the slip distance at $p = 3$ MPa without lubricants in a pair with (*1*, *2*) steel and (*3*, *4*) ceramics.

the friction coefficient of the ceramics upon their modification can be explained by the increase in the concentration of corundum α-Al_2O_3 and the penetration of graphite particles into the coating during its formation.

The modified coating also exhibits a higher wear resistance than the unmodified coating. Thus, the results showed that the wear resistance of the coating that contains particles of nanodiamonds and nanographite and was tested in a pair with steel increases by a factor of 2.5–3.

The tests under conditions of boundary friction showed that the UDDG modification of the coatings during their formation leads to a significant (3.5-fold) increase in the bearing capacity as compared with the unmodified ceramics (Fig. 9).

The following can probably affect the enhancement of the efficiency of the microarc oxidation of aluminum in the modification of the coatings with carbon nanoparticles. During the electrolysis, the aluminum workpiece, being an active anode, undergoes oxidation in accordance with the anodic reaction

$$Al - 3e^- = Al^{3+}. \quad (1)$$

The inclusions of graphite particles in the coating can be regarded as parts of an inert anode, on which, according to the laws of electrolysis, the electrochemical oxidation of water with oxygen evolution takes place:

$$4OH^- = O_2 + 2H_2O + 4e^-; \quad (2)$$

subsequently, the oxygen participates in the formation of alumina by the formula

$$Al^{3+} + 3O^{2-} \longrightarrow Al_2O_3. \quad (3)$$

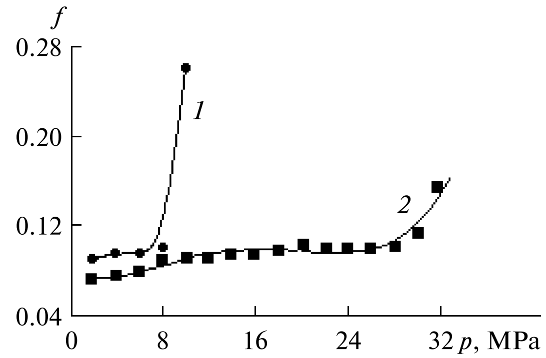

Fig. 9. Dependence of the friction coefficient of the (*1*) unmodified and (*2*) UDDG-modified ceramics on the pressure under conditions of boundary friction.

In the case of cathodic polarization, on the inert particles of graphite, hydrogen evolution occurs due to the electrochemical reduction of water:

$$2H_2O + 2e^- = H_2 + 2OH^-. \quad (4)$$

The ionization of hydrogen contributes to the development of an electric breakdown [4, 5]. In addition, its reaction with oxygen results in the release of a significant amount of heat energy:

$$2H_2 + O_2 = 2H_2O + 483.6\ \text{kJ}. \quad (5)$$

The increase in the temperature of the microplasma discharges with the participation of carbon nanoparticles in the MPO process is of great importance, because coatings are also formed due to thermolysis. Aluminum ions Al^{3+}, which are ejected into the electrolyte under the action of the field, form aluminate complexes there mostly in the form of $[Al(OH)_4]^-$ [6]. After that, these anions are transferred by the field into the discharge channel and, under the effect of temperature, form alumina:

$$2Al(OH)_4^- \rightarrow 2Al(OH)_3 + 2OH^- \xrightarrow{t} Al_2O_3 + 3H_2O. \quad (6)$$

According to [7], the arrival of dispersed graphite particles into a microarc discharge leads to a manifold increase in its current, power, and temperature. In all probability, the cause of the enhancement of the discharge intensity is attributed to the oxidative processes of carbon, which are accompanied by the release of large amounts of heat energy:

$$C + O_2 = CO_2 + 393.5\ \text{kJ}. \quad (7)$$

Carbon that did not react by formula (7) can evidently interact with the resulting carbon dioxide to form carbon monoxide:

$$C + CO_2 = 2CO - 172\ \text{kJ}, \quad (8)$$

which, in the presence of oxygen, burns with the evolution of large amounts of heat:

$$2CO + O_2 = 2CO_2 + 566\ \text{kJ}. \qquad (9)$$

It is obvious that the occurrence of exothermic reactions (7) and (9) contributes to the intense heating of the coating and, consequently, to the formation of the high-temperature modification of alumina α-Al_2O_3, the intensification of the thermolysis processes, and the partial melting of the coating pores. These reactions occur more easily in the case of weak interatomic bonds, which are characteristic of amorphous forms of carbon and are found in the UDDG. This fact can probably explain the higher efficiency of UDDGs in the MPO processes as compared with purified UDDs.

CONCLUSIONS

The use of carbon nanoparticles for the MPO formation of ceramic coatings on aluminum alloys has an intensifying effect on the rate of crystallization of the products of plasma chemical reactions, which is accompanied, on the one hand, by the growth of the coating thickness and, on the other hand, by the phase transition γ-$Al_2O_3 \longrightarrow \alpha$-$Al_2O_3$.

ACKNOWLEDGMENTS

This work was supported by the Joint Project of the National Academy of Sciences of Belarus (T09K-107) and the State Foundation for Basic Research of Ukraine (F29.2/015).

REFERENCES

1. Suminov, I.V., Epel'fel'd, A.V., Lyudin, V.B., et al., *Mikrodugovoe oksidirovanie (teoriya, tekhnologiya, oborudovanie)* (Microarc Oxidation: Theory, Technology, and Equipment), Moscow: EKOMET, 2005.
2. Malyshev, V.N., Coating Formation by Anodic–Cathodic Microarc Oxidation, *Zashch. Met.*, 1996, vol. 32, no. 6, pp. 662–667 [*Prot. Met.* (Engl. Transl.), vol. 32, no. 6, p. 607].
3. BY Patent no. 7607 MPK S25 D 11/06.
4. Brown, S.D., Kuna, K.J., and Van, T.B., Anodic Spark Deposition from Aqueous Solutions of $NaAlO_2$ and Na_2SiO_3, *J. Am. Ceram. Soc.,* 1977, vol. 54, no. 8, pp. 384–390.
5. McNeil, W. and Grass, L.L., Anodic Film Growth by Anion Deposition in Aluminate, Tungstate and Phosphate Solution, *J. Electrochem. Soc.*, 1963, vol. 110, no. 8, pp. 853–855.
6. Voyutskii, S.S., *Kurs kolloidnoi khimii* (Handbook of Colloid Chemistry), Moscow: Khimiya, 1976.
7. Markov, G.A., Belevantsev, V.I., Terleeva, O.P., Shulepko, E.K., and Slonova, A.I., Microarc Oxidation, *Vestn. Mosk. Gos. Tech. Univ., Ser. Mashinostr.,* 1992, no. 1, pp. 34–56.

ISSN 1068-3755, Surface Engineering and Applied Electrochemistry, 2011, Vol. 47, No. 1, pp. 23–27. © Allerton Press, Inc., 2011.
Original Russian Text © A.V. Paustovskii, R.A. Alfintseva, V.E. Shelud'ko, T.V. Kurinnaya, V.S. Tereshchenko, 2011, published in Elektronnaya Obrabotka Materialov, 2011, No. 1, pp. 30–34.

ELECTRICAL SURFACE TREATMENT METHODS

A Study of the Dependence of the Mass Transfer on the Structural Factors of the Electrodes in Electrospark Alloying with Ni–Cr–Al Alloys

A. V. Paustovskii, R. A. Alfintseva, V. E. Shelud'ko, T. V. Kurinnaya, and V. S. Tereshchenko

Frantsevich Institute for Problems of Materials Science, National Academy of Sciences of Ukraine,
3 Krzhizhanovsky Str., Kiev, 03142 Ukraine
e-mail: dep65@ipms.kiev.ua

Received July 2, 2010

Abstract—The dependence of the mass transfer parameters on the structure of the Ni–Cr–Al and Ni–Cr–NiAl electrode systems in the electrospark alloying of steel 45 is studied. The phase composition of the cast, sintered, and hot-pressed alloys is a mixture of solid solutions based on nickel, chromium, and NiAl intermetallide. The mass-transfer coefficient in the case of alloying with cast and hot-pressed alloys is 2 to 3.5 times higher than that in the event of alloying with sintered alloys. This difference is due to the different structures of the electrodes prepared by different techniques.

DOI: 10.3103/S1068375511010157

INTRODUCTION

Upon the exhaustion of the service life of materials, various techniques of hardening and recovery of the working surfaces are used; as a result, the lifetime of the basic materials increases. In this case, the most effective method is electrospark alloying (ESA) using a compact electrode. For choosing the electrode's material, two main factors are taken into account: its chemical composition, which determines the functional purpose of the coating, and the structural state, which depends on the electrode's production technique.

The basic principle of the preparation of electrode materials for wear-resistant coatings is the condition of the heterogeneity of their structure [1, 2]. One of the versions of this structure is the presence of an eutectic consisting of solid solutions based on metals with high solubility in the substrate and phases with high hardness [3, 4].

The analysis of the literature data showed that the results of studies of the dependence of the mass transfer coefficients on the electrode's structure in ESA are limited.

EXPERIMENTAL

Taking into account the above principle of preparing materials for wear-resistant coatings, compact Ni–Cr–Al electrode systems were developed at the Frantsevich Institute for Problems of Materials Science of the National Academy of Sciences of Ukraine. The concentration of Ni, Cr, and Al in them is in the range of ternary eutectics. The electrodes had the following composition, wt %: 50.3 Ni, 40.2 Cr, and 9.5 Al (hereinafter 4A). They were prepared by casting, pulsed hot pressing (PHP), and sintering. This made it possible to obtain different structures and determine their effect on the kinetics of the mass transfer in the ESA of steel 45.

The developed alloys of the Ni–Cr–Al and Ni–Cr–NiAl systems are intended to restore pieces whose wear exceeds 100 μm. The studies [5] showed that the microhardness of these alloys is in the range of 6–12 GPa depending on their composition. The wear in dry sliding friction is 5–12 μm/km at a specific load of 0.6 MPa and a rate of motion of the counterbody (steel 65G) of 10 m/s; the friction coefficient is 0.27–0.29. The microhardness of the electrospark coatings of these alloys is 8–10 GPa, the wear is 6–14 μm/km depending on the composition, and the coating thickness is 0.7–1.2 mm [6].

The Ni–Cr–Al alloys were melted in an electric resistance furnace in alundum crucibles with N–O nickel, ERKh–O chromium, and high-purity aluminum 9-995 used as the feed stock. The electrodes were prepared by fusion casting in the form of rods with a diameter of 4–7 mm.

The PHP of these alloys was carried out in two stages: the sintering of a powdered mixture of PNE nickel, PKhM chromium, and PAR-41 aluminum and the subsequent pressing in a closed press mold with the maximum pulse impact under a pressure of 100–1200 MPa and a temperature of 1300°C. The density of the samples prepared by this technique was 89–99%.

Since the sintered alloys of the Ni–Cr–Al system exhibited significant deformation due to the melting of

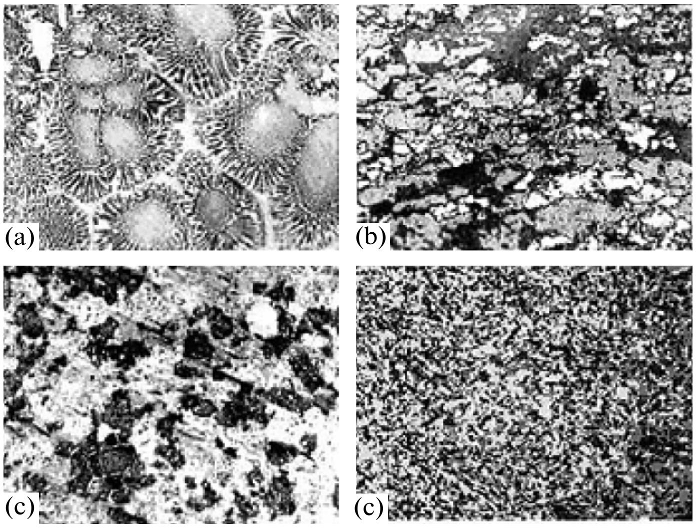

Fig. 1. Microstructure of the (a) cast and (b) hot-pressed 4A alloy and (c) the sintered and (d) PHP 4AS1 alloy.

the aluminum, it was replaced by an NiAl intermetallide with a high melting point. The following compositions were studied: 4AS1 (wt %: 33 Ni, 41 Cr, 26 NiAl), 4AS2 (wt %: 39 Ni, 35 Cr, 26 NiAl), and 4AS3 (wt %: 32 Ni, 40 Cr, 2 Al, 26 NiAl). The ratio of Ni, Cr, and NiAl corresponded to the composition of the 4A alloy. Powder mixtures of nickel, chromium, and NiAl intermetallide were sintered in vacuum for 2 h at a temperature of 1070°C, which was 0.8 T_{melt} of the Ni–Cr–NiAl eutectic alloy. The density of the samples after the sintering was 82–88%.

The microstructure of the prepared electrodes was studied using an Neophot-32 microscope. The X-ray studies were performed using a DRON-3M instrument with filtered copper K_α radiation. The diffraction patterns were interpreted using the ASTM card files. The ESA was carried out using an EFI-46A device in the following mode: the frequency of the vibrator was 100 Hz, the short circuit current intensity $I_{\text{SC}} = 1.5$ A, and the treatment time was 10 min/cm^2. The mass transfer coefficient $K = \Delta k/\Delta a$ was found via determining the following parameters: the specific erosion of the anode Δa and the specific weight gain of the cathode Δk measured for each minute of treatment of 1 cm^2 of steel 45.

RESULTS AND DISCUSSION

The microstructure of the 4A alloy prepared by casting and PHP and the 4AS1 alloy obtained by sintering and PHP is shown in Fig. 1. In the 4A cast alloy (Fig. 1a), a ternary eutectic is observed. The microstructure of the hot-pressed (PHP) and sintered alloys (Figs. 1b, 1c) is a mixture of three phases: light, gray, and dark. The microstructure of the 4AS1 alloy derived by PHP differs from that of the sintered and hot-pressed 4A alloy by the smaller phase components; it can be described as a fine-grained structure. The X-ray diffraction data showed that three main phases of γ-, α-, and β-solid solutions based on nickel, chromium, and NiAl intermetallide are observed in all the alloys.

The studies of the kinetics of the ESA with 4A alloys (cast and hot-pressed) and sintered 4AS1, 4AS2, and 4AS3 alloys (Fig. 2) indicate that the erosion of the sintered alloys (Figs. 2a–2c) is 2 to 4 times higher than that of the 4A alloy in the cast and hot-pressed state (Figs. 2d, 2e).

At present, there is no generally accepted ESA model that would give the possibility to explain the phenomenon that occurs during one treatment cycle. The ESA model is described to the best advantage in the works of the inventor of the method B.R. Lazarenko [7, 8]. The principle of this model is that the electric field intensity increases as the electrodes approach each other. At a certain distance between the electrodes, an electric spark discharge occurs, which results in the formation of a conduction channel and a beam of electrons emanating from the cathode and impinging onto the anode surface. As a result of the impact energy, a droplet of the melted metal is separated from the anode and moves toward the cathode. The droplet heats up, boils, and explodes. Melted particles precipitate on the cathode and crystallize. This model assumes that the substance is mostly transferred in the liquid state. A large bulk of data on the erosion of various materials can be found in the literature; the model is described most convincingly in [9]. In accordance with this model, the weight of the material ejected from the anode is defined by the relation

$$\gamma = qEft,$$

where γ is the weight of the ejected material, g; E is the single-pulse energy, J; f is the pulse repetition fre-

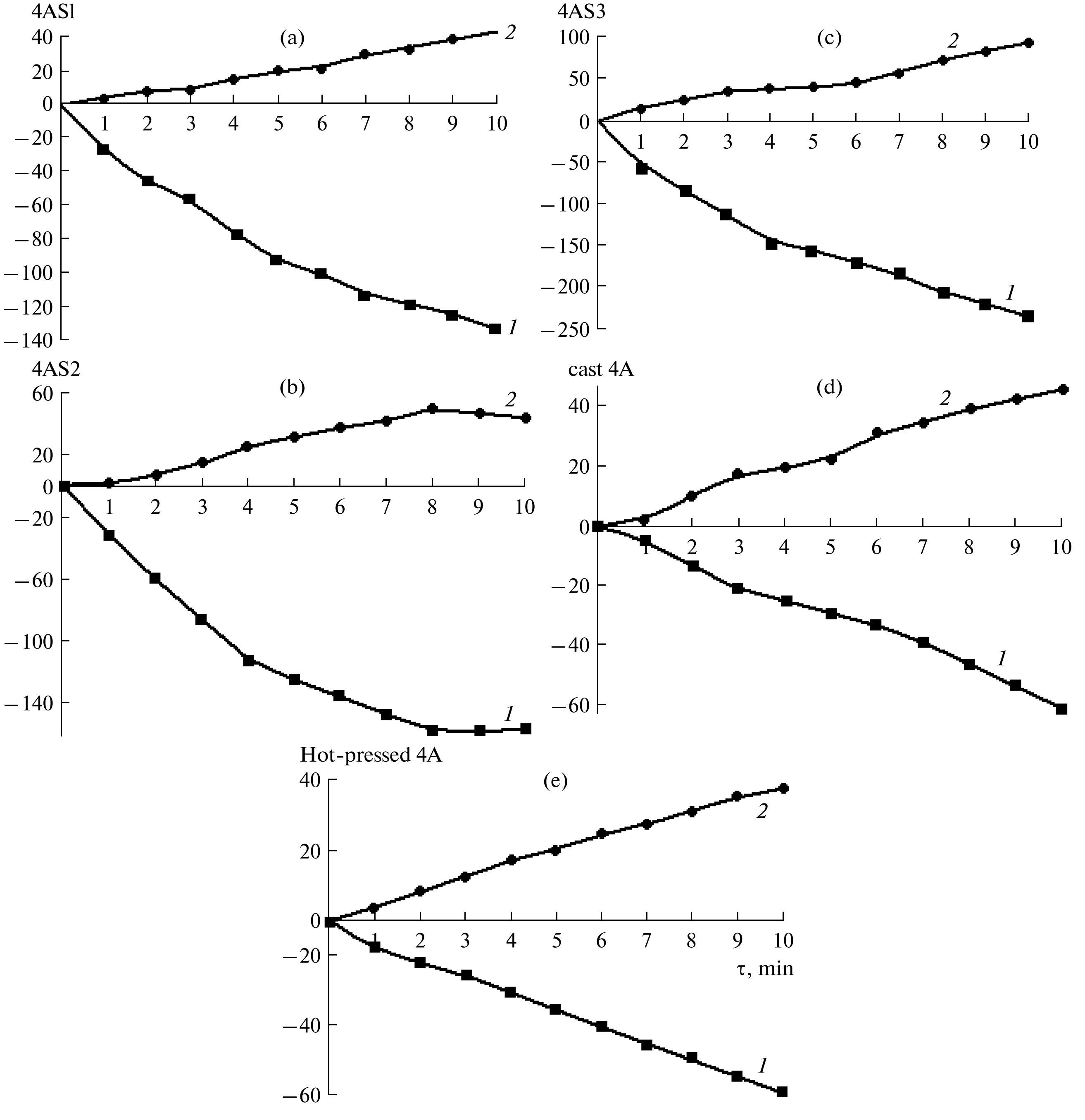

Fig. 2. Kinetic dependences of the erosion of the anode Δa and the weight gain of the cathode Δk in the ESA of 1 cm^2 of steel 45 with different alloys (alloying time τ = 600 s/cm^2): (a) 4AS1, (b) 4AS2, (c) 4AS3, (d) cast 4A, and (e) hot-pressed 4A; (*1*) % (Δa, mg/cm^2) and (*2*) % (Δk, mg/cm^2).

quency, Hz; q is the proportionality coefficient, which is determined by the physical constants of the electrode, the medium's composition, and the pulse duration; and t is the treatment time, s.

In this particular case, the original electrodes have the same elemental composition and are deposited in the same ESA mode; however, they differ in the structure (Fig. 1) due to their production technology. It is the difference in the original microstructure of the electrodes that is responsible for the difference in their erosion. In addition, sintering-derived electrodes exhibit residual porosity, which also affects the degree of erosion. It is obvious that the high values of the erosion of the sintered alloys are explained by the less strong bond between the separate fragments of the structure, which leads to a more severe disruption in an electrospark pulse.

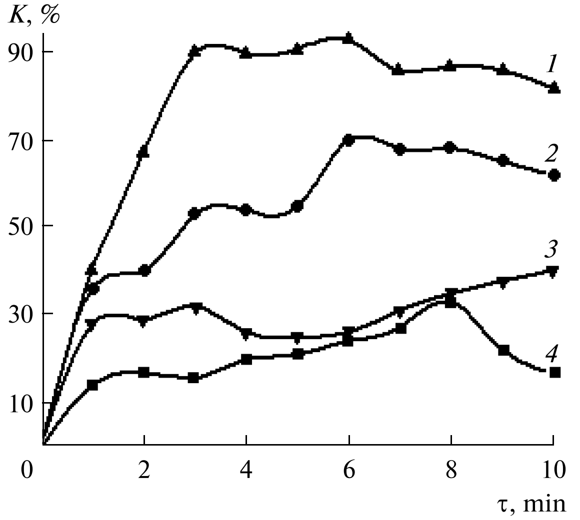

Fig. 3. Dependence of the mass transfer coefficient on the alloying time for the 4A, 4AS1, and 4AS3 alloys: (*1*) 4A (PHP), (*2*) 4A (cast), (*3*) 4AS3 (sintered), and (*4*) 4AS1 (sintered).

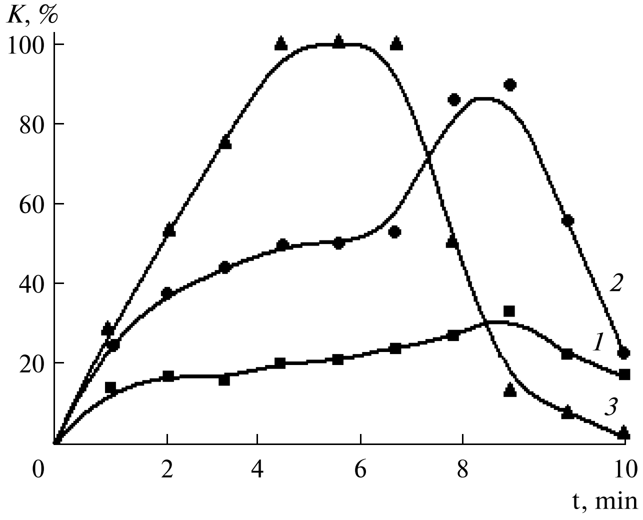

Fig. 4. Dependence of the mass transfer coefficient on the time of alloying with the 4AS1 alloy in the sintered and hot-pressed states, %: (*1*) sintered, $T = 1300°C$; (*2*) hot-pressed, $T = 1100°C$; and (*3*) hot-pressed, $T = 1300°C$.

Despite the large erosion, the amount of material that is transferred to the cathode hardly depends on the degree of the erosion. The weight gain of the cathode in the ESA with sintered 4AS1, 4AS2, and 4AS3 alloys differs little from that in the case of ESA with cast and hot-pressed alloys. We can assume that the relatively low weight gain of the cathode in the ESA with sintered alloys is due to the fact that most of the eroded particles were in the solid state and, therefore, could not fix to the substrate and were transferred to the products of the erosion.

The monotonic weight gain of the cathode with the increasing time of the alloying indicates that the brittle fracture threshold of the surface layer was not achieved within 10 min of alloying. The thickness of the resulting layer is 500–700 μm, which affords grounds to recommend this alloy for restoring worn surfaces of pieces. A coating deposited from cast and hot-pressed electrodes exhibits a high continuity, which provides high values of heat resistance. A coating of sintered alloys has a lower continuity.

The mass transfer coefficient in the ESA with cast and hot-pressed 4A alloys is 2 to 3.5 times higher than that in the case of alloying with 4AS1, 4AS2, and 4AS3 alloys (Fig. 3). The highest mass transfer coefficient (an average value of 81.2%) is observed for the ESA with the PHP alloy. The comparison of the mass transfer coefficients for the 4AS1 alloy prepared by sintering and PHP (Fig. 4) showed that the average mass transfer coefficient is 20% for the sintered alloy and 50% for the hot-pressed sample. This difference in the values of the mass transfer coefficient is governed by the pattern of the microstructure, which results from the technique of their production.

CONCLUSIONS

The mass transfer coefficient in the ESA of steel 45 using electrodes with the phase composition in the ternary eutectic range of α, γ, and β-solid solutions, which were prepared by different techniques and have different structures, varies from the maximum value of 81.2% for the hot-pressed alloy to 20% for the sintered sample. This difference is due to structural factors.

Based on the above, we can conclude that the ESA using hot-pressed electrodes is more efficient than that with sintered electrodes.

ACKNOWLEDGEMENTS

This work was supported by the State Fund for Fundamental Researches of Ukraine, grant no. 29.2/011.

REFERENCES

1. Kragel'skii, I.V., *Trenie i iznos* (Friction and Wear), Moscow: Mashinostroenie, 1968.
2. Kindrachuk, M.V., Dushik, Yu.A., and Luchka, M.V., Local Pattern of the Stress–Strain State of a Composite Material Loaded by Friction Forces, *Poroshk. Metall.*, 1994, nos. 9–10, pp. 56–61.
3. Kindrachuk, M.V., Shurin, A.K., and Panarin, V.E., Wear Resistance of Corrosion-Proof Eutectic Alloys with Interstitial Phases, in *Problemy treniya i iznashivaniya* (Problems of Friction and Wear), Kiev: Tekhnika, 1981, no. 19, pp. 17–28.
4. Borisov, Yu.S., Kharlamov, Yu.A., Sidorenko, S.L., and Ardatovskaya, E.N., *Gazotermicheskie pokrytiya iz poroshkovykh materialov. Spravochnik* (Handbook of Gas-Thermal Coatings of Powdered Materials), Kiev: Naukova Dumka, 1987.

5. Paustovs'kii, O.V., Tkachenko, Yu.G., Anisimov, G.M., Alfintseva, R.A., Kirilenko, S.M., and Bovkun, G.O., Technology and Materials for Electrospark Hardening and Restoration of Machine Pieces, in *Tsil'ova kompleksna programa NAN Ukraini "Problemy resursu i bezpeki ekspluatatsi konstruktsii, sporud ta mashin". Zb. nauk. statei*, (Target Complex Program of the National Academy of Sciences of Ukraine "Problems of Lifetime and Safety of Constructions, Buildings, and Machinery": Collection of Scientific Papers), Kiev: Inst. Elektrosvarki im. Patona, Nats. Akad. Nauk Ukr., 2006, pp. 553–557.
6. Paustovs'kii, O.V., Tkachenko, Yu.G., Alfintseva, R.A., Kirilenko, S.M., Yurchenko, D.Z., and Anisimov, G.M., Development and Use of Electrospark Surface Hardening and Restoration of Machine Pieces and Tools, in *Tsil'ova kompleksna programa NAN Ukrani "Problemy resursu i bezpeki ekspluatatsi konstruktsii, sporud ta mashin". Zb. nauk. Statei*, (Target Complex Program of the National Academy of Sciences of Ukraine "Problems of Lifetime and Safety of Constructions, Buildings, and Machinery": Collection of Scientific Papers), Kiev: Inst. Elektrosvarki im. Patona, Nats. Akad. Nauk Ukr., 2009, pp. 589–594.
7. Lazarenko, B.R. and Lazarenko, N.I., *Elektricheskaya eroziya metallov* (Electric Erosion of Metals), Moscow: Gostekhizdat, 1946.
8. Lazarenko, B.R. and Lazarenko, N.I., *Elektroiskrovaya obrabotka tokoprovodyashchikh materialov* (Electrospark Machining of Conductive Materials), Moscow: Akad. Nauk SSSR, 1959.
9. Lazarenko, N.I., On the Mechanism of Formation of Coatings by Electrospark Alloying of Metal Surfaces, *Elektron. Obrab. Mater.*, 1965, no. 1, pp. 49–53.

ISSN 1068-3755, Surface Engineering and Applied Electrochemistry, 2011, Vol. 47, No. 1, pp. 28–34. © Allerton Press, Inc., 2011.
Original Russian Text © A.V. Ivanov, A.V. Sinchuk, A.S. Bogoslavskaya, 2011, published in Elektronnaya Obrabotka Materialov, 2011, No. 1, pp. 35–42.

ELECTRICAL PROCESSES IN ENGINEERING AND CHEMISTRY

A Study of the Electromagnetic and Hydrodynamic Processes in a Liquid-Metal Conductor Exposed to Current Pulses

A. V. Ivanov, A. V. Sinchuk, and A. S. Bogoslavskaya

Institute of Pulse Processes and Technologies, National Academy of Sciences of Ukraine,
pr. Oktyabr'skii 43-a, Nikolaev, 54018 Ukraine
e-mail: iipt@iipt.com.ua

Received August 9, 2010

Abstract—In this work, we describe the results of a mathematical simulation of the electromagnetic and hydrodynamic processes that occur in a liquid-metal aluminum conductor while the passing of a kiloampere single-pulse current of microsecond duration through it. It is found that the compression of the liquid conductor by the magnetic pressure occurs upon exceeding a certain threshold value of the pulse current, which is governed by the metallostatic pressure. The fields and absolute values of the flow velocities in the conductor depending on the current pulse parameters are determined.@

DOI: 10.3103/S1068375511010078

INTRODUCTION

At present, to improve the quality of castings, researchers propose using methods based on the exposure of liquid and crystallizing alloys to an electrodynamic force. One of these methods is the pulse current treatment of melts. Unlike direct or alternating current, pulse modes allow currents of tens and hundreds of kiloamperes. Due to this, it is possible, first, to reduce the duration of the treatment of melts from 15–30 (direct current) to a few minutes and, second, to effectively use the force effect of electromagnetic fields on the metal with an insignificant level of losses due to Joule heating. It is possible to minimize the consumption for heating conductors owning to the short-duration current localized in a thin skin layer and the presence of time intervals between the pulses.

The results of the experiments described in [1–5] showed that the exposure of a liquid and crystallizing metal to a pulse current leads to a size reduction in the grain structure and an improvement of its homogeneity. The short-term periodic intensification of the heat-and-mass transfer processes in the near-wall region makes it possible to minimize the temperature difference in the treated volume, which provides conditions for the bulk crystallization. However, the multifactorial nature of a pulse impact (the pulse's amplitude, the duty cycle, the oscillation frequency of the pulse current, its shape and spectrum, etc.) causes difficulties in selecting the optimum electrical parameters and treatment schemes, unlike for a direct current, for which the main process parameter is its density [6]. The problem of switching power supplies is also controversial. In particular, the authors of [1–4] use discharge pulses from pulse current generators based on capacitive energy storages with a maximum current amplitude $I_{\max}$ of 0.3 to 40 kA, an oscillation frequency of the pulse current of 0.1 to 1 kHz, and a repetition frequency in the melt up to 1 kHz. In this case, one or more immersion electrodes were used for introducing the pulses into the melt. In [5], an alternating-current generator and broadband pulses of 1 to 8000 kHz were used; the current was fed to a conducting mold with the melt. In addition, the publications concerned with the pulse current treatment of melts describe, as a rule, results of physicometallurgical experimental studies. The mechanisms of the effects on the metal are hardly ever discussed (e.g., in [4]).

It is obvious that a number of coupled electromagnetic and hydrodynamic processes occur in a liquid-metal conductor while a current pulse flows through it; the role of these processes in the change in the structure and properties of the treated metal may be crucial. It is relevant to study them not only in terms of science but also in a strictly practical aspect, which makes it possible to optimize the process parameters of the pulse current treatment and to expand this method beyond laboratory research.

The aim of this work is to estimate the contribution of the electrodynamic forces to the change in the state of a bulk liquid-metal conductor by the mathematical simulation of the electromagnetic and hydrodynamic processes that occur while a single pulse current passes through the conductor. This estimation was carried out as applied to the treatment of an aluminum melt with recurrent discharge current pulses of microsecond duration, whose source was a high-voltage pulse current generator with a capacitive storage (Fig. 1a). This method provides pulses with a current oscillation frequency on the order of 10^5 Hz (Fig. 2). The preliminary experimental studies [7, 8] showed that the exposure of melts to these pulses for 1 min leads to a size reduction of the dendrite structure, eutectic modification, compaction of the intermetallide phases, and improvement of the mechanical properties.

PROBLEM FORMULATION

The process of passing of a single high-frequency current pulse through a metal conductor can be conventionally divided into several consecutive stages.

(i) The current and magnetic field are displaced to the conductor surface and concentrated in a skin layer with thickness δ, which is determined from the expression

$$\delta = \sqrt{\frac{1}{\mu_0 \mu \sigma \omega}}, \qquad (1)$$

where μ_0 is the magnetic constant, $4\pi \times 10^{-7}$ H/m; μ is the relative magnetic permeability, $\mu = 1$; σ is the specific conductivity of the metal $(\Omega \cdot \text{m})^{-1}$; and ω is the circular frequency of the current pulse, rad/s^{-1}.

(ii) The melt is affected by the volume electromagnetic forces F_{em} that occur in the interaction between the current pulse passing through the melt and the magnetic field induced by it, which are directed from the periphery to the center of the conductor with the current.

(iii) The conductor is compressed by the magnetic pressure P_{m}, and eddy currents are excited in it.

A noninductive approximation is used in the simulation; that is, the electromagnetic field and hydrodynamic processes are analyzed independently of each other. In this case, the problem was solved in a two-dimensional axisymmetric formulation for a “tip–tip” electrode system (Fig. 1b).

To solve the electromagnetic problem, we shall use the set of Maxwell equations written for the case of a quasi-stationary field:

$$\nabla \times H = \sigma(E + \nu \times B) + J^{\text{e}}, \qquad (2)$$

$$\nabla \times E = -\frac{\partial B}{\partial t}, \qquad (3)$$

$$\nabla \cdot B = 0, \qquad (4)$$

$$\nabla \cdot D = 0, \qquad (5)$$

$$\nabla \cdot J = 0, \qquad (6)$$

where ∇ is the Hamilton operator, H is the intensity of the magnetic field in the melt, A/v; J is the current density, A/m^2; E is the electric field intensity, V/m; ϖ is the subject velocity, m/s; B is the magnetic field induction in the melt, T; J^{e} is the density of the induced (extrinsic) currents, A/m^2; and D is the electric induction, C/m^2.

After simple transformations and the introduction of a cylindrical coordinate system (Z, r, φ), we obtain

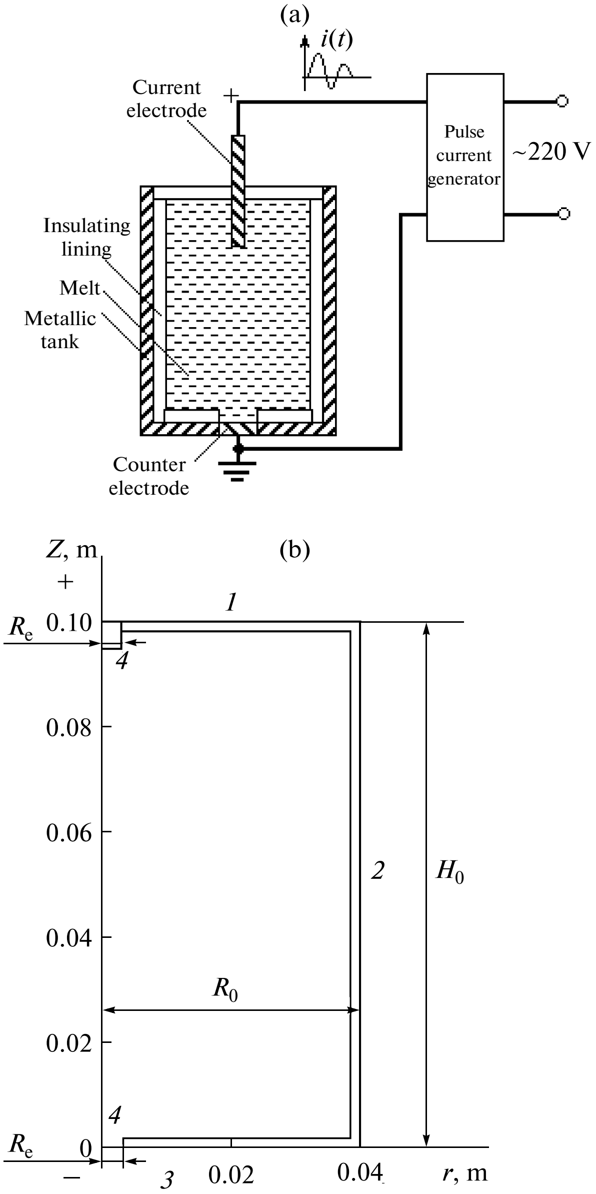

Fig. 1. Electric current treatment of a melt: (a) the treatment diagram and (b) the geometric model of a conductor, (*1*) the melt face, (*2*) the lateral surface, (*3*) the back surface, and (*4*) the electrodes.

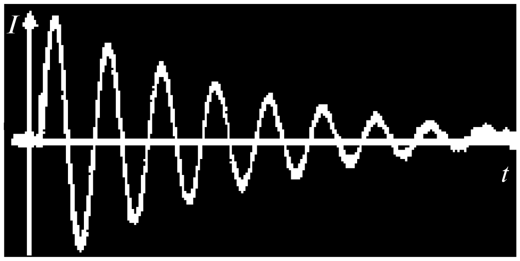

Fig. 2. Discharge current oscillogram: $mI = 10$ V/div and $mt = 10$ μs/div.

Varying parameters

Mode	U_0, kV	C, μF	L, μH	I_{max}, kA	ω, 10^{-6} s^{-1}	τ, μs
1	12	0.25	0.5	8.5	2.8	17.6
2	12	4	8	8.5	0.18	284.0
3	31	0.25	0.5	22	2.8	17.6
4	31	1	2	22	0.71	70.4
5	31	4	8	22	0.18	284.0

the equation for the magnetic field intensity H_φ, which depends on the angle φ:

$$\mu_0\mu\frac{\partial H_\varphi}{\partial t}+\nabla \times (\sigma^{-1}(\nabla\times H_\varphi - J^e) - \nu\times(\mu_0\mu H_\varphi)) = 0. \tag{7}$$

The geometric dimensions of the model elements are taken identical to those used in the experiments in [8]: the height of the liquid-metal conductor $H_0 = 100$ mm, its radius $R_0 = 40$ mm, the depth of immersion of the electrode into the melt is 5 mm, and the radius of the immersed electrode R_e and the counter electrode is 2 mm. The electrode material is copper; the liquid conductor is an aluminum melt at a temperature of 700°C.

We assume that the density of the extrinsic currents $J^e = 0$ and $H_\varphi = 0$ along the Z axis. The initial conditions are defined as $H_\varphi|_{t=0}$, $I|_{t=0} = 0$; and $\nu|_{t=0} = 0$.

The boundary conditions for the regions marked in Fig. 1b are as follows:

for region *1*: $H_\varphi = \frac{I(t)}{2\pi r}$;

for region *2*: $H_\varphi = \frac{I(t)}{2\pi R_0}$;

for region *3*: $H_\varphi = \frac{I(t)}{2\pi r}$;

for region *4*: $H_\varphi = \frac{I(t)r}{2\pi R_e^2}$.

The current pulse $I(t)$ is given in the form of a damped sinusoid, which adequately approximates the real current curve:

$$I(t) = \frac{U_0}{\sqrt{\frac{L}{C}}}e^{(-R/2L)i}\sin(\omega t), \tag{8}$$

where U_0 is the charging voltage of the capacitor bank, V; C is the capacitance of the capacitor bank, μF; L is the inductance of the discharge circuit, μH; and R is the active resistance of the discharge circuit, Ω.

The parameters of the discharge circuit are chosen so as to estimate the effect of the intensity and the oscillation frequency of the pulse current on the characteristics of the electromagnetic field in the conductor under treatment (table). The pulse duration τ in the calculation is limited to eight periods, which are recorded in the discharge current oscillograms for the chosen discharge circuit parameters and a given resistance of the conductor.

The magnetic pressure P_m is determined from the expression

$$P_m(t, r) = \frac{\mu\mu_0 H_\varphi^2(t, r)}{2}. \tag{9}$$

We assume that the motion of the liquid metal occurs only under the action of the volume electromagnetic force, which is determined from the expression

$$F_{em} = J \times B. \tag{10}$$

The hydrodynamic processes in the conductor are analyzed by the numerical solution of the Navier–Stokes equation for an incompressible liquid at $\nabla \times \nu = 0$:

$$\frac{\partial \nu}{\partial t} = -(\nu\cdot\nabla)\nu + \gamma\Delta\nu - \frac{1}{\rho}\nabla P_m + \frac{F_{em}}{\rho}, \tag{11}$$

where Δ is the Laplace operator; γ is the kinematic viscosity coefficient, m^2/s; and ρ is the density of the melt, kg/m^3.

SIMULATION RESULTS

The equations were numerically solved using the COMSOL Multiphysics 3.3 simulation software. Figure 3 shows the results of the calculation of the magnetic field intensity in different cross sections of the conductor at a depth h from the melt face at the instant of the first peak of the discharge current I_{max}. A nonpotential behavior of the field in the sample and a characteristic increase in the field intensity are observed as I_{max} increases. In addition, the field is concentrated in the surface skin layer with a thickness of 0.3 (modes 1, 3), 0.7 (mode 4), and 1.4 mm (modes 2, 5).

The calculations also show (Fig. 4) that, while the selected kiloampere current pulse passes through the

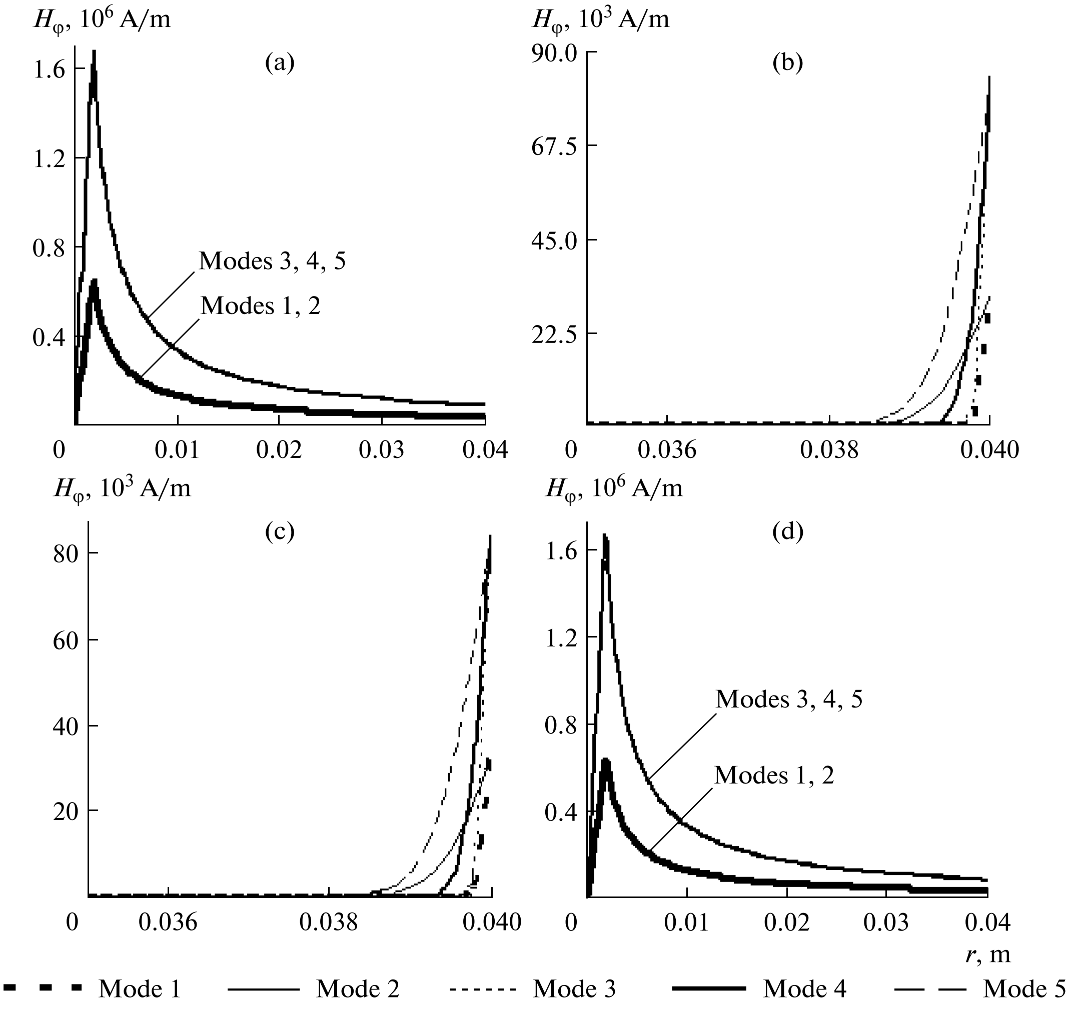

Fig. 3. Magnetic field distribution along the radius of the conductor at a depth from the melt face h at the instant of the first current peak: (a) $h = H_0$, (b) $h = 98 \times 10^{-3}$ m, (c) $h = 50 \times 10^{-3}$ m, and (d) $h = 0$.

conductor, the maximum magnetic pressure induced by the action of the electromagnetic force $F_{\rm em}$, which is directed from the surface to the center of the conductor, is 0.65 to 4.4 kPa in the near-wall region of the melt. When the conductor experiences this pressure, it is compressed. However, since the case in hand is a metallic liquid, which, in turn, exerts pressure on the walls of the mold, then the resulting pressure along the side wall of the conductor will be determined by the difference

$$P = P_{\rm m} - P_{\rm st},$$

where $P_{\rm st}$ is the metallostatic pressure in the melt, Pa.

If we assume that $P_{\rm st}$ is 2.3 kP at the depth $H_0 =$ 100 mm of a liquid aluminum conductor, then the inequality $P_{\rm m} > P_{\rm st}$, which determines the beginning of the real compression, will be fulfilled under the condition $I_{\max} > 15$ kA. In this case, the magnetic pressure will already have a formative effect on the crystallization process, which is confirmed by the experimental data of [8]; in this work, the structure parameters and mechanical properties of the metal are significantly improved using mode 3 of the pulse current treatment.

Analyzing Figs. 3 and 4, we can also single out a significant concentration of the electromagnetic field and pressure in the characteristic regions of the conductor, i.e., the junctures of the walls and the near-electrode regions, where jumps in the magnetic pressure up to 10^5–10^6 Pa take place. Obeying the rule of the addition of vector forces, the resulting effects in these areas could be significant so as to form a nonuniform velocity field and cause different types of eddy currents in the melt.

The velocity fields in the aluminum melt for modes 3–5 with $I_{\max}$ = const are shown in Fig. 5. In all the cases, a two-circuit flow velocity field is observed for the "tip–tip" electrode system. We can see that two distinct regions with opposite flows enclosed by a peripheral zone with a chaotic distribution of the

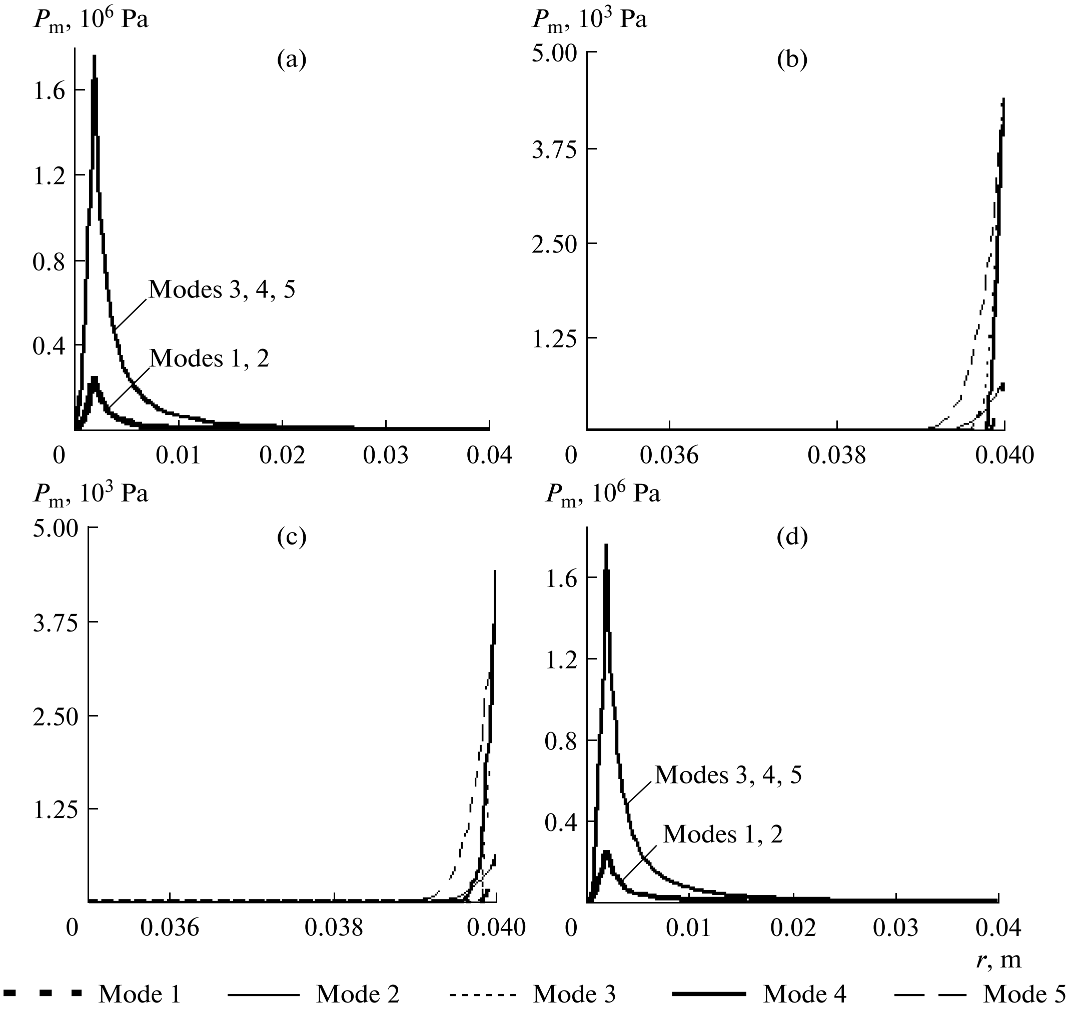

Fig. 4. Magnetic pressure distribution along the radius of the conductor at a depth from the melt face h at the instant of the first current peak: (a) $h = H_0$, (b) $h = 98 \times 10^{-3}$ m, (c) $h = 50 \times 10^{-3}$ m, and (d) $h = 0$.

velocities are formed in the central part of the conductor. These flows are directed to the central section of the conductor, in which they converge, and then the liquid moves in a radial direction. The maximum values of the velocity in the central section of the conductor v_c and the maximum values of the velocity of the liquid in the skin layer v_δ are calculated. As the current frequency decreases and the pulse duration accordingly increases by 16-fold, v_δ and v_δ increase by factors of 42 and 33, respectively. The mixing is more intense on the peripheral skin layer. Taking into account the differently directed movement of the liquid layers and the absolute values of the velocities, we can also state that the complete mixing of the conductor with the given sizes occurs in the time interval of a few seconds (mode 5) to a few tens of seconds (mode 3). For comparison, in [8], where positive changes in the structure and properties of the aluminum alloy were obtained, the time of the pulse current treatment was 60 s.

To reveal the effect of the geometry of the liquid-metal conductor on the formation of the flow velocity field, we calculated the maximum flow velocities in the central section of the conductor with different radius/height ratios R_0/H_0 (Fig. 6). It is evident that the velocity v_c varies nonmonotonically depending on the pulse duration and the R_0/H_0 ratio. More intense mixing processes can be expected for long pulses and with decreasing R_0/H_0, i.e., in long and narrow conductors. As R_0/H_0 increases, the value of the velocity settles at approximately the same level.

Note the applied relevance of these calculations, in which the range of the varying process parameters U_o, C, and L, which determine the current pulse, was fairly narrow in comparison with the feasible range. In fact, the currently available high-voltage pulse equipment with capacitive storages gives the possibility to vary these parameters in much wider ranges [9]. This makes it possible to process conductors of most diverse sizes and shapes.

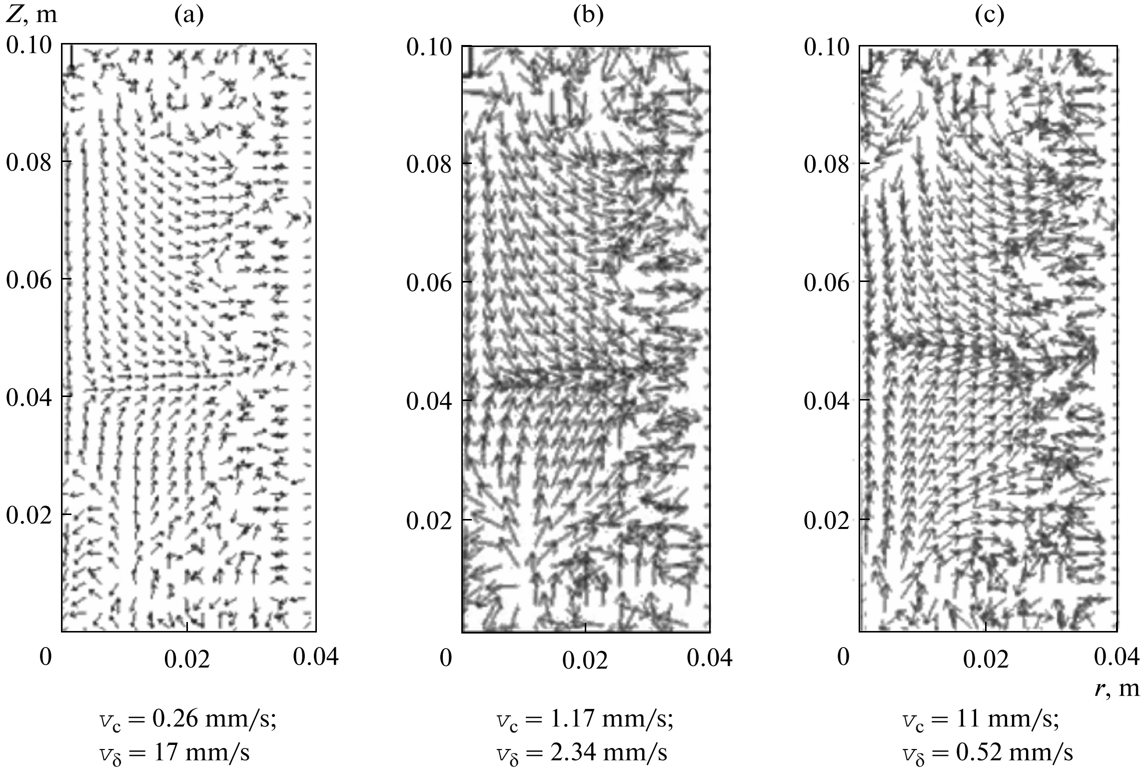

$v_c = 0.26$ mm/s; $v_\delta = 17$ mm/s

$v_c = 1.17$ mm/s; $v_\delta = 2.34$ mm/s

$v_c = 11$ mm/s; $v_\delta = 0.52$ mm/s

Fig. 5. Velocity field in a liquid-metal aluminum conductor: (a) mode 3, (b) mode 4, and (c) mode 5.

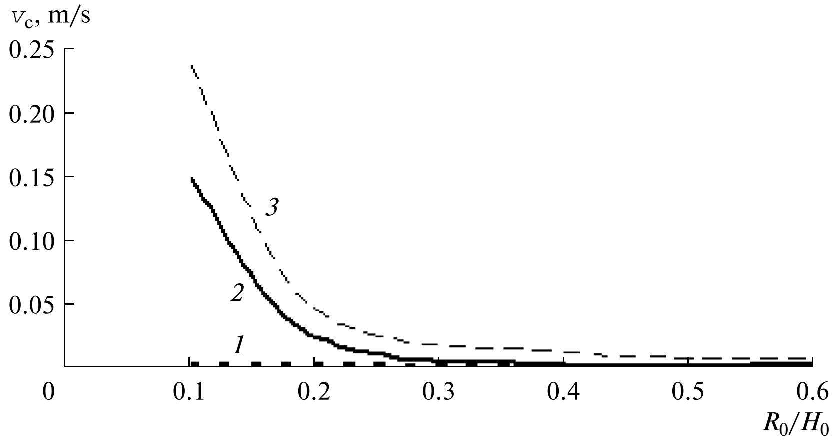

Fig. 6. Maximum flow velocities in the central part of a liquid-metal aluminum conductor: (*1*) mode 3, (*2*) mode 4, and (*3*) mode 5.

CONCLUSIONS

The exposure of a liquid-metal conductor to a pulse current leads to the development of highly nonlinear electromagnetic and hydrodynamic processes that are sensitive to changes in the current pulse characteristics, which provides greater functional capabilities of the pulse current treatment in comparison with direct current treatment.

The contribution of the electrodynamic forces, which are responsible for the compression and mixing processes in a liquid-metal conductor, to the change in its state becomes appreciable while passing a current pulse with certain parameters.

—The compression of the conductor occurs upon exceeding a certain threshold value of the pulse current; this can change the thermodynamic conditions of the crystal formation inside the liquid volume, particularly, in the near-wall regions of the melt.

—The mixing of a liquid is significantly affected by the pulse current frequency, the pulse duration, and the geometrical parameters of the conductor, which must be taken into account through the selection of the appropriate modes of the pulse current treatment of real casting molds with melts.

REFERENCES

1. Zhang, F., Zhang, M., Li, B., and Li, J., Effect of High Energy-Density Pulse Current on Solidification, *Mater. Sci.*, 2007, vol. 13, no. 2, pp. 120–123.
2. Liao, X., Zhai, Q., Luo, J., Chen, W., and Gong, Y., Refining Mechanism of the Electric Current Pulse on the Solidification Structure of Pure Aluminum, *Acta Mater.*, 2007, vol. 55, no. 9, pp. 3103–3109.
3. Ban, C., Han, Y., Ba, Q., and Cui, J., Influence of Pulse Electric Current on Solidification Structure of Al–Si Alloy, *Mat. Sci. Forum*, 2007, vols. 546–549, pp. 723–728.
4. Qin, R., Solidification under Electropulsing, *Int. J. Cast Met. Res.*, 2007, vol. 25, no. 7, pp. 92–98.
5. Zarembo, V.I., Kiseleva, O.L., Kolesnikov, A.A., Podgorskaya, E.S., and Suvorov, K.A., Effect of Current Pulses on Melting and Crystallization of Metals, *Metall. Mashinostr.*, 2003, no. 1, pp. 11–15.
6. Petrov, S.S., Prigunova, A.G., and Prigunov, S.V., Silumin Structure Transformation under the Exposure of the Melt to Direct Electric Current, *Teor. Prakt. Metall.*, 2006, nos. 4–5, pp.89–91.
7. Vernidub, A.G., Volkov, G.V., Grabovyi, V.M., Semenchenko, A.I., Fedchenko, N.A., Tsurkin, V.N., Sheigam, V.Yu., and Shenevid'ko, L.K., Exposure of the AK7 Alloy to Pulsed Electric Current, *Protsessy Lit'ya*, 2005, no. 1, pp. 64–67.
8. Ivanov, A.V., Tsurkin, V.N., Sinchuk, A.V., and Kreptyuk, Ya.V., Effect of Parameters of Electric Pulse Treatment on the Structure and Properties of Aluminum Alloys, *Materialy Mezhdunarodnoi nauchno-tekhnicheskoi konferentsii "Materialy i mekhanizmy morskogo transporta. Metody issledovaniya i uprochneniya. Tekhnologiya proizvodstva"* (Proc. Int. Sci.-Tech. Conf. on Materials and Mechanisms of Marine Transport, Methods of Research and Hardening, and Production Technology), Sevastopol: Ukr. Morskoi Inst., 2008, pp. 72–78.
9. Shcherba, A.A. and Dubovenko, K.V., *Vysokovol'tnye elektrorazryadnye kompaktnye sistemy* (High-Voltage Electric-Discharge Compact Systems), Kiev: Naukova Dumka, 2008.

ISSN 1068-3755, Surface Engineering and Applied Electrochemistry, 2011, Vol. 47, No. 1, pp. 35–43. © Allerton Press, Inc., 2011.
Original Russian Text © M.S. Apfel'baum, 2011, published in Elektronnaya Obrabotka Materialov, 2011, No. 1, pp. 43–52.

ELECTRICAL PROCESSES IN ENGINEERING AND CHEMISTRY

On the Energy Release in an Oil Heat Carrier During Transformer Cooling

M. S. Apfel'baum[a, b]
[a]Joint Institute of High Temperatures, Russian Academy of Sciences, ul. Izhorskaya 13, stroeniye 2, Moscow, 125412 Russia
[b]Moscow Institute of Physics and Technology, per. Institutskii 9, Dolgoprudnyi, Moscow oblast, 141700 Russia
e-mail: msa@ihed.ras.ru

Received August 24, 2010

Abstract—A theoretical model of the electrohydrodynamic prebreakdown phenomena in a weakly conductive media is proposed. Differential equations and the initial conditions for describing this model are written. The analytical and numerical solutions of these equations are given. The breakdown energy value for the oil in a transformer is calculated.

DOI: 10.3103/S1068375511010029

INTRODUCTION

Considerable deviations from Ohm's linear law in a solid weakly conducting media at the time-constant prebreakdown applied fields of a plate capacitor were experimentally discovered by Poole [1]. A similar nonlinear increase in the electric current upon an increase in the voltage both in homogeneous and strongly heterogeneous applied electric fields was later obtained experimentally in a liquid (a type of transformer oil) and gaseous weakly conducting media.

The growth in the conductivity of the media under study upon an increase in the modulus of the electric field intensity was theoretically grounded by Frenkel [2] using the Arrhenius equations for the volumetric rate of ionization taking into account a decrease in the potential in such ionization upon a strong electric field. Similarly, a decrease in the effect of the yield in the prebreakdown field was determined by Schottky. Onsager [3] obtained an expression mathematically close to that of Frenkel for the dependence of the prebreakdown rate of dissociation in weak electrolytes on the intensity modulus of the electric field using the methods of physical kinetics. Postulating the fulfillment of the law of a chemical equilibrium (of active masses) not only for the studied media of the transformer oil, Onsager [3] and Frenkel [2] also managed to obtain the dependences of their conductivity on the intensity modulus of the electric field up to its breakdown value. The effects of the drift of the charges and the motion of the liquid in this field were not taken into account in [2, 3]. In addition, in these and some of the more recent studies, their diffusion resulting from the gradient of the volume concentrations of the charges was also ignored. The time changes of the prebreakdown electrodynamic characteristics registered in the tests even with a high-voltage source of applied constant voltage and low power were not examined theoretically both in the works of these famous scientists and in some of the more recent papers. We also considered earlier [4] the case of an alternating prebreakdown electric field, e.g., generated by a transformer. In this paper, just as in the recent one, we examine only the case when the Maxwell time of the relaxation of the volume charge is far less than the period of the oscillating of the prebreakdown electric field generated by the transformer, which, in this case, allows us to reduce to quasi-stationary the calculations concerning the energy release in the considered heat carriers.

Taking into account such microscopic processes, we derived the electrohydrodynamic equations of the prebreakdown formation of the charges in a weakly conducting liquid media of transformer oil type. It was shown (e.g., in [5]) that, in order to use the Frenkel and Onsager formulas to calculate the sustained conductivity of the examined media, it is sufficient to preserve the condition of their electric (plasmic) quasineutrality in the fields under consideration. In this case, the density of the volume charge formed in the prebreakdown fields must be much lower in the entire space (beyond the non-quasi-neutral boundary layers) compared to the volume density of the self-neutralizing background of the charges with different signs. Then, according in particular to [5], a set of electrodynamic equations of the charge formation can be solved irrespective of the hydrodynamic ones at the smallness and commensurability of the rate of the medium's flows compared to the rate of the ion drift in the electric field. Note also that, in the obtained equations of motion for the sufficiently dense and heat-conductive media under consideration in a strong electric field, the effect of the viscosity should be taken into account [6]. In such fields, the molecules of the liquids of the transformer oil type, along with their possible impurities, partially disintegrate into ions. It is also assumed that the free electrons in the media under consideration (which are fairly dense), prior to the electric arc formation and their electric breakdown, mostly stick to neutral molecules. Therefore, we shall not discuss here an additional microscopic electronic component in the proposed theoretic modeling of the prebreakdown phenomena in the media under study. Nevertheless, we assume that the value of the sought ampere–time characteristics and the energy release are affected only by the ion components.

In the case of a high-voltage plate capacitor, quasistationary exponential volt–ampere characteristics can easily be obtained using Frenkel's formula for conductivity and an appropriate charge conservation equation in a differential form. In the case of a spherical capacitor, the distribution of a steady potential of the electric field in its interelectrode gap satisfies a fairly complicated ordinary first order differential equation obtained from the above charge conservation law and the Frenkel conductivity under the integral condition of the equality between the differences of these potentials (at the plates of a capacitor) and the applied voltage.

From the analytical solution of this equation that we obtained in [5] that satisfies this condition, there follow the ohmic linearity of the volt–ampere characteristics in weak fields and its quadraticity in the prebreakdown ones, which are observed at their strong heterogeneity. The obtained solution also describes more explicitly (than the unipolar solutions of the set of equations for these fields in the case of Townsend rare gases) the transition section (from linear to quadratic) of the volt–ampere characteristics. In this solution, instead of the Townsend empirical constant of the corona ignition voltage for the calculation of these characteristics, one may use a constant of low voltage conductivity, which can be taken from a handbook or determined accurately using the measured ohmic volt–ampere characteristics, and, in some cases, it can be calculated according to the composition of the molecules of the medium. The obtained theoretical high voltage volt–ampere characteristics, unlike those of the relevant Townsend, consider the effects of the temperature and charge composition of the molecules of the medium (which dissociates partially into ions) on the prebreakdown characteristics. The constant of the corona-ignition voltage is found to be not so valid for calculating the volt–ampere characteristics of the media under consideration as for weakly ionized rare gases, since it is hard to measure this voltage, which fails to be always detected in a sufficiently dense, viscous, and thermal conducting media. The problems in calculating the ionization release of energy (which leads to the formation of the discharge arcs in such media and to their breakdown in the proximity of the high-voltage electrodes) are of high priority. We previously calculated this energy for a high-voltage electrode close to a point electrode [5] without taking into account the energy contribution in the non-quasineutral boundary layers. Calculations of such energy for the diagnostics of the electrical breakdown to the extent of failures in oil-filled transformers are of high priority. Below, the analytical solution for the electrohydrodynamic differential equations will be obtained for such a nonstationary problem in the case of plate-parallel electrodes with an interelectrode gap $d \ll \sqrt{S}$ (here, S is the surface area of the capacitor plate) and a numerical solution of the equations of the hydrodynamic approximation for a similar problem in the case of coaxial cylinder electrodes whose interelectrode gap is far less than the length of their constituents. According to the results of the solutions, the time required for the energy release in a heated cylindrical surface layer of oil in a transformer will be estimated (as a rule, in the technical literature, a transformer's surface is considered to be cylindrical; however, an appropriate mathematical approximation to the real surface of the transformer is implied). In addition, a theoretical model for cooling the transformers using a derived set of macroscopic equations will be described, and the order of magnitude of the energy released by the heat carrier will be estimated.

THEORETICLAL MODEL AND MACROSCOPIC EQUATIONS

The following inequalities should be solved for the volume concentrations of the charges and the possible available impurities in the case of a weakly conducting media:

$$\begin{cases} n_{\pm} \ll n_a; \\ n_p \ll n_a. \end{cases} \tag{1}$$

We assume that the volume rate of the ionization with the subsequent attachment of free electrons to the molecules of the considered heat carriers or depending on the composition of their partial dissociation (the case of a purified transformer oil) or the partial dissociation of the available impurities is a continuous thermodynamic function of the volume concentrations of the molecules (with a complicated composition) of the medium and such impurities, as well as of the temperature and the electric field's intensity. The recombination of the charges occurring, as a rule, due to the attachment of free electrons to the molecules of the liquids under consideration is regarded to be only ionic:

$$W_I = W_I(n_a, n_p, T, |\mathbf{E}|) = W_I(n_a, n_p, T, 0) f(|\mathbf{E}|) \tag{2}$$

$$\begin{cases} W_r = K_r n_+ n_- \\ K_r = Z\dfrac{(b_+ + b_-)|e|}{\varepsilon\varepsilon_0}. \end{cases} \tag{3}$$

The expression we used for K_r was derived by Langevin in 1903. Using the methods of physical kinetics, Onsager grounded in [3] a weak effect of electric fields, including breakdown fields, on the value of the ion coefficient of the recombination. A sufficiently strong effect of the electric field on the value of the constant (coefficient) of the dissociation of the weak liquid electrolytes under consideration was also described in [3]. In addition, the second of equations (3) was obtained for the coefficient of recombination also in [3]. For the monotonic increasing dependence of the dissociation constant on the modulus of the intensity of the macroscopic electric field, an expression in the form of an analytical zero Bessel function of the first order of an imaginary argument close (in the prebreakdown fields) to the nonanalytic zero Frenkel exponent from the root of that modulus was obtained.

For the coefficient of the diffusion of the free charges, the Nernst–Townsend–Einstein correlation is used:

$$D_{\pm} = \frac{k_B T b_{\pm}}{Z|e|}. \tag{4}$$

The form of the continuous scalar function f of the vector argument in (2) is used, considering everything aforementioned, according to Frenkel [2]:

$$f(\vec{E}) = \exp(\beta|\vec{E}|^{1/2}); \quad \beta = \frac{|Ze|^{3/2}}{\sqrt{\pi\varepsilon\varepsilon_0}k_B T}. \tag{5}$$

Taking into account (1)–(5), the equations of the charge formation [5] look as follows:

$$\frac{\partial q}{\partial t} + (\vec{V}, \nabla q) - \frac{k_B T b}{Z|e|}\Delta q + (\vec{E}, \nabla\sigma) = -\frac{q\sigma}{\varepsilon\varepsilon_0}, \quad \Delta\phi = \left(-\frac{q}{\varepsilon\varepsilon_0}\right), \tag{6A}$$

$$\frac{\partial\sigma}{\partial t} + (\vec{V}, \nabla\sigma) + b^2(\vec{E}, \nabla q) - \frac{k_B T b}{Z|e|}\Delta\sigma - \frac{\sigma_0^2}{\varepsilon\varepsilon_0}\exp(\beta|\vec{E}|^{1/2})\exp\left[\frac{A}{k_B T_0}\left(1 - \frac{T_0}{T}\right)\right] + \frac{\sigma^2}{\varepsilon\varepsilon_0} = 0. \tag{6B}$$

The system of the electrohydrodynamic equations (6), where the diffusion and convective transfers of the ionic components in the moving medium and the Poisson equation for the potential of a macroscopic electric field are taken into account, should be enclosed mathematically by hydrodynamic equations for its neutral component close to the equations for the total mixture performing correlations (1). In this context, the differential equation that describes the mass continuity of the incompressible media is as follows according to [6]:

$$div\vec{V} = 0. \tag{7}$$

We took this equation into account when deriving Eqs. (6). According to [6], the equations of motion, of energy conservation, and of the state of the oil should be added to (7): in cooling the transformers, it is sufficient to use the Bussinesk linear equation of state for the dependence of density on T due to the small coefficient of the thermal expansion of the viscous media compared to the coefficient of the thermal expansion of rarefied gases. A standard equation of the heat gain [6] may be used instead of the equation of energy conservation without taking into account the weak Joule heating and the effect of the energy of the electric polarization along with the dissipation of the energy that results from the liquid viscosity and ion-molecular diffusion. The field of forces of the electric polarization of the bound charges merely redistributes the pressure of the media being examined. This allows the vortex-transport equation [6] to be used instead of the pulse equation in the theoretic modeling of the transformer cooling:

$$\vec{\chi} = rot\vec{V} \tag{8}$$

$$\rho\frac{d\vec{\chi}}{dt} - \rho(\vec{\chi}, \nabla)\vec{V} - \rho\nu\Delta\vec{\chi} = [\nabla q, \vec{E}]. \tag{9}$$

At the initial moment of time,

$$q(t = 0) = V(t = 0) = 0; \quad \sigma(t = 0) = \sigma_0 \tag{10}$$

We obtained in [5] an analytical solution of the above equations for the quasi-stationary distribution of the potential of an isolated high voltage sphere in an isothermal case along with the conditions of the quasi-neutrality of the weakly conducting media that were also derived there. This equation is as follows:

$$\phi(r) = \left(\frac{I}{4\pi\sigma_0}\right)^{1/2}\left[\frac{8}{\beta} - \sqrt{\frac{\varepsilon\varepsilon_0}{\tau\sigma_0}\left(|\vec{E}|^{1/2} + \frac{8}{\beta}\right)}\right]\mathrm{sgn}(\phi(r_0));$$

$$|\vec{E}|\exp\left(\frac{\beta}{2}|\vec{E}|^{1/2}\right) = \frac{1}{4\pi\sigma_0 r^2}; \quad |\phi(r_0)| = U.$$

$$\phi(r_0) = \left(\frac{I}{4\pi\sigma_0}\right)^{1/2}\left[\frac{8}{\beta} - \sqrt{\frac{\varepsilon\varepsilon_0}{\tau\sigma_0}\left(|\vec{E}|^{1/2} + \frac{8}{\beta}\right)}\right]\mathrm{sgn}(\phi(r_0));$$

$$|\vec{E}|\exp\left(\frac{\beta}{2}|\vec{E}|^{1/2}\right) = \frac{1}{4\pi\sigma_0 r^2}; \quad |\phi(r_0)| = U. \tag{11}$$

The solution looks similar in the case of a spherical high voltage capacitor with a specified quasi-stationary difference of the U potentials between its plates. The linearity of the volt–ampere characteristics of weak fields and the quadraticity of strongly heterogeneous prebreakdown fields can be obtained from (11) using the appropriate limitation transitions. The distribution of the prebreakdown quasi-stationary potential of spherical symmetry according to (11) differs greatly from the Laplace distribution due to the effect of the field of the forming volume charge in a self-consistent field.

In the case of a high voltage plate capacitor, the electric field outside of the near-electrode boundary layers of violation of the quasi-neutrality of the electric charges at the corresponding small parameters that we determined previously (e.g., in [5]) remains uniform owning to the law of the charge conservation. And the nonuniformity of the spatial distribution of the fields, which depends on the boundary conditions across the electrodes, forms upon an overlapping of the prebreakdown voltage and the volume charge in such layers only. Note that the thickness of such layers may increase with an increase of the values of the similarity criteria that we obtained previously [5, 8, 9]. In view of their smallness, the results of various experiments in the field of a plate capacitor confirm the formula for the calculation of the quasi-stationary isothermal prebreakdown volt–ampere characteristics under conditions of the Frenkel formula (5). Theoretically, it can be obtained from (5) and from the integral of a one-dimensional equation of the charge conservation in a differential form, which follows from (6) under the conditions of a stationary quasi-neutrality. Then, in the case of the determination of the constant of such an integration over the measured electric current, this dependence has the following form:

$$\sigma_0 \frac{U}{d} \exp\left[\frac{\beta}{2}\left(\frac{U}{2}\right)^{1/2}\right] = \frac{I}{S}. \qquad (12)$$

NONSTATIONARY SOLUTIONS AND THE APPLICATION OF THEM FOR THE CALCULATION OF THE PRE-BREAKDOWN AMPERE–TIME CHARACTERISTICS AND THE ENERGY RELEASED BY THE HEAT CARRIERS UPON COOLING OF TRANSFORMERS

Regardless of the vortex characteristics of the prebreakdown flows of the considered media in the interelectrode gap of a plate capacitor, a particular solution is found to satisfy the electrodynamic Eqs. (6) and the initial conditions (10):

$$I = \sigma S U/d, \quad q = 0, \quad |\vec{E}| = U/d,$$

$$\sigma = \frac{\varepsilon\varepsilon_0[\sigma_0\tau + \varepsilon\varepsilon_0 - (\varepsilon\varepsilon_0 - \sigma_0\tau)e^{-2t/\tau}]}{\tau[\sigma_0\tau + \varepsilon\varepsilon_0 - (\varepsilon\varepsilon_0 - \sigma_0\tau)e^{-2t/\tau}]},$$

$$\tau = \frac{\varepsilon\varepsilon_0}{\sigma_0 \exp(0.5\beta|\vec{E}|^{1/2})}. \qquad (13)$$

This solution is obtained by the ordinary time integration of Eq. (6B) and its independence on the Cartesian coordinate x in a one-dimensional approximation. The solutions of these equations, which satisfy the electrochemical (in the case of dissociation) or ionization boundary conditions on the capacitor plates, are close to Eq. (13) outside of the quasi-neutral boundary layers. This can be explained theoretically using the methods of the expansion of the asymptotic boundary layers based on small parameters from [7], which correspond to the modes of quasi-neutrality with the equation terms (6) having major spatial derivatives.

The rates of the prebreakdown flows of the considered weakly conductive medium may thus be both small and commensurable as compared to the rates of the ion drift in the electric field. We have derived the expressions for such similarity criteria of the described phenomena in [5, 8]. Also, there, the estimations of the values of those parameters for the prebreakdown modes were presented. Moreover, it was shown that, for a fairly wide variety of the considered media, the conditions of the electric (plasma) quasi-neutrality may be fulfilled also upon the overlapping of strong electrical fields. It is easy to show [5, 8] that these conditions can be fulfilled also for the oil heat carrier in a prebreakdown nonuniform electric field generated by a transformer.

Then, irrespective of the boundary conditions on the electrodes, the time–ampere characteristics of a plate capacitor with a time-constant source of voltage or a source of low frequency [4] may be calculated according to (13) in a one-dimensional approximation. It follows from (13) that, with an increase of the applied voltage (prior to a breakdown), the time deviations of the prebreakdown currents also intensify until they reach their stationary value. Moreover, as follows from (13) (and as should have been expected), the Frenkel formula from [2], where f is determined using (5), that describes the dependence of the quasi-stationary conductivity on the field voltage is obtained in the form of an asymptotic approximation. At the same time, according to (13), it turns out that this well-known formula for ideal dielectrics actually becomes invalid, since the time of the relaxation of the volume charge of the described media increases substantially. In the solution of (13), the time for the occurrence of the chemical reactions and establishing the conductivity appears to equal half the time required for the relaxation of such a charge. Therefore, the Maxwell time of the relaxation of the volume charge becomes the time for the energy accumulation resulting from the prebreakdown ionization (dissociation) in the heat carriers under study. The high value of this energy leads to electric disruptions, e.g., in the transformers.

As follows from the results of [8], formula (13) can also be obtained at various values of the mobility of positive and negative charges under the conditions of quasi-neutrality. The analytic analogue of formula (13) in the case of cylindrical and spherical capacitors and, moreover, for the two-dimensional configurations of high-voltage needle-plane electrodes is found impossible to obtain from (6) even without account for the effect of the hydrodynamics on the hydrodynamic characteristics. In these cases, the calculation of the ampere–time characteristics until establishing the current stationary value may be performed numerically using a simplified set of Eqs. (6) with initial conditions (10) for solving the external problems reported in [7].

An analogue of formula (13) for strong nonuniform electric fields of any complex configuration was obtained in [9] only under the conditions of the weak effect of the field of the forming volume charge on them. In order to obtain the simplest numeric solution in the case of the cylindrical symmetry close to the surface of an oil-filled transformer and the consequent calculations of the nonlinear volt-ampere and prebreakdown ampere-time characteristics, we used a set of nonstationary one-dimensional electrodynamic equations derived from equations (6), while applying in the one-dimensional cases the Gauss equation for the electric field intensity of cylindrical symmetry instead of the Poisson equation for its potential:

$$\frac{\partial q}{\partial t}+\frac{E\partial\sigma}{\partial r}=\left(-\frac{q\sigma}{\varepsilon\varepsilon_0}\right),$$

$$\frac{\partial\sigma}{\partial t}=\frac{\sigma_0^2\exp(\beta E^{1/2})-\sigma^2}{\varepsilon\varepsilon_0},$$

$$\frac{\partial E}{\partial r}+\frac{E}{r}=\frac{q}{\varepsilon\varepsilon_0}. \tag{14}$$

When obtaining set of equations (14), the terms that describe the nonstationary changes of the quasi-neutral conductivity are preserved in the left-hand parts of Eq. (6). In this situation, we can also analyze the formation of the volume charge with its increase from zero (at the initial moment of time) to the quasi-stationary. Previously, the possibility of the formation of a stable charge was indicated by Ostroumov [10)], but we derived [9] a mathematically closed equation system to describe such a formation. In obtaining one-dimensional equations (14) from this system, there were considered the estimations of the activation energy A of the partially dissociating oil molecules, which attest to the weak effect of the temperature difference on the conductivity of the oil carrier during the prebreakdown heating of transformers. Here, a nonisothermal component from (6B) in Eq. (14) is not taken into account (it is regarded negligibly small compared to the Frenkel exponent). Eliminating, just like in [11], the terms with major spatial derivatives affects the fulfillment of the quasi-neutrality criterion only on the change of the sought distributions of the electrodynamic characteristics in quasi-neutral thin layers near the boundaries of volumes filled with the media under consideration. To obtain the numerical solution of set of Eqs. (14), the initial conditions (10) were used for the conductivity and density of the volume charge along with the Laplace condition of the electric field's symmetry at the initial moment of time:

$$E(r,0)=\frac{U}{r\ln\left(\frac{r_1}{r_2}\right)}. \tag{15}$$

In Eq. (15), unlike in the analogous problems solved numerically in our previous studies [12, 13], r_1 and r_2 are the internal and external radii of a not cylindrical high voltage capacitor not filled with the considered medium but with a corresponding layer of a liquid (i.e., oil in a transformer near its surface cooled with such an oil). The algorithm and the program for the numerical calculations of the above equations that are used for the analysis of the prebreakdown processes in an oil heat carrier were selected just like as in the previous works. The algorithm elaboration was performed at a much larger step of the spatial–time array along the radial coordinate than the sizes of the non-quasi-neutral boundary layers, which form both in a strong electric field and due to the ion diffusion. The calculations were carried out from the internal to the external cylindrical surfaces of the layer on the supposition that this surface was positively charged. When the sign of the surface changes, the problem of the calculation of the energy released in such a layer reduces to the previous one with a change of the sign of the distributions of the field intensity and the density of the volume charge. This statement for the nonstationary problems of the type under consideration is grounded numerically in [11]. Namely, in [11], using generalizations of equations of type (14) for a nonisometric case, this was shown by solving a similar nonstationary problem concerning the electric field in the proximity of a cooling finely divided spherical particle. But, unlike the above nonisometric problem, when solving the problem described in the present study, a nonstationary integral of the charge conservation

$$\varepsilon\varepsilon_0\frac{\partial E}{\partial t}+\sigma E=\frac{I}{2\pi rl} \tag{16}$$

fails to be used for the deflation of set of Eqs. (14).

In the calculations (the results are presented below), integral (16) was used to control the numerical calculation of the finite-difference equations obtained from Eqs. (14) in a dimensionless form. In addition, the sought dependence of the time on the electric current until it has reached a stationary value was determined. In (16), l is the length of the constituent on the considered cylindrical layer ($l = 1.626$ m for the cylinder's surface (see the figure), which can be used to approximate the transformer's surface). Strictly speaking, a one-dimensional problem should not be regarded, but, for the analysis of the prebreakdown cooling of transformers, a one-dimensional approach is sufficient taking into account only the r changes (see the figure). The transition to the dimensionless equa-

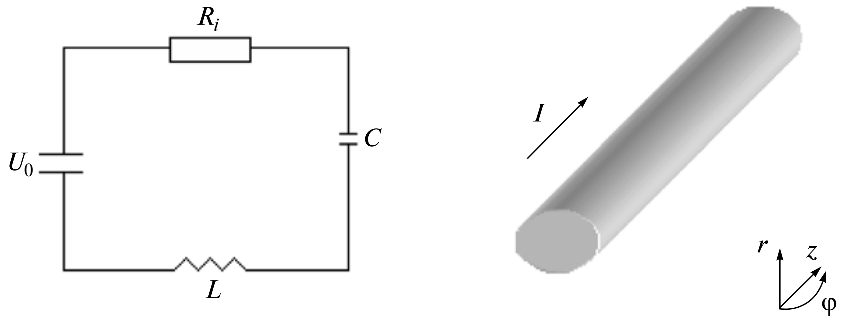

A scheme of the designations for the numerical calculations of the equations of a one-dimensional approximation (18) (see the text for the explanations).

tions was realized by varying the sought and initial values in the following way:

$$\tilde{t} = \frac{t}{\tau}, \quad \tilde{E} = \frac{Ed}{U}, \quad q = \frac{qd^2}{\varepsilon\varepsilon_0 U},$$

$$\vec{\beta} = \beta\left(\frac{U}{d}\right)^{1/2}, \quad \tilde{r} = \frac{r}{d},$$

$$\tilde{\sigma} = \frac{\sigma}{\sigma_0 \exp\left(\frac{\tilde{\beta}}{2}\right)}. \tag{17}$$

Then, the set of equations obtained from (14) is as follows:

$$\frac{\partial\tilde{E}}{\partial\tilde{r}} + \frac{\tilde{E}}{\tilde{r}} = \tilde{q},$$

$$\frac{\partial\tilde{q}}{\partial\tilde{t}} + \frac{E\partial\tilde{\sigma}}{\partial\tilde{r}} = -\tilde{q}\tilde{\sigma},$$

$$\frac{\partial\tilde{\sigma}}{\partial\tilde{t}} = \exp\{\tilde{\beta}(\sqrt{\tilde{E}} - 1)\} - \tilde{\sigma}^2. \tag{18}$$

The initial conditions for the dimensionless variables look as follows:

$$\tilde{\sigma}(\tilde{r}, 0) = \exp\left(\frac{\tilde{\beta}}{2}\right),$$

$$\tilde{q}(\tilde{r}, 0) = 0,$$

$$\tilde{E}(\tilde{r}, 0) = \frac{1}{\tilde{r}\ln\left(\frac{r_1}{r_2}\right)}. \tag{19}$$

Integral (16) in a dimensionless form is

$$\frac{\partial\tilde{E}}{\partial\tilde{t}} + \tilde{\sigma}\tilde{E} = \frac{\tilde{I}}{\tilde{r}},$$

$$\tilde{I} = \frac{I}{2\pi l\sigma_0 U \exp\left(\frac{\tilde{\beta}}{2}\right)}. \tag{20}$$

From a similar problem for a plate capacitor and its analytical solution (13), it follows that the conductivity's establishing occurs at times that equal half the time of the relaxation of the volume charge and the self-coordinated (with this charge) prebreakdown nonuniform electric field of a low frequency. Therefore, to obtain the sought numerical solution, a step in time $\Delta\tilde{t} = 0.02$ was taken. The stationary solution was reached within about 50 steps. To carry out specific numerical calculations along the radial coordinate, the near-surface layer of a transformer with an internal radius of 0.25 m and an external of 0.42 m (equal to the radius of the transformer's surface) was selected. That is the layer to be cooled near the surface of a transformer filled with oil was assumed to be approximated by a d-thick cylindrical layer ($d = r_2 - r_1$). During the calculations, we took from a handbook the dielectric permeability of the medium (2.24) and its low-voltage conductivity at $T = 400$ K; i.e., the conductivity in the heated transformer oil under study was 10^{-11} S/m. For the theoretic analysis of cooling with account of the effect of the prebreakdown electrohydrodynamic flows on it (not only for a transformer), extra electrohydrodynamic similarity criteria should be introduced into both the quasi-neutrality the criteria of the oil and the Re and Pr. Such criterion for an electrohydrodynamic interaction will be introduced below similarly to the criterion of a magnetohydrodynamic interaction (the Hartmann number). For the present calculations, in the case of cylindrical symmetry, the modulus of the very high effective voltage (average in value in the case of harmonic oscillations) generated by the transformer was 100 kV.

In calculating along the spatial coordinate, the step was 0.1. Differential equations (18) were replaced, as in [9], by the corresponding difference ones according to [14]. The time changes of the total current up to the quasi-stationarity at a low frequency were determined using the obtained numerical solutions of those equations. Previously [8, 9], we presented the results of calculations at the first time steps. In these works, we have already described the difference between the results of the q and E calculations for a Laplace high-voltage plate and cylindrical capacitors.

Moreover, in [9], the distinction of the sought electrodynamic characteristics in the case of the uniformity of the prebreakdown applied voltage from the case of its strong nonuniformity was also analyzed at stationary q and E. We also described previously the distinction of the structure of the flows in a strong nonuniform applied field from the cellular flows in a plate capacitor. Note that a sign of the forming charge outside of the non-quasi-neutral layers in a nonuniform field coincides with that of a transformer surface with the flows being directed from it irrespectively of its sign. Therefore, we proposed a theory that may be used in cooling transformers upon the field generation of a sufficiently low frequency. In addition, we shall describe in the present study, just as in [13], the similarity of the sought characteristics for the case of uniform and strongly nonuniform applied fields. It consists in the rather fast time evolution in both cases and the fairly rapid energy accumulation, which leads to the electric breakdown, e.g., in transformers. It follows from (13) that such an energy release (e.g., for transformer oil) may occur in a split second. We did not examine the computational stability of the difference scheme described in our study, but this can be done using the analogy with the stability analysis [14] for close and one-dimensional problems. The $\tilde{\sigma}$ change results from the effect of the prebreakdown field on the rate of the dissociation (ionization) reaction of the considered media. In this situation, for the basic data used in the numerical calculations, whose scheme is described above, a rather fast stabilization of the conductivity occurred for a fairly short time (also for fractions of a second). After such a time, for stabilization, the following equation of the charge conservation is obtained:

$$|\tilde{E}|\exp\left(\frac{\beta}{2}|\vec{E}|^{1/2}\right) = \frac{I}{2\pi\sigma_0 lr}. \qquad (21)$$

where I is the quasi-stationary current in the case of low frequencies in accordance with [4]. Then, the integral charge Q outside of the near-electrode layers of the quasi-neutrality violation is as follows:

$$Q = \int\limits_V q dV, \qquad (22)$$

where q is obtained from the last equation of (14) and equation (21) and is calculated analytically:

$$Q = \tau I\left[\exp\left(\frac{-\beta\sqrt{E_2}}{2}\right) - \exp\left(\frac{-\beta\sqrt{E_1}}{2}\right)\right]; \qquad (23)$$
$$E_1 = E(r_1), \quad E_2 = E(r_2).$$

According to (23) for the data that was used in the described numerical calculations upon stabilizing, $Q = 10^{-4}$ coulomb may be reached for the transformer oil without even considering the volume charge that forms in the non-quasi-neutral boundary layers (such layers are known as Langmuir ones for the arc electron-ion plasma [15]). This theoretical result is indicative of the high-degree charging in high-voltage facilities, particularly, in transformers, which is confirmed experimentally for big volumes of oil, e.g., in transformers that generate effective voltages up to 100 kV, and the order of the accumulated energy in the heated oil layer near its surface is calculated the same as in [5] ($A = QU$) and reaches 0.001 MJ/kg ignoring even the energy released in the Langmuir boundary layers of the quasi-neutrality violation [15] and without account for the energy of the Joule heating as well. The specific density of the released energy in the case of transformer oil for the order of magnitude for transformers designed for higher voltages is close to the order of an explosive one [16]. We determined the energy as was in [5]. A more exact analytic integration of the energy density according to [17] leads to a small correction factor for the case of spherical symmetry in the prebreakdown fields. Therefore, for the approximated case of a cylindrical symmetry close to spherical, it is enough to determine the sought energy such as QU (as it was mentioned above, we believe that, in the case of a strong nonuniform electric field, just like in [5], the time during which the energy is accumulated in the heat carrier is the period of the relaxation of the volume charge in the medium (rather than the time of the occurring of the relevant chemical reactions [16]). Here, the calculation of the energy released in the liquid that results from the prebreakdown electrodynamic and ionization processes, according to the model that we have proposed, may be used for the diagnostics of the electric breakdown as one type of an explosion with a corresponding energy accumulation over time, which is observed in high-voltage facilities, e.g., in transformers.

Note also that the coefficients like the dissociation or ionization constants may not be determined by Arrhenius but are rather calculated using the methods of physical kinetics with a more complicated release of the sought energy of a breakdown. The analysis of the prebreakdown transformer cooling that we carried out in [18] using set of equations (6)–(9) can also be performed. It can be shown.

Using the methods of physical kinetics for the calculations, we obtain the f function, which is different from the Frenkel exponent (in particular, the Onsager function of Bessel [3], analytical and zero). But here, refining of the formula

$$Nu = C, \tag{24}$$

which is present both in numerous technical literature sources and study [6], what we obtained in [18],

$$Nu = C + kU, \tag{25}$$

remains applicable. Indeed, formula (24) is derived in [6] using the methods of similarity and dimensionalities with small Re and equations (6)–(9) without taking into account the heat carrier flows that resulted from the strong electric field. Therefore, with the effect of these flows in a transformer on its cooling, we should take into account the dependence of Nu on the electrohydrodynamic analog of the Hartmann magnetohydrodynamic number. We introduced in [18] this parameter of the electrohydrodynamic interaction, and it showed that it is proportional to the effective electric voltage generated by a transformer. This criterion is a ratio of not the amperic, as in magnetic hydrodynamics, but rather of the coulomb forces to the forces of the viscous friction. Moreover, the density of such forces should be determined from (6) at the initial moments of time. This density is only slightly affected by the specific form of f. In addition, such a density is also hardly affected by the influence of the electric field on the recombination coefficient according to [19], where appropriate corrections to the Langeven–Onsager formula (3) were obtained. This is what leads to (25) in the case of the smallness of this extra (for Re and Pr) electrohydrodynamic similarity criterion,

$$1 \gg Eh \sim U, \tag{26}$$

for the above calculations for a 100–500 kV transformer. Formula (25), in which k depends on the viscosity, heat conductance, and density of the oil, in accordance with [18], can be used. And for the transformers of a more effective electrical voltage of $Eh \sim 1$ and $Eh \gg 1$, it is inadequate to be restricted only to the first Taylor-series approximation. Therefore linear dependence (25) is inapplicable for such transformers. It is also inapplicable for pulse transformers, since, due to their cooling, a volume charge in the oil fails to accumulate [8–10].

However, the transformers of an alternating current are used more often in industry and households than pulse ones, which allows us to recommend the proposed theoretic modeling (in particular, formula (25)) for application in the analysis of their affectivity.

The main designations: U is the generated electric voltage; d is the interelectrode gap; e is the proton charge; k_B is the Boltzmann constant; D is the diffusion coefficient; b is the mobility coefficient; q is the volume density of a charge; V is the rate of a media motion; n is the concentration; E is the intensity of the electric field; S is the area of an electrode surface; r is the radial coordinate; t is the time; τ is the time of charge relaxation; χ is vorticity; ε is the dielectrical permeability; I is the electric current strength; T is the absolute temperature; f is the function of a scalar or vector argument; W is the volume rate of formation of charges or neutrals; Z is the ion valence; σ is the conductivity of a medium; Nu is the Nusselt number; Pr is the Prandtl number; A is the energy, work; Ha is the Hartmann number (criterion of magnetohydrodynamic interaction); Eh is the criterion for the electrohydrodynamic interaction.

REFERENCES

1. Poole, H.H., On the Dielectric Constant and Electrical Conductivity of Mica in Intense Field, *Philosoph. Mag.*, 1916, Ser. 6, vol. 2, no. 187, pp. 112-129.
2. Frenkel, Ya.I., To the Theory of the Electrical Breakdown in Dielectrics and Electron Semiconductors, *Zh. Eksp. Teor. Fiz.*, 1938, vol. 8, no. 12, pp. 1291–2001.
3. Onsager, L., Deviations from Ohm's Law in Weak Electrolytes, *J. Chem. Phys.,* 1934, no. 2, pp. 599–611.
4. Apfel'baum, M.S., On Application of Resolvent Operators in Electrohydrodynamics, *Elektron. Obrab. Mater.*, 1987, no. 2, pp. 59–61.
5. Apfel'baum, M.S., The Problem on Point Electroexplosion of Weakly Conductive Media, *Elektron. Obrab. Mater.*, 2000, no. 6, pp. 31–42.
6. Landau, L.D. and Lifshits, E.M., *Teoreticheskaya fizika T. 6. Gidromekhanika* (Theoretical Physics, vol. 6. Hydromechanics), Moscow: Nauka, 1989.
7. Vasil'eva, A.B. and Butuzov, V.F., *Asimptoticheskie razlozheniya reshenii singulyarno vozmushchennykh uravnenii* (Asymptotic Expansions of Solutions of Singularly Disturbed Equations), Moscow: Nauka, 1973.
8. Apfel'baum, M.S. and Kozyrenko, V.E., Physical Modeling and Calculation of Electrohydrodynamic Flows, *Elektrokhimiya*, 1991, no. 7, pp . 855–863.
9. Apfel'baum, M. S., Ionization and Flow of Weakly Conductive Liquid in Non-Uniform Electric Field, *Elektron. Obrab. Mater.,* 1988, no. 1, pp. 60 – 65.
10. Ostroumov, G.A., *Vzaimodeistvie elektricheskikh i gidrodinamicheskikh polei* (Interaction of the Electric and Hydrodynamic Fields), Moscow: Nauka, 1979.
11. Apfel'baum, M.S. and Apfel'baum, E.M., On Electric Field Distribution in the Vicinity of Particles in a Weakly Ionized Disperse Medium, *Chem. Phys.*, Report, 2000, vol. 18, pp. 2313–2328.
12. Apfel'baum, M.S., One-Dimensional Stationary Problems of Calculation of Pre-Breakdown Volt Ampere Characteristics in Weakly Ionized Media, *Elektron. Obrab. Mater.*, 2005, no. 2, pp. 50–53.
13. Apfel'baum, M.S., One-Dimensional Non-Stationary Problems of Calculation of Pre-Breakdown Electrody-

namic Characteristics of Weakly Ionized Media, *Elektron. Obrab. Mater.*, 2008, no. 3, pp . 36–45.

14. Marchuk, G.I., *Metody vychislitel'noi matematiki* (Methods of Computational Mathematics), Moscow: Nauka, 1970.
15. Tonks, L. and Langmuir, I.A., A General Theory of the Plasma of an Arc, *Phys. Rev.*, 1929, vol. 14, pp. 876–992.
16. Apfel'baum, M.S., On One Model of Calculation of Ionization Release of Energy in a Weakly Conductive Liquid upon Its Interaction with a Pre-Breakdown Electric Field, *Elektron. Obrab. Mater.*,2009, no. 4, pp. 38–46.
17. Apfel'baum, M.S., The Pre-Breakdown Electrohydrodynamic Equations for Liquid Insulators *Proc. 7th Int. Conf. on Modern Problems of Electrophysics and Electrohydrodynamics of Liquids*, St. Petersburg, 2003, pp. 9–13.
18. Apfel'baum, M.S., On Theoretic Modeling of a Transformer Cooling, *Elektron. Obrab. Mater.*,2010, no. 4, pp. 56–59.
19. Zhakin, A.I., Ion Eletroconductivity and Comlex—Formation in Liquid Dielectrics, *Usp. Fiz. Nauk*, 2003, no. 5, pp. 51–68.

ISSN 1068-3755, Surface Engineering and Applied Electrochemistry, 2011, Vol. 47, No. 1, pp. 44–52. © Allerton Press, Inc., 2011.
Original Russian Text © D.A. Ignat'kov, 2011, published in Elektronnaya Obrabotka Materialov, 2011, No. 1, pp. 53–62.

ELECTRICAL PROCESSES IN ENGINEERING AND CHEMISTRY

Determination of the Characteristics of the Elasticity of Heterogeneous Materials Using the Dynamic Method

D. A. Ignat'kov
ul. Gagarina 4, kv. 14, 223037 a/g Petrishki, Minskii rn, Republic of Belarus
e-mail: dmig@rambler.ru; dm.ignatkov@gmail.com

Received June 8, 2010

Abstract—Settlement formulas and examples of the definition of the characteristics of the elasticity of heterogeneous multilayer materials are established using a dynamic resonant method.

DOI: 10.3103/S1068375511010054

INTRODUCTION

Modern methods of modification of surface layers and application of coatings lead, as a rule, to the production of heterogeneous materials with multilayer structures, the elasticity characteristics of which become functions of the position of the hardenable parts. As the elasticity moduli and the Poisson ratio are the main parameters at the calculations of the strength, rigidity, stability, resonance frequencies, and residual stresses [1, 2], the development of efficient methods in order to determine them for materials with multilayer heterogeneous structures is a topical problem.

The dynamic resonance method to determine the characteristics of isotropic materials' elasticity is regulated by some written standard [3]. The elasticity moduli are calculated by the relations considering the linear dimensions of the specimen; the resonance frequencies of the longitudinal, torsional, and bending vibrations; the geometric characteristics of the cross section; and the material's density. To excite the resonances and to record the resonance frequencies, there are used different circuits of the specimen's fixing (Fig. 1). The circuit in Fig. 1a is used to excite and record the natural longitudinal vibrations of prismatic and cylindrical rods. It provides the measurement of

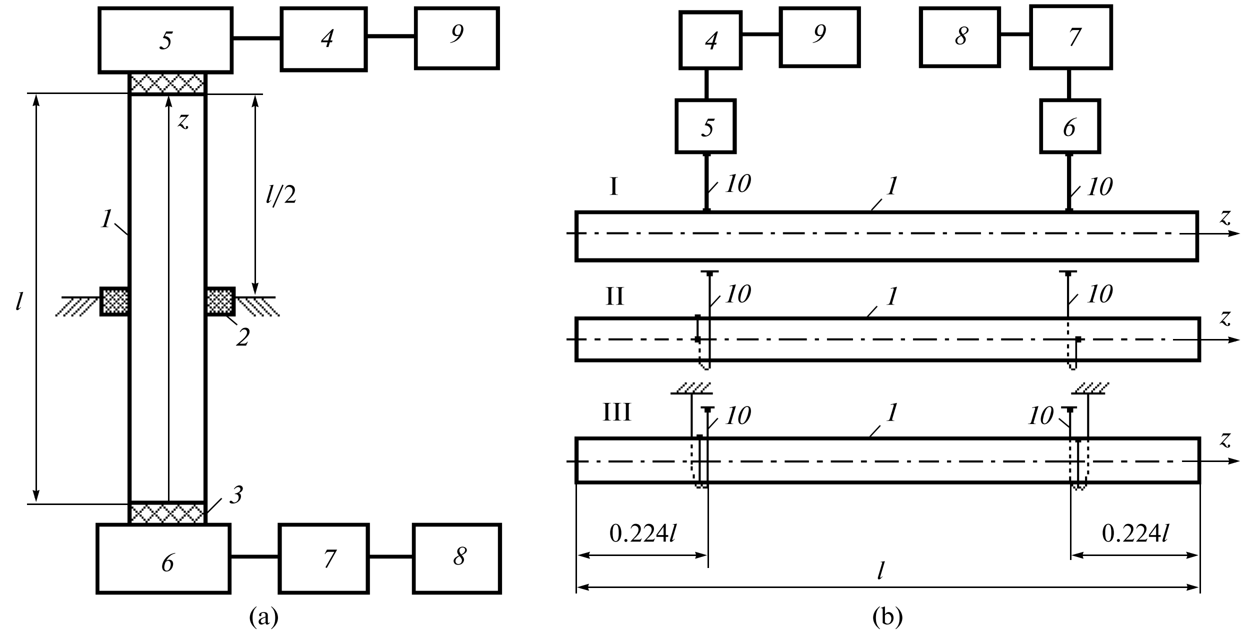

(a) (b)

Fig. 1. Circuits of fixing, agitating, and recording vibrations: (*1*) the specimen; (*2*) the diaphragm; (*3*) the viscous liquid; (*4*) the sinusoidal oscillator; (*5*) the vibration exciter; (*6*) the receiver; (*7*) the amplifier; (*8*) the vibration indicator; (*9*) the frequency meter; (*10*) the wires to suspend the specimen (with a diameter of up to 0.1 mm).

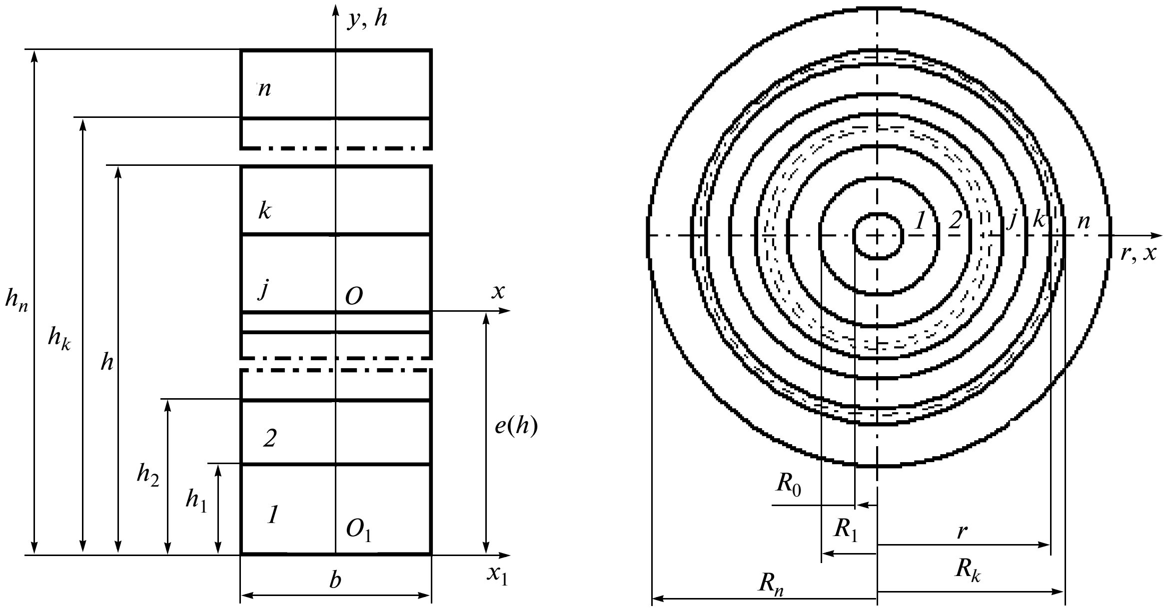

(a) (b)

Fig. 2. Cross sections of piecewise heterogeneous rods with their outer dimensions, the enumeration, and the conjugation coordinates of a packet of heterogeneous materials.

the Young's modulus E. Circuits I and II in Fig. 1b are used to excite and record the natural bending (I) and torsional (II) vibrations, and, by circuit III, there are excited simultaneously bending and torsional vibrations. Circuit I provides the measurement of the Young's modulus E; circuit II, the shear modulus G; and, according to circuit III, there is simultaneously found E and G followed by the calculation of the Poisson factor ν and the bulk modulus of the elasticity K.

This work is dedicated to the determination of the elasticity characteristics of heterogeneous materials with multilayer structures by the dynamic method.

FORMULATION OF THE PROBLEM

Let us obtain in the standard form the computation formulas to determine the elasticity characteristics of heterogeneous materials of a multilayer or, in other words, piecewise-heterogeneous rod consisting of a packet of firmly connected layers; in the limits of each, the elastic characteristics are some determinate functions of the position. Such a formulation allows one to derive subexpressions for rods with continuous elastic heterogeneity and piecewise-homogeneous ones with the elastic characteristics of the materials being within the limits of every layer (but different from each of them) as well as homogeneous ones.

For the materials of piecewise-heterogeneous prismatic (Fig. 2a) and cylindrical (Fig. 2b) rods as systems, the piecewise-continuous functions of Young's modulus $E(\xi)$, the shear modulus $G(\xi)$, the Poisson factor $\nu(\xi)$, and the material density $\rho(\xi)$ of the variables $\xi = y, h, r$ are presented in the following form [4]:

$$p(\xi) = p_1(\xi) + \sum_{k=1}^{n-1}[p_{k+1}(\xi) - p_k(\xi)]S_{-}(\xi - \xi_k), \quad (1)$$

where $p_k(\xi)$ denotes, respectively, the functions of Young's modulus $E_k(\xi)$, the shear modulus $G_k(\xi)$, the Poisson factor $\nu_k(\xi)(\nu_k \neq \nu_{k+1})$, and the density $\rho_k(\xi)$ of the material of the k-th layer, where $k = 1, 2 \ldots, n$ is the general number of layers; $S_{-}(\xi - \xi_k) = \begin{cases} 1, & \text{if } \xi \geq \xi_k \\ 0, & \text{if } \xi < \xi_k \end{cases}$ is the asymmetric unit function; and $\xi_k = y_k$, h_k, R_k are the coordinates of the conjugation planes of the k-th and $k+1$-th layers.

Let within the k-th layer of the rectangular and circular cross sections of the rod of length l the elasticity moduli with respect to the coordinates $\xi = y$, h, r be some unknown functions $E_k(\xi)$ and $G_k(\xi)$, the form of which is required to be established experimentally. For this purpose, the layers of the material are sequentially removed or built up; then, every time there are measured the linear dimensions; the resonance frequencies of the longitudinal $f_n(\xi)$, torsional $f_\kappa(\xi)$, and bending $f_u(\xi)$ vibrations; and the weight $Q(\xi)$ of the remaining part or the rod being built up. Next, the experimental data are approximated by the analytic relationships, the values of the elasticity characteristics are calculated by the corresponding formulas, and the functions of their change with respect to the section coordinates are established as well. In the context of a technical theory of the longitudinal, torsional, and bending vibrations of piecewise-heterogeneous rods, we obtain the required calculation formulas and illustrate the application of them by numerical examples.

DETERMINATION OF THE YOUNG'S MODULUS AT EXCITING THE LONGITUDINAL VIBRATIONS

The equation for steady natural longitudinal vibrations with angular frequency $\omega(\xi)$ of a piecewise-heterogeneous rod is written in the following form [5]:

$$u''(z) + \frac{\omega^2(\xi)m(\xi)}{A(\xi)}u(z) = 0, \tag{2}$$

where $a(z)$ is the amplitude of the longitudinal displacement of the cross section in the line of the longitudinal axis z; $\xi = h, r$; $m(\xi) = Q(\xi)/gl$ is the bulk weight; g is the body's gravitational acceleration; $A(\xi)$ is the rigidity of the cross section at extension–compression; and $u''(z) = d^2u(z)/dz^2$.

The general integral of equation (2) we express in the form

$$u(z) = B\cos\alpha z + D\sin\alpha z, \tag{3}$$

where B and D are the constants of the integration, where $\alpha = \sqrt{\dfrac{\omega^2(\xi)m(\xi)}{A(\xi)}}$.

The boundary conditions of the rod fixing with the free ends (Fig. 1a) at $z = 0$ $A(\xi)u'(0) = 0$ and $z = lA(\xi)u'(l) = 0$ mean that $D = 0$; $B\sin l = 0$. As the const $B \neq 0$, from the solution of the frequency equation $\sin\alpha l = 0$, there follow the values of the free angular frequencies:

$$\omega_{ni}(\xi) = \frac{\pi i}{l}\sqrt{\frac{A(\xi)}{m(\xi)}} \quad (i = 1, 2, \ldots). \tag{4}$$

Introducing $\omega_{ni}(\xi)$ into relation (3) and considering that $D = 0$, we obtain a formula to calculate the forms of the main longitudinal vibrations:

$$u_i(z) = B_i\cos\frac{\pi i z}{l}. \tag{5}$$

From equality (4), there follows the relationship expressing the cross section rigidity through the measured free frequencies $f_{ni}(\xi) = \omega_{ni}(\xi)/2\pi$,

$$A(\xi) = \frac{4l^2m(\xi)}{i^2}f_{ni}^2(\xi) = \frac{4l^2F(\xi)}{i^2}\rho(\xi)f_{ni}^2(\xi), \tag{6}$$

where $F(\xi)$ is the cross section area; $F(h) = bh$; $F(r) = \pi(r^2 - R_0^2)$; $\rho(\xi)$ is the heterogeneous material's density; $\rho(\xi) = \dfrac{Q(\xi)}{gV(\xi)} = \dfrac{Q(\xi)}{gF(\xi)l} = \dfrac{m(\xi)}{F(\xi)}$; $V(h) = bhl$ and $V(r) = \pi(r^2 - R_0^2)l$ are the volumes of the prismatic and cylindrical rods, respectively.

Considering the presentation of the piecewise-continuous functions $E(h)$ and $E(r)$ by expressions (1), the formulas to calculate the rigidities of the cross sections at the extension–compression in the case of the removal or building up of the material up to the height of $\xi = h$ (Fig. 2a) or radius $\xi = r$ (Fig. 2b) are written as

$$\begin{aligned} A(h) &= \int_0^h Ebdy \\ &= b\left[\int_{h_{k-1}}^{h} E_k(y)dy + \sum_{j=1}^{k-1}\int_{h_{j-1}}^{h_j} E_j(y)dy\right] \quad (h_0 = 0), \end{aligned} \tag{7}$$

$$\begin{aligned} A(r) &= 2\pi\int_{R_0}^{r} E\xi d\xi \\ &= 2\pi\left[\int_{R_{k-1}}^{r} E_k(\xi)\xi d\xi + \sum_{j=1}^{k-1}\int_{R_{j-1}}^{R_j} E_j(\xi)\xi d\xi\right]. \end{aligned} \tag{8}$$

Now the equations of relationships (6) and (7), and (6) and (8) are written in the form of the Volterra equations of the first kind:

$$\int_{h_{k-1}}^{h} E_k(y)dy + \sum_{j=1}^{k-1}\int_{h_{j-1}}^{h_j} E_j(y)dy - \frac{4l^2h}{i^2}\rho(h)f_{ni}^2(h) = 0; \tag{9}$$

$$\begin{aligned} &\int_{R_{k-1}}^{r} E_k(\xi)\xi d\xi + \sum_{j=1}^{k-1}\int_{R_{j-1}}^{R_j} E_j(\xi)\xi d\xi \\ &- \frac{2l^2(r^2 - R_0^2)}{i^2}\rho(r)f_{ni}^2(r) = 0. \end{aligned} \tag{10}$$

On differentiation with respect to the variables h and r and rearrangements, we obtain the desired formulas to calculate the Young's modulus of the materials of prismatic or cylindrical piecewise-heterogeneous or piecewise-homogeneous rods:

$$\begin{aligned} E_k(h) &= \frac{4l^2}{i^2}f_{ni}(h) \\ &\times \{[h\rho_k'(h) + \rho_k(h)]f_{ni}(h) + 2\rho_k(h)f_{ni}'(h)\}: \end{aligned} \tag{11}$$

$$\begin{aligned} E_k(r) &= \frac{2l^2}{i^2 r}f_{ni}(r) \\ &\times \{[(r^2 - R_0^2)\rho_k'(r) + 2r\rho_k(r)] \\ &\times f_{ni}(r) + 2\rho_k(r)(r^2 - R_0^2)f_{ni}'(r)\}. \end{aligned} \tag{12}$$

As for the rod of a heterogeneous material $\rho'_1(\xi) = 0$ and $f'_{ni}(\xi) = 0$, from general expressions (11) and (12), there follows the formula ($r = r_1$; $E = E_1$):

$$E = \frac{4l^2}{i^2}\rho f_{ni}^2. \tag{13}$$

From expression (5), it follows that, at natural longitudinal vibrations of the rod with the main form ($i = 1$), the cross section displacement at $z = l/2$ is zero. Thus, the rod with free ends is fixed half-length (Fig. 1a). As the resonance frequencies for the highest forms of the vibrations differ by 2, 3, and more times, they are recognized according to these relations over the whole frequency spectrum.

DETERMINATION OF THE SHEAR MODULUS AT EXCITING THE TORSIONAL VIBRATIONS

We consider the equation for steady natural torsional vibrations with the angular frequency $\omega(r)$ of a piecewise-heterogeneous cylindrical rod (Fig. 1b, circuits II, III) in the following form [5]:

$$\theta''(z) + \frac{\omega^2(r)J_m(r)}{C(r)}\theta(z) = 0, \tag{14}$$

where $\theta(z)$ is the amplitude of the cross section torsion angle, $J_m(r)$ is the length moment of the body inertia, and $C(r)$ is the torsion rigidity of the cross section.

With the piecewise-continuous function of the density $\rho(r)$ in form (1), we present the function of the length moment of the body's inertia in the following way:

$$J_m(r) = 2\pi\left[\int\limits_{R_{k-1}}^{r}\rho_k(\xi)\xi^3 d\xi + \sum_{j=1}^{k-1}\int\limits_{R_{j-1}}^{R_j}\rho_j(\xi)\xi^3 d\xi\right]. \tag{15}$$

It is not difficult to notice that equation (14) is identical to expression (2) upon the condition of the substitution of $\theta(z)$ for $u(z)$, of $J_m(r)$ for $m(\xi)$, and $C(r)$ for $A(\xi)$. Taking into account that, in the case of the free fixing of a twisted rod, the torsional moments at $z = 0$ $C(r)\theta'(0) = 0$ and $z = l$ $C(r)\theta'(l) = 0$, dropping out the computation similar to above mentioned one, we immediately write down the formulas to find the natural frequencies:

$$\omega_{\kappa i}(r) = \frac{\pi i}{l}\sqrt{\frac{C(r)}{J_m(r)}} \quad (i = 1, 2, 3\ldots) \tag{16}$$

and the forms of the main torsional vibrations

$$\theta_i(z) = B_i\cos\frac{\pi i z}{l}. \tag{17}$$

From relation (16) we get the formula to calculate the cross section's rigidity at the torsion through the measured resonance frequencies $f_{\kappa i}(r) = \omega_{\kappa i}(r)/2\pi$:

$$C(r) = \frac{4l^2}{i^2}J_m(r)f_{\kappa i}^2(r). \tag{18}$$

On the other hand, the rigidity of the composite circular section (Fig. 2b) under torsion in the case of the removal or build up of the material layers up to the radius r is

$$\begin{aligned} C(r) &= 2\pi\int\limits_{R_0}^{r}G\xi^3 d\xi \\ &= 2\pi\left[\int\limits_{R_{k-1}}^{r}G_k(\xi)\xi^3 d\xi + \sum_{j=1}^{k-1}\int\limits_{R_{j-1}}^{R_j}G_j(\xi)\xi^3 d\xi\right]. \end{aligned} \tag{19}$$

The equality of relations (18) and (19) is written down in the form of a Volterra integral equation of the first kind:

$$\begin{aligned} &\int\limits_{R_{k-1}}^{r}G_k(\xi)\xi^3 d\xi + \sum_{j=1}^{k-1}\int\limits_{R_{j-1}}^{R_j}G_j(\xi)\xi^3 d\xi \\ &- \frac{2l^2}{\pi i^2}J_m(r)f_{\kappa i}^2(r) = 0. \end{aligned} \tag{20}$$

On differentiation and rearrangement, we obtain the desired formula to calculate the shear modulus:

$$G_k(r) = \frac{4l^2}{i^2}f_{\kappa i}(r)\left[\rho_k(r)f_{\kappa i}(r) + \frac{2}{r^3}I(r)f'_{\kappa i}(r)\right]. \tag{21}$$

Here, in the integral

$$I(r) = \int\limits_{R_{k-1}}^{r}\rho_k(\xi)\xi^3 d\xi + \sum_{j=1}^{k-1}\int\limits_{R_{j-1}}^{R_j}\rho_j(\xi)\xi^3 d\xi \tag{22}$$

the density variation functions $\rho_j(\xi)$ for the materials of the piecewise-heterogeneous or piecewise-homogeneous rods are established experimentally if they are unknown in advance.

Obviously, for the rod of a homogeneous material, $f'_{\kappa i}(r) = 0$. For this particular case, from expression (21), we have the known formula ($\rho = \rho_1$; $G = G_1$)

$$G = \frac{4l^2}{i^2}\rho f_{\kappa i}^2. \tag{23}$$

As the frequencies of the resonance vibrations for the highest forms of the natural torsional vibrations differ by 2, 3, and more times, they are recognized according to these relations over the whole frequency spectrum.

DETERMINATION OF THE YOUNG'S MODULUS AT EXCITING THE BENDING VIBRATIONS

We consider the equation for the steady natural bending vibrations according to circuits I, III in Fig. 1 of the piecewise-heterogeneous rods with rectangular (Fig. 2a) and circular sections (Fig. 2b) in the following form [5]:

$$y''''(z) - \frac{\omega^2(\xi)m(\xi)}{B_x(\xi)}y(z) = 0, \qquad (24)$$

where $y(z)$ is the amplitude of the cross section movement; $\omega(\xi)$ is the angular frequency; $m(\xi)$ is the bulk weight; and $Bx(\xi)$ is the cross section bending rigidity with respect to the axis of the abscissas.

We write down the general integral of equation (24) as follows:

$$y(z) = AS(kz) + BT(kz) + CU(kz) + DV(kz), \qquad (25)$$

where $S(kz)$, $T(kz)$, $U(kz)$, $\mathrm{V}(kz)$ are the Krylov's functions; and $k = \sqrt[4]{\frac{\omega^2(\xi)m(\xi)}{B_x(\xi)}}$; A, B, C, D are the constants of integration.

We find the spectrum of the natural angular frequencies and the relevant forms of the bending vibrations of the piecewise-heterogeneous rod with free ends: with $z = 0$ $B_x(\xi)y''(0) = 0$, $B_x(\xi)y'''(0) = 0$; with $z = l$ $B_x(\xi)y''(l) = 0$, $B_x(\xi)y'''(l) = 0$. These boundary conditions lead expression (25) to the frequency equation

$$\cos k_i l \cosh k_i l = 1, \qquad (26)$$

the roots of which are at $i = 2$ $\alpha_2 = 4.730$; at $i = 3$ $\alpha_3 = 7.853$; at $i = 4$ $\alpha_4 = 10.996$; at $i = p$ $\alpha_p = 0.5\pi(2p - 1)$, as well as to the equations for the relevant forms of the vibrations

$$\begin{aligned} y_i(z) = A_i[&(\cosh k_i l - \cos k_i l)(\sinh k_i z + \sin k_i z) \\ &- (\sinh k_i l - \sin k_i l)(\cosh k_i z + \cos k_i z)]. \end{aligned} \qquad (27)$$

The solution of frequency equation (26) with respect to the natural angular frequencies ω_{ui} gives the following relationship,

$$\omega_{ui}(\xi) = \frac{\alpha_i^2}{l^2}\sqrt{\frac{B_x(\xi)}{m(\xi)}} \quad (i = 1, 2, 3, \dots), \qquad (28)$$

from which there follows the formula to determine the section's bending rigidity:

$$B_x(\xi) = \frac{4\pi^2 l^4}{\alpha_i^4}F(\xi)\rho(\xi)f_{ui}^2(\xi), \qquad (29)$$

where $f_{ui}(\xi) = \omega_{ui}(\xi)/2\pi$ are the frequencies of the vibrations per time unit.

First we determine the Young's moduli of the materials of the piecewise-heterogeneous rod with the cross section area $F(h) = bh$ (Fig. 2b). The cross section's rigidity to bending with respect to the axis of the abscissas is expressed by the following relation:

$$B_x(h) = B_{x_1}(h) - e^2(h)A(h). \qquad (30)$$

Considering the presentation of the piecewise-variable function $E(h)$ in form (1), we write down the formulas to calculate the elastically geometric characteristics:

—the cross section's rigidity to bending with respect to the axis x_1

$$B_{x_1}(h) = b\left[\int_{h_{k-1}}^{h} E_k(y)y^2dy + \sum_{j=1}^{k-1}\int_{h_{j-1}}^{h_j} E_j(y)y^2dy\right] \times (h_0 = 0); \qquad (31)$$

—the ordinate of the cross section's center

$$e(h) = \frac{S_{x_1}(h)}{A(h)}; \qquad (32)$$

—the first moment of the cross section's inertia with respect to the axis x_1

$$S_{x_1}(h) = b\left[\int_{h_{k-1}}^{h} E_k(y)ydy + \sum_{j=1}^{k-1}\int_{h_{j-1}}^{h_j} E_j(y)ydy\right] \times (h_0 = 0); \qquad (33)$$

—the cross section's rigidity to extension

$$A(h) = b\left[\int_{h_{k-1}}^{h} E_k(y)dy + \sum_{j=1}^{k-1}\int_{h_{j-1}}^{h_j} E_j(y)dy\right](h_0 = 0). \qquad (34)$$

Now the equality of relations (29) and (30) is written in the form of an integral equation:

$$B_{x_1}(h) - \frac{S_{x_1}^2(h)}{A(h)} - \frac{4\pi^2 l^4}{\alpha_i^4}bh\rho(h)f_{ui}^2(h) = 0. \qquad (35)$$

On differentiation with respect to the variable h and rearrangement, we obtain the desired formula to calculate the Young's modulus of the materials of the piecewise-heterogeneous or piecewise-homogeneous prismatic rods:

$$\begin{aligned} E_k(h) = &\frac{4\pi^2 l^4}{\alpha_i^4[h - e_k(h)]^2}f_{ui}(h) \\ &\times \{[h\rho_k'(h) + \rho_k(h)]f_{ui}(h) + 2h\rho_k(h)f_{ui}'(h)\}. \end{aligned} \qquad (36)$$

The usage of formula (36) is complicated as it is impossible to find the elastically geometric characteristics of the cross section because the values of the elasticity modulus are unknown. This problem is overcome by employing the numerical method of successive approximations. The essence of it is in the following: according to the given sequence of inferred values of $E_m(h)$, there are computed the quantities $A_m(h)$, $e_m(h)$, and $B_{x_1m}(h)$ ($m = 1, 2, ..., \nu$), which are substituted into expression (35). The convergence criterion is in the satisfaction of equation (35). We illustrate this method by an example.

Let a single-element coating $t = h_2 - h_1$ thick be applied to a rod of width b and height h_1 of a homogeneous material with known values of E_1 and ρ_1. Determine the unknown value of the coating material's Young's modulus E_2 according to the measured resonance frequencies $f_{u2}(h)$ of the main form ($i = 2$) of the bending vibrations and the calculated density ρ_2 of the coating material after each successive removal of the layers within the thickness t and weighing the remaining part of the two-layer rod ($n = 2$).

By formulas (30)–(34), the elastically geometric characteristics are precisely the cross section's rigidity to extension–compression,

$$A(h) = b\left[\int_0^{h_1} E_1 dy + \int_{h_1}^{h} E_2 dy\right] = b[E_1h_1 + E_2(h - h_1)], \tag{37}$$

the first moment of the cross sections inertia with respect to the axis x_1,

$$S_{x_1}(h) = b\left[\int_0^{h_1} E_1 y dy + \int_{h_1}^{h} E_2 y dy\right] = \frac{b}{2}[E_1h_1^2 + E_2(h^2 - h_1^2)], \tag{38}$$

the ordinate of the cross section's center

$$e(h) = \frac{S_{x_1}^2(h)}{A(h)} = \frac{E_1h_1^2 + E_2(h^2 - h_1^2)}{2[E_1h_1 + E_2(h - h_1)]}, \tag{39}$$

the cross section's rigidity to bending with respect to the axis x_1,

$$B_{x_1}(h) = b\left[\int_0^{h_1} E_1 y^2 dy + \int_{h_1}^{h} E_2 y^2 dy\right] = \frac{b}{3}[E_1h_1^3 + E_2(h^3 - h_1^3)], \tag{40}$$

the cross section's rigidity to bending with respect to the axis of the abscissas,

$$B_x(h) = B_{x_1}(h) - e^2(h)A(h) = \frac{b}{3}\left\{E_1h_1^3 + E_2(h^3 - h_1^3) - \frac{3}{4}\frac{[E_1h_1^2 + E_2(h^2 - h_1^2)]}{E_1h_1 + E_2(h - h_1)}\right\}. \tag{41}$$

Thus, the equality of expressions (29) and (41) gives the resulting equation

$$E_1\frac{h_1^3}{3}\left\{1 + \beta(\gamma^3 - 1) - \frac{3}{4}\frac{[1 + \beta(\gamma^2 - 1)]^2}{1 + \beta(\gamma - 1)}\right\} - \frac{4\pi^2 l^4}{\alpha_2^4}h\rho_2 f_{u2}^2(h) = 0, \tag{42}$$

where $\beta = E_2/E_1$ and $\gamma = h/h_1$ are dimensionless factors.

Let now, at the s-th stage of the removal of the coating material layers, the linear dimensions, the resonance frequency $f_{u2s}(h)$, and the weight $Q_s(h)$ of the remaining part of the rod be measured. So, the current density of the coating material is

$$\rho_{2s} = \frac{1}{\gamma_s - 1}\left[\frac{1}{bh_1 l}\frac{Q_s(h)}{g} - \rho_1\right]. \tag{43}$$

Solving equation (42) with respect to the coefficient β_s, we obtain $E_{2s} = E_1\beta_s$. The averaging of the values of E_{2m} ($m = 1, 2, ..., s, ..., \nu$) gives the desired value of the Young's modulus E_2.

If in a particular case the coefficients $\gamma = 1$ and $\beta = 1$, then, from equation (42), there follows the known formula to calculate the elasticity modulus of the homogeneous material of prismatic or cylindrical rods ($\rho = \rho_1$; $E = E_1$):

$$E = \frac{48\pi^2 l^4}{\alpha_i^4 h_1^2}\rho f_{ui}^2 \quad (i = 2, 3, \dots). \tag{44}$$

Let us consider now the determination of the Young's modulus E_k of the materials of a piecewise-heterogeneous cylindrical rod. Presenting the piecewise-variable function $E(r)$ in form (1), we write down the formula to calculate the cross section's rigidity to bending with respect to the axis of the abscissas (Fig. 2b):

$$B_x(r) = \pi\int_{R_0}^{r} E(\xi)\xi^3 d\xi = \pi\left[\int_{R_{k-1}}^{r} E_k(\xi)\xi^3 d\xi + \sum_{j=1}^{k-1}\int_{R_{j-1}}^{R_j} E_j(\xi)\xi^3 d\xi\right]. \tag{45}$$

Table 1. Experimental data

i	r, m	$Q(r)$, N	$f_{n1}(r)$, Hz	$f_{\kappa1}(r)$, Hz	$f_{u1}(r)$, Hz
0	0.01000	1.736	13119	8145	2990
1	0.01050	1.998	12636	7282	2872
2	0.01089	2.210	12417	6897	2799
3	0.01105	2.304	12276	6897	2799
4	0.01130	2.443	12099	6663	2790
5	0.01165	2.653	11916	6459	2785
6	0.01215	2.954	11701	5459	2785
7	0.01240	3.117	11556	6241	2795
8	0.01270	3.309	11455	6170	2807
9	0.01300	3.505	11326	6059	2823

We express the equality of formulas (29) and (45) in the form of the Volterra integral equation of the first kind:

$$\int_{R_{k-1}}^{r} E_k(\xi)\xi^3 d\xi + \sum_{j=1}^{k-1} \int_{R_{j-1}}^{R_j} E_j(\xi)\xi^3 d\xi - \frac{4\pi^2 l^4}{\alpha_i^4}(r^2 - R_0^2)\rho(r) f_{ui}^2(r) = 0. \tag{46}$$

On differentiation with respect to the variable r and rearrangement, we obtain the formula to determine the Young's modulus of the materials of the piecewise-heterogeneous or piecewise-homogeneous cylindrical rods:

$$E_k(r) = \frac{4\pi^2 l^4}{\alpha_i^4 r^3} f_{ui}(r) \times \{[(r^2 - R_0^2)\rho'_k(r) + 2r\rho_k(r)] f_{ui}(r) + 2(r^2 - R_0^2)\rho_k(r) f'_{ui}(r)\}. \tag{47}$$

As for the homogeneous cylindrical rod, the cross section's rigidity to bending is

$$B_x(r) = \pi \int_{R_0}^{R_1} E_1 \xi^3 d\xi = E_1 \pi \frac{R_1^4 - R_0^4}{4}, \tag{48}$$

so, from the equality of expressions (29) and (48), we get the known formula to calculate the Young's modulus of a homogeneous material ($\rho = \rho_1$; $E = E_1$):

$$E = \frac{16\pi^2 l^4}{\alpha_i^4 (R_1^2 + R_0^2)} \rho f_{ui}^2. \tag{49}$$

It follows from equation (27) for the forms of the natural bending vibrations that, at the main form ($i = 2$) of the vibrations, the node points are at a distance of $0.224l$ and $0.776l$ from the left end, which are shown in Fig. 1b. Therefore, the specimens are fixed with the help of thin wires at these points. The frequencies of the highest forms of the natural bending vibrations differ from the main form ($i = 2$) by 2, 76, 5, 41, 8, 94, ... times. These relations serve to recognize the resonance frequencies over the whole resonance spectrum, as well as to separate the resonance frequencies of the bending and torsional vibrations in the case of the simultaneous determination of the elasticity moduli E and G according to circuit III in Fig. 1b.

The Poisson ratio ν and the bulk modulus of the elasticity K are computed by the formulas

$$\nu = \frac{E}{2G} - 1; \tag{50}$$

$$K = \frac{EG}{3(3G - E)} = \frac{E}{3(1 - 2\nu)}. \tag{51}$$

CALCULATION OF THE ELASTICITY CHARACTERISTICS AND THE ANALYSIS OF THE RESULTS

Let us compute the elasticity characteristics of the material of a yttrium plasma coating $t = 3$ mm thick sprayed on a hollow cylindrical rod of alloyed steel with the following composition (%): C—0.14; Si—0.12; Mn—0.52; Cr—13,6; Ni—0.48. The dimensions of the rod are as follows: the length $l = 200$ mm; the radii $R_0 = 8$ mm; $R_1 = 10$ mm; $R_2 = 13$ mm. The linear dimensions and the weight of the rod and the resonance frequencies of the main forms of the natural longitudinal ($i = 1$), torsional ($i = 1$), and bending ($i = 2$) vibrations are measured upon each removal of a layer. The test results are presented in Table 1; they are approximated by the analytical relationships in the mathematical system Mathcad 14 by the least squares method employing the linear and polynomial regressions by linear and quintic polynoms.

The calculation results of the elasticity characteristics by formulas (12), (21), (47), (50), and (51) are tabulated in Table 2, where the variable thickness is $a = r - R_1$.

Table 2. Calculated values of the elasticity characteristics of sprayed yttrium

m	1	2	3	4	5	6	7
$r \times 10^3$, m	10.0	10.5	11.0	11.5	12.0	12.5	13.0
$a \times 10^3$, m	0	0.5	1.0	1.5	2.0	2.5	3.0
with exciting the natural longitudinal vibrations							
Q, N	1.696	1.992	2.289	2.585	2.881	3.178	3.474
Q', N/m	592.737	592.737	592.737	592.737	592.737	592.737	592.737
$\rho \times 10^{-3}$ kg/m^3	7.821	7.015	6.472	6.093	5.811	5.589	5.418
$\rho' \times 10^{-6}$ kg/m^4	–1.955	–1.312	–0.895	–0.643	–0.497	–0.395	–0.279
$f_{n1} \times 10^{-4}$, Hz	1.311	1.266	1.230	1.201	1.175	1.153	1.133
$f'_{n1} \times 10^{-6}$, Hz/m	–1.013	–0.799	–0.649	–0.546	–0.475	–0.423	–0.375
E_2, HPa	58.5	55.8	57.8	58.6	57.2	55.7	58.4
$\rho_1 = 7.82 \times 10^3$ kg/m^3; $\rho_2 = 4.1 \times 103$ kg/m^3; $E_1 = 215.2$ HPa; $E_2 = 57.4 \pm 1.2$ HPa; $\Delta_E = 2.1\%$							
with exciting the natural torsional vibrations							
$I \times 10^5$, kg/m^2	1.154	1.576	2.062	2.619	3.254	3.973	4.784
$f_{\kappa 1} \times 10^{-3}$, Hz	8.130	7.350	6.873	6.573	6.363	6.199	6.075
$f'_{\kappa 1} \times 10^{-6}$, Hz/m	–1.964	–1.208	–0.743	–0.488	–0.365	–0.293	–0.193
G_2, HPa	23.8	22.7	23.6	24.4	23.7	22.5	23.8
$G_1 = 82.7$ HPa; $\nu_1 = 0.3$; $K_1 = 180.9$ HPa; $G_2 = 23.5 \pm 0.6$ HPa; $\nu_2 = 0.22$; $\Delta_G = 2.6\%$							
with exciting the natural bending vibrations							
$f_{u2} \times 10^{-4}$, Hz	2.990	2.870	2.807	2.783	2.784	2.798	2.823
$f'_{u2} \times 10^{-6}$, Hz/m	–3.130	–1.760	–0.813	–0.198	0.176	0.402	0.571
E_2, HPa	57.7	56.4	57.3	58.1	58.0	57.4	56.8
$E_1 = 215.3$ HPa; $\nu_1 = 0.3$; $E_2 = 57.4 \pm 0.6$ HPa; $\nu_2 = 0.22$; $K_2 = 34.3$ HPa; $\Delta_E = 1.1\%$							

The variation of the weight on the radius r ($R_1 \le r \le R_2$) or through the thickness a of the coating is described by the linear regressive relationship

$$Q(r) = 1.696 + 592.737(r - R_1), \text{ N};$$

$$Q'(r) = 592.737 \text{ N/m}.$$

It follows from it that the alloyed steel density $\rho_1 = 7.82 \times 10^3$ kg/m^3, and the sprayed yttrium density does not change on the rod's radius and is

$$\rho_2 = \frac{Q_\Sigma}{\pi(R_2^2 - R_1^2)lg} - \frac{R_2^2 - R_0^2}{R_2^2 - R_1^2}\rho_1 = 4.1 \times 10^3 \text{ kg/m}^3,$$

where $Q_\Sigma = 3.505$ N is the total weight of the rod before the test. This fact indicates the sprayed yttrium elasticity moduli are constant. The alloyed steel elasticity characteristics $E_1 = 215.3$ GPa, $G_1 = 82.7$ GPa; $\nu_1 = 0.3$; $K_1 = 180.9$ GPa are in agreement with the reference data.

The calculated values of the elasticity moduli of the yttrium plasma coating material are distributed through the thickness with small deviations Δ_E and Δ_G about 1.1–2.6% from the average values $\bar{E}_2 = 57.4$ GPa and $\bar{G}_2 = 23.5$ GPa (Table 2) computed by the following formulas:

$$\bar{E}_2 = \frac{1}{\nu}\sum_{m=1}^{\nu} E_{2m}; \quad s_E^2 = \frac{1}{\nu - 1}\sum_{m=1}^{\nu}(E_{2m} - \bar{E}_2)^2;$$

$$\Delta_E = \frac{s_E}{\bar{E}_2}100;$$

$$\bar{G}_2 = \frac{1}{\nu}\sum_{m=1}^{\nu} G_{2m}; \quad s_G^2 = \frac{1}{\nu - 1}\sum_{m=1}^{\nu}(G_{2m} - \bar{G}_2)^2;$$

$$\Delta_G = \frac{s_G}{\bar{G}_2}100,$$

where $\nu = 7$, and S_E and S_G are the root-mean-square deviations.

The presence of the mentioned deviations is caused by the following fact. Properly, nonlinear formulas (11), (12), (21), (36), and (47) contain two main summands, one of which has the squared approximated functions of the frequencies, and the other is a product of these functions of their negative derivatives. Thus, due to the inaccuracy of the measurement and approximation of the experimental data, there arises some error in the calculation of the true difference of the summands, which causes the inevitable appearance of the indicated deviations. Therefore, there should be ensured the accuracy of the measurement of the weight to about 0.1 % and of the resonance frequencies to not more than 0.05 %. The calculations should be performed with accuracy to four digits, thus imposing heavy demands to the selection of the approximating relationships, employing, for example, the generalized regression. For the sprayed yttrium, we assume the value of the Young's modulus $E_2 = 57.4$ GPa, and that of the shear modulus $G_2 = 23.5$ GPa. Then, by formulas (50) and (51), we obtain the value of the Poisson factor $\nu_2 = 0.22$, and of the bulk elasticity modulus $K_2 = 34.3$ GPa.

The values of the sprayed yttrium's elasticity characteristics are smaller than those of the metal yttrium produced through the metallurgical method. According to the data from reference book [6], for metal yttrium, $\rho = 4.55 \times 10^3$ kg/m^3 and $E = 63.3$ GPa, as for the information from source [7] with regard for correcting the errors, $\rho = 4.45 \times 10^3$ kg/m^3, $E = 66$ GPa, $G = 26.4$ GPa, and $\nu = 0.25$. The difference of the values of the elasticity characteristics of the sprayed and metal yttrium is apparently caused by the presence of porosity in the coating. Taking into account the connection of the Young's modulus with porosity [8], we find its value by the formula

$$\Pi_E = \frac{(1-\lambda)(7-5\nu_2)}{15(1-\nu_2)-2(1-\lambda)(4-5\nu_2)}, \tag{52}$$

where $\lambda = E_2/E$. Introducing the averaged reference data and the obtained value $\lambda = E_2/\bar{E} = 0.866$, where $\nu_2 = 0.22$, we get the value of the sprayed yttrium porosity $\Pi_E = 7.2\%$, which is somewhat smaller than the usual estimation considering only the density of the compared materials:

$$\Pi_\rho = \left(1 - \frac{\rho_2}{\bar{\rho}}\right) \cdot 100 = 8.9\%.$$

Thus, the porosity of the plasma yttrium coating is the main reason causing the diminution of the characteristics of the sprayed yttrium's elasticity.

REFERENCES

1. Ignat'kov, D.A., *Ostatochnye napryazheniya v neodnorodnykh detalyakh*, (Residual Stresses in Heterogeneous Parts), Kishinev: Shtiintsa, 1992.
2. Ignat'kov, D.A., Determining Methods and Control of Residual Stresses in Bodies with Heterogeneous Structure, *Dr. Sci. (Eng.) Dissertation*, Yekaterinburg, 2005, p. 23.
3. *GOST* (State Standard) 25156-82: *Metals. Dynamic Method of Determination of Elasticity Characteristics*, 1982.
4. Podstrigach, Ya.S., Lomakin, V.A., and Kolyano, Yu.M., *Termouprugost' tel neodnorodnoi struktury*, (Thermoelasticity of Bodies with Heterogeneous Structure), Moscow: Nauka, 1984.
5. *Stroitel'naya mekhanika korablya*, (Theory of Ship Structures), Reference Book, Palii, O., Ed., Leningrad: Sudostroenie, 1982.
6. *Svoistva elementov* (Properties of Elements), Reference Book, Samsonov, G.V., Ed., Moscow: Metallurgiya, 1976.
7. *Khimicheskaya entsiklopedia* (Encyclopedia of Chemistry), http://www.xumuk.ru/tncyklopedia/1767.
8. Hashin, Z., Relations between Young's Modulus and Temperature, *J. Appl. Mech.*, 1962, vol. 29, no. 1, pp. 143–147.

ISSN 1068-3755, Surface Engineering and Applied Electrochemistry, 2011, Vol. 47, No. 1, pp. 53–55. © Allerton Press, Inc., 2011.

ELECTRICAL PROCESSES IN ENGINEERING AND CHEMISTRY

Novel Platform for Direct Electron Transfer to/from Hemoproteins Based on a Single Layer Graphite Electrode[1]

E. V. Ivanova

Materials and Surface Science Institute, Department of Chemical and Environmental Sciences, University of Limerick, Plassey, Co. Limerick, Ireland Astbury Centre for Structural Molecular Biology, University of Leeds, Leeds, LS2 9JT

e-mail: e.ivanova@leeds.ac.uk

Received July 21, 2010

Abstract—A novel cheap and easy way of producing carbon electrodes from single layer graphite is proposed. Low production cost allows to generate multiple disposable carbon layer electrodes. The electrodes were tested in a model bioelectrocatalytic process, such as electrochemical regeneration of hemoproteins, and positive results were obtained.

DOI: 10.3103/S106837551101008X

Importance of electrode material choice could be compared to that of solvent in chemical reaction. Since electron transfer rate and effectiveness of electrochemical conversion depends on electrode substrate material [1–3].

There is a scope for development of electrochemical device, with an improved sensitivity to biological samples. Direct electron transfer to/from redox proteins was observed on highly ordered pyrolitic graphite electrodes, [4–6; 7–9]. Pyrolitic graphite is a material with a highly ordered crystal structure and anisotropic properties, which electrochemical properties depend on it orientation. However, highly ordered carbon materials are expensive, which limits its area of its application in bioelectrocatalysis, where most of the samples are short living and therefore demands frequent surface regeneration.

Current study suggests design of multiple carbon layer electrodes with similar surface properties from a single piece of highly order pyrolitic graphite (HOPG).

Surface layer of the (HOPG) was stripped off by a carbon conductive selotape [10], which was connected via the silver nanowire into the standart three electrode cell as a working electrode. Resulting carbon layer electrodes (CLEs) were evaluated by cyclic voltammetry so that to evaluate its electrochemical intertness. The obtained CVs of CLEs in buffered solution showed no peaks, which indicates that there was no internal electrochemical reaction occurring within the structure of CLEs (data not shown). The next step we tested the area electro active surface of CLEs, which we compared with total surface area of CLE, obtained by another method.

There were two peaks observed on CV of 0.01 M $K_3[Fe(CN)_6]$ in buffered solution measured with CLEs (Fig. a). The observed peaks had similar shape, which indicates a reversible reduction/oxidation process of the $K_3[Fe(CN)_6]$ (Fig. a). Peak separation values was 93 mV at the scan rate 20 mV, which corresponds to the quasi-reversible system and could be due to the low concentration of the supporting electrolyte in the system. The peak current values were linearly proportional to square root of the scan rate, indicating lack of side electrochemical processes in the system (Fig. a, inset). Electrode surface area was estimated in therms of Eq. (1) and was found 0.53 cm^2 respectively.

$$i_p = 0.4463nFA\sqrt{\frac{nF\nu D}{RT}} \tag{1}$$

where, n is the number of electrons appearing in half-reaction for the redox couple, ν is the rate of potential sweeping (ν/s^{-1}), F is Faraday's constant (96485 Q/mol), A is the electrode area (cm^2), R is the universal gas constant (8.314 J/mol K), T is the absolute temperature (K), and D is the $K_3[Fe(CN)_6]$ diffusion coefficient (cm^2/s). Alternatively the surface area was estimated by weighting the backpaper of the selotape and was 0.55 cm^2. Determined values were in a good agreement showing that all CLE's surface was electroactive.

The next step we tested the obtained CLEs in a model bioelectrocatalytic process, such as electrochemical regeneration of hemoproteins. The model proteins shoes were myoglobin (Mb) and hemoglobin (Hb). As it was previously reported, Mb and Hb could be electrochemically regenerated on basal plane pyrolitic graphite electrodes while casted in didodecyldimethylammonium bromide (DDAB) film, so we

---

[1] The article is published in the original.

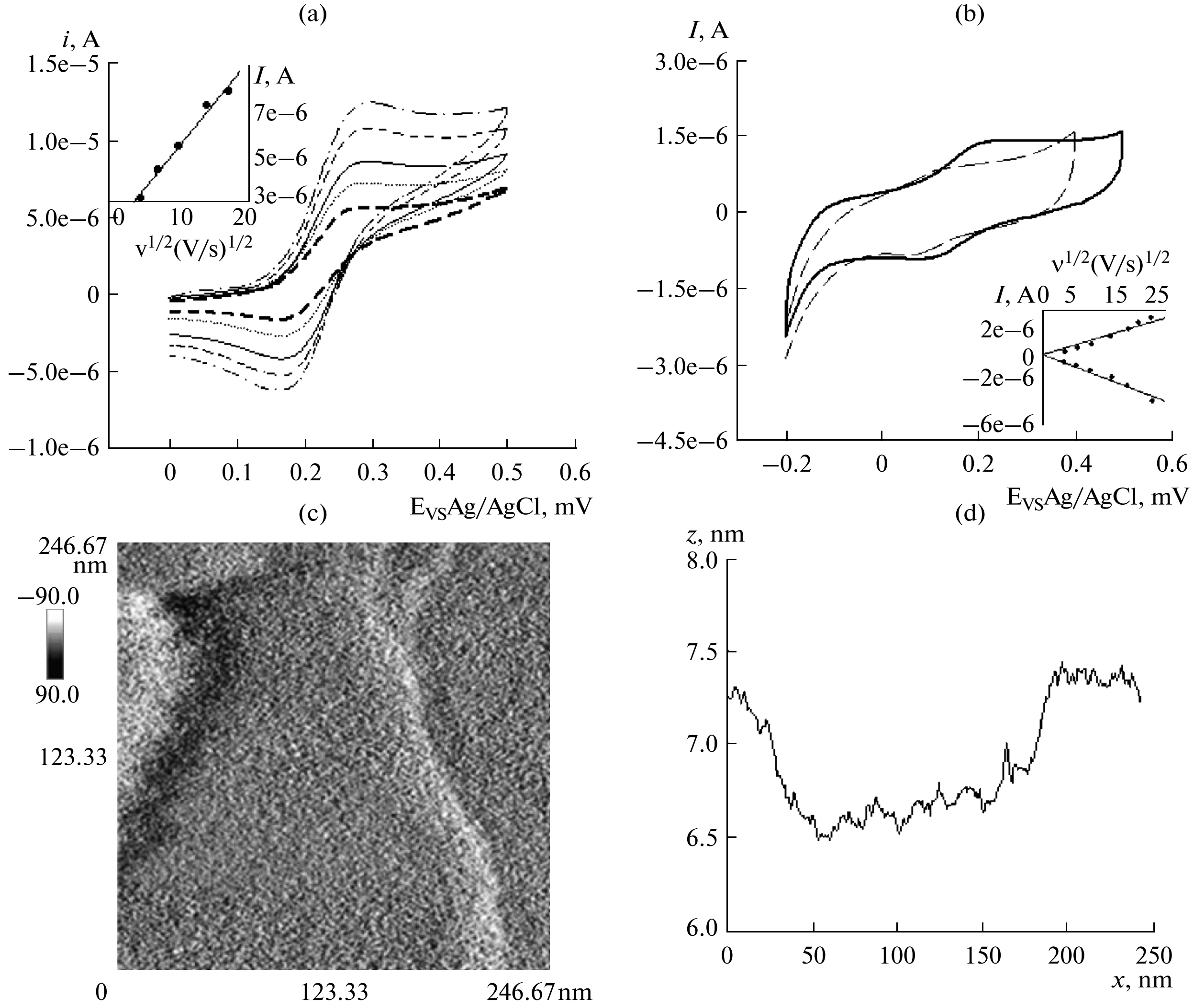

(a) Cyclic votammogramms of the HOPG electrode in the 0.1 KCl, 50 mM *tris*-HCl, 0.01 M $K_3[Fe(CN)_6]$ at the scan rates 20, 50, 100, 200, 300 mV/s. (b) Cyclic votammogramms of the HOPG electrode immobilized of Hb-DDAB (black line)/Mb-DDAB (dashed line) scan rates 20 mV/s, 50 mM *tris*-HCl. (c) *AFM* image of surface of CLE. (d) Line analysis of CLE surface.

used DDAB film so that immobilise Mb and Hb on CLEs [11, 12].

The cyclic voltamperogramm of obtained CLE/Mb/DDAB is shown at the Fig. b. As it could be seen, immersion of CLE/DDAB in Mb solution was accompanied by appearance of two peaks on CV, which corresponds to oxidative and reductive process of Mb. The ΔE_p was 73 mV for Mb and 150 mV for Hb, which could be due to the low ionic strength of the tested solution. However it clearly indicates the ability of a Mb and Hb to transfer electrons directly on the CLEs surface on, without any need for a mediator.

Next step, we tested morphology of electrode surface by the atomic force microscopy (AFM), which is shown at (Figs. c, d). Overage of the surface roughness was 1 nm as it could be seen on the AFM image. Observed step was 1 nm, which matches the size of a single carbon layer. The distance between the steps were reproducible for all studied CLEs and well match quality of the original HOPG material, which suggest that defects are inherited from the precursor HOPG.

MATERIALS AND METHODS

HOPG was ordered from SP and was SPI-3 grade. The carbon double layered selotape was from Nishin em. Co. ltd. The silver wire was from Goodfellow Cambridge and has 0.025 mm diameter. Myoglobin (horse skeletal muscle), haemoglobin (human), and tris[hydroymethyl]aminomethane were obtained from Sigma. (DDAB) and potassium ferrocyanide and potassium chloride were from Aldrich. The surface of the HOPG was cleaved with the carbon conductive selotape. The carbon selotape was pressed into the flat surface and then gently pulled off. Tape invariable takes off the thin layer of HOPG. The area covered with HOPG was cut off with scissors and stick onto the non-conductive glass. The electrical contact was established via silver wire connected to the carbon selotape on the other side. The square of the electrode surface was estimated by weighting the backpaper of the carbon selotape. The electrical connection was established via the silver wire.

Immobilisation of Hb and Mb was performed as it was described [12]Didodecyldimethylammonium bromide (DDAB) vesicles were prepared by sonication of the 1 mM solution of the DDAB film in water. Formed vesicles were misxied with 1 μM solution of protein (Hb or Mb) and filtered throught the 0.22 μ so that the reformed vesicles would occlude protein molecules. ClE's surface was immersed in to the solution and let dry on air.

The AFM images reported in this study were obtained using an Explorer^{TM}, Scanning Probe Microscope, (TopoMetrix-ThermoMicroscope-VEECO). Non-contact mode was used throughout. The tips used were high resonance frequency silicon tips (frequency range 354–409 KHz), with a 120 micron long cantilever and tip of 3–6 micron base, 10–20 micron in length and with a 20 nm tip radius. The raw data collected were processed by the TopoMetrix SPMLab NT Version 5.0, using left shadowing.

Therefore, current study is suggesting novel cheap and easy way of producing highly ordered CLEs, which could be used for bioelectrochemical application. Low production cost allows to generate multiple disposable CLE, which highly ordered structure maintain the properties of original piece of HOPG.

ACKNOWLEDGMENTS

Authors are thankful to MSSI for the making the AFM and electrochemical facilities available for the study and IRCET for the funding.

REFERENCES

1. Brookes, B., Davies, T., Fisher, A., Evans, R., Willkins, S., Yunus, K., Wadhawan, J., and Compton, R., Compuntational and Experimental Study of the Cyclic Voltammetry Responce of Partially Blocked Electrodes. Part 1. Nonoverlapping, Uniformly Distributed Blocking System, *J. Phys. Chem. B.*, 2003, vol. 107, pp. 1616–1627.
2. Davies, T., Brookes, B., Fisher, A., Yunus, K., Willkins, S., Greene, P., Wadhawan, J., and Compton, R., Compuntational and Experimental Study of the Cyclic Voltammetry Responce of Partially Blocked Electrodes. Part 2. Randomly Distributed and Overlapping Blocking System, *J. Phys. Chem. B.*, 2003, vol. 107, pp. 6431–6444.
3. Davies, T., Moore, R., Banks, C., and Compton, R., The Cyclic Voltammetric Responce of Electrochemically Heterogeneous Surfaces, *J. Electroanal. Chem.,* 2004, vol. 574, pp. 123–152.
4. Armstrong, F., Bond, A., Hill, A., Oliver, B., and Psalti, I., Electrochemistry of Cytchrome *c*, Plastocyanin, and Ferridoxin at Edge and Basal-Plane Graphite Electrodes Interprteted via a Model Based on Electron Transfer at Electroactive Sites of Microscopic Dimensions in Size, *J. Amer. Chem. Soc*, 1989, vol. 111, pp. 9185–9189.
5. Armstrong, F., Bond, A., Hill, A., Psalti, I., and Zoski, C., A Microscopic Model of Electron Transfer at Electroactive Sites of Molecular Dimensions for Reduction of Cytochome *c* at Basal- and Edge-Plane Graphite Electrodes, *J. Phys. Chem.*, 1989, vol. 93, pp. 6485–6493.
6. Armstrong, F.A., Recent Developments in Dynamic Electrochemical Studies of Adsorbed Enzymes and Their Active Sites, *Curr. Opin. Chem. Biol.*, 2005, vol. 9, pp. 110–117.
7. Armstrong, F.A., Bond, A.M., Bunchi, F.N., Hamnett, A., Hill, H.A.O., Lannon, A.M., Lettington, O.C., and Zoski, C.G., Electrocatalytic Reduction of Hydrogen Peroxide at a Stationary Pyrolytic Graphite Electrode Surface in the Presence of Cytochrome *c* Peroxidase: a Description Based on a Microelectrode Array Model for Adsorbed Enzyme Molecules, *Analyst*, 1993, vol. 118, pp. 973–978.
8. Armstrong, F.A., Camba, R., Heering, H.A., Hirst, J., Jeuken, L.J.C., Jones, A.K., Leger, C., and McEvoy, J.P., Fast Voltammetric Studies of the Kinetics and Energetics of Coupled Electron-Transfer Reactions in Proteins, *Faraday Discuss.*, 2001, vol. 116, pp. 191–203.
9. Yaropolov, A.I., Karyakin, A.A., Varfolomeev, S.D., and Berezin, I.V., Mechanism of Hydrogen Electrooxidation with Immobilized Hydrogenase, *Bioelectrochem. Bioenerg.*, 1984, vol. 12, pp. 267–277.
10. Novoselov, K.S., Geim, A.K., Morozov, S.V., Jiang, D., Zhang, Y., Dubonos, S.V., Grigorieva, I.V., and Firsov, A.A., Electric Field Effect in Atomically Thin Carbon Films, *Science*, 2004, vol. 306, pp. 666–669.
11. Lu, Z., Huang, Q., and Rusling, J., Films of Haemoglobin and Dodidecyldimethylammonium Bromide with Enhanced Electrone Transfer Rates, *J. Electroanal. Chem.*, 1997, vol. 423, pp. 59–66.
12. Rusling, J. and Nassar, A., Enhanced Electron Transfer for Myoglobin in Surfactant Films on Electrodes, *J. Amer. Chem. Soc.*, 1993,vol. 115, pp. 11891–11897.
13. Ivanova, E. and Magner, E., Direct Electron Transfer of Haemoglobin and Myoglobin in Methanol and Ethanol at Didodecyldimethylammonium Bromide Modified Pyrolytic Graphite Electrodes, *Echem. Comm.*, 2005, vol. 7, pp. 323–327.

ISSN 1068-3755, Surface Engineering and Applied Electrochemistry, 2011, Vol. 47, No. 1, pp. 56–60. © Allerton Press, Inc., 2011.
Original Russian Text © V.N. Tsurkin, A.V. Mel'nik, A.V. Ivanov, 2011, published in Elektronnaya Obrabotka Materialov, 2011, No. 1, pp. 66–70.

ELECTRICAL PROCESSES IN ENGINEERING AND CHEMISTRY

Analysis of the Pulse Current Behavior in a Massive Cylindrical Conductor at the Electric Current Treatment of a Melt

V. N. Tsurkin, A. V. Mel'nik, and A. V. Ivanov

Institute of Pulse Processes and Technologies, National Academy of Sciences of Ukraine,
pr. Oktyabr'skii 43-a, Nikolaev, 54018 Ukraine
e-mail: dpta@iipt.com.ua, iipt@iipt.com.ua

Received July 15, 2010

Abstract—The spectral analysis results for the time dependences of the pulse current at the electric current treatment of the melt are shown. It is established that the most favorable conditions of treatment are reached at the oscillating discharge mode. The possibility to control the parameters of the impact by means of the duration of the current pulses is shown.

DOI: 10.3103/S1068375511010194

INTRODUCTION

The quality improvement of cast metal production is the main scientific technical problem of foundries. It is solved by different approaches and technologies, including the treatment of a liquid and crystallizable metals by physicotechnical methods based on different physical principles of impact. The functional capabilities of these methods are multivariable and multiaimed, but there is no single universal method that can influence the qualitative characteristics of cast metals equally effectively yet. Now, the improvement of the traditional methods and a search for other alternative technological methods of treatment are being carried out. The treatment of liquid and crystallizable metals by periodic-pulse electric currents is one of the new methods. Unfortunately, works on these issues did not get their innovative development due to the insufficient investigation of the electropulse treatment processes of liquid-metal mediums, although some authors have proposed an hypothesis of the possible mechanism occurring at the periodic-pulse electric current treatment. [1–3].

The processes of treating metal melts by alternating or periodic-pulse electric currents involve the generation of a self-induction electrical vortex field that leads to the appearing of a skin effect, i.e., the displacement of the current to the surface of the conductor at the increasing of the current frequency. The electric self-induction vortex field occurring in the conductor upon the passing an alternating current through it prevents a change in the current inside the conductor and assists in the change in current near the surface. Thus, the maximum alternating current density is on the surface of the conductor, and the minimum is on its axis. In the case of high-frequency currents, the current density is nonzero only in the thin layer near the conductor's surface, which causes some peculiarities in the mechanisms of the electric current treatment of materials, and, for massive conductors, the skin effect occurs at lower values of the frequency [4].

For a sinusoidal alternating current, the dependences of the distributions of the electromagnetic field and of the current along the conductor cross section; of the relations between the active and reactive powers; of the thicknesses of the skin layer; and of the effective resistance of the conductor, whose value is higher than the value of the direct current resistance, on the frequency and δ/r relation have been properly studied [5]. For a periodic-pulse current, the $I = I(t)$ dependence, which is nonsinusoidal in a stable regime; the issue about the behavior and distribution of the current; the electromagnetic pulse field; the presence of the skin layer in massive conductors; and its value remain unclear [6]. The solution of these problems is very complicated and topical.

In this paper, we propose to use the spectral analysis method [7] for the investigation of a pulse current's behavior.

The purpose of the present work is to investigate the typical features of the pulse current behavior for different regimes at the electric current treatment of a melt using the example of a massive liquid-metal conductor using spectral analysis.

SPECTRAL ANALYSIS

Let us consider the experimental $I = I(t)$ curves for three typical modes of capacitive storage discharge (Fig. 1): oscillating ($\eta = 0.37$), matched ($\eta = 0.79$), and aperiodic ($\eta = 1$). Here, η is the fraction of energy evolved in the first?half period?of the discharge?current.

In the pulse-periodic mode, the current behaves as a damped?sinusoid within one pulse, and its spectrum

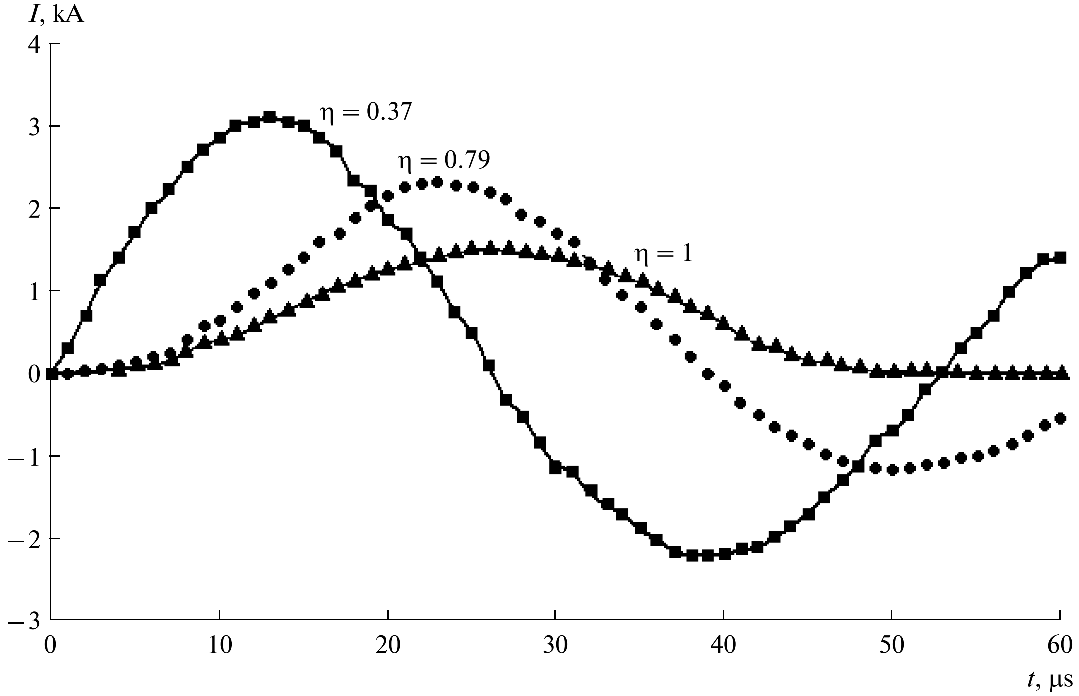

Fig. 1. Experimental oscillograms of the current in different modes of discharge.

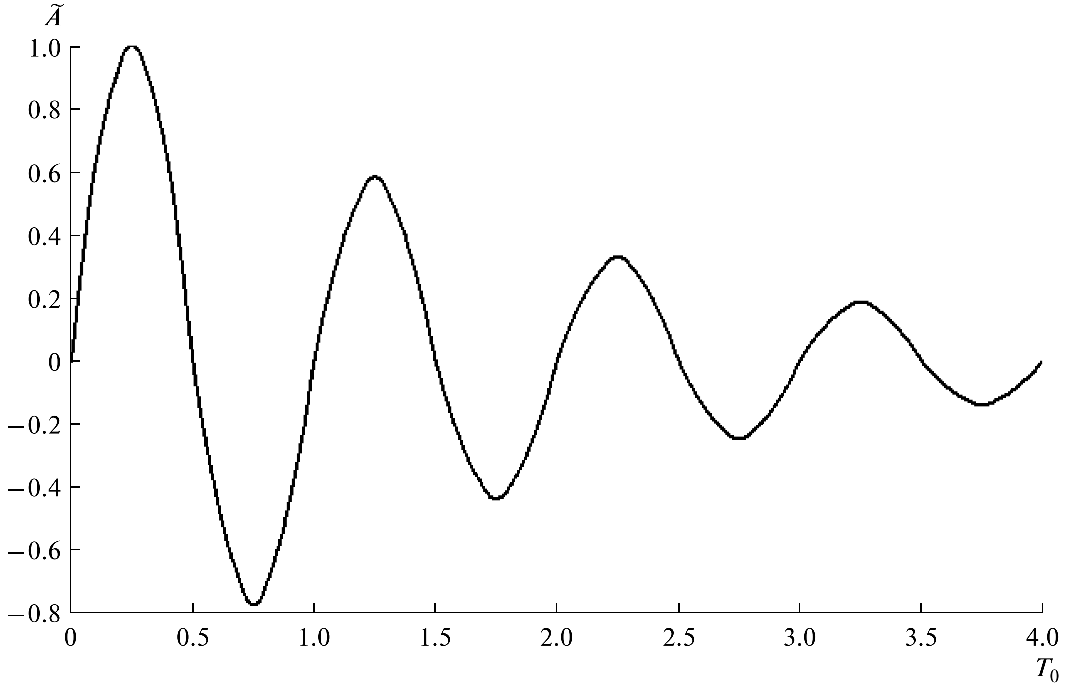

Fig. 2. Typical oscillogram of the current at the pulse current treatment of melts.

is “smeared” unlike an alternating current, whose spectrum is concentrated in one frequency.

A typical oscillogram of a pulse current at the electric current treatment of a melt is shown in Fig. 2. The data are in relative units. The relative amplitude of the current ($\tilde{A} = A/A_{\max}$) is in the Y-direction, and the relative time ($T_0 = t/\tau$ (τ) is in the X-direction. The duration of the pulse is 4τ.

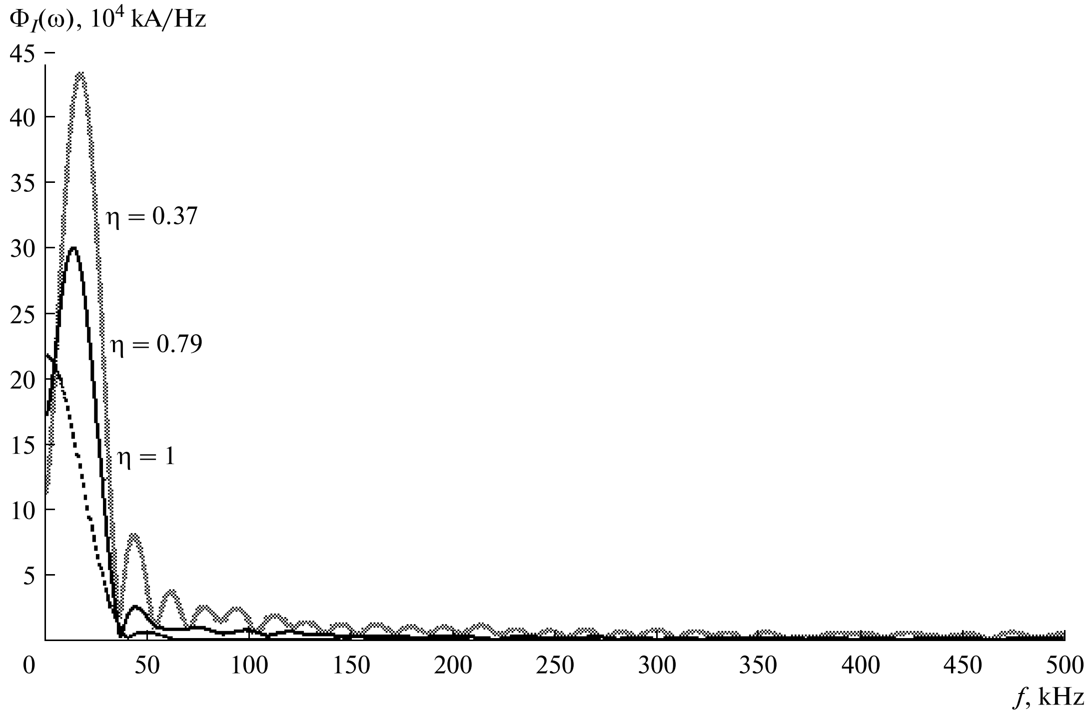

Fig. 3. Spectra of the current measured for different modes of discharge

The spectral analysis of these functions fully defined in the time interval from 0 to T consists of calculating their complex spectral density, $S(\omega)$ [7]:

$$S(\omega) = S_c(\omega) + iS_s(\omega),$$

where ω is the angular frequency, and

$$S_c(\omega) = \int_0^T I(t)\cos\omega t dt; \quad S_c(\omega) = \int_0^T I(t)\sin\omega t dt.$$

The modulus of the spectral density is $\Phi(\omega) = \sqrt{[S_c(\omega)]^2 + [S_s(\omega)]^2}$.

DISCUSSION

The spectra of the current curves for the studied modes of discharge are shown in Fig. 3. One can see from the plots that the spectral density of the current is higher in the oscillating mode, in which the first maximum corresponds to the frequency range of 15–20 kHz, and the second is observed at about 44 kHz. Periodic maximums occur almost in the whole frequency range, but the values of the spectral density are considerably lower. The lowest spectral density corresponds to the aperiodic mode, the first maximum is in the range of 0–5 kHz, and the second occurs at 50 kHz. For the matched mode of discharge, the first maximum of the spectral density is observed in the frequency range of 12–16 kHz, and the second is at 45 kHz. Consequently, for the electric current treatment of melts, it is more energetically favorable to use an oscillating mode of the discharge, at which the parameters of the impact are maximal. Notice that the oscillating mode of discharge that provides the maximum pressure in the melt and the maximum width of the?acoustic?spectrum is also preferential for practical uses at electro-hydro-impulse treatment [8]. Comparing the spectral mode densities of the discharge current for different values of η at the same frequencies, we can conclude that the functional capabilities of the treatment at any selected frequency for each regime are different. Taking into account the efficiency of the processes occurring in the melt and having a positive impact on the structure of cast metals (the ohmic heating, the electromagnetic force impact, the electrotransfer, the changing of the kinematics of the inclusions, etc.) as defined by the value of I in the case of the direct passage of a current through the treated melt, the oscillating mode has significant advantages.

Thus, the use of the oscillating mode of electric discharge allows one to treat melts more effectively, thus affecting the different structural levels of metals [9].

The main mechanism of the impact of the electric current treatment on the melt state is related to the impact on the nucleation rate, which depends on the change of the difference of the free energies between the liquid and solid states and the change in the interfacial surface energy [10]. The extent of how the electric current treatment affects the metal treated depends on the following processes that, in turn, are affected by the nonuniformity of the current distribu-

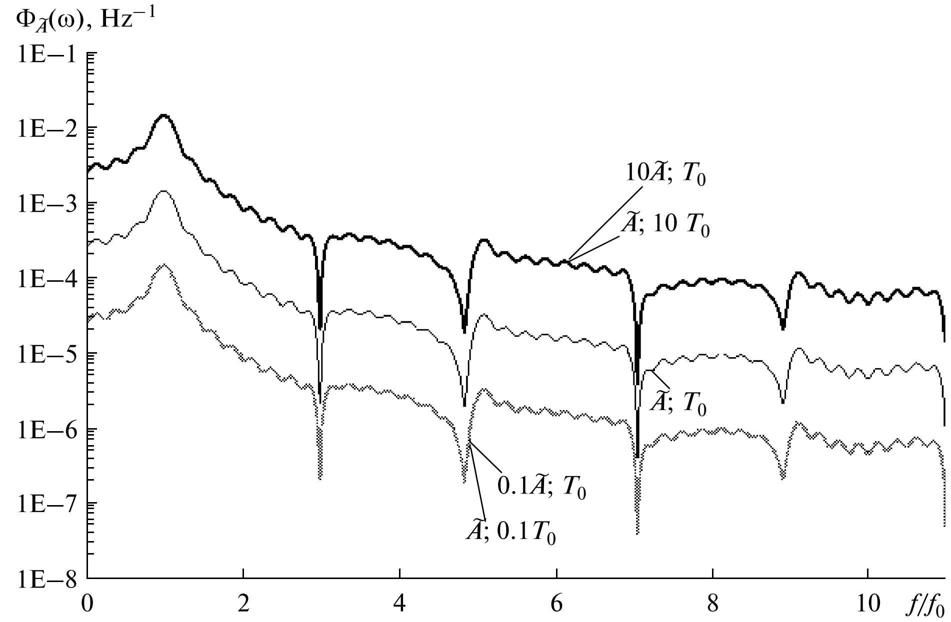

Fig. 4. Spectra of the current measured at different values of the relative amplitude and time

tion and by the electromagnetic pulse field in the liquid–metal conductor: the ohmic heating, which assists in the reduction of the temperature gradient at the "melt–pot" interface (the heterogeneous nucleation is prevented on the pot's walls due to the heating of the skin layer); the pinch effect, which is the compressing electromagnetic force directed from the lateral surface to the center of the conductor (it prevents the nucleation process on the pot's walls). According to Fig. 3, in the oscillating mode, the current density is the maximal (the maximum of the spectral current density corresponds to the higher frequency) compared to the other modes, when the thickness of the skin layer is relatively small. It indicates a significant effect of the capacitive storage discharge mode on the processes and mechanisms of the electric pulse current treatment of melts. The maximum impact corresponds to the oscillating mode.

Let us analyze the pulse current spectra (Fig. 2) at different relations between the period and the amplitude of the current. In Fig. 4, the spectra measured at relative current amplitudes of $\tilde{A}$, $10\,\tilde{A}$, and $0.1\,\tilde{A}$, and at periods of $0.1T_0$ and $10T_0$ are shown. The X-direction corresponds to the relative frequency f/f_0, where f_0 is the carrier frequency of the pulse current. These spectra are almost the same quantitatively; however, they differ by orders of magnitude quantitatively. The identity of the spectra measured at $0.1\,\tilde{A}$ and $0.1T_0$, and also at $10\,\tilde{A}$ and $10T_0$ should be noted. Thus, to obtain the needed parameters of the impact at the electric current treatment of a melt, the amplitude value of the pulse current or the duration of the pulse should be varied. Since an increase in the current amplitude is unreasonable due to the energy expenditures and is limited by the equipment's operational performance, an increase in the duration of the current pulses is a more efficient and constructively implemented method of controlling the treatment parameters.

In addition, the time dependence spectra (Fig. 2) were analyzed at reducing the curve to 3τ, 2τ, τ, τ/2, τ/4, and τ/8. On decreasing the time of the current oscillations, the spectral density decreases (the most intensively in the range from τ to τ/8), but the frequency range of the impact broadens significantly in this case.

CONCLUSIONS

Thus, on the basis of the spectral analysis carried out for the time dependences of the pulse current, we can conclude that the oscillating mode of the capacitive storage discharge is the most effective for the electric pulse current treatment of melts (the spectral density in this case is an order of magnitude higher than for the matched mode and two orders of magnitude higher than for the aperiodic mode).

The ways to control the parameters of the pulse impact (by varying the amplitude or the duration of the current pulse) were discussed. It was shown that the most preferable method in accordance with the energy expenditures is varying the duration of the current pulses, whose effect is comparable to an increase in the current amplitude by the same order.

REFERENCES

1. Vil'skii, G.B., and Farnasov, G.A., Pulse Ponderomotive Effect on the Crystallizing Metal, *Elektricheskii razryad v zhidkosti i ego primenenie v tekhnologii mashinostroeniya i metalloobrabotki, Tezisy. dokl. I vses. nauchno-tekh. konf.* (Electric Discharge in Liquid and Its Application in Engineering Technologies and Metal Working. Abstracts of Papers, I All-Union Sci. Tech. Conf.) (Nikolaev, 1976), Kiev: Naukova Dumka, 1976, pp. 78–79.
2. Vernidub, A.G., Volkov, G.V., Grabovyi, V.M., Semenchenko, A.I., Fedchenko, N.A., et al., Treatment of AK 7 alloy by pulse electric current, *Protsessy Lit'ya*, 2005, no. 1, pp. 64–67.
3. Rongshan, Qin., Solidification Under Electropulsing, *Int. J. Cast Metal Res.,* 2007, vol. 25, no. 7, pp. 92–98.
4. Kompan, Ya.Yu., and Shcherbinin, E.V., *Elektroshlakovaya svarka i plavka s upravlyaemymi MGD-protsessami* (Electroslag Welding and Melting?with Controllable?MHD-Processes), Moscow: Mashinostroenie, 1989.
5. Bessonov, L.A., *Teoreticheskie osnovy elektrotekhniki. Elektromagnitnoe pole* (Theoretical Foundations?of Electrical Engineering: Electromagnetic Field), Moscow: Vysshaya Shkola, 1986.
6. Shneerson, G.A., *Polya i perekhodnye protsessy v apparature sverkhsil'nykh tokov* (Fields and Transient?Processes in?Ultra-High Current Equipment), Leningrad: Energoizdat, 1981.
7. Kharkevich, A.A., *Spektry i analiz* (Spectra and Analysis), Moscow: Fizmatiz, 1962.
8. Tsurkin, V.N., Sinchuk, A.V., and Ivanov, A.V., Calculation Technique for Determination of Discharge Parameter Influence on Acoustic Field Characteristics in the Melt at Electrohydropulse Treatment, *Elektron. Obrab. Mater.*, 2004, no.1, pp. 82–87.
9. Tsurkin, V.N., Sinchuk, A.V., and Ivanov, A.V, Influence of Electric Discharge Regime on the Quality of the Metal That is Subjected to Electrohydroimpulsive Processing in the Liquid State, *Elektron. Obrab. Mater.*, 2005, no. 1, pp. 98–103 [*Surf. Engineer. Appl. Electrochem.* (Engl. Transl.), 2005, no. 1, pp. 96–103]
10. Flemings, M., *Hardening Processes* [Russian Translation], Zhukov, A.A., and Rabinovich, B.V., Eds., Moscow: Mir, 1977.

ISSN 1068-3755, Surface Engineering and Applied Electrochemistry, 2011, Vol. 47, No. 1, pp. 61–65. © Allerton Press, Inc., 2011.
Original Russian Text © V.Yu. Baklar', 2011, published in Elektronnaya Obrabotka Materialov, 2011, No. 1, pp. 71–76.

ELECTRICAL PROCESSES IN ENGINEERING AND CHEMISTRY

Optimization of the Synthesis of Different Carbon Allotropes by Electric Explosion of Graphite Conductors

V. Yu. Baklar'

Institute of Pulse Processes and Technologies, National Academy of Sciences of Ukraine,
pr. Oktyabr'skii 43-a, Nikolaev, 54018 Ukraine
e-mail: iipt@iipt.com.ua

Received July 15, 2010

Abstract—The analytical relations for the prediction of the structural phase transformations of carbon in cylindrical graphite conductors induced by high-powered current pulses are obtained theoretically. The parameters of the electric circuit and the size of the conductor that are optimal for the synthesis of fullerenes and nanodiamonds are determined. The reliability of the proposed algorithm for selecting the parameters of the electric circuit and the size of the conductor is confirmed experimentally.

DOI: 10.3103/S1068375511010030

INTRODUCTION

The known physical methods of obtaining carbon nanomaterials based on evaporation and condensation of carbon-containing substances (the electroarc method, the laser method, the detonation method, the method of electron beams, catalytic pyrolysis, etc.) allow one to obtain only one and, rarely, two individual classes of nanocarbon allotropic modifications [1, 2]. Furthermore, each of these methods has a number of significant shortcomings such as laboriousness, multistageness, and low yields of fullerenes in the electroarc and laser methods. The detonation method requires an expensive infrastructure and special conditions for using explosives [3, 4].

Predicting how high-powered pulses influence carbon-containing compounds is an important scientific and technical problem, whose solution will enable one to determine the optimal conditions and to develop new methods for obtaining different allotropes of nanocarbon.

The electric explosion of conductors is one of the methods of an electrical discharge's influence on substances. An electric explosion as a process of rapid conversion of the electric field energy into the intrinsic energy of the conductor is one of the most high-powered sources of pulse influence on materials according to its specific characteristics. The heating of a graphite conductor by a high-powered current pulse leads to a number of phase transformations of carbon (sublimation or melting and evaporation). The electric explosion method enables one to measure the whole spectrum of carbon nanomaterials [5, 6].

The previous experimental studies of the electric explosion of graphite conductors and of the phase composition of the products obtained by this method have shown that there is a correlation between the value of the specific energy introduced into the conductor, w, and the value of the specific heat of the graphite sublimation, w_s ($w_s = 59.7$ MJ/kg) [6, 7]. At the low-energy regimes of the explosion ($w < w_s$), the carbon nanomaterials contain fullerene-like clusters (10 MJ/kg $< w <$ 20 MJ/kg) and nanotubes (8 MJ/kg $<$ $w <$ 10 MJ/kg), and, at the high-energy regimes ($w >$ 60 MJ/kg), they contain a diamond phase [8]. However, using only one "energy" relation is not enough to determine the parameters of the electric circuit (the charging voltage, U_0; the capacity of the capacitor bank, C; and the inductance, L) and the conductor size required for the synthesis of a particular allotropic form of carbon.

The purpose of this work is to obtain analytical relations for the prediction of the carbon structural phase transformations induced by high-powered current pulses in cylindrical graphite conductors, to determine the parameters of the electric circuit and the size of the conductor that are optimal for the synthesis of fullerenes and nanodiamonds, and to compare the results obtained with the experimental data.

THEORETICAL INVESTIGATION

The first stage of obtaining fullerenes and nanotubes during the explosion process is, most likely, the fracture of the layered structure of the graphite conductor into individual graphene layers occurring due to the ohmic heating. These individual graphene layers may contain various defects, including broken covalent bonds between the carbon atoms. That is why the specific energy introduced into the conductor, w, must be several times less than the energy of the graphite sublimation, w_s. In terms of the thermodynamic state of the carbon defined by the phase diagram, the partial sublimation of the graphite into graphene layers and clusters occurs at pressure and temperature values that are not higher than their respective values at the first triple point, graphite–liquid carbon–gas ($P < 10^7$ Pa, $T < 5 \times 10^3$ K). These pressures and temperatures take place at low-energy regimes of the conductor’s heating if $(dP/dT)_1 < 2 \times 10^3$ Pa/K.

In the second stage of the electric explosion, presumably, the assembly of different clusters into a fullerene molecule or the folding of the graphite layers into a nanotube occurs. This takes place in a rapidly expanding steam-gas cavity at a pressure of $P \approx 1$ kPa and a temperature of $T \approx 2000$ K depending on the size of the cluster (the greater w is, the less the size is).

The synthesis of the diamond allotropic modification at the high-energy regimes of electric explosion also occurs in two stages. During the first stage, the rapid compression of the graphite due to the pinch effect, the melting of the conductor in the central part, and the formation of liquid carbon likely occur. At the “diamond regimes,” the pressure and temperature must be higher than the respective values of the second triple point in the carbon phase diagram: graphite–liquid carbon–diamond ($P > 10^{10}$ Pa, $T > 5$ kK) [8]. In this case, the condition that $(dP/dT)_2 > 2 \times 10^6$ Pa/K [4] must be satisfied for the phase trajectory of the carbon during the process of the heating, and the energy introduced into the conductor must be higher than the melting heat. During the second stage, the crystallization of the liquid carbon into diamond likely occurs on fast quenching.

These listed constraints (above and below) for the pressure change rate, dP/dT, allow one to find a dependence of the phase composition of the carbon nanomaterials obtained on the rate of the current increase and on the current density in the conductor [9]:

$$\frac{dP}{dT} = \frac{\mu\sigma\rho c}{2\pi j}\frac{dI}{dT}, \qquad (1)$$

where μ is the magnetic permeability,

is the current, j is the current density, $\sigma$is the specific electrical conductivity, ρ is the density, and c is the specific heat capacity.

On the basis of the above conditions (P, T) for synthesizing new carbon phases and on expression (1), the relations between the current densities and the rates of the current increase required for obtaining diamonds (2) and fullerenes (3) are found:

$$j < k_1\sigma\rho c\mu(dI/dt), \qquad (2)$$

$$j > k_2\sigma\rho c\mu(dI/dt), \qquad (3)$$

where $k_{1,2} = [2\pi(dP/dT)_{1,2}]^{-1}$.

Since the synthesis of the diamond phase from graphite is possible due to the high pressures, it is seen from (2) that the rate of the current increase in the conductor plays a decisive role, whereas the growth of the current density value (in the thin conductors) leads to an increase in the rate of the competing process, that is, the heating of the conductor, which causes the sublimation of the graphite at low pressures.

The approximate relations between the radius of the conductor, a, and the electric parameters, C and L, can be obtained from expressions (2) and (3). Based on the analysis of the electric explosion oscillograms previously obtained, in which the curve of the electric-explosion current coincides with the curve of the short circuit current at the starting stage, the following expression for the time dependence of the current (which holds before the phase transition starts) can be used to find the parameters:

$$I \approx U_0\sqrt{C/L}\sin(t/\sqrt{LC}). \qquad (4)$$

From expression (4), we obtain

$$j \approx U_0\sqrt{C/L}\sin(t/\sqrt{LC})/\pi a^2; \qquad (5)$$

$$dI/dT \approx (U_0/L)\cos(t/\sqrt{LC}); \qquad (6)$$

$$\frac{j}{dI/dt} = \frac{\sqrt{LC}}{\pi a^2}\tan\frac{t}{\sqrt{LC}}. \qquad (7)$$

If the regimes of the electric explosion for performing the structural phase transformations of the carbon are selected so that the melting and sublimation start at $t/\sqrt{LC} \approx \pi/4$, the $\tan(t/\sqrt{LC}) \approx 1$. Then, the following conditions for the synthesis take place:

for diamonds, at $W_{\text{sp}} = \dfrac{CU_0^2}{2m} > 60$ MJ/kg:

$$\sqrt{LC} < k_1\sigma\rho c\mu\pi a^2; \qquad (8)$$

for fullerenes, at $W_{\text{sp}} = \dfrac{CU_0^2}{2m} < 20$ MJ/kg:

$$\sqrt{LC} < k_2\sigma\rho c\mu\pi a^2, (9) \qquad (9)$$

where m is the mass of the conductor that allows one to choose the conductor of the needed diameter without performing the oscillographic testing of the electric explosion.

Thus, using the above discussed conditions for the synthesis of diamonds (8) and fullerenes (9) at the appropriate energetic characteristics, the parameters of the electric circuit and graphite conductor that are optimal for the “diamond” or “fullerene” regimes of the electric explosion of the conductor can be estimated.

On the basis of analytical expressions (2)–(9), the algorithm for selecting the appropriate combination of the electric circuit and conductor parameters was developed and carried out using MathCad software. This algorithm is shown in Fig. 1.

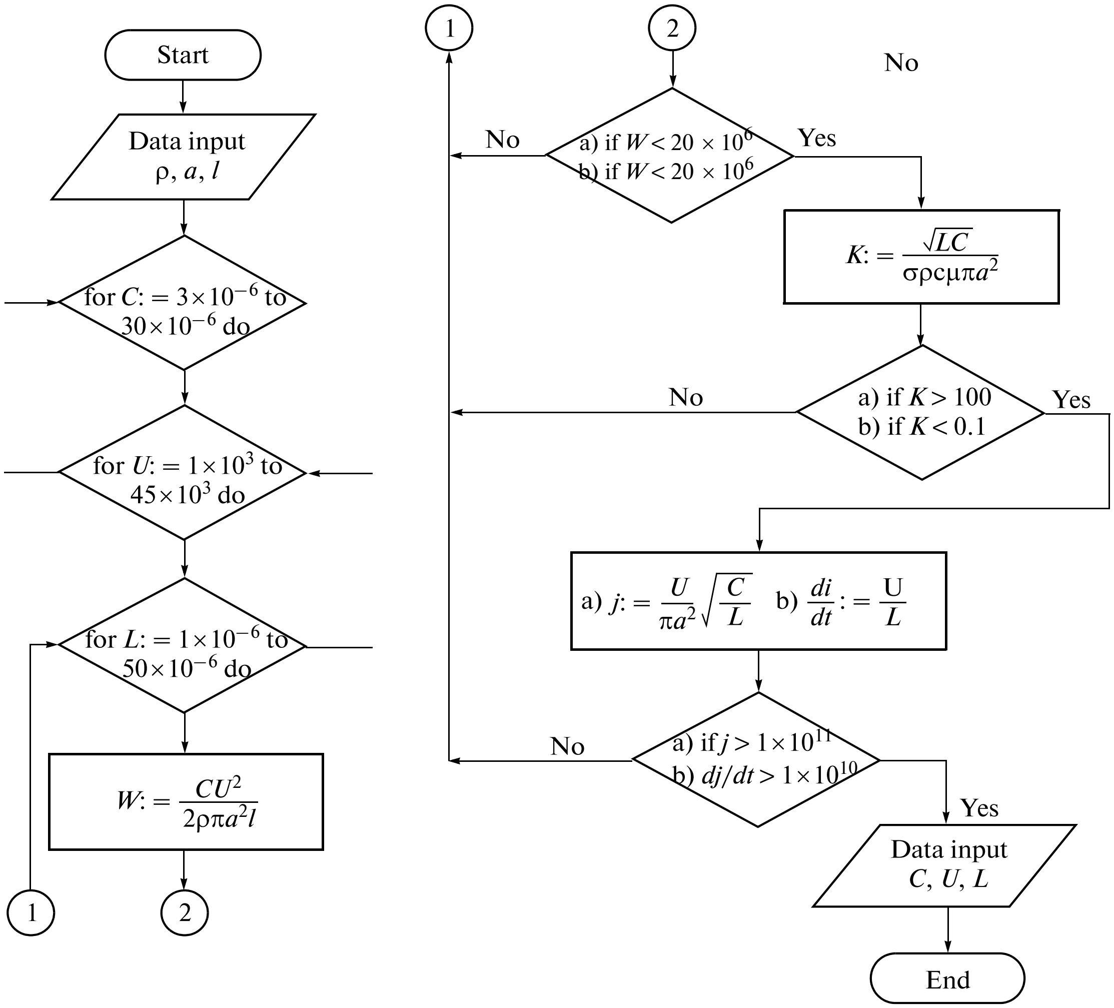

(a) (b)

Fig. 1. Algorithm for selecting the combination of the parameters of the electric circuit and the conductor to perform different regimes of electric explosion of the graphite conductor: (a) "fullerene," (b) "diamond."

The developed algorithm allowed us to calculate the regimes of the electric explosion of conductors with a given size (the radius and length (l)) that are optimal for obtaining fullerenes and nanodiamonds.

EXPERIMENTAL

The experimental studies were performed in accordance with the theoretically calculated regimes for the synthesis of carbon nanomaterials. The purpose of these experiments was the obtaining of carbon nanomaterials with given properties and the comparison of the experimental parameters of the electric explosion process with the theoretical ones.

In this work, the electric explosion of graphite conductors in carbon-containing liquids was performed. By virtue of spring-loaded electrode contacts, reliable electric contacts and a decrease of the noise level were provided during the measurements. The liquid containing the products of the explosion was drained through an outlet located on the bottom of the device. A coaxial low-resistance shunt (R_{sh}) and a capacitive shielded divider (Z_{D1}/Z_{D2}) were used as the electric sensors. The registration of the electric signals was carried out using a C8-18 dual trace storage oscilloscope.

The digitization of the current and voltage oscillograms obtained in the experiment was carried out using the Grafdigitizer program package with the further treatment by means of MathCad software.

RESULTS AND DISCUSSION

In Fig. 2, the typical current and voltage oscillograms for the electric explosion of the graphite conductor performed in one of the "fullerene" regimes (the parameters of which were calculated using the above described algorithm) are shown. For the investigation of the influence of the medium on the nature of the electrical discharge, two types of carbon-containing liquids were used in the experiments: hexane and

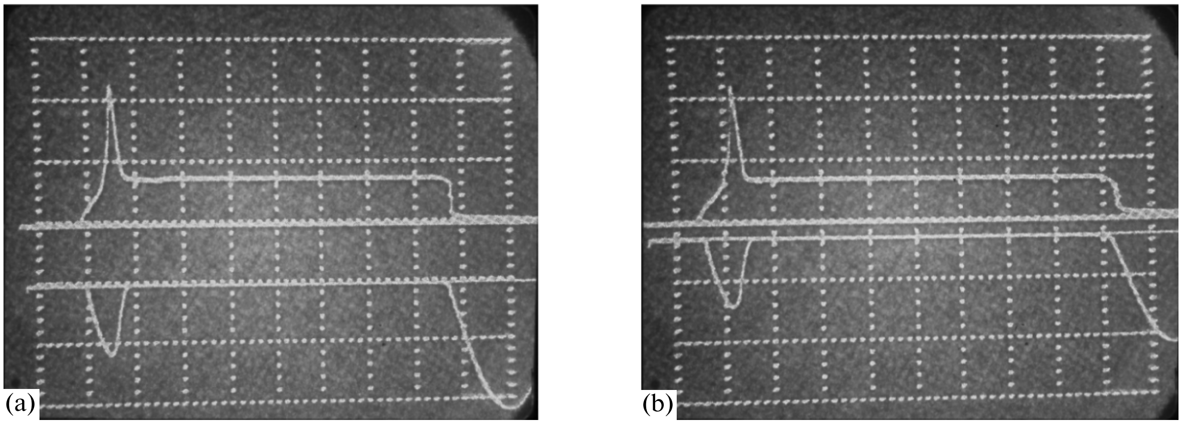

Fig. 2. Oscillograms for the electric explosion of the graphite conductor in hexane (a) and in ethanol (b) at performing the "fullerene" regime. The upper curve is the voltage, and the lower, the current. $m_t = 10$ µs/div, $m_u = 10$ kV/div, $m_i = 2.38$ kA/div; $U_0 = 10$ kV, $C = 6$ µF, $L = 10.5$ µH, $a = 0.3$ mm, $l = 50$ mm.

ethanol. By analyzing the behavior of the current and voltage curves, it may be deduced that the electrical discharge has an explosive nature since the amplitude of the overvoltage peak is more than two times higher than the initial voltage. Consequently, the process is accompanied by the sublimation of the graphite conductor. Also, it can be noticed that the electrical discharge process has an intermittent behavior and the amplitude of the secondary breakdown current is much higher than the amplitude of the electric explosion current and is comparable with the short circuit current.

The changing of the medium from hexane to ethanol leads to a 20% longer duration of the current pause, which is most likely due to the liquid's characteristics, but, in general, the behavior of the electric explosion remains the same. Thus, it indicates that the medium influences not the electric explosion of the conductors themselves but only the arc stage of the electrical discharge and the rate of the cooling of the electric explosion products in the expanding gas cavity.

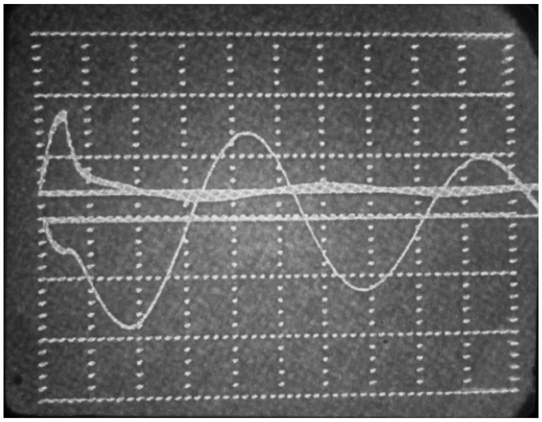

Fig. 3. Oscillograms for the electric explosion of the grahite conductor in hexane at performing the "diamond" regime. The upper curve is the voltage, and the lower, the current. $m_t = 5$ µs/div, $m_u = 25$ kV/div, $m_i = 23.8$ kA/div; $U_0 = 37$ kV, $C = 6$ µF, $L = 2.639$ µH, $a = 2$ mm, $l = 25$ mm.

The analysis of the electric explosion products that were obtained using the theoretically calculated parameters of the circuit, which was carried out at The Institute of Metal Physics of the National Academy of Sciences of Ukraine, showed the presence of fullerenes [9].

In Fig. 3, a typical oscillogram of the electric explosion of graphite conductors in hexane in a "diamond" regime is shown. We can see from the oscillogram that the electric explosion has an uninterrupted behavior, and the breakdown takes place along the evaporating surface of the conductor, which leads to the compression of the central part, thereby creating the pressure in the core of the conductor needed for the synthesis of diamonds.

The analysis of the electric explosion products obtained using the theoretically calculated parameters of the circuit, which was carried out at The Institute of Metal Physics of the National Academy of Sciences of Ukraine, showed the presence of the diamond phase [9].

The treatment and analysis of the oscillorgams for each electric explosion performed with the purpose to determine the actual maximum of the rate of increase of the current and the maximum of the current density showed that these maximums are reached at different points in time, their values are $dI/dt = 4.6 \times 10^8$ A/s and $j = 4 \times 10^{10}$ A/m^2, and their relation is $j/(dI/dt) = 86.9$ s/m^2. Since, in the theoretical calculations of the ratio between the current's density and the current's rate of increase, ideal values of the graphite conductor parameters (pure carbon) were used, the experimental values of $j/(dI/dt)$ differ from the theoretical ones by 15%. This is a good result, since the error that occurred in the digital processing of the analog signals and the instrumental errors are of the same values. For the "diamond" regime, we also have good results, since the actual rate of increase of the current and the current density are $dI/dt = 3.7 \times 10^{10}$ A/s and $j = 3.9 \times 10^9$ A/m^2, and their relation is $j/(dI/dt) = 0.11$ s/m^2, which differs from the theoretical value by 10%.

Thus, the synthetic processes of the different carbon forms by electric explosion of graphite conductors were optimized.

CONCLUSIONS

The theoretical expressions that define the conditions for the synthesis of fullerenes and nanodiamonds by the electric explosion of cylindrical graphite conductors were obtained.

On the basis of these theoretical relations, an algorithm for selecting the combination of the parameters of the electric circuit and conductor that are optimal for synthesizing fullerenes or nanodiamonds was developed.

The reliability of the obtained theoretical relations satisfying the conditions for the formation of different allotropic modifications of carbon was confirmed experimentally.

REFERENCES

1. Ivanova, V.S., Folmanis, G.E., From Nanomaterials to Nanotechnologies, *Metallurgiya Mashinostroeniya*, 2007, no. 1, pp. 2–10.
2. Eletskii, A.V., Smirnov, B.M., Fullerenes and Carbon Structures, *Usp. Fiz. Nauk*, 1995, vol. 165, no. 9, pp. 977–985 [*Phys. Usp.*, (Engl. Transl.), 1995, vol. 38, no. 9, pp. 935–964].
3. Khodorkovskii, M.A., Artamonova, T.O., Murashov, S.V., Shakhmin, A.L., Belyaeva, A.A., Rakcheeva, L.P., Fonseca, I.M., and Ljubčik, S.B., Composition of Higher Fullerenes Obtained by Laser Ablation of Carboniferous Materials, *Zh. Tekh. Fiz.,* 2005, vol. 75, no. 10, pp. 51–54 [*Tech. Phys.* (Engl. Transl.), vol. 50, no. 10, pp. 1301–1304].
4. Dolmatov, V.Yu., Veretennikova, M.V., Marchukov, V.A., Sushchev, V.G., Currently Available Methods of Industrial Nanodiamond Synthesis, *Fiz. Tverd. Tela*, 2004, vol. 46, no. 4, pp. 600–605 [*Phys. Sol. State*, 2004, vol. 46, no. 4, pp. 611–615].
5. Rud, A.D., Perekos, A.E, Ogenko, V.M., Shpak, A.P., Uvarov, V.N., Chuistov, K.V., Lakhnik, A.M., Voynash, V.Z., Ivaschuk, L.I., Different States of Carbon Produced by High-Energy Plasmochemistry Synthesis, *J. Non-Crystalline Solids*, 2007, vol. 353, pp. 3650–3654.
6. Kuskova, N.I., Rud', A.D., Uvarov, V.N., Ivashchuk, L.I., Perekos, A.E., Boguslavskii, L.Z., and Oreshkin, V.I., Electroblasting Mehtods of Synthesizing Carbon Nanomaterials, *Metallofiz. i Noveishie Tekhnol.*, 2008, vol. 30, no. 6, pp. 833–847.
7. Pierson, O.H., *Hand Book of Carbon, Graphite, Diamond and Fullerenes: Properties, Processing and Application*, Park Ride, New Jersey: USA: NoesPublications, 2003.
8. Kuskova, N.I., Phase Transformations of Carbon Heated by a High-Power Current Pulse, *Pis'ma v Zh. Tekh. Fiz.*, 2005, vol. 31, no. 17, pp. 28–34 [*Tech. Phys. Lett.*, (Engl. Transl., 2005, vol. 31, no. 9, pp. 732–734].
9. Kuskova, N.I., Rud', A.D., Baklar', V.Yu., and Ivashchuk, L.I, Physical Aspects of the Formation of Various Allotropic Modifications of Nanocarbon During Electric Explosion, *Zh. Tekh. Fiz.*, 2010, vol. 80, no. 9, pp. 57–62 [*Tech. Phys.* (Engl. Transl.), vol. 55, no. 9, pp. 1288–1293].

ISSN 1068-3755, Surface Engineering and Applied Electrochemistry, 2011, Vol. 47, No. 1, pp. 66–69. © Allerton Press, Inc., 2011.
Original Russian Text © E.G. Sprinchan, M.K. Bologa, T.G. Stepurina, Al.M. Bologa, A.A. Polikarpov, 2011, published in Elektronnaya Obrabotka Materialov, 2011, No. 1, pp. 77–80.

ELECTRICAL TREATMENT OF BIOLOGICAL OBJECTS AND FOOD PRODUCTS

Peculiarities of the Electric Activation of Whey

E. G. Sprinchan, M. K. Bologa, T. G. Stepurina, Al. M. Bologa, and A. A. Polikarpov
Institute of Applied Physics, Academy of Sciences of Moldova, ul. Akademiei 5, Chisinau, MD 2028 Republic of Moldova
e-mail: vrabie657@yahoo.com

Received March 3, 2010

Abstract—The main peculiarities of the electro-physico-chemical activation of whey are described; the parameters of the activation of whey and its behavior in the course of the relaxation process are analyzed. The variations of the main parameters under the action of the electrical activation were rationalized. The results of the investigations of the pH values of the activated whey immediately after the process and during its storage are presented. These pH values are among the most significant conditions of the protein–mineral concentrate recovery and the lactose–lactulose isomerization.

DOI: 10.3103/S1068375511010182

The substantiation of new approaches to the processing of whey, as well as of biological liquids, has becomes more and more urgent and is attracting the attention of a wide range of research workers and engineers interested in the possibilities of the elaboration of efficient ecological technologies. The high-level processing of whey allows one to obtain products for food, including for medical and preventative purpose. Electro-physico-chemical activation (EPCA) is providing for the generation of new products and preparations in a metastable state in aqueous solutions of different compounds with a substantial reduction and even exclusion of chemical reagents.

Electro-physico-chemical activation is a complex of electro-physico-chemical actions performed in the region of a space charge at the surface of electrodes in a medium containing ions and molecules of dissolved substances with nonequilibrium charge transfer through the "electrode–electrolyte" boundary under the conditions of the least heat evolution. The main structural transformations of water molecules happen at the electrode's surface, where the electric voltage is some orders of magnitude higher [1]. With the help of different electrolyzers, there are recognized three groups of factors determining the physico-chemical activity of a catholyte and anolyte: 1—stable products of electrochemical reactions, stable bases, etc; 2—highly active unstable products with lifetimes up to dozens of hours (including free radicals); and 3—long-lived quasi-stable structures built up in the region of a spatial charge at the surface of electrodes in the form of free structural complexes as well as hydrated shells of ions, molecules, radicals, and atoms [2]. The first group of factors mainly determine the medium's alkali properties defining the pH values, the second group of factors enhance the catholyte reducing (electron-donor, antyoxygenic) properties determining the anomalous characteristics of the oxidation–reduction potential (ORP), and the third group of factors impart catalytic (including biocatalytic) properties to the media. The products of the second and third groups can be obtained only under the unique conditions of electro-physico-chemical synthesis. They cause the modification of the activation energy barriers between the interacting atom–molecule components performing the activation of the processed medium with respect to the parameters of the catalytic activity. The main processes that occur in the electrolyzer can be represented in a simplified form as the oxidation of water on the anode: $2H_2O - 4e \longrightarrow 4H^+ + O_2$; the reduction of water on the cathode: $2H_2O + 2e^- \longrightarrow H_2 + 2OH^-$; the generation of gaseous chlorine on the anode: $2Cl^-\ 2e^- \longrightarrow Cl_2$; the generation of the highly active oxidants Cl_2O, ClO_2, ClO^-, $HClO$, Cl^*, O_2^*, O_3, HO_2, and OH^* in the anode chamber; and the generation of the highly active reducers OH^-, $H_3^-O_2^-$, H_2, HO_2^*, HO_2^-, and O_2^- in the cathode chamber.

The catholyte saturated with reducers gains high absorption–chemical activity [3]. The specimens of the anolyte and catholyte of aqueous media with different degrees of salt content are characterized by sharp shifts of the pH and ORP with respect to the initial values: in the anolyte, the pH is less and the ORP increases up to the extreme positive (oxidizing) values, while, in the catholyte, the pH is greater and the ORP decreases to the extreme negative (reducing) values.

With the electrolyte dissolved in water, there occurs ionization, the degree of which is determined by the electron-donor and electron-acceptor properties of the dissolved substance and the water. Ions are in the form of hydrates in the aqueous solution. The hydration energy is so great that there are formed aquacomplexes (in which water molecules serve as ligands). The formed complex cations and anions, in turn, hydrate with the generation of aquacomplexes [4], which behave as acids. Their acid properties are the greater expressed the higher the degree of the atom–complex-former oxidation. They dissociate and pass in hydrocomplexes (containing hydroxide ions (OH^-) as ligands), thus bypassing the intermediate form of aquahydrocomplexes. The equilibrium of their reciprocal transition is displaced to the aquacomplexes in an acidic medium and to the hydrocomplexes in an alkaline medium [5].

The water with a modified structure easily forms aquacomplexes enhancing the reactive and catalytic activity of the water–mineral medium. This is one of the most important manifestations of EPCA.

Aquacomplexes within the composition of strong solutions electrochemically processed have no substantial effect on the electron state by virtue of their slight stability. In diluted solutions, the concentration of stable ions is lower than in mineralized ones. Accordingly, the electron equilibrium in electrochemically processed diluted solutions is mainly determined by the aquacomplexes generated due to the hydration of highly active metastable charged particles, the activity of which comes to the fore.

Superactive particles appearing in the case of electrochemical synthesis by virtue of their metastability are subject to spontaneous decay in the course of the solution's relaxation. Correspondingly, the values of the ORP of the processed diluted water–mineral medium also relax, and the pH values are also subjected to relaxation.

The solutions are activated only in the period of the existence of abnormal properties, at the close of which this evidence disappears and the thermodynamic equilibrium of the pH and ORP typical for these solutions is established.

Unlike in known electrochemical processes, diluted water–salt solutions and fresh and brackish water, that is, liquids with low electric conduction, are used in the case of EPCA [6].

There exist design (and processing) methods allowing one to carry out unipolar (anode and/or cathode) EPCA of water with a low degree of mineralization (0.01–0.02 g/l). Under such conditions of treatment of fresh, ultrafresh, and even distilled water there are produced an anolyte and catholyte similar in physical and chemical properties (pH and ORP characteristics) to strong (inactivated) solutions of acids and alkalis. The anolyte and catholyte produced at a unipolar EPCA display properties and combinations of pH and ORP that cannot be modeled in common chemical solutions not subjected to electrochemical actions and are the most pronounced manifestation of the EPCA process [7].

The diminution or complete exclusion of the chemical reagent's expenditure, the decrease of the solution's contamination, the increase of the quality of the desired products, the reduction of the treatment's duration, the growth of the efficiency, and the simplification of various engineering processes is the aim of EPSA. That is to say, EPSA is used to create highly effective and nonpolluting processes of aqueous media treatment.

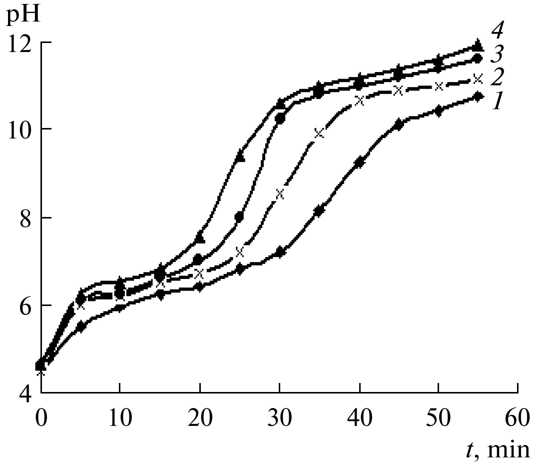

Fig. 1. Change of the pH of the residual whey (RW) at different current densities, mA/cm^2: (*1*) 12; (*2*) 14; (*3*) 18; (*4*) 20 (with a canvas membrane).

Milk whey (MW) is of particular interest for EPSA. Having a relatively high content of mineral substances (0.05 g/l), it possesses the necessary properties for the rapid and efficient accumulation of actively charged particles [8].

As is known, the changing of the main physical and chemical parameters (with the pH among them) and, above all, the relaxation of them as observed after the process of electrophysical processing points to the presence of EPSA phenomenon. Thus, it is interesting to study the changing of the active acidity and to elucidate the most important factors determining it at the MW treatment, as well as to establish the fact of its relaxation upon the completion of the process.

The experiments were carried out in a double-chamber flow electrolyzer. The whey supply into both chambers was fixed at 5 ml/min. The processing was performed at different current densities in the range from 12 to 20 mA/cm^2. The pH values were determined in the specimens of the processed whey (PW) obtained from the cathode chamber every 5 minutes. The protein–mineral concentrate (PMC) was separated in the field of the mass forces. The remaining PW, partly deproteinizated and demineralised, can be used for the further treatment.

In the course of the treatment of the whey and the examination of the pH at different current densities (12–20 mA/cm^2), there can be recognized three stages of its changes, the character of which persists for all the studied variations (Fig. 1). The slight change of the pH at the first stage of the treatment shows a high pois-

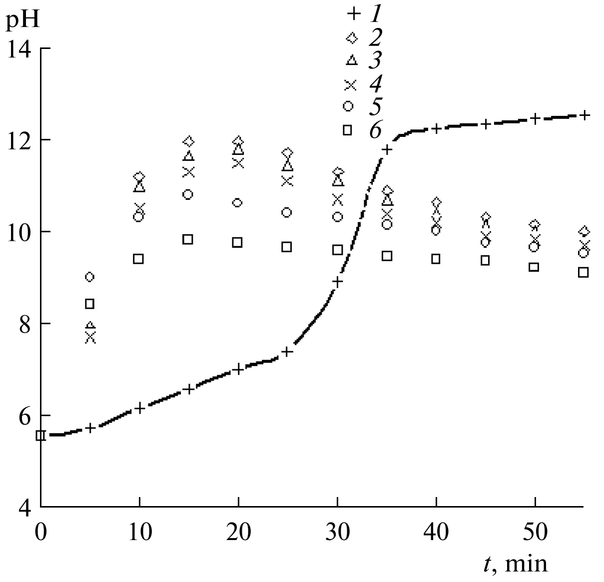

Fig. 2. Change of the pH in the residual whey during the treatment (t, min) and upon the completion of the process: (*1*) 5 min; and (*2*) 2, (*3*) 6, (*4*) 8, (*5*) 24, and (*6*) 30 hours of storage.

ing action of the system serving for the stability of the aquacomplexes.

In the second stage (20–40 min), there is observed a drastic growth of the pH caused chiefly by the migration of ions (positive ones to the cathode as well as negative ones to the anode) and metastable radicals generated due to the electrolysis of water. In this case, there evidently occurs the transition of aquacomplexes into hydrocomplexes, and the higher the current density, the quicker the transformation of the aquacomplexes into hydro ones. At the same time, there is recorded the augmentation of the recovery of the protein fractions and of the isomerization of lactose into lactulose. There is observed the direct dependence of the protein passage into the concentrate on the current density [9, 10]. Then, the growth of the active acidity slows down and the processes proceeding stop. By the time when the pH growth rate decreases, the main processes of the recovery of the protein fractions into the PMC and of the isomerization of the lactose into lactulose are finished. Thus, the processing of the MW is accomplished upon the pH reaching 11.0–11.5. Its further increase can cause the alkaline hydrolysis of proteins, as well as the generation of undesired colored coproducts of the lactose isomerization reaction with acid properties [11, 12]. Besides, the strong heating of the whey during the further treatment can cause the thermal denaturation of the protein fractions.

The change of the pH upon the completion of the treatment process was observed in RW specimens (after the separation of the PMC) produced (under a flow mode) with the use of 1% calcium chloride in RW as the anode liquid with a current density of 20 mA/cm^2. The flow mode in both chambers was 5 ml/min. The taken RW specimens were stored (at +10°C) for 30 hours. The active acidity was measured at certain intervals after the treatment (Fig. 2).

The greatest growth of the pH (up to strongly alkaline values) is observed after two hours in the specimens after 10–30 minutes of treatment. The largest change of the acidity is reached only 24 hours after the treatment in the specimens taken after 5 minutes. Probably, during this time, in the RW, there proceeds the transition of the aqua- into hydrocomplexes due to the presence of excess amounts of aquacomplexes of alkaline and alkaline-earth metals as well as of highly active reducers formed as a result of EPSA. The greatest changes happen in the specimens with initially acidic or neutral pH. On further keeping, their active acidity decreases. Evidently, there occurs the autodecomposition of the metastable substances arising from the electrochemical synthesis. In the whey taken after 30 minutes of treatment, the initial active acidity is in the range from 11.8 to 12.5, and the change of the pH has an originally opposite trend—slow diminution. It should be noted that the products of the oxidation of the lactose decomposition during the storage of RW with a strongly alkaline pH are favorable for acidifying the medium [13].

Obviously, during the treatment, the whey transits into the metastable state, whose tendency to equilibrium has been observed during the whole storage period. Such behavior of the whey under treatment appears to be caused by the presence of chemical and physical excited states for some time after the end of the electrochemical action.

Thanks to the performed experiments on the electric activation of milk whey and to the examination of the parameters of the active acidity immediately after the EPSA and in time, it can be concluded that, after the termination of the activating action of the electric current, the treated whey is in a metastable state that can be kept for some time; the RW in the metastable state is a nonequilibrium system and, with time, enters the period of the slow stage of electrochemical relaxation. In the reactions with the participation of an electroactivated substance, there occurs irreversible physical and chemical changes allowing one to gain the optimal release of the protein fractions into the PMC with the simultaneous isomerization of the lactose into lactulose.

REFERENCES

1. Bakhir, V.M., Zadorozhnii, Yu. G., Leonov, B.I., Panicheva, S.A., Prilutskii, V.I., and Sukhova, O.I., *Elektrokhimicheskaya aktivatsiya: istoriya, sostoyanie, perspektivy*, (Electrochemical Activation: History, State, Prospects), Moscow: VNIIIMT, 1999.
2. Bakhir, V.M., *Elektrokhimicheskaya aktivatsiya*, (Electrochemical Activation), Moscow: VNIIIMT, 1992.

3. Leonov, B.I., Prilutskii, V.I., and Bakhir, V.M., *Fiziko-khimicheskie aspekty biologicheskogo deistviya elektrokhimicheski aktivirovannoi vody*, (Physical and Chemical Aspects of Biological Action of Electrochemically Activated Water), Moscow: VNIIIMT, 1999.
4. Prilutskii, V.I. and Bakhir, V.M., *Elektrokhimicheski aktivirovannaya voda: anomal'nye svoistva, mekhanizm biologicheskogo deistviya*, (Electrochemically Activated Water: Abnormal Properties, Mechanism of Biological Action), Moscow: VNIIIMT, 1997.
5. Kukushkin, Yu.N., *Soedinenya vysshego poryadka*, (Highest Order Compounds), Leningrad: Chemistry, 1991.
6. Bakhir, V.M., Zadorozhnii, Yu.G., Leonov, B.I., Panicheva, S.A., and Plilutskii, V.I., *Elektrokhimicheskaya aktivatsiya: ochistka vody i poluchenie poleznykh rastvorov*, (Electrochemical Activation: Purification of Water and Production of Useful Solutions), Moscow: VNIIIMT, 2001.
7. Bakhir, V.M., Tsikoridze, N.G., Spektor, L.E., et al., Electrochemical Activation of Aqueous Solutions and its Technological Use in Food Industry, *Pishch. Prom-st.*, 1988, no. 3, pp. 81–84.
8. Khramtsov, A.G., *Molochnaya syvorotka*, (Milk Whey), Moscow: Agropromizdat, 1990.
9. Khramtsov, A.G., Ryabtseva, S.A., and Suyuncheva, B.O., Investigation of Process of Isomerization of Lactose into Lactulose in the Course of Electric Activation of Milk Whey, *Vestnik SevKavGTU, Ser. "Prodovolstvie"*, 2004, no. 7, pp. 20–27.
10. Sprinchan, E.G. and Bologa, M.K., Salt Composition of a Protein-Whey Concentrate Produced by Electric Contact Method, *Elektr. Obrab. Mater.*, 2006, no. 4, pp. 50–55.
11. Sprinchan, E.G., Optimization of Technological Modes of Production of a Protein-Mineral Concentrate from Secondary Milk Materials, *Elektr. Obrab. Mater.*, 2009, no. 1, pp. 73–80.
12. Khramtsov, A.G., Ryabtseva, S.A., and Zhurba, L.N., Regularities of the Process of Isomerization of Lactose into Lactulose in Cheese Whey, *Vestnik SevKavGTU, Ser. "Prodovolstvie"*, 2003, no. 6, pp. 16–20.
13. Bologa, M.K., Stepurina, T.G., Bologa, Al.M., Polikarpov, A.A., and Sprinchan, E.G., Optimization of Isomerization of Lactose into Lactulose by Electrophysical Method, *Elektr. Obrab. Mater.*, 2009, no. 5, pp. 80–85.

ISSN 1068-3755, Surface Engineering and Applied Electrochemistry, 2011, Vol. 47, No. 1, pp. 70–75. © Allerton Press, Inc., 2011.
Original Russian Text © S.N. Maslobrod, L.B. Korletyanu, A.I. Ganya, S.A. Burtseva, 2011, published in Elektronnaya Obrabotka Materialov, 2011, No. 1, pp. 81–86.

Influence of Millimetric Radiation on the Viability of Plants: 3. Changes in Seeds Metabolism after the Mediated Influence of a Factor

S. N. Maslobrod[a], **L. B. Korletyanu**[a], **A. I. Ganya**[a], **and S. A. Burtseva**[b]
[a] *Institute of Genetics and Plant Physiology, Academy of Sciences of Moldova,*
ul. Padurii 20, Chisinau, MD-2002 Republic of Moldova
e-mail: maslobrod37@mail.ru
[b] *Institute of Microbiology and Biotechnology, Academy of Sciences of Moldova,*
ul. Academiei 1, Chisinau, MD-2028 Republic of Moldova

Received June 16, 2010

Abstract—At the direct and mediated influence of millimetric radiation with a wavelength of 5.6 mm, the density of the stream of 6–10 mW/cm^2, and several minutes' exposition on seeds of tomato, tobacco, wheat, and maize, we observed the stimulation of the sprouting energy and the seeds germinating power and an increase in the number of right sprouts. The mediated influence is more effective than the direct one. The mediated influence consisted of the following: we processed with millimetric radiation (1) water in which afterwards the seeds were presoaked, and (2) microorganisms from which were exuded exometabolites in order to soak the seeds in their solutions. There was found out the effect of the water "memory." This effect is better expressed with tap water in comparison with distilled water and is better maintained at a low temperature than at room temperature. There has been drawn a conclusion that water is the receiver, inductor, and carrier of information about the influence of a physical factor.

DOI: 10.3103/S1068375511010145

From previous papers [1, 2], it has became clear that dry and presoaked seeds show a practically similar reaction to millimetric radiation (MMR). At the same time, the metabolism stimulation was more distinct in the irradiated presoaked seeds rather than in the irradiated dry seeds. Apparently, the difference in the results can be explained by the fact that the dry seeds contain only bound water, while the presoaked ones also contain absorbed free water, which becomes a primary receptor during the MMR's influence.

To develop this point of view, which is known with respect to animals [3], it was decided to test the direct influence that MMR processed water has on seeds. Such water is an independent factor of the influence on seeds, having, however, the characteristics of both pure MMR (a field generator) and of a substrate complementary to the water of the seeds. Thus, it is possible to obtain more precise data about the water as the receiver, inductor, and carrier of information about the MMR contained in seeds. In this connection, the research of the "memory" effect in the water treated with MMR [3, 4] is worth paying attention to provided that the water's evaluation is carried out according to the physiological parameters of the seeds [5]. An interesting aspect of the mediated MMR influence on seeds was revealed in the experiments where MMR was first released on microorganisms [6], from which exometabolites were exuded. Subsequently, exometabolite solutions were prepared and used to influence the seeds [6, 7]. Technically, the strain of a microorganism grown on an agar is per se a complexly organized water solution, where MMR also first affects the water.

1. INFLUENCE THROUGH WATER

1.1. Comparison of the Effects on the Water Conducted for Dry and Presoaked Seeds

A comparison of the germinating power of tomato seeds with MMR-processed distilled water (DW) was conducted for dry seeds and seeds presoaked for three hours. The seeds germinating power grew considerably in comparison with the reference (Fig. 1).

It turned out that the most stimulating were the water exposures lasting for 2, 4, and 10 minutes and the seeds exposures lasting two and four minutes. The stimulation resulting from the water exposures was as significant as that of the seeds.

In another test, we used two exposures—8 and 30 minutes: (1) to apply MMR to seeds and distilled water and (2) when presoaking the seeds in the irradiated water. The latter acted as an imitator of the MMR as a factor of influence on the seeds. The dry and imbibed seeds were used within 12 hours. Thus, we took into account the period of the most active absorption and the period when the absorption had already

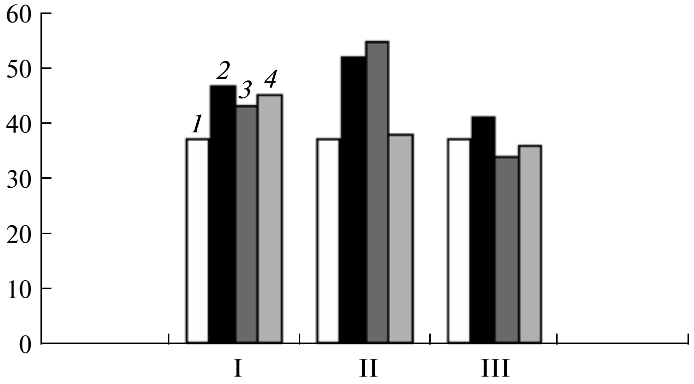

Fig. 1. Germinating power (%) of the tomato seeds (Muromskii variety) on the sixth day of the sprouting depending on how the MMR was delivered to the seeds (directly or through water). I—water, II—dry seeds, and III—seeds presoaked for three hours; 2, 4, and 10 minutes—the time of the MMR exposures.

stopped. The sprouting energy of the seeds (on the second day of the presoaking) and the sprouts bioisomery (left–right sprouts) formed the assessment criterion for the factor's influence on the object [1].

As can be seen from Table 1, the direct MMR treatment of the dry seeds produces no bioeffect on the sprouting energy of the seeds and on the number of right (D) sprouts, which is a somewhat surprising result, because, in other tests, such exposures led to stimulation. In our case, the influence of the irradiated water on the objects' parameters seems even more significant. The dry seeds presoaked in the MMR processed water showed increased sprouting energy after the two exposures.

As for the imbibed seeds, the sprouting energy and the number of D sprouts rose both for the direct MMR delivery on the seeds (30-minute exposure) and for the mediated influence through the water (8- and 30-minute exposures).

Therefore, (1) the mediated MMR influence on the seeds carried out through water is more effective than the direct influence, and (2) the imbibed seeds are more responsive to the direct and mediated influence of MMR than the dry seeds. It seems that the results obtained prove the key role of water in the induction of the physiological and morphological modifications of objects when this process is stimulated using MMR. It is well-known that distilled water, when influenced by MMR, becomes electroconductive as well as less viscous [4], which facilitates its faster penetration into dry seeds, thus creating the continuity of the aqueous medium both outside and inside the seeds. In the case with imbibed seeds, the MMR's influence immediately affects the water inside the

Table 1. Sprouting energy of the seeds and the number of right (D) sprouts of wheat (H335 variety) as influenced by the MMR (direct influence) and the water processed using MMR (mediated influence), %

Method of MMR influence on the seeds	Exposures	Dry seeds		Imbibed seeds	
		Sprouting energy	Number of right sprouts	Spouting energy	Number of right spouts
Direct	8	33.3 ± 2.08	46.8 ± 4.62	64.0 ± 4.08	40.1 ± 1.18
	30	36.0 ± 6.11	43.0 ± 3.09	76.8 ± 4.06*	45.9 ± 1.41**
Mediated	8	53.3 ± 6.74*	39.8 ± 5.71	72.7 ± 7.68	52.6 ± 0.28***
	30	62.0 ± 1.15***	49.2 ± 8.90	76.0 ± 2.00*	51.1 ± 2.81***
Reference		32.0 ± 2.31	50.2 ± 2.29	56.0 ± 2.00*	51.1 ± 1.89

Note: *, **, and ***—the results different from the reference values are significant at p-0.1, 0.01, and 0.001, respectively.

Table 2

Storage times, h	+25°C	+5°C
Reference	27	17
0	42*	–
3	33*	37*
6	19	26*
24	26	23*

* —the differences are significant.

seeds. Water is a generator of a weak field with a number of certain frequencies, including the range of extremely high frequencies (EHF) [4, 8, 9]. The weak field of the irradiated water is more complementary to the weak field of the seeds than the MMR. For this reason, the field of the irradiated water has a greater influence on the seeds than the MMR.

1.2. Water's "Memory" of the MMR's Influence

1.2.1. Influence of low temperatures on the duration of the "memory." Tomato seeds were presoaked in distilled water processed with MMR. This water was previously stored for 0, 3, 6, and 24 hours at temperatures of +25°C and +5°C . We used two-minute radiation exposures, which is enough to stimulate tomato seeds. For those stored at +25°C , the water "memory" and its stimulating effect on the seeds germinating power were active for up to three hours, while those stored at +5SurfEng1101014Maslobrod retained the water's "memory" during all the storage times, while decreasing gradually (Table 2). The effect can be attributed to the MMR-induced structural changes in the water [4].

The germinating power of the tomato seeds (Santa Maria variety) on the sixth day of the sprouting was influenced by the distilled water processed with MMR and stored for varying storage times at varying temperatures.

1.2.2. Influence of the water's type on the duration of the "memory" of the water treated with MMR and stored at low temperatures. While treating tap water with MMR, we discovered an unexpected effect of a gradual increase of the water's "memory" during long-term storage. The seeds germinating power grew considerably when they were influenced by irradiated water after it had been stored for three days, while the irradiated distilled water had no "memory" effect (Table 3). Apparently, during the long-term and low-temperature storage of the tap water, some further internal irradiation occurs in the test portion of the water with the stable MMR-induced structural changes in the water reaching a new level of information about the influence [4].

Thus, MMR processed water stimulates the germinating power of seeds (using the example of tomato seeds); the water receives information about the MMR's influence, and the "memory's" duration increases when the seeds are stored at low temperatures. The long-term and low-temperature storage of tap water results in longer water "memory" as compared to that of distilled water.

2. INFLUENCE THROUGH EXOMETABOLITES EXUDED FROM MMR TREATED STREPTOMYCES

The physiological state of the culture liquor (CL) yielded by MMR treated microorganisms was assessed according to the germinating power of seeds presoaked in this liquor. We used two *Streptomyces* strains: *Streptomyces canosus* CNMN-71 from a strain collection and *Streptomyces massasporeus* CNMN-36 taken from a Moldovian soil. Having the ability to synthesize a

Table 3. Germinating power of the tomato seeds (Nota variety) on the seventh day of the sprouting; the seeds were influenced by tap and distilled water (TW, DW) treated with MMR and stored for 24, 48, and 72 hours at a temperature of +5°C

Water storage times, h	Tap water		Distilled water	
	Test	Reference	Test	Reference
24	74.0 ± 3.6	70.7 ± 1.4	74.7 ± 2.9	71.3 ± 3.7
48	82.7 ± 3.5	76.0 ± 2.3*	76.0 ± 3.1	75.3 ± 2.7
72	81.3 ± 0.7	68.7 ± 2.4***	74.0 ± 5.3	76.0 ± 0.7

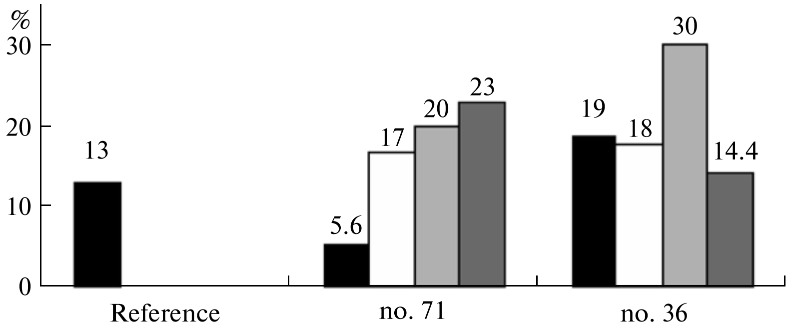

Fig. 2. The germinating power of the tobacco seeds (Barley variety) influenced by the exometabolites exuded from the MMR-treated Streptomyces. nos. 36 and 71—the Streptomyces strains; the test bars on the bar chart correspond to the MMR exposures lasting for zero, one, three, and five minutes, respectively.

number of bioactive substances, including phytohormone substances, they are different from other collection strains [7]. Following the irradiation, the culture was transferred into flasks containing a liquid medium. The culturing was carried out during five days using a vibration table. After that, the biomass was separated from the CL by centrifugation. The seeds were presoaked in the CL for 24 hours with a concentration of 1 : 100, which is considered sufficient to stimulate the seeds [6, 7].

2.1. Influence of Radiation Exposures

The germinating power of tobacco seeds presoaked in solutions of exometabolites exuded from *Streptomyces* and not treated with MMR was lower for no. 71 and higher for no. 36 as compared to a reference (soaking in distilled water). The MMR treatment of *Streptomyces* resulted in their solution having a stimulating effect on the germinating power of tobacco seeds in all the types of treatments (Fig. 2). The best results were obtained after a five-minute exposure for form no. 71 (23%) and a three-minute exposure for form no. 36 (30%).

To conclude, the *Streptomyces* treatment with MMR leads to a significant growth of the physiological activity of their exometabolites as evaluated by the changes in the seeds' germinating power.

2.2. Influence of the Density of the Stream

The experiments demonstrated a considerable growth of the biomass of the *S.c.* CNMN-71 strains as compared to the reference for the capacity density (CD) of 6.22 mW/cm^2 and a decrease in the biomass with the CD of 10.4 mW/cm^2 (Fig. 3). According to Fig. 3, the "biomass–capacity density" curve follows a nonlinear pattern.

Next, we used solutions of exometabolites (EM) exuded from MMR processed *Streptomyces* with a CD of 4.7 and 10.4 mW/cm^2 in order to evaluate the physiological activity of the *Streptomyces* exometabolites in a sprouting energy test; the test was performed for the seeds of haploid maize form 245 × rf. In comparison with the reference, we observed much longer coleoptiles for the five-day sprouts and the considerable growth of the main root in the variant with the CD of 10.4 mW/cm^2 (Table 4). No differences were found in the number of lateral roots or the dry weight of the coleoptiles and roots. It is interesting though that the variant that turned out to be stimulating for the microorganisms irradiation (according to the biomass yield) was also stimulating for the seeds presoaked in the solutions of *Streptomyces*' exometabolites of the same variant.

Supposedly, treating *Streptomyces* with MMR with a CD of 10.4 mW/cm^2 facilitates the increased synthesis of phytohormone substances (auxins, gibberellins, etc.) by this strain, as well as the synthesis of proteinogenic and essential amino acids, as established earlier for the stimulating variant of the radiation treatment of this strain with gamma and UV rays [7].

Later, a check was conducted to test whether these exometabolites retained their biological effect after long-term storage (six months at a temperature of +5°C). The assessment criterion was the change in the length of the coleoptiles and roots of maize sprouts (Debut hybrid) as a result of the processing with exometabolites. At the preliminary stage, the exome-

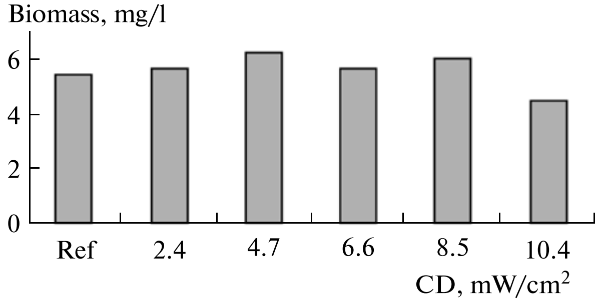

Fig. 3. The Streptomyces strains' biomass after the treatment with MMR of various densities.

Table 4. Physiological parameters of the haploid maize sprouts after the seeds had been treated with exometabolites (EM) of Streptomyces (Streptomyces canosus CNMN-71) that had been influenced by MMR of various density of capacity

Variant no.	Variant name	Length, mm		No. of lateral roots	Dry weight, mg	
		coleoptiles	main root		coleoptiles	rootage
1	H_2O (ref.)	16.0	56.3	2.09	433.0	538.0
2	EM (ref.)	15.9	61.6	2.34	406.0	523.0
3	4.7 mW/cm^2	21.8*	59.2	1.96	400.0	521.0
4	10.4 mW/cm^2	17.8	59.2*	2.31	431.0	539.0

* —the differences are significant.

tabolites were kept in their native state (variant *1*) and pasteurized (variant *2*). We found out that after long-term storage, the variant *1* curve of the "sprout growth–density of the radiation applied to the *Streptomyces*" remained nonlinear in nature, and this was typical for the initial state of the exometabolites (before storage). The coleoptile length stimulation was seen at 8.5 mW/cm^2, and clear signs of inhibited root length were noted at 4.7 and 10.4 mW/cm^2. At the same time, the dosage curve for variant *2* (pasteurized exometabolites) was not nonlinear; inhibition was observed, which increased along with the rising capacity density of the radiation applied to the *Streptomyces* (Fig. 4).

CONCLUSIONS

For wheat seeds, the mediated MMR's influence coming through water was more effective than the direct influence.

Imbibed wheat seeds are more responsive to direct and mediated MMR's influence than dry seeds.

MMR treated water stimulates tomato seeds' germinating power. These effects are comparable with the results of MMR's influence on dry and presoaked seeds.

Water can develop a "memory" for the MMR's influence (evaluated according to the germinating power of tomato seeds presoaked in this water). The "memory's" duration increases if the seeds are stored at low temperatures. During the long-term and low-temperature storage, tap water's "memory" of the influence lasts longer than in the case with distilled water.

Microorganisms of the *Streptomyces* genus (*Streptomyces canosus* CNMN (no. 71 and 36)) influenced by MMR undergo a change in the physiological activity of their exometabolites' solutions (evaluated according to the germinating power of seeds presoaked in these solutions). The effect depends on the exposures and the density of the radiation capacity. Thus, the germinating power of the tobacco seeds presoaked in a solution of exometabolites of strain no. 71 became 1.8 times higher during a five-minute exposure, and it grew by 2.3 times more during a three-minute expo-

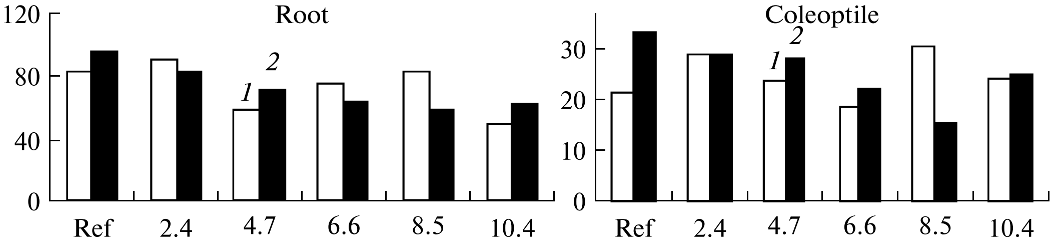

Fig. 4. Length of the coleoptiles and roots of the four-day maize sprouts (Debut hybrid) with the seeds exposed to the mediated MMR influence conducted through the Streptomyces exometabolites. The seeds were presoaked in a solution of the exometabolites exuded from the Streptomyces for 24 h. The Streptomyces were pretreated with MMR with a wavelength of 5.6 mm for five minutes with the following densities: 2.4, 4.7, 6.6, 8.5, and 10.4 mW/cm^2. (*1*, *2*) native and pasteurized exometabolites, respectively.

sure of strain no. 36. When treating stain no.71 with MMR of various densities followed by five-minute exposures, we observed stimulation in the variants with 4.7 and 8.5 mW/cm^2; the stimulation was reflected in the growth of both the strain's biomass and the germinating power of the maize seeds presoaked in the solution of the exometabolites exuded from this strain.

REFERENCES

1. Maslobrod, S.N., Korletyanu, L.B., and Ganya, A.I., Influence of Millimetric Radiation on the Viability of Plants. 1. Changing the Metabolism of Seeds at the Factors Influence on Dry Seeds, *Elektr. Obrab. Mater.*, 2010, vol. 46, no. 5, pp. 93–105.
2. Maslobrod, S.N., Korletyanu, L.B., and Ganya, A.I., Influence of Millimetric Radiation on the Viability of Plants. 2. Changing the Metabolism of Seeds at the Factors Influence on Presoaked Seeds, *Elektr. Obrab. Mater.*, 2010, vol. 46, no. 6, pp. 88–90.
3. Betskii, O.V., Lebedeva, N.N., and Kotrovskaya, T.I., Peculiar Features of Water in Weak Electromagnetic Fields, *Biomed. Tekhnol. Radioelektron.*, 2003, no. 1, pp. 37–41.
4. Zenin, S.V., Development of the Informational Concepts of the Structural State of Water, *ECWATECH-2006*, Moscow, 2006, Part 2, pp. 1052–1054.
5. Maslobrod, S.N., Korletyanu, L.B., Ganya, A.I., and Gaidei, N.A., Water "Memory" for Millimetric Radiation Influence Traced in Seeds Germinating Power, *ECWATECH-2006*, Moscow, 2006, Part 2, pp. 1049–1050.
6. Maslobrod, S.N., Burtseva, S.A., Karanfil, V.G., et al., Comparative Evaluation of the Influence of a Thought Field, Low Intensity Electromagnetic Field and Chemical Biogenic Regulators on Primary Metabolic Processes in Plants, *Mater. Pervoi Mezhdunarodnoi nauchno-praktich. konferentsii "Netraditsionnye metody v meditsine, biologii i rastenievodstve. Eniologiya. Ekologiya i zdorov'e"*, (Proc. First Int. Theor.–Pract. Conf. "Non-conventional Methods in Medicine, Biology and Plant Cultivation. Eniol. Ecol. and Health"), Chisinau, 2005, pp. 313–322.
7. Burtseva S.A., Apostolyuk N.V., Ryabchuk N.S., Rastimeshina I.O. Fiziologie si bioshimie vegetale, Chisinau, 201, 114–117.
8. Savel'ev, S.V. and Kuznetsov, I.V., Line of a Long-range Intercellular Contact of the Interface of Intercellular Information Interaction, *Millimetrovye Volny Biol. Med.*, 2005, vol. 3, no. 39, pp. 36–41.
9. Slesarev, V.I. and Shabrov, A.V., Long–distance Interaction of Water–Containing Systems, *ECWATECH-2006*, Moscow, 2006, Part 2, p. 1030.

ISSN 1068-3755, Surface Engineering and Applied Electrochemistry, 2011, Vol. 47, No. 1, pp. 76–83. © Allerton Press, Inc., 2011.
Original Russian Text © M.K. Kerimov, M.A. Kurbanov, F.N. Tatardar, A.A. Mekhtili, I.S. Sultankhamedova, G.G. Aliev, F.F. Yakh'yaev, U.V. Yusifova, 2011, published in Elektronnaya Obrabotka Materialov, 2011, No. 1, pp. 87–95.

EQUIPMENT
AND INSTALLATIONS

A New Technology of the Immobilization of Nanoparticles in Polymers and the Development of Piezoelectrics Based on a Hybrid Matrix of Nano- and Micropiezoceramic Composites

M. K. Kerimov, M. A. Kurbanov, F. N. Tatardar, A. A. Mekhtili, I. S. Sultankhamedova, G. G. Aliev, F. F. Yakh'yaev, and U. V. Yusifova

Institute of Physics, National Academy of Sciences of Azerbaijan, pr. G. Dzhavida 33, Baku, Az-1143 Azerbaijan
e-mail: mKurbanov@physics.ab.az

Received August 6, 2010

Abstract—Given the rapidly developing areas of physical and chemical sciences, the physics and chemistry of a new class of piezoelectric materials on the basis of a hybrid matrix of nano- and mikropyezoelektric composites has arisen. For this goal, we developed the following technologies of hybrid composites and a method of controlling the nanostructure of the polymer phase: (1) the immobilization of nano-sized dielectric particles in a polymer solution using the energy of the plasma channels of powerful electric discharges in air bounded by dielectrics, (2) the creation of active centers in the composites of clusterization by crystallizing them in terms of the plasma electric discharge in an electronegative gas environment, and (3) the control of the polymer phase of the composite by the spectrum analysis of the thermodepolarized current. A technology of obtaining a matrix of hybrid piezoelectric-based nanocomposites and micropezoelectrics is proposed. We propose possible mechanisms for the effects of the immobilization and formation of active origins of clusterization centers of nanoparticles in the polymer phase of the composite.

DOI: 10.3103/S1068375511010121

INTRODUCTION

It is known that one of the main problems of the preparation of nanocomposites is the prevention of the mobilization of nanoparticles and their homogeneous distribution in the bulk polymer phase [1–3]. There are physical and chemical methods for the immobilization of nanoparticles in the solution of polymers during the preparation of polymer nanocomposites [1]. It should be noted that the use of the mentioned methods for the prevention of the mobilization of nanoparticles considerably depends on the properties of the polymers and nanoparticles. Numerous experimental data demonstrate that the active centers of the stabilization present in a polymer can be the areas of nucleation (regions of clusterization) and mobilization of nanoparticles. However, the development of the large clusterization of nanoparticles cannot be accepted, because, at the cluster sizes of more than 300 nm, the composite obtained is transformed into a macrocomposite; that is, it loses the nanoproperties [1].

If we proceed from the fundamental concept, which assumes that the physicomechanical and, consequently, electromechanical properties of the matrix composites depend on the mobility of the macromolecules of the polymer phase and the interface interaction, then the piezoelectric and electromechanical characteristics of the composites can be intentionally regulated and be effective during the creation of energy-intensive sources of energy and acoustic waves by the variation of the factors mentioned. The advances in nanotechnology make it possible to solve this problem by combining matrix polymer composites with nanosized dielectric and microsized piezoceramic particles. For the first time, we suggest a technology of the creation of a novel class of piezoelectric composites combining nano- and microcomposites with a single polymer matrix (a hybrid system). The principle of the development of hybrid nano- and microcomposites is based on the difference in the temperatures of the dissolution and fusion of the regions of the polymer phase of the composite, the structure of which is formed under the effect of and not under the effect of the surface of the micropiezoelectric particles. It is known that, in matrix piezocomposites used as piezoelectric transducers, the source of the mechanical and electrical energy loss is mainly the near-electrode (or near-surface) area of the composite element. The substantial decrease in the mechanical compliance (S_{11}^E) and the mechanical (Q_M^{-1}) and electrical ($\tan\delta$) losses and the increase in Young's modulus (Y_{11}^E) of the near-electrode area of the composite by the application of nanotechnologies represent topical problems. The possibility of "hybridization" of composites based on various polymer matrix and nanoparticle composites with the aim to obtain materials with novel properties is a topical problem, the emerging of which is directly related to the achievements of nanotechnology [4, 5].

There are the following purposes of this work:

(1) to develop a more effective technology of the immobilization of nanoparticles in a polymer medium of nanocomposites by the use of the plasma of an electric discharge;

(2) to reveal the physicotechnological features of the creation of a novel class of high-performance piezoelectric materials based on a hybrid of a matrix nano- and micropiezoelectric composites.

In order to accomplish this, the following problems were solved:

—the creation of active centers of localization of nanoparticles in the polymer phase of a composite by the crystallization of a composite under the conditions of the plasma of an electrical discharge, that is, the creation of the seeds for subfine clusters;

—the realization of the technology of the immobilization of nanoparticles in polymer solutions by local electrical discharges of various energies;

—the development of the technology of the preparation of piezoelectrics based on a hybrid matrix of nano- and micropiezoelectric composites;

—the design of a method of control of the immobilization of nanoparticles in a polymer matrix.

ROUTINE OF THE EXPERIMENT

Matrix composites (type 0–3) based on piezoceramics of the family of zirconate–titanate–lead of the PKR-3M type (rhombohedral, PZT-5A) thermoplastic polymer of polyvinylidenefluoride (PVDF) of the production of OAO Plastpolimer (Saint Petersburg) and $BaTiO_3$ nanoparticles with a diameter of 50 nm were considered. The choice of the carbochain polymer PVDF was determined by the fact that it is characterized by high reproduction due to its composition, structure, and physicochemical properties. The choice of the piezoceramic PKR-3M (PZT-5A) is related to the fact that it has a sufficiently high piezomodulus ($d_{33} = 110 \times 10^{-12}$ C/N), Young's modulus ($Y_{11}^E = 0.57 \times 10^{11}$ Pa), and dielectric permittivity ($\varepsilon_{33}/\varepsilon_0 = 450$). The plasma crystallization of the composite provides for the formation of active centers of physical and chemical natures in the polymer phase [6–8]. The duration of the effect of the discharge changed in the range from 5 to 30 minutes depending on the properties and the volume content of the polymer and the piezoceramic in the composite, the thickness of the gas gap where the microdischarges were initiated, and the amplitude of the voltage applied to the dielectric–gas–composite system [7–10].

The selected $BaTiO_3$ nanoparticles have substantial surface activity and sufficiently high chemical activity. This is determined by the large fraction of the surface of the atoms relative to the total amount in the bulk particles. The high surface energy of the nanoobjects gives rise to the formation of unusual surface characteristics and reactions. Therefore, one of the problems of the development of polymer nanocomposites is the effective dispersion and stabilization of the nanoparticles and prevention of their mobilization in the polymer matrix of the composite. The problems indicated were solved by the technology of the modification of the polymer phase suggested by us, which involves the crystallization starting from the fusion temperature under the conditions of the plasma of an electrical discharge in an electronegative gas and electroplasmic crystallization [7, 8].

The stabilizing effect is determined by the formation of active centers of oxidation and submicrosized ranges of cross linking of macromolecules under the effect of the plasma of an electrical discharge in the polymer phase of the composite for the localization of the dielectric nanoparticles. This results in the formation of a robust structure from the $BaTiO_3$ particles and oxidized and crosslinked local areas of the polymer macromolecules. The dielectric nanoparticles occupy the active areas in the polymer matrix. It should be noted that the enhancement of polymers with disperse nanofillers is a fundamental problem for the creation of polymer materials for various applications [1–5]. It is considered that the two main factors of the enhancement are the particle sizes or the specific surface of the filler and the polymer–filler bond [1, 2]. Notably, among the broad class of polymer composites, polymer nanocomposites (NC) represent a novel type of filled materials in which at least one of the sizes of bond disperse phase (length, width, and height) does not exceed 100 nm [1, 4]. Due to the ultradispersity of inorganic dispersants (fillers), such systems may have unusual electric [1, 2], mechanical [1, 5], and thermophysical [1] properties not represented by microcomposites. Composites of the indicated type were obtained from a homogeneous powder mixture of the components. The temperature and pressure of the pressing of the composites were set in the range from 437 to 463 K and 30 MPa, respectively. The thickness of the piezocomposite was set at 250×10^{-6} m, and the diameter of piezoparticles was $(160–200) \times 10^{-6}$ m. The piezoelectric modulus of the composites was determined in the quasi-static mode with an accuracy of 10%.

Notably, the process of hot pressing results in the additional purification of the bonded composite from the solvent molecules and the abandonment of the microphase separation of the nano- and microcomposites. Thus, a quasi-monolithic structure is formed on the basis of which piezoelectric transducers of various uses with high electromechanical and piezoelectric characteristics are obtained. The volume content of the nanophase was varied in the range from 0.1 to 3%.

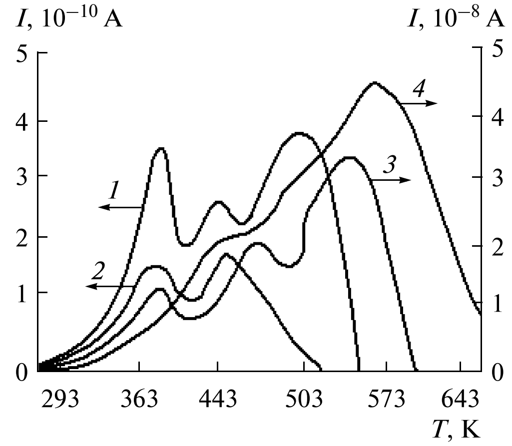

Fig. 1. Spectra of the thermostimulated depolarization current PVDF and the composites on its basis. (*1*) PVDF; (*2*) PVDF+50 vol % PZT-5A; (*3*) PVDF+1 vol % $BaTiO_3$ + 49.9 vol % PZT-5A, $W = 26.3 \times 10^{-6}$ J; and (*4*) PVDF + 1 vol % $BaTiO_3$ + 49 vol % PZT-5A, $W = 335 \times 10^{-6}$ J. The conditions of the polarization: the electric field of the polarization $E_p = 3 \times 10^6$ V/m, the temperature is T_p = 413 K, and the time of the polarization is t_p = 0.5 h.

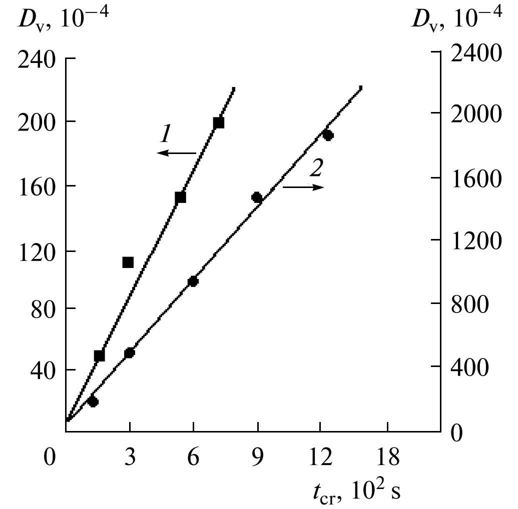

Fig. 2. Change in the optical density of the bands evolved in the IR spectrum of the polymer phase of the composite PVDF+50 vol % PZT-5A during the electrothermodischarges of the crystallization. The cooling rate is 2K/min, U_p = 11.8 kV, $W = 1.4 \times 10^{-6}$ J. (*1*) ν = 3380 (OH) cm^{-1}, (*2*) ν = 1735 (C–O) cm^{-1}, and (*3*) ν = 1280 (C–O–C) cm^{-1}.

RESULTS AND DISCUSSION

Let us primarily consider the technology of the creation of active centers of clusterization of nanoparticles in the polymer phase of the composites by the performance of their crystallization under the effect of the plasma of an electrical discharge. The crystallization of the composites under the plasma of an electric discharge involves heating of the material up to the melting point and keeping it at that temperature for 5–30 min (and, not relieving the effect of the discharge) with further cooling down to the temperature of the crystallization of the polymer phase with a rate from 0.5 to 4 K/min with the aim of the directed changing of the chemical (oxidation) and physical (supramolecular) structures of the polymer matrix. The melting point of the composite was determined by the temperature of the third peak of the spectrum of the thermodepolarization current (Fig. 1, curve *2*). The duration of the crystallization t_{kr} was limited to the saturation of the optical density of the oxygen-containing groups (for example, OH and C=O), which evolved in the IR spectrum of the polymer–piezoceramic composite as a result of the action of the electrical discharge, and changed in the range from 5 to 30 minutes.

The experimental results demonstrate that, in the IR-spectrum of the polymer matrix (PVDF) of the composite, after its crystallization under the effect of the plasma of the electrical discharge, new highly polar oxygen-containing groups, C=O and OH, are formed. In Fig. 2, the change in the optical density *D* of the IR spectrum is given for the mentioned groups in the polymer matrix that crystallized under the conditions of the plasma of an electrical discharge. It is seen that the change in the optical density *D* within the time of the crystallization up to 15 min has a linear character. The centers of oxidation can be the seeds for the clusterization of nanoparticles. The next stage of the immobilization is the dissolution of the polymer in toluene. After that, the $BaTiO_3$ nanoparticles (≤50 nm) are introduced into the solution in the range from 0.5 to 3.0 vol %.

Let us consider the processes providing the immobilization of the nanoparticles in the polymer solution. The immobilization of the nanoparticles in the dissolved polymer phase of the composite was performed in the following way:

—the introduction of dielectric nanoparticles $BaTiO_3$ into the solvent (toluene);

—the dissolution of the polymer used in toluene at the temperature determined from the spectrum of the thermostimulated depolarization current (Fig. 1, the first maximum, curve *2*) of the composite;

—the preparation of a mixture of the toluene–polymer and toluene–nanoparticle solutions;

—the conduction of the chemical precipitation of the polymer nanostructured by the $BaTiO_3$ particles on the piezocomposite under the conditions of the plasma of an electrical discharge.

Now, let us consider the process of the immobilization of $BaTiO_3$ nanoparticles in a polymer under chemical precipitation. In Fig. 3, a cell is represented where the immobilization of $BaTiO_3$ dielectric particles in the polymer solution is performed during the $BaTiO_3$ chemical precipitation. The dielectric structure composed of the metal–dielectric–gas medium–polymer solution–dielectric and metallic electrode is under the effect of a sinusoidal voltage with an ampli-

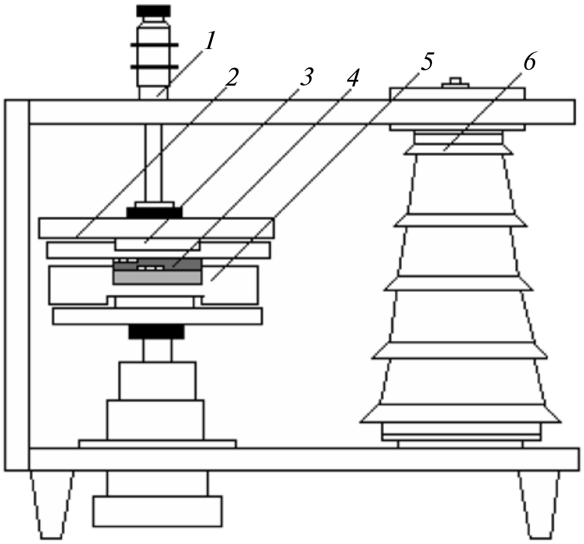

Fig. 3. Experimental cell of the conduction of the immobilization of the dielectric particles of $BaTiO_3$ in the polymer solution under the effect of powerful channels of electrical discharge: (*1*) microscrew, (*2*) dielectric leaf, (*3*) electrode, (*4*) gas and liquid medium, (*5*) dielectric cup, and (*6*) insulator.

tude of 35×10^3 V and a frequency of 50 Hz. At a definite value of the voltage applied to the system mentioned, the electrical discharge is formed in the gas phase between the upper dielectric barrier and the solution of the polymer with nanoparticles.

The structure of the discharges in the gas phase between the dielectric and the polymer solution with $BaTiO_3$ nanoparticles was recorded by an electron–optical transducer (Fig. 4). As is seen, the discharge forms at various sites of the dielectric surface and the polymer solution. The solution is under the influence of intensive impacts of powerful microdischarges. The energetical parameters of the discharges can be controlled in broad ranges by the variation of the distance between the dielectric attached to the high-voltage electrode and the surface of the solution or the thickness of the air gap between the dielectric anode and the surface of the polymer solution. By trying the modes of the processing and the energetical parameters of the discharge, the formation of large clusters can be prevented. Under the effect of intensive impacts of the plasma channels of the discharge, the partitioning of the large clusters into subfine ones takes place and the conditions for their capture by the nucleation centers are provided, and the conditions for the homogeneous distribution of the nanosized particles by the bulk polymer solution are created. The energy W and the transferred charge Q of the microdischarge in the gas phase (gap) of the dielectric–air medium–polymer solution–dielectric system can be calculated in the following way:

$$W = \frac{1}{2}\frac{\Delta S}{S}(C_{\text{dielectric}} + C_{\text{gas}})(U^2_{\text{initial}} - U^2_{\text{extinction}}), \quad (1)$$

$$Q = \frac{\Delta S}{S}(C_{\text{dielectric}} + C_{\text{gas}})(U_{\text{initial}} - U_{\text{extinction}}), \quad (2)$$

if we experimentally determine the following parameters included in the expressions indicated: U_{initial}, $U_{\text{extinction}}$, and ΔS [11, 12]. Here, C_d and C_g are the capacities of system dielectric and gas medium, respectively; U_{initial} and $U_{\text{extinction}}$ are the initial and extinction microdischarge voltages, respectively; and ΔS is the area of the surface of the composite (dielectric) discharged by the microdischarge.

We demonstrated that the energy of the microdischarge can be determined by the synchronous recording of the optical image of the microdischarge's development (Fig. 4) and microdischarge corresponding voltage or current impulse [11 12]. After the determination of U_{initial} and $U_{\text{extinction}}$, as well as the value ΔS (by EO converter images), the values of W and the charge Q were calculated for various values of the thickness of the gas phase of the discharge cell at a constant high sinusoidal voltage applied to the cell (Table 1).

It was experimentally determined that the immobilization of the $BaTiO_3$ nanoparticles in the polymer solution substantially depends on the structure (Fig. 4) and the energy (Table 1) of the individual microdischarges. Under the effect of microdischarges with an energy of $W = 8.2 \times 10^{-6}$ J propagating in the air medium with a thickness of 4 mm between the dielectric and the surface of the polymer solution (Fig. 4, a),

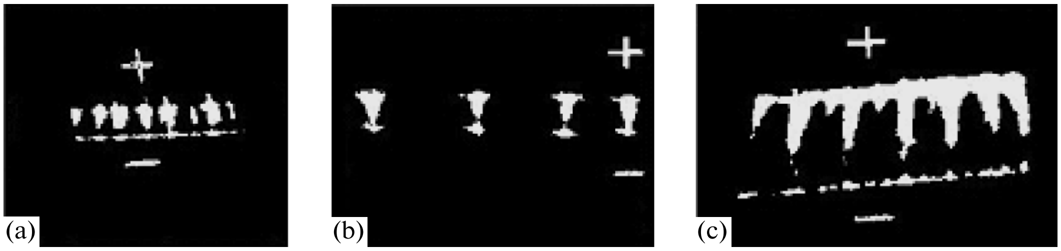

Fig. 4. Optical image of the development of microdischarges in the air medium between the dielectric (polytetrafluoroethylene with a thickness of $d = 2$ mm) and the surface of the polymer solution. (a) $d = 4$ mm, (b) $d = 6$ mm, and (c) $d = 10$ mm; $U = 35 \times 10^3$ V.

Table 1. Parameters of the discharge depending on the thickness d of the gas phase between the insulators

d, 10^{-3} m	3	4	5	6	7	8	9	10
Q, 10^{-9} Coulomb	0.46	0.93	1.48	2.11	3.15	5.0	8.4	16.4
W, 10^{-6} J	3.2	8.18	15.7	26.3	47.3	89.4	166.2	335.2

the immobilization of the nanoparticles almost does not take place. The first and second maximum are recorded clearly, as in the spectrum of the initial PVDF; that is, the nanostructuring of the polymer phase does not take place (Fig. 1, spectra *1* and *2*). Under the effect of microdischarges with an energy of $W = 26.3 \times 10^{-6}$ J propagating in the air medium with a thickness of 6 mm between the dielectric and the surface of the polymer solution (Fig. 4, b), the development of the immobilization of the nanoparticles starts to take place: the shift of the second and third maxima to the high-temperature range is observed (spectrum *3*, Fig. 1). Under the effect of the microdischarges with an energy of $W = 335.2 \times 10^{-6}$ J propagating in the air medium with a thickness $d = 10$ mm between the dielectric and the surface of the polymer solution (Fig. 4, c), the immobilization of the nanoparticles and their homogeneous distribution in the bulk polymer solution take place: the first and the second maxima are not observed, which are related to the initial PVDF and the composites on its basis (Fig. 1, spectrum *4*).

For the composites with immobilized nanoparticles, the amplitude of the maxima related to the polymer phase drastically decreases and the heating up to 473 K does not give rise to the formation of the first and the second maxima.

Proceeding from the values of the activation energies of the maxima (0.57, 0.69, and 1.23 eV, respectively), it can be suggested that the first two maxima are related to the relaxation of the charge in the polymer. The transition of the spectrum of the thermodepolarization current from the complex structure (three maxima) into the simple one (one maximum, Fig. 1) demonstrates that, at a definite energy ($W \geq 335 \times 10^{-6}$ J) of the local discharges, the immobilization of nanoparticles takes place in the polymer phase.

During the chemical precipitation, the energetical parameters of the local discharges change due to the change in the thickness of the air gap. During the termination of the chemical precipitation, the plasma channels of the discharge have direct contact with the surface of the hybrid piezocomposite. After that, the process of the plasma treatment and immobilization of the $BaTiO_3$ nanoparticles in the polymer phase terminates. Thus, the immobilization and homogeneous distribution of the nanoparticles in the polymer phase precipitated on the surface of the piezocomposite element take place.

The main difficulty is in the selection of the experimental method for the control of the immobilization and the study of its effect on the properties of the composites. The control of the immobilization of the nanoparticles in the hybrid composite is performed by the analysis of the spectrum of the thermostimulated depolarization current [13, 14]. The spectrum of the thermostimulated depolarization current of the composites only with micropiezoelectric particles, i.e., nonhybrid composites, has three maxima: the first and second maxima correspond to the polymer phase not having direct contact with the micropiezoparticles, and the third maximum, to the polymer phase having direct contact with the micropiezoparticles. The spectrum of the thermodepolarization current of the hybrid composites has one broad maximum, and it is considerably shifted to the high temperatures. The absence of the first and second maxima in the spectrum confirms the nanostructuring of the polymer matrix. Really, the introduction of the nanoparticles in the polymer phase is limited by the heat oscillations of the polymer chains and restricts the thermorelaxation of the charges. Thus, using the spectrum of the thermostimulated depolarization current, the nanostructuring of the polymer phase of the composite can be predicted.

Let us consider the possible mechanism of this interesting and quite complex effect of the immobilization of the nanoparticles in the polymer solution. The thermal motion of the macromolecules in the solution determines not only the translational but also the rotational motion. If any force field is applied to the solution, for example, an electrical discharge, then, both the electrical, hydrodynamic, acoustic, thermal, and light fields and the torsional moment are applied to the chaotically oriented macromolecules so that the homogeneous distribution of the $BaTiO_3$ nanoparticles becomes more probable without the formation of large clusters. The comparison of the spectra of the thermostimulated depolarization currents shows that the introduction of the dielectric $BaTiO_3$ nanoparticles into the PVDF results in a considerable change (decrease) in the molecular mobility and the packing of the macromolecules around the nanoparticles. The conditions of the proceeding of the relaxation processes change. The higher the number of the polymer molecules taking part in the interaction with the surface of the $BaTiO_3$ nanoparticles, the greater the degree of the mobility of the polymer chains is restricted and the greater this affects the properties and structures of the polymer phase and the composition on the whole.

Let us consider the technology of the preparation of the hybrid composed of nano- and micropiezoelec-

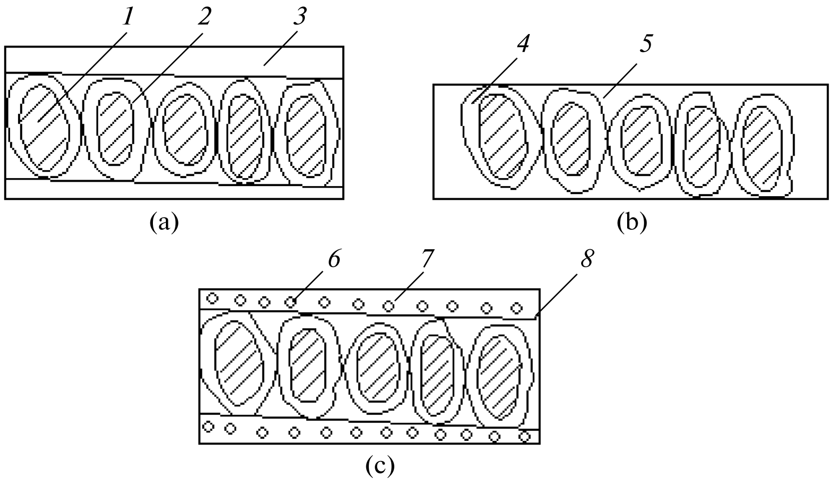

Fig. 5. Scheme of the structure formation of the hybrid of nano- and micropiezoelectric composites PVDF—nanoparticle and $BaTiO_3$—piezoceramics PZT-5A. (a) micropiezoelectric composite PVDF—PZT-5A, (b) the micropiezoelectric composite in the case of the dissolved subsurface polymer layer, and (c) the hybrid nano- and micropiezocomposite PVDF—$BaTiO_3$—PZT-5A: (*1*) piezoparticle, (*2*) interface polymer layer, (*3*) subsurface polymer range (phase); (*4*) interface layer in the case of the absence of the subsurface polymer range, (*5*) piezocomposite structure (substrate) (b, *5*), (*6*) nanoparticle $BaTiO_3$, (*7*) nanostructure polymer subsurface layer, and (*8*) nano- and piezohybrid composite.

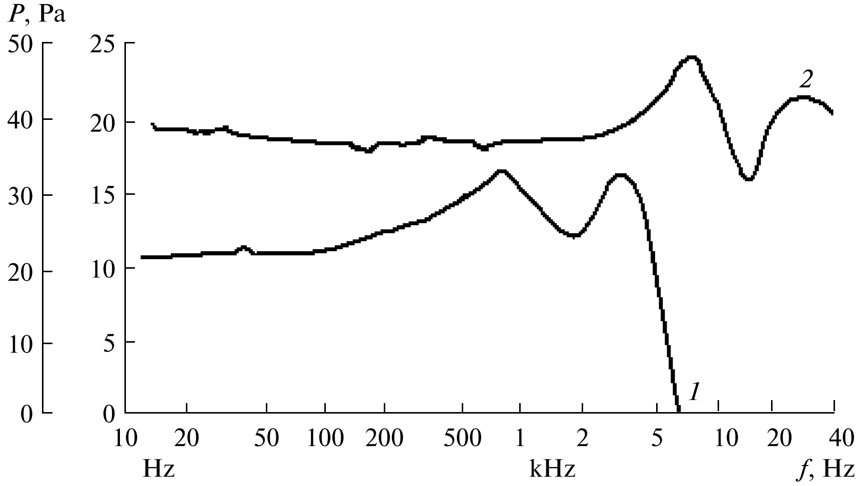

Fig. 6. Amplitude—frequency characteristics of the output acoustic signal of the electroacoustic transducers based on micropiezocomposite PVDF + 50 vol % PZT-5A and hybrid nano- and micropiezocomposite PVDF + 0.4 vol % $BaTiO_3$ + 49.6 vol % PZT-5A. (*1*) for the micropiezocomposite, the scale is *1*, and the excitation voltage is $U = 25$V, and, (*2*) for the hybrid nano- and micropiezocomposite, the scale is *2*, and the voltage of the excitation is $U = 5$ V. The conditions of the polarization of the piezocomposite elements are as follows: $E_p = 3.6$ MV/m, $T_p = 383$ K, and $t_p = 0.5$ h.

tric composites. We used for the first time the effect of nanostructuring of polymers for the creation of a novel class of piezoelectric composites. A general model and a scheme of the individual steps of the technology suggested are given in Fig. 5. The technology involves the following main stages: the preparation of the piezocomposite composed of micropiezoceramic particles, a polymer interface layer, and a near-surface polymer region (Fig. 5, a); the dissolution of the near-surface polymer phase (area) and the preparation of the piezocomposite structure (substrate) composed of piezoceramic particles and the polymer interface layer having direct contact with the piezoparticles (Fig. 5, b); the nanostructuring of the dissolved polymer phase (Fig. 5, a, element *3*) by the dielectric $BaTiO_3$ nanoparticles; the chemical precipitation of the nanostructured dissolved polymer on the surface of the piezocomposite substrate; and the preparation of the hybrid (Fig. 5, c) from the polymer—nanoparticle $BaTiO_3$ and polymer—micropiezoceramic particle matrix systems.

For the realization of the indicated technological processes, the important factor is the selection of the value of the dissolution temperature of the near-surface polymer phase of the composite. This temperature should be considerably lower than the fusion temperature of the polymer interface layer with an aim to

Table 2. Parameters of the micropiezocomposite PVDF–50 vol % PZT-5A and the hybrid nano- and micropiezoomposite PVDF–0.4 vol % $BaTiO_3$–49.6 vol % PZT-5A

Parameters	Piezocomposites	
	Micropiezocomposite PVDF–50 vol % PZT-5A	Hybrid piezoomposite PVDF–0.4 vol % $BaTiO_3$–49.6 vol % PZT-5A
$\varepsilon_{33}/\varepsilon_0$	95	134
Coefficient of the electromechanical coupling at extension K_{31}	0.17	0.28
Coefficient of the electromechanical coupling at contraction K_{33}	0.34	0.55
Piezomodulus at extension – $d_{31} \times 10^{12}$, C/N	57	90
Piezomodulus at contraction – $d_{33} \times 10^{12}$, C/N	120	185
Q_m	28	126
$Y \times 10^{-10}$, Pa	2.5	10.34
$\tan\delta \times 10^2$, $E = 5 \times 10^3$ V/m	0.16	0.06
Specific acoustic power $(d_{31}Y)^2$, $(C/m^2)^2$	2.04	86.5
Piezoelectric quality $K_{31}^2 \times Q_m$	0.81	9.88
Electromechanical efficiency $K_{33}^2/\tan\delta$	72.25	504
Value of the acoustic power $K_{31}^2 \times Q_m \times \varepsilon_{33}/\varepsilon_0$	76.9	1324
Diameter of the piezoelement, 10^{-3} m	20	20
Thickness of the piezoelement, 10^{-6} m	250	250
Diameter of the piezoparticles, 10^{-6} m	160–200	160–200
Diameter of the nanoparticles, 10^{-9} m	–	–
Structure of the piezophase	Rhombohedral	Rhombohedral
Structure of the nanoparticles	–	Tetragonal

preserve the integrity (consolidation) of the piezocomposite substrate (Fig. 5, b). In Table 2, the electromechanical parameters of the piezocomposite material and the nanostructured hybrid piezoelectrical composite are given. The results of the investigation demonstrated that the electrophysical, mechanical, and electromechanical parameters of the hybrid piezocomposites are considerably higher than the analogous parameters of the polymer–piezoceramics composites. In Fig. 6, the amplitude–frequency characteristics of the acoustic output signal are given in pascals of the electroacoustic transducers based on the miropiezocomposite PVDF+50 vol % PZT-5A and the hybrid nano- and micropiezocomposite PVDF + 0.4 vol % $BaTiO_3$ + 49.6 vol % PZT-5A. It is seen that the hybrid piezoelectric elements have a wide frequency range and a large output signal.

CONCLUSIONS

Thus, the approach to the preparation and control of the immobilization of nanoparticles in polymer matrices by the use of the plasma of an electrical discharge (the affecting factor) and the method of the thermodepolarization analysis (the method of control) can be considered sufficiently reasonable. Thus, the preparation of a novel class of piezocomposite materials with high piezoelectric and electromechanical characteristics based on a hybrid matrix of nano- and micropiezoceramic composites becomes possible.

REFERENCES

1. Pomogailo, A.D., Rozenberg, A.S., and Uflyand, I.E., *Nanochastitsy metallov v polimerakh* (Metal Nanoparticles in Polymers), Moscow: Khimiya, 2000.
2. Petrov, Yu.I., *Klastery i malye chastitsy* (Clusters and Small Particles), Moscow: Nauka, 1986.
3. *Novye materialy* (Novel Materials), Karabasov, Yu.S., Ed., Moscow: MISIS, 2002.
4. Suzdalev, I.P., *Nanotekhnologiya: fizikokhimiya nanoklasterov, nanostruktur i nanomaterialov* (Nanotechnology: Physicochemistry of Nanoclusters, Nanostructures and Nanomaterials), Moscow: Kom-Kniga, 2006.
5. *Polimernye kompozitsionnye materialy: struktura, svoistva, tekhnologiya* (Polymer Composition Materials: Structure, Properties, Technology), Berlin, A.A., Ed., St. Petersburg: Professiya, 2008.
6. Kurbanov, M.A., Kerimov, M.K., Musaeva, S.N., and Kerimov, E.A., Effect of Crystallochemical Parameters

of Piezophase on Piezo- and Pyroelectric Properties of Composite Polymer-Piezoceramic, *Vysokomol. Soedin., Ser. B*, 2006, vol. 48, no. 10, pp. 1892–1897.

7. Kerimov, M.K., Kurbanov, M.A., Agaev, F.G., Musaeva, S.N., and Kerimov, E.A, Pyroelectric Effect in Composites, Crystallized under Conditions of Effect of Plasma of Electric Discharge, *Fiz. Tverd. Tela*, 2005, vol. 47, no. 4, pp. 686–690.
8. Kerimov, M.K., Kerimov, E.A., Musaeva, S.N., Panich, A.E., and Kurbanov, M.A., Effect of Structure and Electrophysical Parameters of Pyrophase on Pyroelectric Properties of Composite Polymer-Pyroelectric Ceramics, *Fiz. Tverd. Tela*, 2007, vol. 49, no. 5, pp. 877–880.
9. Kurbanov, M.A., Sultanakhmedova, I.S., Kerimov, E.A., Aliev, Kh.S., Aliev, G.G., and Geidarov, G.M., Plasma Crystallization of Composites Polymer-Segnetopiezoelectric Ceramic and Their Piezoelectric Properties, *Fiz. Tverd. Tela*, 2009, vol. 51, no. 6, pp. 1154–1160.
10. Kurbanov, M.A., Sultanakhmedova, I.S., Aliev, G.G., and Geidarov, G.M., Piezoelectric Properties of Composites Polymer-Piezoelectric Ceramic, Crystallized under Conditions of Effect of Plasma of Electric Discharge, *Zh. Tekh. Fiz.*, 2009, vol. 79, no. 7, p. 63.
11. Bagirov, M.A., Kurbanov, M.A., and Shkilev, A.V., Study of Electrical Discharge in Air between Electrodes Covered by Dielectrics, *Zh. Tekh. Fiz.*, 1971, vol. 16.
12. Bagirov, M.A., Burziev, K.S., and Kurbanov, M.A., Study of Energetical Characteristics of Discharge, Formed in Air Between Dielectrics under Reduced Pressures, *Zh. Tekh. Fiz.*, 1979, vol. 49, no. 2, pp. 339–344.
13. Gorokhovatskii, Yu.A., *Osnovy termodepolyarizatsionnogo analiza* (Bases of Thermal Depolarization Analysis), Moscow: Nauka, 1981.
14. Gol'dade, V.A. and Pinchuk, L.S., *Elektretnye plastmassy: fizika i materialovedenie* (Electret Plastic Materials: Physics and Material Research), Minsk: Nauka i Tekhnika, 1987.

ISSN 1068-3755, Surface Engineering and Applied Electrochemistry, 2011, Vol. 47, No. 1, pp. 84–88. © Allerton Press, Inc., 2011.

EQUIPMENT AND INSTALLATIONS

Design and Make a Triangular Wave Oscillator with Application to Extract the *V–I* Characteristics of ZnO Varistors[1]

F. Harirchi[a] **and S. M. Hasanli**[b]

[a] *Islamic Azad University, Tehran South Branch (IRAN)*
[b] *Institute of Physics, National Academy of sciences of Azerbaijan, H. Javid pr. 33, Baku, AZ1143, Azerbaijan*
e-mail: harirchi@Gmail.com, hasanli sh@rambler.ru

Received July 19, 2010

Abstract—To determine the (current-voltage) characteristics for the fabricated Disks of varistors, we need to design a circuit, which can generate voltages with different Amplitudes and frequencies. This device can change the voltage and frequency automatically and linearly. We can use this device to study characteristics of the fabricated components or in QC procedures. Device gets the frequency of output voltage from 46 quantized values between 0.001 HZ to 100 HZ in the computer software. The peak to peak Amplitude of symmetric triangular voltage can change from 0 V to 600 V.

DOI: 10.3103/S1068375511010091

1. INTRODUCTION

Varistors (variable resistors) are poly crystal line ceramic devices exhibiting highly nonlinear (nonohmic) electrical behavior and greater energy absorption capabilities. Several conduction mechanisms for the varistor have been proposed based on this ceramic microstructure, which has led to varistor behavior being widely interpreted as resulting from the series-parallel network formed by the zinc–oxide intergranular-phase junctions. Capacitance measurements as a function of voltage have supported the model of Schottky barriers at grain boundaries. Electrically, the varistors show highly nonlinear (*I–V*) characteristics similar to the back-to-back Zener diode, but with much higher voltage, current and energy handling capabilities [1]. As a result, they are widely used as surge absorbers in electronic circuits and core elements of surge arresters in electric power systems.

The fabrication of zinc–oxide varistors is done by mixing semiconducting zinc–oxide powder with other oxide powders such as Bi, Co, Mn, and Pr, and subjecting the powder mixture to conventional ceramic pressing and liquid-phase sintering techniques [2]. A simple equivalent circuit for varistor is shown in Fig. 1a. The sintering results in a poly crystalline ceramic with a singular grain boundary property which produces the nonlinear current-voltage (*I–V*) characteristic of the device. A typical (*I–V*) characteristic of a varistor is shown in Fig. 1b.

Microstructurally, the zinc–oxide varistors are comprised of semiconducting n-type zinc–oxide grains, surrounded by very thin ($1–10^{-3}$ μm) insulating intergranular layers.

Testing new fabricated varistors in recent years is done using old methods. These old methods are based on an operator, who measures voltage and current of varistor point by point, and using measured values, he estimates the *I–V* characteristic plot. This procedure is time consuming, operator based and not accurate [3]. Moreover in the quality control (QC) systems, we need an automatic system in order to test varistors.

In many cases hysteresis occurs in specific frequencies in the *I–V* characteristic of varistors. For finding these hystereses and to illustrate them, we can use the proposed device in this paper.

In this paper we proposed a device, which can test new fabricated varistors automatically. This device is produced for the first time and it is independent from operator. We can illustrate *I–V* characteristic of varistors in the forward and backward case, so we can see hysteresis in the illustrated figures. Proposed device can work in the frequency range of 0.001 Hz to 100 Hz and amplitude range of 0 V to 600 V.

2. CIRCUIT BLOCK DIAGRAM

Device consists of five main parts:

1. Power Supply
2. Main Oscillator
3. Power Amplifier
4. Personal Computer
5. Oscilloscope Card

The connection of various Blocks of the device is shown in Fig. 2.

---

[1] The article is published in the original.

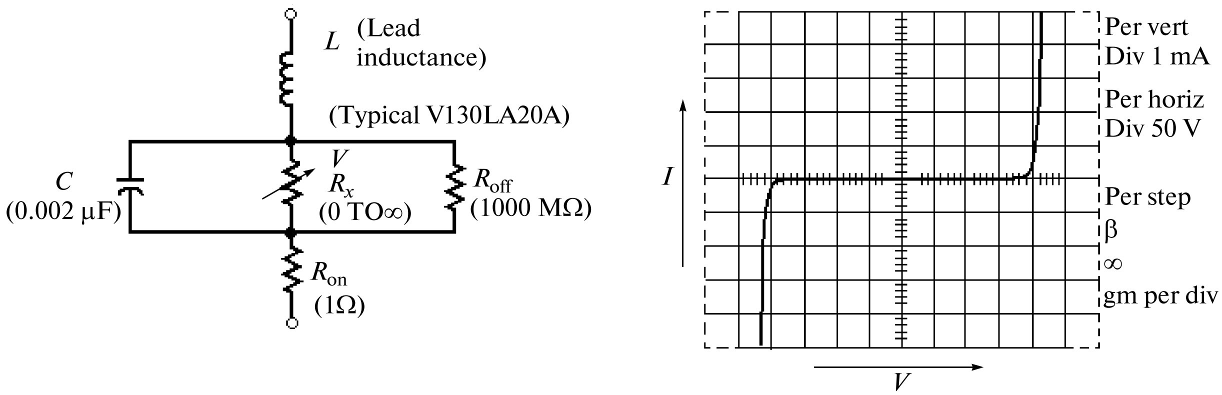

(a) (b)

Fig. 1. (a) Varistor equivalent circuit model, (b) Typical Varistor's (V–I) Characteristics.

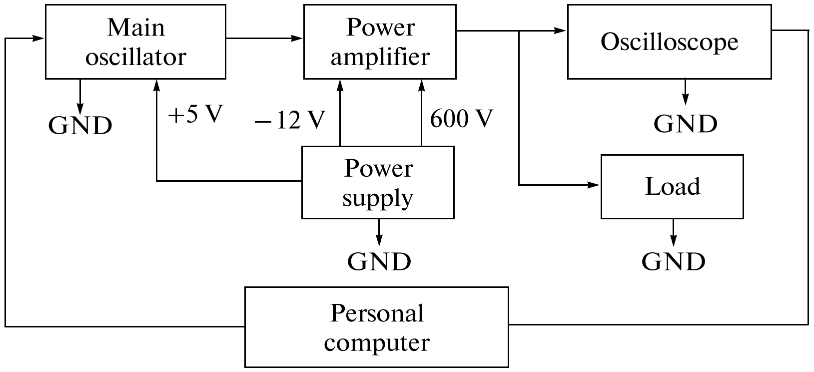

Fig. 2. Block Diagram of the Proposed Oscillator.

3. POWER SUPPLY

The block diagram of the power supply is shown in Fig. 3. To reduce the noise of main supply we put on RF-filter in the input of circuit, output of filter pass through a rectifier and a low pass filter to become DC. The next step is a switching element which makes a square wave from the DC input. Amplitude of the square wave reduces via an isolated transformer and after rectifying and filtering goes to an Optocoupler to have a constant voltage in output. The PWM controller supplies the pulses which should apply to the switching element which is a power Mosfet here. These two blocks as shown in Fig. 10 are named power switch. If we look at the feedback loop of the diagram we can see the optically isolated error amplifier, which consists of two parts. The first part is the voltage reference block which takes a reference from output and

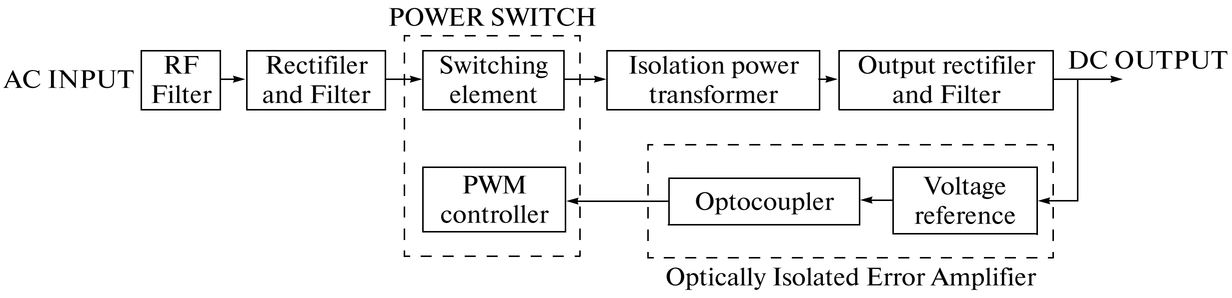

Fig. 3. Power supply Block Diagram.

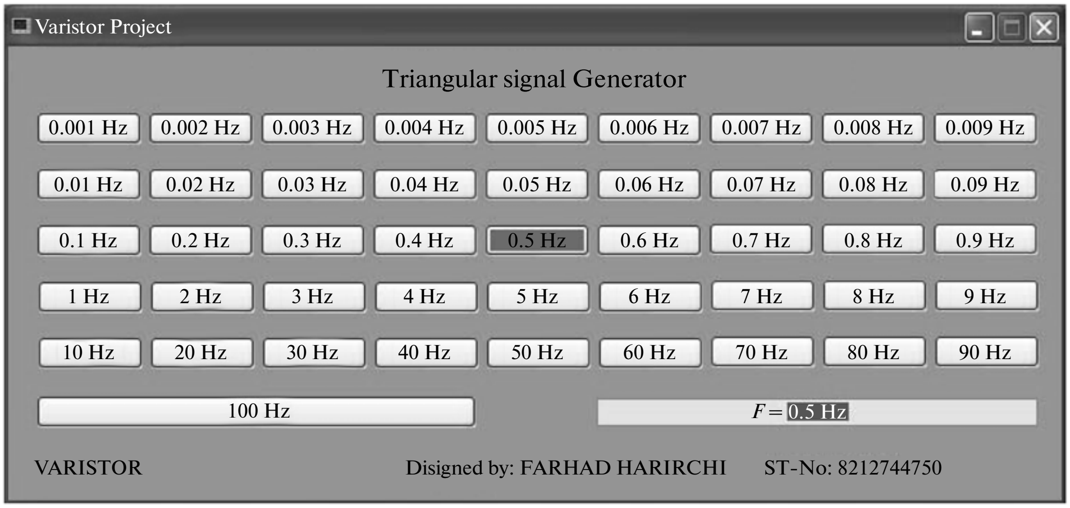

F = 0.5 Hz

VARISTOR Disigned by: FARHAD HARIRCHI ST-No: 8212744750

Fig. 4. Software Scheme.

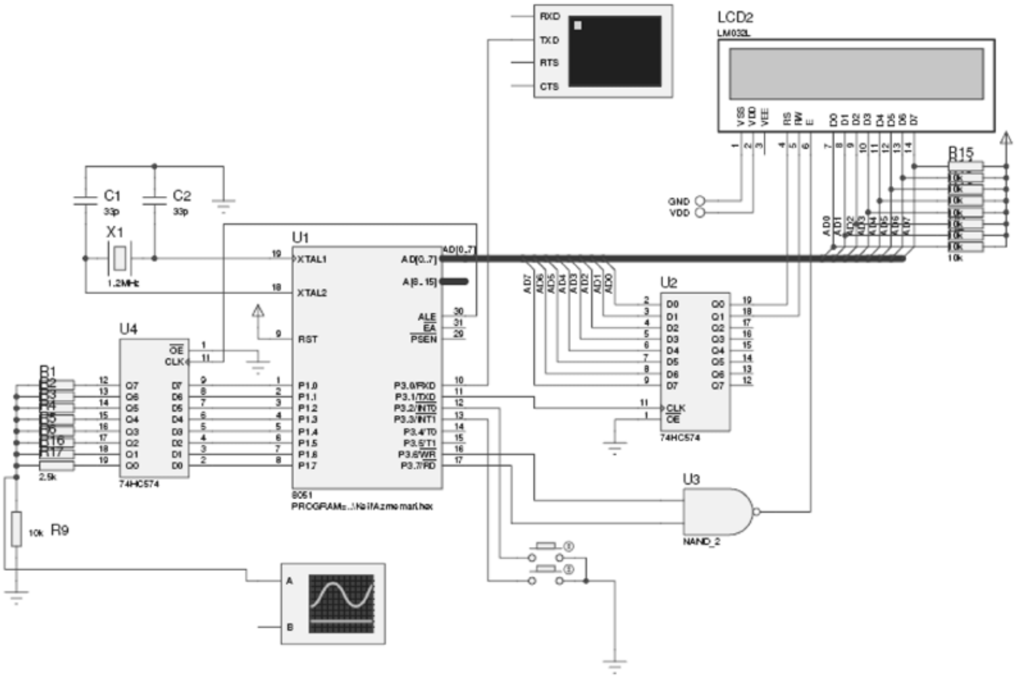

Fig. 5. Main Oscillator Schematic.

the second part is the Optocoupler which compare and isolate the reference voltage and send a control signal to the PWM block to fix the output voltage of power supply. The efficiency of this circuit is more than 70% and the peak to peak ripple voltage in maximum load is less than 20 mV. The 20% variations in main supply (180–260 volt) in maximum load make 15% changes in the DC output of the power supply.

4. MAIN OSCILLATOR

The main part of this circuit is an 8051 Microcontroller which is connected to PC via a RS232 connection. A program is written in C# Language which gives user friendly interface to select the output frequency. The schematic of this software is shown in Fig. 4. As shown in the figure there are 46 Buttons, each one for selecting a frequency. When the user click on one of

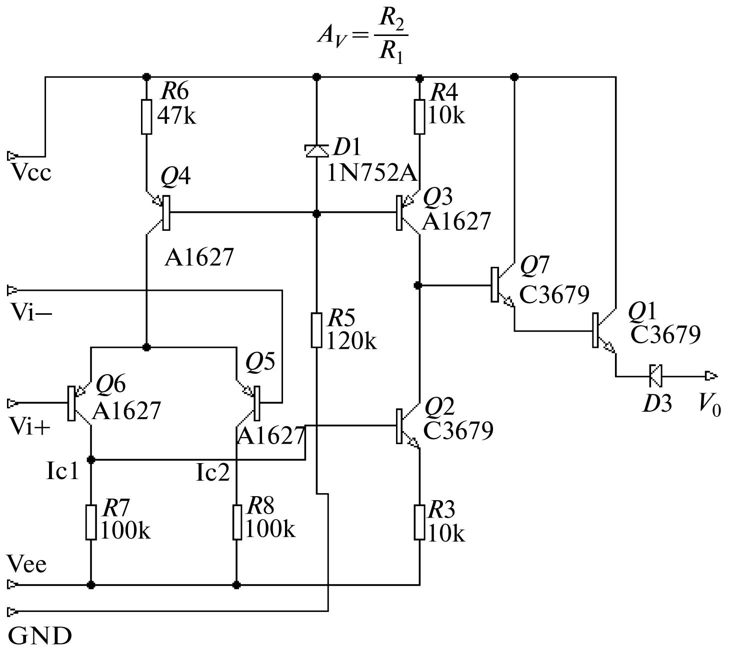

Fig. 6. A typical differential amplifier.

the Buttons, the frequency goes to the microcontroller via serial port and the frequency of output signal will be selected. The structure of circuit to make a symmetric Triangular wave as shown in Fig. 5 includes of a Microcontroller and some Latches and the resistors which put in the circuit in a Ladder form.

5. POWER AMPLIFIER

In this project, we need an op-amp with the working voltage of 620 volts, but according to our best knowledge, we don't have such an op-amp in market. Instead of using an op-amp, we make a differential amplifier, which its output is consisting of a buffer and a Darlington amplifier. A differential amplifier, make a relation among its output, input and the current of current source. This relation is shown in Eq. 1.

$$\Delta I = I_{c2} - I_{c1} = \dot{K}I(\nu_{i+} - \nu_{i-}). \quad (1)$$

Where ($\nu_2 - \nu_1$) is the differential input, I is the current of the current source and $\dot{K}$ is a constant.

A typical differential amplifier is shown in Fig. 6. In this figure, transistors Q5 and Q6 are connected in the differential form. The amplification factor of this circuit is proportional to I.

Using the internal circuit of an op-amp and adjusting the parameters of it, we could make an op-amp which could act on the 0–620 volts range. The schematic diagram of this circuit and the frequency response of it are shown in Fig. 7. Like all of the amplifiers we should discuss on important parameters to understand the efficiency of circuit. The input impedance of the circuit, which is derived from a simulation, is about 800 kOhm and the output impedance is less than 50 Ohm. The voltage gain of this circuit is derived from the following equation:

$$A_V = \frac{R_2}{R_1}. \quad (2)$$

If we consider That R is a 1 kOhm resistor then we will calculate A_v according to the following equation

$$A_V = R_2(\text{kOhm}). \quad (3)$$

If the maximum of peak to peak input voltage is 5 V, and we want to have 600 V in output, so we need to use a 120 kOhm resistor instead of R_2. We use Pspice simulator this circuit in Transient, DC and AC Analysis Fig. 6 shows the frequency response, input and output wave forms.

6. CONCLUSIONS

In this paper we discussed a device which can be used to achieve the (I–V) characteristics of varistors and even for many other power components in different frequencies and in an automatic way. Previously testing new fabricated varistors was a time consuming and operator based procedure, which could estimate I–V characteristics after finding some discrete points. With our proposed device this procedure will be done automatically and can accurately estimate the I–V characteristics of new fabricated varistors. In the prepared device we can make some changes to be more effective to multipurpose analysis, for example we can change the discrete frequency range to a continues one

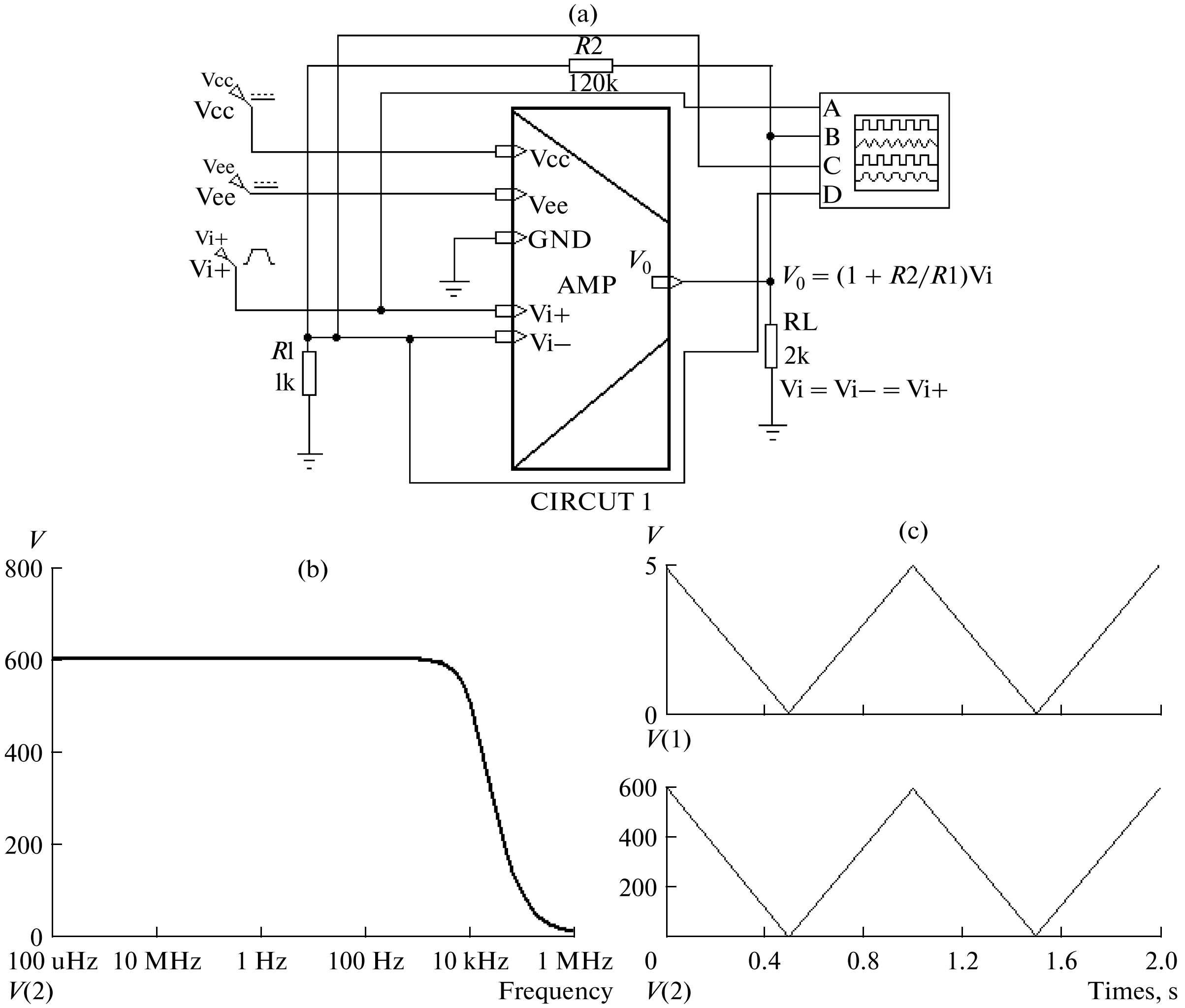

Fig. 7. (a) Schematic Diagram of Power Amplifier; (b) the frequency response; (c) top figure shows triangular wave, which is the input of the circuit and the bottom one shows the output voltage.

with changing the microcontroller's and C# program, and another change which can be occurred is to replace the symmetric triangular wave with a square wave to achieve to other aims.

REFERENCES

1. Matsuoka, M., Nonohmic Propierties of Zinc Oxide, *Jpn. J. Appl. Phys.*, 1971, no. 10, pp. 736–741.
2. Lou, L.F., Current-Voltage Characteristics of ZNO–Bi_2O_3 Heterojunction, *Journal of Applied Physics*, 1979, vol. 50, p. 555.
3. Hasanli, Sh.M. and Harirchi, F., Influence of Impurities on Electrophysical Characteristics of the ZnO-base Varistors, *POWER ENGINEERING PROBLEMS*, 2008, p. 92–95.
4. Milman, J. and Halkias, C.C., *Integrated Electronics: Analog and Digital Circuits and Systems*, McGraw-Hill, 1972.
5. Sedra, A.S. and Smith, K.C., *Microelectronic Circuits*, Oxford Universitypress, 1998.
6. Mazidi, M.A., Mazidi, J., and Mckinlay, R., *The 8051 Microcontroller and Embedded Systems Using Assembly and C. 2nd Edition*, Prentice Hall.

ISSN 1068-3755, Surface Engineering and Applied Electrochemistry, 2011, Vol. 47, No. 1, pp. 89–93. © Allerton Press, Inc., 2011.
Original Russian Text © V.G. Zhekul, S.G. Poklonov, A.P. Smirnov, 2011, published in Elektronnaya Obrabotka Materialov, 2011, No. 1, pp. 101–105.

OPERATING EXPERIENCE

Experimental Studies of the Effectiveness of the Electrodischarge Effect on a Physical Model of the Bottom-Hole Zone of the Productive Layer

V. G. Zhekul, S. G. Poklonov, and A. P. Smirnov

Institute of Impulse Processes and Technologies, National Academy of Sciences of Ukraine,
pr. Oktyabrskii 43A, Nikolaev, 54018 Ukraine
e-mail: iipt@iipt.com.ua

Received June 25, 2010

Abstract—In this work, an experimental technique has been developed, and experimental research concerning the comparison of the efficiency of various technological modes of an electrodischarge's influence on a physical model of the bottom zone of the productive layer of a well has been performed. Research has shown the necessity of the use at well treatment of a closed electrode system.

DOI: 10.3103/S1068375511010200

INTRODUCTION

During many years of service, the production rate of operating petroleum, gas, pumping, and water wells decreases due to the decrease in the permittivity of the bottom-hole zone (BHZ) due to its mudding by deposits of various natures. In order to increase the performance of a well, different methods of demudding are used, one of which is the electrodischarge method [1].

The basic operating factor of the electrodischarge effect is believed to be the pressure wave caused by the electric discharge in the liquid, the amplitude of which depends on the length of the interelectrode gap (IEG). The maximal amplitude of the pressure wave is achieved at the electrical discharge at the optimal interelectrode gap [2]. During the electrodischarge treatment of a well, an uncontrolled change in the electroconductivity of the down-hole liquid takes place. When using electrode systems of the open type (OES), this leads to the necessity to perform the electrical discharges in a short interelectrode gap in order to provide its stable breakdown. This negatively affects both the working of the equipment (its endurance considerably decreases) and the effectiveness of the electrodischarge treatment (the amplitude of the pressure wave substantially decreases). In order to solve this problem, an electrode system of the closed type was designed (CES) [3]. Its main difference from OES involves the presence of an impermeable acoustically transparent screen isolating the liquid in the discharge zone from the well liquid and not allowing their mixing. The use of CES makes it possible to permanently perform the electrical discharge with the optimal interelectrode gap, which considerably decreases the pre-breakdown losses of energy, stabilizes the electrical discharge, and makes it possible to work at the maximal amplitude of the pressure wave. At the same time, the problem concerning the influence of the shell of the closed electrode system on the transformation of the parameters of the pressure wave caused by the electrical discharge in the liquid and the reasonability of its use has evolved.

Earlier, we performed a series of experimental and theoretical works on the study of CES [4–8]. For example, the experimental comparison of the effectiveness of the electrode systems of the open and closed types and the transformation of the impulse of the pressure wave was performed while passing through the shell under various hydrostatic pressures in a well with the use of waveguide sensors of the pressure [4, 5]. In [6], for the study of the transformation of the impulse of the pressure during its passing through the shell, a procedure of the measurement of the specific impulse was used given by the discharge to the pipe by the deviation of a pendulum from its vertical position. It was also determined that the electrode systems have the highest effectiveness at the optimal interelectrode gap [7]. Work [8] is devoted to the mathematical simulation of the effect of the shell of the electrodischarge instrument on the hydroimpulse stress in the well.

However, the ultimate answer to the problem mentioned earlier can be given only by the experimental investigation of a physical model of the bottom-hole zone of the productive layer, which should include the following:

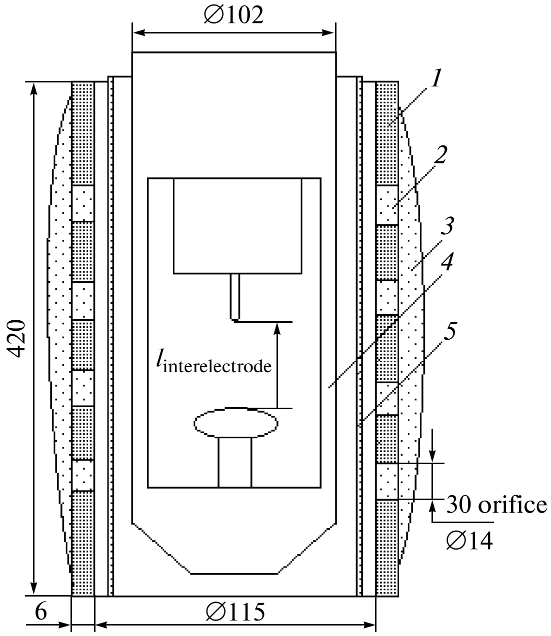

Fig. 1. The investigation scheme: (*1*) pipe, (*2*) orifice, (*3*) cement rendering, (*4*) electrode system, and (*5*) acoustically transparent screens.

—the study of the influence of the length of the interelectrode gap on the effectiveness of the electrodischarge effect, and

—the experimental comparison of the effectiveness of electrode systems of various types.

Therefore, the purpose of this work is to perform an experimental investigation of a physical model for the determination of the reasonability of the use of CES for the electrodischarge effect in the bottom-hole zone of the productive layer.

In order to do this, the following problems should be solved:

—the development of a procedure for the determination of the effectiveness of the electrodischarge effect on the physical model of the bottom-hole zone of the productive layer,

—the performance of experimental studies on the determination of the effect of the length of the interelectrode gap on the effectiveness of the electrodischarge effect, and

—the performance of experimental studies on the comparison of the effectiveness of the electrode systems of the open and closed types.

ROUTINE OF THE PERFORMANCE OF THE EXPERIMENTAL STUDIES

A procedure was developed with the aim to determine the effectiveness of the electrodischarge effect in the demudding process. This procedure made it possible to perform experimental studies on the comparison of the effectiveness of the electrode systems of the open and closed types for physical models of the cement sheath of the casing string of wells under atmospheric pressure and on the effect of the length of the interelectrode gap on the effectiveness of the electrodischarge effect. The experiments were performed according to the following algorithm:

(1) The experiments were performed using the investigation scheme given in Fig. 1. The scheme is composed of a model of the BHZ of a well composed of steel pipe *1* with the orifices (*2*) uniformly distributed over the surface of the pipe at a distance of 55 mm from each other. The pipe *1* is surrounded by a cylinder made from chain link with a 10 × 10 mm outer diameter (not shown in the figure) for the retention of the cement rendering *3* with a thickness from 10 to 15 mm. Inside the model, an open electrode system was placed (*4*) with an electrodischarge submersible pump (Skif-100). For the simulation of the conditions of a closed electrode system, it was sealed with an acoustically transparent screen *5*.

(2) The experiments were performed in a 670 × 700 × 520 mm steel pit with windows filled with the working medium (tap water with the specific conductivity $\sigma_0 = 0.06$ S/m) in which the model with the electrode system was placed. The parameters of the experimental equipment corresponded to the parameters of the electrodischarge equipment for the treatment of wells (the Skif type): the charge voltage of the bank of capacitors $U_0 = 30$ kV, the capacity of the bank of capacitors $C = 1$ mcF, the pulse repetition frequency of is 0.25 Hz, and the number of impulses is 15.

(3) The preparation of the model was performed by the application of a cement solution on the surface of the pipe *1*. The solution was obtained from mark 400 cement and sand at a one-to-four ratio. A solution of 4 dm^3 sand, 1 dm^3 mark 400 cement, and 750 ml water was prepared for one model. After the preparation of the model, it was dried for two days.

(4) The electrode system of the open type was tested on the model of a cement sheath at the following interelectrode distances l_{IE}, mm: 5, 10, 15, 22, and 35, where 22 mm is the optimal value of the interelectrode distance for the given parameters of the setup calculated using the formula from [2]:

$$l_{\text{optimal}} = \sqrt[4]{r^2\sqrt{L/C}\,0.5\frac{U_0^2 C}{A}}, \qquad (1)$$

where r is the distance to the object of the treatment, m; L is the inductance, H; and A is the spark constant, V^2 s m^2 (for the spark discharge, $A = 10^5$ V^2 s m^{-2}).

(5) An electrode system of the closed type was tested with the model of the cement sheath (at the optimal interelectrode distance $l_{\text{IE}} = 22$ mm) with two

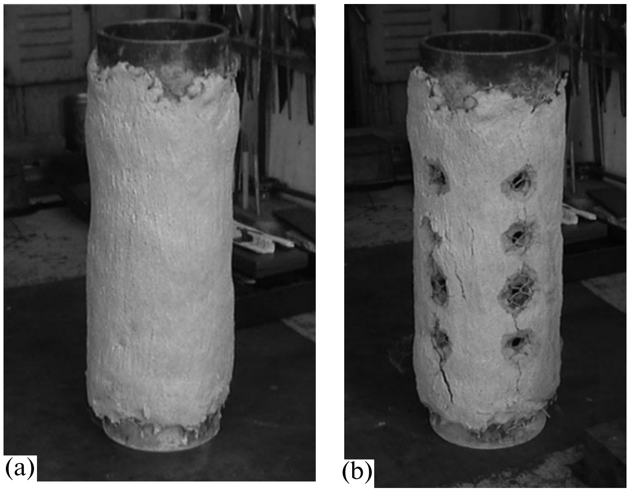

Fig. 2. Outer view of the model of the bottom-hole zone of the productive layer (a) before and (b) after the treatment.

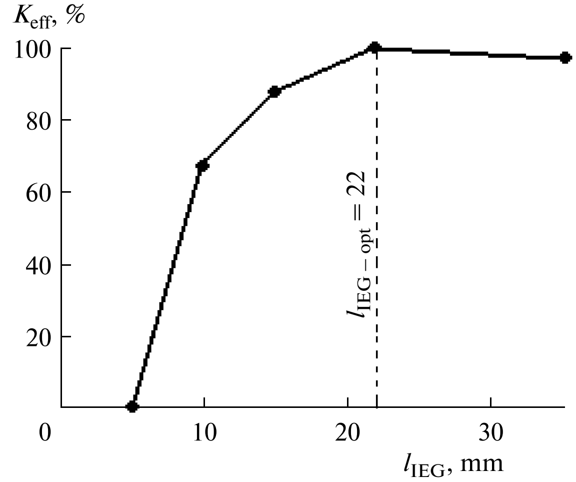

Fig. 3. Effectiveness coefficient of the treatment vs. the length of the IEG.

types of acoustically transparent screens: a resin pressure pipe with thread reinforcements and a polyethylene pipe.

(6) The influence on the model in the dynamical mode was recorded with the use of video cameras, and the moment of the first destruction of the cement sheath in the orifice zone was recorded.

(7) The integral effect on the model was recorded by the number of orifices purified from the cement rendering as a result of the effect of the pressure wave after 15 discharges.

It should be noted that this procedure at a slight processing of the working object was also used for the evaluation of the effectiveness of the electrodischarge effect on viscous deposits [9].

RESULTS OF THE EXPERIMENTAL STUDY

For the comparison of the effectiveness of the electrode systems of the open and closed types and the determination of the effect of the length of the interelectrode gap on the effectiveness of the electrodischarge effect on the model of the bottom-hole zone in the experiment, we determined the following:

—the moment of the first destruction of the cement sheath in the orifice zone, and

—the integral effect on the model determined by the number of orifices purified from cement in the model after 15 discharges.

During the estimation of the integral parameter of the effectiveness of the treatment, a nondimensional coefficient of the effectiveness (K_{ef}) was used, which was calculated according to the following expression:

$$K_{\text{effective}} = \frac{N_i}{N_{\text{optimal}}} 100\%, \qquad (2)$$

where N_i is the number of purified orifices during the i-th experiment, and N_{opt} is the number of purified orifices during the pilot experiment (the open electrode system, IEG is optimal for this mode).

A series of experiments were performed in which we investigated the following:

—the dependence of the effectiveness of the treatment on the length of the IEG in the case of an open electrode system, and

—the comparison of the effectiveness of the open and closed electrode systems.

The following results were obtained.

In Fig. 2, the physical environment of the model of the bottom-hole zone of the productive layer (a) before and (b) after the treatment is given.

The variation of the interelectrode gap demonstrated that it substantially influences the effectiveness of the treatment of the model of the bottom-hole zone of a well (Fig. 3), which is in complete accordance with the considerations concerning the optimal length of the IEG and its correlation with the amplitude of the pressure wave [2].

An analogous tendency is observed at the analysis of the start of the first destruction (N_{d}) of the cement sheath in the orifice zone (Fig. 4).

These results make it possible to draw a conclusion that the main factor of the electrodischarge effect on the fragile sediments during demudding of a well is the amplitude of the pressure wave. Conse-

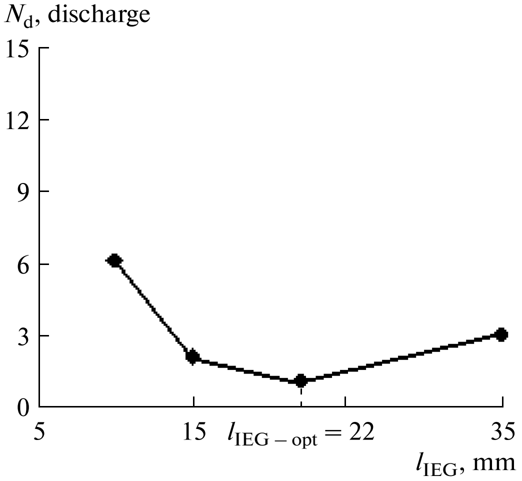

Fig. 4. Start of the destruction of the cement sheath of the model vs. the length of the IEG.

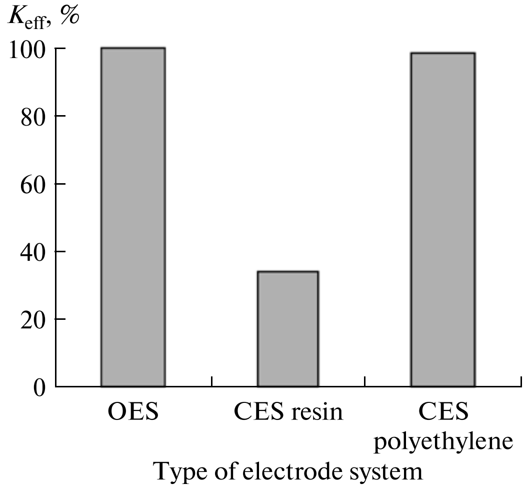

Fig. 5. Coefficient of the effectiveness of the treatment vs. the type of electrode system and the material of the shell.

quently, during the treatment, the maximal possible amplitude of the pressure wave should be achieved, which can be accomplished by setting the optimal length of the IEG at the given parameters of the generator (the electrodischarge instrument). The electrodischarge treatment at low interelectrode gaps (5 and 10 mm) is characterized by the low effectiveness of the electrodischarge effect. For example, at an interelectrode gap of 5 mm, orifices not purified from the cement were not recorded when using the model.

For the simulation of the working conditions of a closed electrode system in the space between the zone of the electrical discharge and the working object, a bold acoustically permeable screen was placed, which gives a minimal change in the amplitude of the pressure wave while passing through it. A polyethylene (as the acoustically most transparent material with impedance close to the impedance of water) and a rubber pressure hose (as the most technological material) were selected as the material of the shell [4, 5]. The results obtained (see Fig. 5) demonstrated that the installation of the shell made from polyethylene practically does not influence the effectiveness of the treatment. While using the rubber pressure hoses as the shells for the closed electrode system, the effectiveness slightly decreases, which agrees with the data obtained earlier [4, 5].

CONCLUSIONS

The electrodischarge treatment of a well with the aim of its demudding is recommended to be performed using the optimal interelectrode gap, which provides the maximal amplitude of the pressure wave. The electrodischarge effect at low values of the interelectrode gap is characterized by the low effectiveness of the influence on fragile sediments: while working with an interelectrode gap of 10 mm, K_{eff} decreases by 32% relative to the work performed at the optimal gap. At an interelectrode gap of 5 mm, no orifices purified from cement were recorded using the model. Due to the specific features in a well, only a closed electrode system can provide constant work at the optimal interelectrode gap.

It is better to use a material with an impedance close to that of water, for example, polyethylene, which provides the minimal decrease in the amplitude of the pressure wave while passing through the shell, as the material of the CES shell.

REFERENCES

1. Gulyi, G.A., *Osnovy razryadnoimpul'snykh tekhnologii* (Bases of Discharge Impulse Technology), Kiev: Naukova Dumka, 1990.
2. Shamko, V.V. and Kucherenko, V.V., Teoreticheskie osnovy inzhenernykh raschetov energeticheskikh i gidrodinamicheskikh parametrov podvodnogo iskrovogo razryada (Theoretical Bases of Interesting Calculations of Energetical and Hydrodynamic Parameters of Underwater Spark Discharge), *Preprint of IIPT, Natl. Acad. Sci. Ukr.*, Nikolaev, 1991, no. 20.
3. Zhekul, V.G., Poklonov, S.G., and Shvets, I.S., Electrodischarge Submersible Pumps with Stabiled Working Parameters, *Neft. Khoz.,* 2006, no. 2, pp. 89–91.
4. Poklonov, S.G., Zhekul, V.G., and Smirnov, A.P., Procedure and Results of Experimental Studies of Effect of Elastic Barrier on Parameters of Pressure Wave at Electrical Discharge in Water, *Elektron. Obrab. Mater.*, 2007, no. 5, pp. 56–60.
5. Sofiiskii, K.K., Zhekul, V.G., Smirnov, A.P., and Poklonov, S.G., Effect of Elastic Barrier on Parameters of

Pressure Wave, Excited by Discharge in Liquid, *Geotekh. Mekh.*, 2005, vol. 5, pp. 123–129.

6. Kovyazin, N.I., Ippolitov, V.V., Urosov, S.A., Sorokin, V.F., Kosenkov, V.M., Zhekul, V.G., and Poklonov, S.G., Procedure of Determination and Experimental Study of Specific Impulse, Given by Disturbances from Source of Electrodischarge Type, *Izv. Vyssh. Uchebn. Zaved., Neft' i Gaz*, 2000, no. 1, pp. 25–30.
7. Kovyazin, N.I., Urosov, S.A., Shishkov, D.A., Poklonov, S.G., Zhekul, V.G., and Trofimova, L.P., Experimental Study of Effectiveness of Electrode Systems of Electrohydroimpulse Installations, *Izv. Vyssh. Uchebn. Zaved., Neft' i Gaz*, 2001, no. 2, pp. 32–35.
8. Barbashova, G.A., Zhekul, V.G., Smirnov, A.P., Kosenkov, V.M., and Sofiiskii, K.K., Effect of Shell of Chamber of Electrodischarge Installation on Hydroimpulse Stress in Well, *Geotekh. Mekh.*, 2004, vol. 49, pp. 106–114.
9. Sofiiskii, K.K., Zhekul, V.G., Smirnov, A.P., and Poklonov, S.G., Experimental Testing of Mathematical Model of Electrodischarge Effect on Viscous Deposits, *Geotekh. Mekh.*, 2010, vol. 85, pp. 133–139.

ISSN 1068-3755, Surface Engineering and Applied Electrochemistry, 2011, Vol. 47, No. 1, pp. 94–99. © Allerton Press, Inc., 2011.
Original Russian Text © T.G. Lyashuk, B.B. Kolupaev, 2011, published in Elektronnaya Obrabotka Materialov, 2011, No. 1, pp. 106–112.

OPERATING EXPERIENCE

Effect of the PVC System's Topology on the Dielectric Losses in the Region of Strong Electric Fields

T. G. Lyashuk and B. B. Kolupaev
Rovno State Humanitarian University, ul. Ostafova 31, Rovno, 33000 Ukraine
e-mail: nightquesttg@rambler.ru

Received July 15, 2010

Abstract—The electrophysical characteristics of the electric cable's transition into a state of a heterogenic polymer system due to a wire's explosion were examined. Using cyclic heating–cooling of the composite, the changes in its topology were observed. The latter makes it possible to regulate the dielectric characteristics of the system.

DOI: 10.3103/S1068375511010133

INTRODUCTION

The wide use of polymer materials in the electronics industry requires the search for new high-dielectric materials, which is based on the study of their behavior under strong electric fields [1]. Under the above operational conditions, a breakdown is found to be one of the main reasons for the failure of polymer insulation [2]. Therefore, the study of the reasons and consequences of the latter seems to be of certain interest [3]. It should be noted that the kinetics and the reasons (as well as their stages) that induce the failure of the electric strength of polymers have been examined in a great number of works [4]. However, the further behavior of polymer materials that transfer into heterogenic systems (HS) after the breakdown of the wires inside of them has not been sufficiently studied yet under the affect of the temperature fields.

Based on the aforementioned, the goal of this work is to study the behavior and topology of a heterogenic system under an electric field induced by a wire's explosion in a polymeric matrix followed by the heating–cooling of the composite with various contents of a finely divided metal. Here, it is typical that, after the dielectric structural failure of a cable upon an abrupt increase in the current with no increase of the applied voltage, the second phase of the breakdown takes place, i.e., thermal and/or mechanical destruction that involves the appearance of a conductive channel. The transition of a metal into the heterogeneous system that occurs in this case requires the study of the processes correlated with the further possible directed change in its electrical strength due to the structural factors of the material. However, the HS's microstructure (topology) and its effect on the electrophysical properties of the material that experienced a breakdown also have to be examined. It was established that [1] the finely divided metal particles formed in dielectric materials due to a wire's explosion remain surrounded by the polymer matrix. The particles of a dispersed phase can be diversely distributed in the polymer matrix [5]. Assume for simplicity that, due to the conductor's explosion, a system with a statistical topology [6] is formed for which the phases with the dielectric permeability s_1 and s_2 occupy the corresponding volumes V_1 and V_2 ($V_0 = V_1 + V_2$ is the total volume). This approach allows one to obtain the averaged values of the dielectric characteristics of the material:

$$\bar{\varepsilon} = \varepsilon_1 + f_2\theta_2(\varepsilon_2 - \varepsilon_1), \tag{1}$$

where $\bar{\varepsilon}$ is the effective dielectric permittivity,

$$f_2 = V_2/V_0,\ \theta_2 = E_2/E_1;\ E_1 = \frac{1}{V_0}\int_{V_1} E dV;\ E_2 = \frac{1}{V_0}\int_{V_2} E dV.$$

Taking into account that the finely dispersed metal particles in the form of a system of small spheres (phase 2) distributed in the matrix (phase 2) are in the external electric field E, we have the following according to [7]:

$$\theta_2 = \frac{3\varepsilon_1}{\varepsilon_2 + 2\varepsilon_1}, \tag{2}$$

and then

$$\bar{\varepsilon} = \varepsilon_1 + 3f_2\varepsilon_1\frac{\varepsilon_2 - \varepsilon_1}{\varepsilon_2 + 2\varepsilon_1}. \tag{3}$$

Since, the electric field induced by this metal phase at a distance r from the latter is a value on the order of $\frac{R^3}{r^3}E_0\frac{\varepsilon_2 - \varepsilon_1}{\varepsilon_2 + 2\varepsilon_1}$ [2] (where R is the radius of the sphere, and E_0 is the intensity of the external field), then r_0 (the distance at which this induced field may be ignored) will be as follows:

$$r_0 \gg R\left(\frac{\varepsilon_2 - \varepsilon_1}{\varepsilon_2 + 2\varepsilon_1}\right)^{1/3}. \tag{4}$$

Thus, at $f_2 \leq R^3/r_0^3$, we have

$$f_2 \ll \left|\frac{\varepsilon_2 + 2\varepsilon_1}{\varepsilon_2 - \varepsilon_1}\right|, \tag{5}$$

which corresponds to the region of the considered contents of the ingredient $|f_2 \leq 0.1$ vol %$|$. Taking into account that, for the considered systems of $\varepsilon_2 > \varepsilon_1$, the $\bar{\varepsilon}$ values for the upper and lower boundaries are, correspondingly, equal,

$$\bar{\varepsilon}_{\text{up}} = \varepsilon_2 + \frac{f_1}{(\varepsilon_1 - \varepsilon_2)^{-1} + f_2\varepsilon_2/3}, \tag{6}$$

$$\bar{\varepsilon}_1 = \varepsilon_1 + \frac{f_2}{(\varepsilon_2 - \varepsilon_3)^{-1} + f_1\varepsilon_1/3}. \tag{7}$$

Using an analytical representation [8], we managed to separate the dependence of $\bar{\varepsilon}$ on the topology of the composite structure. The gist is that the introduction of the functions

$$F = 1 - \bar{\varepsilon}/\varepsilon_1, \tag{8}$$

and not separately as ε_1 and ε_2 for the HS, as well as

$$L = (1 - \varepsilon_2/\varepsilon_1)^{-1}, \tag{9}$$

allow one to consider $F(L)$ as an analytic function of the complex variable L, since the composite must dissipate energy. If it is dissipated by at least one phase (1, 2), then $Im\bar{\varepsilon} > 0$, where $Im\varepsilon_1 > 0$. In our case, $ImL \neq 0$; then, $ImF(L)/ImL < 0$ for $0 \leq L \leq 1$.

Thus, in the HS, the dielectric losses of energy are fixed, and, taking into account the uniformity of the electric field, the free energy of a volume unit of the HS is [2]

$$dW = -Sdt + \xi d\rho + \frac{1}{4\pi}EdD, \tag{10}$$

where S is the entropy, ξ is the chemical potential, and ρ is the mass of a volume unit of the substance. Correspondingly, when the composite undergoes the effect of the temperature field, its characteristics change by the following value upon heating,

$$dW_{\text{heat}} = -S_{\text{heat}}dT + \xi_{\text{heat}}d\rho + \left(\frac{1}{4\pi}EdD\right)_{\text{heat}}, \tag{11}$$

and upon cooling,

$$dW_{\text{cool}} = -S_{\text{cool}}dT + \xi_{\text{cool}}d\rho + \left(\frac{1}{4\pi}EdD\right)_{\text{cool}}. \tag{12}$$

Hence, in the heating–cooling mode of the composite, the change of the free energy at a constant content of the ingredients is as follows:

$$\begin{aligned} \Delta W &= dW_{\text{heat}} - dW_{\text{cool}} \\ &= -\Delta SdT + \Delta\xi d\rho + \Delta\left(\frac{1}{4\pi}EdD\right), \end{aligned} \tag{13}$$

where the difference ΔS between the entropy of the states characterizes the direction of the process, $\Delta\xi$ is the driving force of the system's transition to a new quasi-stationary state, and $\Delta\left(\frac{1}{4\pi}EdD\right)$ is indicative of the change of the energy value in the electric field that occurs due to the presence of the HS in the field of external forces. Knowledge of its value allows one to ascertain the dissipation of energy in the composite exposed to the external alternating (ω) electric field E. Thus, the energy dissipated in the HS volume unit per a unit of time is as follows [6]:

$$P = \omega E^2\bar{\varepsilon}\tan\delta = cS, \tag{14}$$

where (ω) is the frequency, E is the field intensity, $\bar{\varepsilon} = \mathrm{Re}\bar{\varepsilon}$, δ is the angle of the losses, $\bar{\varepsilon}\tan\delta$ depends on the temperature and the content of ingredients in the system, c is a constant, and S is the area of the curve reduced by $\mathrm{Re}\bar{\varepsilon} - \tan\delta$.

Let us analyze the experimental results of the dielectric losses of energy in the composite using the obtained analytic ratios.

EXPERIMENTAL

A PVKh–S–65 Polyvenyl chloride (PVC) (Kaustik, Bashkortostan) with MM of 1.4×10^5 and $T_d = 354$ K was used as the basic material for the study.

Copper nanoparticles were introduced into the PVC using the conductor's explosion [3] with the conductor being short-circuited to a battery with a capacitor of 50 mfd at a voltage of 10 kV. The predominant size of the particles of the filler was 13 nm, and its content was varied in the range of (0–0.1) vol %.

The dielectric properties ε', ε'', $\tan\delta$ of the PVC systems were studied using a P 5083 bridge at a frequency of 100 kHz in the temperature range of (293–393) K at a heating rate of the specimen of 3 K/min. Melted quartz ($\varepsilon_q = 3.8$; $\tan\delta_q = 2 \times 10^{-4}$) was used as a reference specimen. The error of the measurements was up to 1% [9].

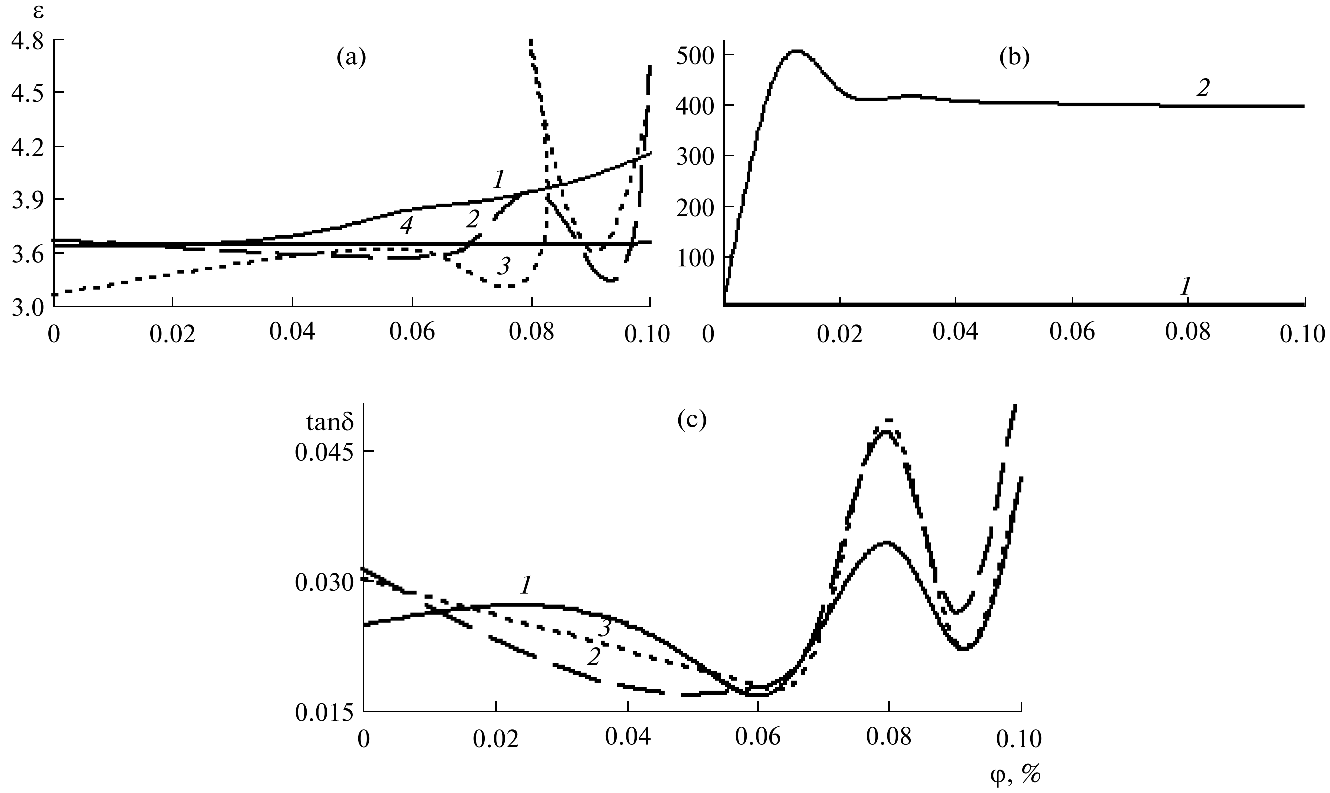

Fig. 1. Concentration dependences of the values of the dielectric characteristics of the HS (PVC + Cu) ($T = 293$ K): (a) $\varepsilon(\varphi)$ (*1*—a basic specimen, *2*—after heating, *3*—after the second heating, *4*—$\bar{\varepsilon}$ (calculation of (3)); (b) $\varepsilon(\varphi)$(*1*—$\bar{\varepsilon}$, $\bar{\varepsilon}_l$ (calculation of (3) and (7)), *2*—$\bar{\varepsilon}_{up}$ (calculation of (6)); (c) $\tan\delta$ (φ) (*1*—a basic specimen, *2*—after the first heating, *3*—after the second heating).

RESULTS AND DISCUSSION

Figure 1 shows the concentration dependence of ε, $\bar{\varepsilon}$, $\bar{\varepsilon}_l$, $\bar{\varepsilon}_{up}$, and $\tan\delta$ at $T = 293$ K. As is seen from the obtained data, the dependence of $\varepsilon(\varphi)$ after the first heating (Fig. 1a, curve 2) in the range of ($0 \le \varphi \le 0.06$) vol % is descending. However, the character of the dependence of $\varepsilon(\varphi)$ varies inversely in the range of the filler content of ($0.06 \le \varphi \le 0.1$) vol %. At the same time, in the region of $\varphi = 0.09$ vol % of Cu, an anomalous character of the dependence relevant to the minimum of the $\tan\delta$ value is observed (Fig. 1c). It is characteristic that, after the second heating of the specimens (Fig. 1a, curve 3), in the range of ($0 \le \varphi \le 0.06$) vol %, a linear increase in the $\varepsilon(\varphi)$ value is registered, but this character of the dependence is violated in the range of ($0.06 \le \varphi \le 0.1$) vol %. However, the dependence of $\varepsilon(\varphi)$ after the first and second heating in the range of ($0.07 \le \varphi \le 0.1$) vol % has a similar *S* character. The calculations of the averaged dielectric permittivity $\bar{\varepsilon}$ showed that its value increases slightly (Fig. 1a) with an increase in the nanofiller concentration and is between the values of $\bar{\varepsilon}_l$ and $\bar{\varepsilon}_{up}$ (ratios (6) and (7)) (Fig. 1b). In the case of the $\tan\delta$ (φ) dependence for the basic material, as well as after the first and second heating, its changes were established to remain in the entire range of the filler concentrations (Fig. 1c). However, as in the case of $\varepsilon(\varphi)$ (Fig. 1a), a pronounced minimum of this value at $\varphi = 0.06$ vol % of Cu is observed.

During the first heating of the specimens under study at 293 K $\le T \le$ 393 K in the range of the filler content of ($0 \le \varphi \le 0.07$) vol %, the size of the areas proportional to the value of the energy dissipation *P* (ratio (14)) increase. However, after reaching $\varphi = 0.08$ vol %, it has a tendency to decrease (Fig. 2a). In the process of the subsequent cooling of the same specimens, a more uniform modifying of the *P* value (Fig. 2b) is observed (the results in the form of histograms are presented). During the following heating–cooling of the specimens under study, the character of the dependence $P(S) = f(T)|_{\varphi}$, which has been observed earlier, occurs as in the case of the first cooling.

Figure 3 shows the values of the areas in the form of histograms that characterize the resulting process of the heating–cooling of the specimens at ($0 \le \varphi \le 0.1$) vol %

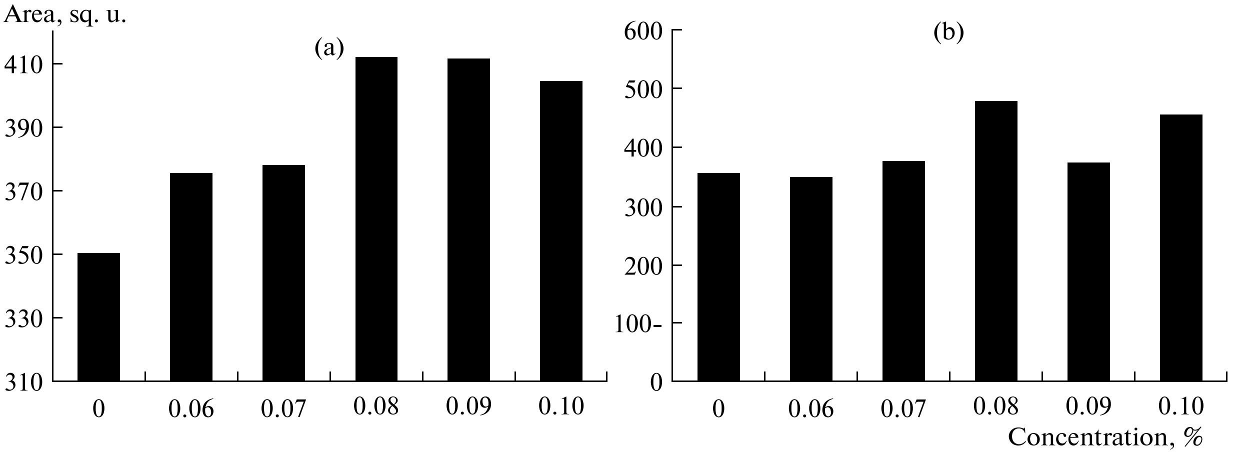

Fig. 2. Histograms of areas of hysteresis curves of $\varepsilon' = f(\varphi)|_T$: (a) heating; (b) cooling.

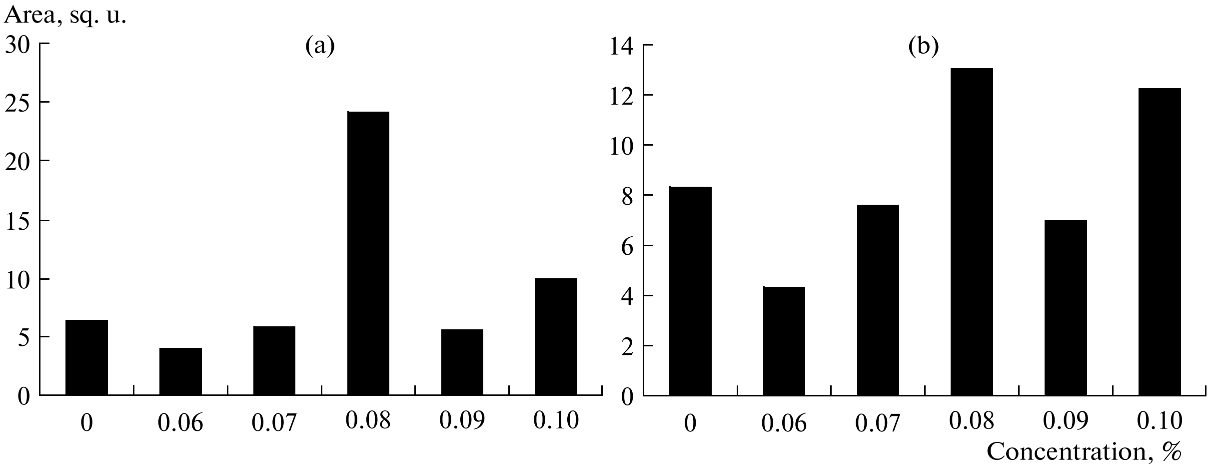

Fig. 3. Histograms of areas of hysteresis curves of $\tan\delta = f(\varphi)|_T$: (a) heating no. 1; (b) cooling no. 2.

of nanodispersed copper. The same as before (Figs. 1–3), a nonlinear character of the modification of the properties of the composite is observed.

The results obtained earlier (Figs. 1–3) allow one, using (14), to trace the character of the changes in the values of $\bar{\varepsilon}\tan\delta = f(T)|_\varphi$ and $\bar{\varepsilon}\tan\delta = \psi(\varphi)|_\tau$, the magnitudes of which are represented as histograms in Figs. 4 and 5. In the process of the repeated heating of the composite after its cyclic heating–cooling, relaxation changes of the topology of the material take place that lead to the ordering of the structural formation of the system.

It was established that, when the rate of the heating of the composite is 3 deg/min, the destruction of the material is not registered [10] in the considered range of temperatures; therefore, the value of the magnitude of $\Delta\left(\frac{1}{4\pi}EdD\right)$ allows one to analyze the character of the ΔS change (13). From the condition of the minimum of ΔW at $d\rho = 0$ (13), it follows that $S_0 < S_1$. The table lists the results of the performed calculations relevant to the values that characterize the electrophysical properties of the material as a consequence of its topological characteristics.

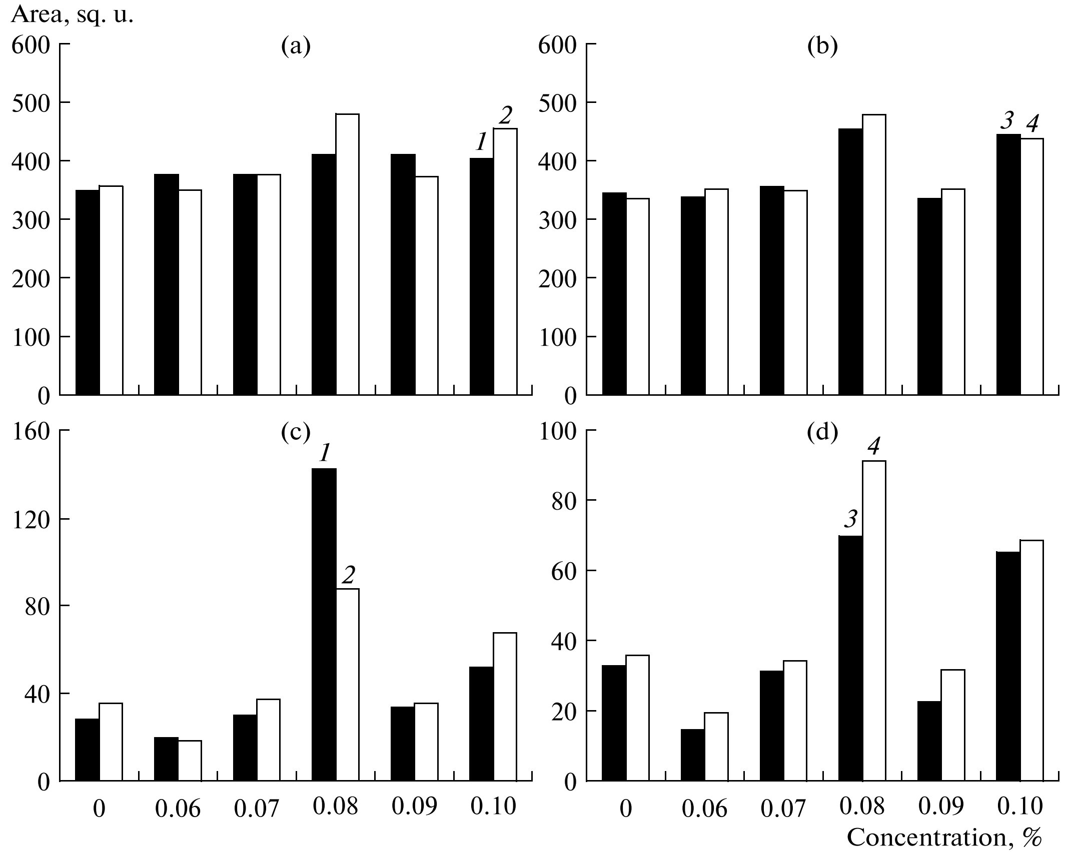

Fig. 4. Histograms of areas of hysteresis curves: (a, b) $\varepsilon' = f(\varphi)|_T$: (b, c) $\varepsilon'' = f(\varphi)|_T$. *1*—heating no.1; *2*—cooling no. 1; *3*—heating no. 2; *4*—cooling no. 2.

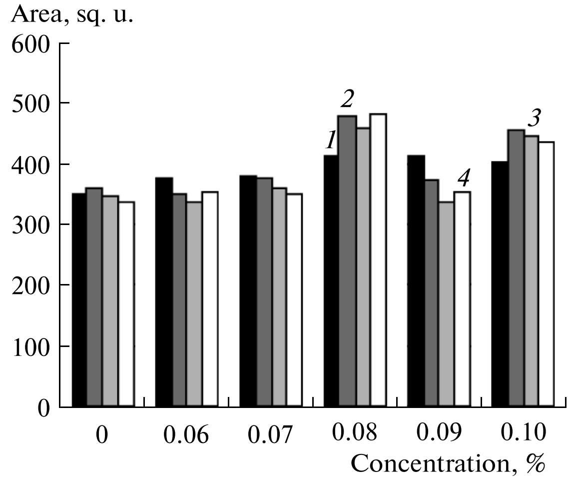

Fig. 5. Histograms of areas of hysteresis curves of $\varepsilon' = f(\varphi)|_T$: *1*—heating no. 1; *2*—cooling no. 1; *3*—heating no. 2; *4*—cooling no. 2.

The values of the areas of the hysteresis curves $\varepsilon' = f(\varphi)|_{T(293-378)}$ of the PCV systems resulting from the heating–cooling of the material

φ, vol %	ε'				ε''				tanδ			
	$S_{\text{heat no. 1}}$	$S_{\text{cool no. 1}}$	$S_{\text{heat no. 2}}$	$S_{\text{cool no. 2}}$	$S_{\text{heat No. 1}}$	$S_{\text{cool no. 1}}$	$S_{\text{heat no. 2}}$	$S_{\text{cool no. 2}}$	$S_{\text{heat no. 1}}$	$S_{\text{cool no. 1}}$	$S_{\text{heat no. 2}}$	$S_{\text{cool no. 2}}$
0	349.36	357.33	346.31	334.84	28.46	35.18	32.78	35.90	6.28	6.87	6.74	8.32
0.06	375.53	348.22	336.55	351.85	19.32	17.68	14.89	19.22	3.86	3.90	3.69	4.30
0.07	377.56	376.44	356.47	349.27	29.85	37.77	31.31	34.03	5.81	8.18	6.43	7.58
0.08	411.52	478.47	455.77	478.88	142.82	87.62	70.23	91.20	24.18	13.29	10.65	12.99
0.09	410.90	373.02	334.71	351.50	33.66	35.05	23.10	31.94	5.46	7.09	5.32	7.00
0.10	404.04	455.72	445.49	436.48	52.22	67.91	65.96	68.92	9.77	11.45	11.78	12.17

CONCLUSIONS

On the basis of the studies, the polymer dielectric materials were found to form heterogenic systems under the effect of the electric breakdown and wire explosion. In this situation, the dissipative processes induced by the effect of the temperature and the alternating electric field may occur due to the heating–cooling of the composite. Using the analytical ratios and the experimental results, it was shown that, in this case, a change in the topology of the material followed by a change in its properties occur. Taking into account the statistic distribution of the nanodispersed metal at $\varphi \leq 0.1$ vol %, the use of a multicore cable is feasible due to the directed effect on the composite structure.

REFERENCES

1. Zel'dovich, Ya. B. and Kompaneets, A.S., *Matematicheskaya teoriya goreniya i vzryva* (Mathematic Theory of Combustion and Explosion), Moscow: Nauka, 1980.
2. Landau, L.D and Lifshits, E.M., *Teoriya polya* (Theory of Field), Moscow: Nauka, 1973.
3. Konel', G.I., Fortov, V.E., and Razorenov, S.V., Shock Waves in Physics of Condensed Stars, *Usp. Fiz. Nauk*, 2007, vol. 177, no. 8, 809–803.
4. Regel', V.P., Slutsker, A.I., and Timoshevskii, E.E., *Kineticheskaya priroda prochnosti tverdykh tel* (Kinetic Nature of Strength of Solid Bodies), Moscow: Nauka, 1974.
5. Robin, T. and Souillard, V., Concentration – Dependent for AC Hopping Conductivity and Permittivity, *Euro-Phys. Lett.*, 1993, vol. 22, no. 9, pp. 729–734.
6. McQuarrie, D.A., *Statistical Mechanics*, New York: Harper and Row, 1976, Ch. 13.
7. Kenyon, W., Texture Effects on Megahertz Dielectric Properties of Calcite Rock Samples, *J. Appl. Phys.*, 1984, vol. 55, no. 8, pp. 3153–3159.
8. Bergman, D.J., Rigorous Bounds for the Complex Dielectric Constants of a Two-Component Composite, *Ann. Phys. (New York)*, 1982, vol.138, no. 1, pp. 78–114.
9. Kolupaev B.S., *Relaksatsionnye i termicheskie svoistva napolnenykh polimernykh system* (Relaxation and Thermal Properties of the Filled Polymer systems), Frenkel',S.L. Ed., Leningrad: Len. Gos. Univ., 1980.
10. Kolupaev B.B., Klepko, V.V., Lebedev, E.V., and Kolupaev, B.S., Phonon Relaxation and Internal Friction in Heterogeneous Systems Based on Polyvenyl Chloride, *Vysokomol. Soedin., Ser. A*, 2010, vol. 52, no. 2, pp. 249–253.

ISSN 1068-3755, Surface Engineering and Applied Electrochemistry, 2011, Vol. 47, No. 1, pp. 100–102. © Allerton Press, Inc., 2011.
Original Russian Text © A.R. Rizun, T.D. Denisyuk, Y.V. Golen', V.Y. Kononov, A.N. Rachkov, 2011, published in Elektronnaya Obrabotka Materialov, 2011, No. 1, pp. 113–115.

OPERATING EXPERIENCE

Electric Discharge Disintegration and Coal Desulphurization in the Manufacture of Water–Coal Fuel

A. R. Rizun, T. D. Denisyuk, Y. V. Golen', V. Y. Kononov, and A. N. Rachkov

Institute of Pulse Processes and Technologies, National Academy of Sciences of Ukraine,
pr. Oktyabr'skii 43-A, Nikolaev, 54018
e-mail: dpcd@iipt.com.ua

Received July 15, 2010

Abstract—The results of monitoring the sulfur content in the components of water–coal fuel at their disintegration with the use of electric discharges were summarized, and a scheme of the desulphurization process was proposed.

DOI: 10.3103/S1068375511010170

The main consumers of coal in Ukraine are the thermal power plants (TPP). A decision to develop the coal strategy of the fuel supply of the TPPs has been adopted for the country's energy security [1]. According to most experts, coal will become a leading energy source of power plants in the XXI century. This in turn should lead to the widespread implementation in practice of fundamentally new methods of preparation of coal for burning in the TPPs. One way of its deep processing is to create a water–coal fuel (WCF). The latter is necessary mainly because, by the ash and sulfur contents and other indicators, coal is of little use in its original form for efficient combustion in power plants.

It is known that about 80% of the coal produced in Ukraine has a sulfur content of more than 1.5%, and, in some cases, it reaches 10%, so the solution to the problem of its desulphurization requires careful consideration and the creation of new high-performance technologies allowing obtaining low-sulfur fuel.

The desulphurization process is rather complicated. The sulfur is contained in coal in the form of pyrite FeS_2 or organic sulfur S. To get rid of it in full by the traditional techniques of enrichment used on an industrial scale (jigging, heavy-media separators, hydrocyclones, countercurrent separation, etc.) is virtually impossible. The level of the sulfur content (less than 1%) is set by environmental standards.

The complexity of the process lies in the fact that the pyrite is in coal in the form of nodules of various shapes and sizes. Fine-grained inclusions of pyrite of less than 100 microns, which are closely related to the matrix with organic matter, are common in most coal [2]. For their separation, the matrix should be cut into a fraction of less than 100 microns followed by the removal of the pyrite or sulfur particles. The operation of crushing is the most time-consuming with high costs of energy and resources.

According to the existing technologies, up to 150 kW h/t is consumed for grinding of the coal to fine fractions (less than 200 microns) [3], and the grinding process does not meet environmental standards for environmental pollution.

In addition, the water–coal suspension obtained by traditional methods of crushing of the coal cannot be used as fuel without clearing it from the sulfur. Additional costs are required for the desulphurization of the suspensions, since in practice the coal preparation using traditional technologies based on gravitational effects for the separation of the combustible mass of the fuel and the inorganic impurities exhibit low efficiency of the desulphurization (no more than 15–20%).

The purpose of this article is the generalization of the results of monitoring the sulfur content in the components of the WCF at their disintegration with the use of electric discharges.

The replacement of the mechanisms of mechanical crushing and grinding of the coal with an electrical discharge provides the following [4]:

—The subtle disintegration of the coal to a fraction below 50 microns with a significantly lower cost of energy (up to 30 kW h/t).

—The decrease of the sulfur content to the standards of the environmental requirements of less than 1%.

—The activation of the solid and liquid phases due to the destruction and thermolysis of the water, the formation in the interfacial environment of H_2O_2 and O_3 molecules, and the formation of a structural-mechanical barrier and the stability of the suspension.

The dynamics of the electric discharge disintegration of coal are that the destruction of the matrix of the original material occurs on the less solid interfaces of the organic grains due to the tension and compression of the matrices by impulsive loads of direct and reflected waves generated by the electric discharge.

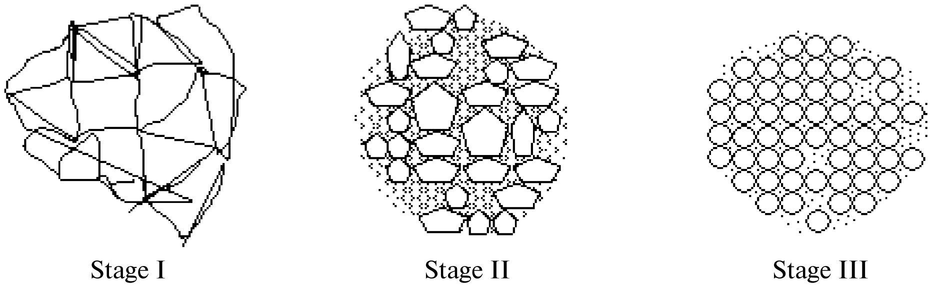

Fig. 1. Stepwise electrical discharge disintegration of coal.

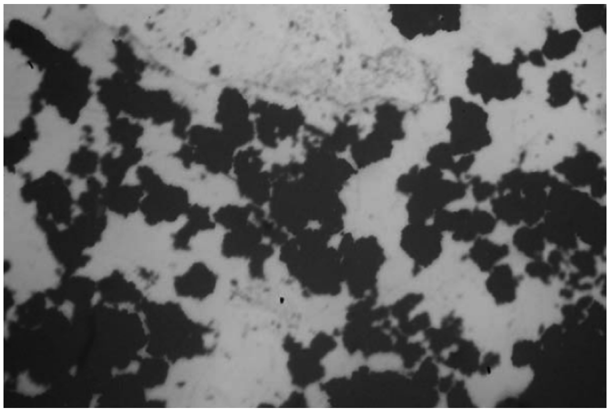

Fig. 2. Optical microscopy of particles (×50).

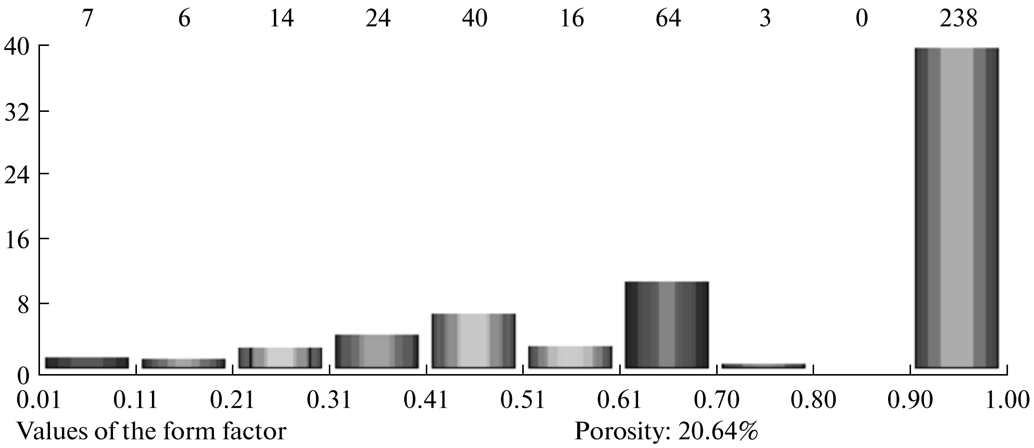

Fig. 3. Distribution of coal particles after processing according to the form factor.

The whole process of the destruction can be divided into three stages (Fig. 1):

Stage I—the formation of cracks at the interfaces between the grains and their development to a critical state;

Stage II—the liberation of grains and their rounding at the expense of breaks of less tough projections;

Stage III—the rounding of grains to sizes of less than 50 microns and the formation of a precipitate from the grains destroyed along the boundaries and fractures.

The dynamics of the electric discharge disintegration of coal and the formation of the final product in the form of small rounded particles are confirmed by the microscopic analysis of the final product (Figs. 2 and 3).

From the distribution of the particles in Fig. 3 by the form factor (the form factor is the ratio of the smallest to the largest particle size), the vast number of

Results of the electrical discharge subtle disintegration and desulphurization of coal grade ASh (0–6)

Experience number	Source material		Energy costs, kW h/t	Finished product	
	Size, mm	Sulfur content, %		Fraction, mm	Sulfur content, %
1	6	3.5	12.0	0.2	2.0
2	6	3.5	16.0	0.1	1.8
3	6	3.5	20.0	0.08	1.2
4	6	3.5	26.2	0.05	0.6
5	6	3.5	29.2	0.05	0.5

particles (238) have a shape close to spherical, and we can assume that their further breakage would require a significant amount of energy. In other words, the grinding has reached its optimum value.

The electric discharge disintegration of coal occurs in conjunction with the processes of its desulfurization.

It is known that the fine-grained particles associated with organic matter and not separated from them during the separation by density even under laboratory conditions [5] are the concentrators of many ash microelements in raw coal. The desulphurization of fine-grained coal and the removing of an amount of the ash microelements may be accomplished using electrical discharge processing.

In the process of the electric discharge desulphurization, part of the organic sulfur is burned at high temperature plasma as the part of pyritic sulfur settles to the bottom of the electric discharge disintegrator and is removed as sludge in the manufacture of water–coal suspensions. The volume of sulfur can be reduced from 3.5 to 0.5% as a result of the electric discharge disintegration of the coal.

Subtle electrical discharge disintegration of coal is possible due to the controllability of the energy dispensed by optimizing the parameters and modes of the discharge. The results of five experiments concerning the complex process of grinding coal and desulphurization are presented in the table.

Since the increase of the energy costs in experiment 5 compared with the experience of 4 does not affect the fractional composition and the amount of sulfur was reduced by only 0.1%, the increase in the energy consumption becomes ineffective. Therefore, experiment 4 is considered the most rational and reasonable, and a further increase in the energy costs is ineffective.

CONCLUSIONS

Electric discharge provides the disintegration and desulphurization of coal and the production of a stable water–coal suspension with an energy consumption 3–5 times smaller than at mechanical crushing and grinding.

The processes of the disintegration and desulphurization were carried out in the complex without violating environmental standards.

Thus, the electrical discharge disintegration not only provides the dispersed phase production in the water–coal suspension but will minimize the emissions of sulfur compounds and a large group of heavy metals into the atmospheric air.

REFERENCES

1. Azarov, S.M., Assessing the Impact of Release of Contaminants to the Environment in the Production of Electricity by Coal Firing, *Ekotekhnol. Resursosberezhenie*, 2001, vol. 3, pp. 53–55.
2. Yudovich, Y.E., and Ketris M.P. *Neorganicheskoe veshchestvo uglei (Inorganic Matter of Coals)*, Ekaterinburg: UrO RAN, 2002.
3. Zaidenberg, V.E., Trubetskoi, K.N., Murko, V. I., and Nehoroshyh, I.H., *Proizvodstvo i ispol'zovanie vodougol'nogo topliva (Production and Use of Coal–Water Fuel)*, Moscow: Izd-vo Akademii Gornyh Nauk, 2001, p. 176.
4. Vysotskii, S.P., Mastika, Y.S., et al., Desulphurization and Coal Preparation prior to Combustion in the TPP, *Energetika Elektrifikaciya*, 1993, vol. 3, pp. 53–56.
5. Rizun, A.R., Golen', Y.V., and Denisyuk, T. D., Development and Implementation of an Electric Discharge Process of Disintegration of the Components of Water–Coal Fuel, *Nauka Innovaci*, 2009, vol. 5, pp. 42–46.